

**b -baryon light-cone distribution
amplitudes and a dynamical theory for
 $[bq][\bar{b}\bar{q}]$ -tetraquarks**

Dissertation
zur Erlangung des Doktorgrades
des Departments Physik
der Universität Hamburg

vorgelegt von

Christian Hambrock

aus Achim, Deutschland

Hamburg

2011

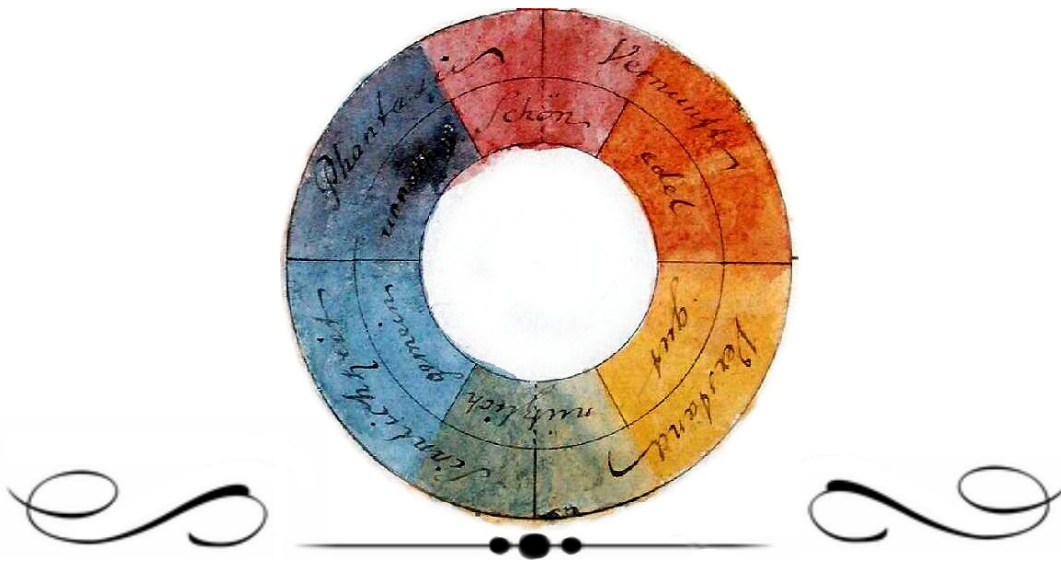
Gutachter der Dissertation: Prof. Dr. A. Ali
Prof. Dr. J. Bartels
Gutachter der Disputation: Prof. Dr. A. Ali
Prof. Dr. G. Kramer
Datum der Disputation: 19.01.2011
Vorsitzender des Prüfungsausschusses: Prof. Dr. G. Sigl
Vorsitzender des Promotionsausschusses: Prof. Dr. J. Bartels
Dekan der Fakultät MIN: Prof. Dr. H. Graener

Abstract

In my thesis I present our work on the bottom-baryon light-cone distribution amplitudes (LCDAs) and on the $[bq][\bar{b}\bar{q}]$ -tetraquarks. For the former we extended the known LCDAs for the ground state baryon Λ_b to the entire b -baryon ground state multiplets and included s -quark mass-breaking effects. The LCDAs form crucial input for the calculations of characteristic properties of b -baryon decays. In this context they can for example be used in the calculation of form factors for semileptonic flavor-changing neutral-current (FCNC) decays. For the $[bq][\bar{b}\bar{q}]$ -tetraquarks, we calculated the tetraquark mass spectrum for all quarks $q = u, d, s, c$ in a constituent Hamiltonian quark model. We estimated the electronic width by introducing a generalized Van Royen-Weisskopf formula for the tetraquarks, and evaluated the partial hadronic two-body and total decay widths for the tetraquarks with quantum numbers $J^{PC} = 1^{--}$. With this input, we performed a Breit-Wigner fit, including the tetraquark contributions, to the inclusive R_b -spectrum measured by BaBar. The obtained $\chi^2/\text{d.o.f.}$ of the BaBar R_b -scan data is fairly good. The resulting fits are suggestive of tetraquark states but not conclusive. We developed a model to describe the transitions $e^+e^- \rightarrow Y_b \rightarrow \Upsilon(nS)(\pi^+\pi^-, K^+K^-, \eta\pi^0)$, in which Y_b is a 1^{--} tetraquark state. The model includes the exchange of light tetraquark and meson states. We used this model to fit the invariant-mass and helicity spectra for the dipionic final state measured by Belle and used the results to estimate the spectra of the channels $e^+e^- \rightarrow Y_b \rightarrow \Upsilon(nS)(K^+K^-, \eta\pi^0)$. The spectra are enigmatic in shape and magnitude and defy an interpretation in the framework of the standard bottomonia, requesting either an interpretation in terms of exotic states, such as tetraquarks, or a radical alteration of the, otherwise successful, QCD-based bottomonium-model. The tetraquark hypothesis describes the current data well. Our fits yield a good $\chi^2/\text{d.o.f.} \approx 1.5$ of the Belle data and show a clear resonant structure originating from the 0^{++} states. Additionally the 2^{++} state $f_2(1270)$ contributes to the transition $Y_b \rightarrow \Upsilon(1S)\pi^+\pi^-$. The predictions for the spectra are distinct from what is expected for the known bottomonia, thus providing specific tests for our tetraquark interpretation. More precise data from not only the Super- B factories at KEK and Frascati, but also from a recent run of the Belle experiment in the first half of 2010 will provide further stringent tests. If our predictions are confirmed by experiments our dynamical model will be the first theoretical work giving rise to the discovery of tetraquarks with a hidden $b\bar{b}$ content.

Zusammenfassung

In der vorliegenden Doktorarbeit präsentiere ich unsere Analyse auf dem Gebiet der Bottom-Baryon Lichtkegeldistributionsamplituden (LCDAs) und der $[bq][\bar{b}\bar{q}]$ -Tetraquarks. Für erstere können wir die bereits bekannten LCDAs des Multiplets der Grundzustandsbaryonen Λ_b auf die Gesamtheit aller bottombaryonischen Grundzustandsmultiplets unter Einbindung der Strange-Quark Massenbrechungseffekte verallgemeinern. Die LCDAs sind unverzichtbare Eingangsgrößen für die Berechnung der charakteristischen Eigenschaften der bottombaryonischen Zerfälle. Für die $[bq][\bar{b}\bar{q}]$ -Tetraquarks haben wir die Tetraquarkmassenspektren für alle Quarks $q = u, d, s, c$ in einem hamiltonischen Konstituentenquarkmodell berechnet. Wir haben für Tetraquarks mit den Quantenzahlen $J^{PC} = 1^{--}$ die elektronische Zerfallsbreite mit einer, für Tetraquarks, generalisierten Van Royen-Weisskopf Formel abgeschätzt, sowie die partielle, als auch die totale, hadronische Zweiteilchen-Zerfallsbreite berechnet. Mit diesen Kenngrößen führten wir eine Breit-Wigner Ausgleichsrechnung, unter Einbeziehung der Tetraquark Beiträge, an das, von BaBar gemessene, R_b -Massenspektrum durch. Das erhaltene χ^2 ist gut. Die resultierenden Parameterabschätzungen sind zwar suggestiv, allerdings nicht eindeutig. Zur Beschreibung der $e^+e^- \rightarrow Y_b \rightarrow \Upsilon(nS)(\pi^+\pi^-, K^+K^-, \eta\pi^0)$ Übergänge entwickelten wir ein Modell, in dem das Tetraquark Y_b mit den Quantenzahlen 1^{--} beiträgt. Unser Modell berücksichtigt den Austausch leichter Tetraquark- und Meson-Zustände. Weiterhin benutzen wir dieses Modell für eine Ausgleichsrechnung der Invarianten-Massen- und Helizitäts-Spektren der von Belle gemessenen dipionischen Endzustände und benutzen die Ergebnisse für eine Abschätzung der Spektren für den Prozess $e^+e^- \rightarrow Y_b \rightarrow \Upsilon(nS)(K^+K^-, \eta\pi^0)$. Die gemessenen Spektren sind rätselhaft in Gestalt und Größenordnung und widersetzen sich einer Interpretation im Rahmen der bereits bekannten Bottomonium-Zustände und verlangen damit nach einer Interpretation durch exotische Zustände, wie beispielsweise Tetraquarks, oder einer radikalen Änderung des, sonst sehr erfolgreichen, QCD basierten Bottomonium-Modells. Unser Modell beschreibt die verfügbaren Daten hingegen sehr gut. Unsere Ausgleichsrechnung für die Belle Daten ergab einen guten Wert von $\chi^2/\#\text{Freiheitsgerade} \approx 1.5$ und wies eine deutlich resonante Struktur mit Ursprung in den 0^{++} Zuständen auf. Zusätzlich trägt der 2^{++} Zustand $f_2(1270)$ bei dem Übergang $Y_b \rightarrow \Upsilon(1S)\pi^+\pi^-$ bei. Unsere Vorhersagen der Spektren sind immanent- und desweiteren gut unterscheidbar von den erwarteten Spektren der bekannten Bottomonia-Familie und stellen damit hervorragende Tests unserer Tetraquark-Interpretation zur Verfügung. Präzisere Daten der Super- B Fabriken am KEK und in Frascati, aber auch von einer in der ersten Hälfte des Jahres 2010 unternommenen Messung am Belle Experiment werden weitere wichtige Tests liefern. Sollte unsere Folgerung von den Experimenten bestätigt werden, wäre unser Modell die erste theoretische Arbeit, die Anlass zur Entdeckung der Tetraquarks mit verstecktem $b\bar{b}$ Quarkgehalt gegeben hat.



Acknowledgments

Foremost I want to thank my supervisor Ahmed Ali for his support and guidance. I very much enjoyed the years during my PhD thesis and the many discussions, in which I had the opportunity to broaden my knowledge in flavor physics thanks to his help and his patience. I am grateful for the support of Prof. Gustav Kramer and Prof. Jan Louis, who wrote me several letters of recommendation and to Gustav Kramer and Joachim Bartels for refereeing my dissertation and my disputation. I am thankful to the many collaborators, Alexander Parkhomenko, Ishtiaq Ahmed, Muhammad Jamil Aslam, Satoshi Mishima, Wei Wang, Yuming Wang and Aoife Bharucha in the past and present works for the nice atmosphere, the opportunity to discuss ideas and to always have someone with an observant eye. Without all these people physics would be pointless for me.

I enjoyed my stay at DESY also thanks to the many nice people and office mates Marco Drewes, Sebastian Mendizabal (vamos chile mierda, weon! - at this point also thanks to Paola Arias), Hao Zou, Cecelie Hector and Sergei Bobrovskiy. During the last years I was (and still am) honored to call many other people friends. I am thankful to Stellan Bohlens, Benjamin Lutz, Tim Köppen, Rüdiger Beisert, Hagen Triendl, Thomas Danckaert, Martin Hentschinski, Tobias Kasprzik, Steffen Fiedler, Johannes Henkel and Flame for the awesome times. To Aoife Bharucha, Stellan Bohlens, Marco Drewes and Tobias Kasprzik I am thankful for proofreading my thesis. Also I want to thank Jeff Hanneman and Chuck Schuldiner along with the people from 2nd-sight for the music and my art teacher Klaus Kehren and the people from the art studio for the inspiring moments and for having the opportunity to free my mind.

Ich möchte auch meiner Familie danken, von der ich weiss, dass sie immer für mich da ist, wenn ich sie brauche, und die mich immer unterstützt hat. Ich danke meinen Eltern Heike und Werner Hambrock, meinen Großeltern Ruth und Arthur Feldmann, meinem Onkel Claus Feldmann und seiner Frau Jutta. Vor allem wünsche ich meiner kleinen Kusine Marie, die jetzt die Jüngste in unserer Familie ist, für ihr zukünftiges Leben Zufriedenheit und alles Gute.

Insbesondere möchte ich Sarah Andreas danken, für ihre Unterstützung und ihre Mühe sich durch meine unfertige Arbeit zu lesen, für ihre Zuwendung und ihre Bereitschaft ihr Leben mit mir zu teilen, ihre Liebe und vor allem einfach dafür, dass sie da ist 🍀.

Contents

Introduction	1
1 HQET in the heavy-quark limit	3
2 b-baryon LCDAs	7
2.1 A compendium of LCDAs	8
2.2 Nonlocal light-cone operators	13
2.3 Local operators	16
2.4 Switching heavy-quark spin on	16
2.5 Correlation functions	17
2.6 The LCDA model	21
2.7 Renormalization	23
2.8 Results	25
3 $[bq][\bar{b}\bar{q}]$-tetraquarks	27
3.1 What are tetraquarks?	27
3.2 Tetraquarks: experimental evidence and history	32
3.3 Our work for tetraquarks in the bottom sector	35
3.4 Mass spectrum of bottom diquark-antidiquark states	40
3.4.1 Lowest lying $[bq][\bar{b}\bar{q}]$ ground states with $L_{Q\bar{Q}} = 0$	43
3.4.2 Excited higher mass $[bq][\bar{b}\bar{q}]$ states with $L_{Q\bar{Q}} = 1$	45
3.5 Isospin breaking and e^+e^- decay widths of the $J^{PC} = 1^{--}$ tetraquarks	48
3.6 $Y_{[bq]}$ decay modes and total decay widths	51
3.7 Analysis of the BaBar R_b energy scan	55
3.8 Analysis of the Belle data on $e^+e^- \rightarrow Y_b \rightarrow \Upsilon(1S)(\pi^+\pi^-, K^+K^-, \eta\pi^0)$	58
3.8.1 Model for the process $e^+e^- \rightarrow Y_b \rightarrow \Upsilon(nS)PP'$	60
3.8.2 Fit to the $\Upsilon(1S)\pi^+\pi^-$ data	67
3.8.3 Predictions for $e^+e^- \rightarrow \Upsilon(1S)K^+K^-$ and $e^+e^- \rightarrow \Upsilon(1S)\eta\pi^0$	69
4 Conclusions and outlook	73

A	Summary of definitions and useful relations	79
A.1	The Dirac field	80
A.2	The gluon field	81
A.3	Spherical harmonics	82
A.4	Master integrals for renormalization	83
B	<i>b</i>-baryon LCDAs	85
B.1	The Borel transform	85
B.2	QCD sum rules	86
B.3	Non-local vertex calculations	88
B.3.1	Vertex calculations lowest order in g_s	88
B.3.2	Vertex calculations first order in g_s	89
B.3.3	Local vertices	90
B.4	Renormalization of the <i>b</i> -baryon LCDAs	91
B.4.1	Lorentz structure of the one-loop diagrams	92
B.5	QCD sum rule results	98
B.6	Numerical results for the LCDAs	99
C	Tetraquarks	101
C.1	Tetraquark interpolating currents	101
C.2	Derivation of the Van Royen-Weisskopf formula	102
C.2.1	Heavy $q\bar{q}$ -quarkonia	103
C.2.2	Heavy $Q\bar{Q}$ -tetraquarks	105
C.3	Kinematics and phase space	106
C.4	Background and resonance contributions	112
C.4.1	Continuum contribution	112
C.4.2	Scalar-resonance contribution $S \rightarrow \pi\pi$	115
C.4.3	$f_2(1270)$ contribution $f_2(1270) \rightarrow \pi\pi$	120
C.4.4	Isospin decompositions	121
C.5	Helicity amplitudes	123
C.6	Decay constant for the η meson	125
C.7	Fitting	126
C.8	Tables for Chap. 3	133

Introduction

This work is concerned with two special topics in heavy-flavor physics: bottom baryon light-cone distribution amplitudes (LCDAs) and hidden bottom tetraquarks. The former describe quark distributions inside single bottom b -baryons. They are needed in the calculations of weak decays in the context of which they are crucial as input in any dynamical model. Weak decays are needed in the determination of the unitary triangle, which is an essential part in the exploration of the validity of the standard model. The attention in flavor physics has so far mostly been focused on the meson sector. Especially in b -physics, the B -factory experiments BaBar and Belle have concentrated on the production and decays of the $b\bar{b}$ resonances, $\Upsilon(1S), \dots, \Upsilon(5S)$, with $\Upsilon(4S)$ and $\Upsilon(5S)$ yielding precise measurements of the B^\pm and $B_d^0 \bar{B}_d^0$ meson characteristics (for a review see for example [1] and references therein). In the future, experiments at the LHC, in particular LHCb, will measure not only the properties of these mesons, but also the copiously produced B_s -mesons and the b -baryons. The LHCb experiment will provide a huge amount of data, pushing the precision in this field of research to the next level. The expected high statistic measurements provide the opportunity to extend the important progress in the B -meson sector achieved over the last decades to the, relatively unexplored, b -baryon sector. Baryons moreover provide access to the exploration of different spin interactions as available from the mesons. Chap. 2, summarizes the work I did on this field of research together with Ahmed Ali and Alexander Parkhomenko.

Tetraquarks are the second topic of my thesis. They are exotic 4-quark hadrons composed of a diquark and an antidiquark, which are bound by attractive QCD forces. A large number of hadrons and their decays have been measured and analyzed theoretically. Especially in the past several years an impressive number of new hadronic states in the mass region of the charmonia have been discovered. Several aspects of the current data are enigmatic in the sense that these states do not fall in line with the known mesons, and so far they have defied unambiguous theoretical interpretation. This charmonium-like exotic hadrons [2], called X , Y and Z , in the literature, which have been measured in a number of experiments [3–18], in particular, BaBar, Belle, CLEO and CDF revived the search for exotic particles. Three different frameworks have been suggested to accommodate these exotic states: (i) $D - D^*$ molecules, containing a hidden $c\bar{c}$ pair ($c\bar{q})(\bar{c}q)$ [19–23, 23–32]; (ii) $c\bar{c}g$ hybrids [33, 34]; and (iii) bound diquark-antidiquark or tetraquark states [35–42]. All these interpretations stretch the current understanding of bound states in QCD, which is mainly restricted to the $q\bar{q}$ mesons and the qqq baryons.

The tetraquarks are also testing grounds for the dynamics of diquarks. Diquarks may play a role in a number of phenomena, such as color superconductivity or in hadronization processes. The proof of the existence of tetraquarks, and hence also the diquarks, will

extend our knowledge of the nature of strong interactions and enormously enlarge the quark model of Gell-Mann and Zweig by the diquarks as new hadron constituents, adding new forms of hadronic interaction and a diversity of bound states. Thus, a quantitative understanding of the exotic mesons, and their kith and kin, in the lighter and heavier $c\bar{c}$ and $b\bar{b}$ sectors, is of utmost importance. In Chap. 3, I present an overview over my studies of the tetraquarks in the bottom sector, which I performed together with Ahmed Ali, two summer visitors at DESY, Ishtiaq Ahmed and M. Jamil Aslam, and Satoshi Mishima. We have calculated the $b\bar{b}$ -tetraquark masses using a constituent quark model and estimated their decay widths. In particular, we have concentrated on the production and decays of the orbital excited P -wave states, having the quantum numbers $J^{PC} = 1^{--}$. They can be produced in e^+e^- annihilation, and we have used our theoretical estimates of the masses and decay widths to search for them in both the BaBar and Belle data in the region above 10.54 GeV [43]. We have also worked out a dynamical model to understand the measured dipionic transitions involving the decays of $Y_b \rightarrow (\Upsilon(1S), \Upsilon(2S))\pi^+\pi^-$, where Y_b is a $b\bar{b}$ bound tetraquark state [44]. Moreover, the model is used to provide testable predictions for the transition $Y_b \rightarrow \Upsilon(1S)(K^+K^-, \eta\pi^0)$. With our work we were able to present a case for the first tetraquark candidates observed in the bottom sector. The analysis of the data of the recent Belle running in the first half of 2010 will hopefully tell us in the near future if our tetraquark interpretation is confirmed.

In Chap. 1 I give a brief account of the theoretical background. Since the two main topics in this work are only remotely related, the common theoretical background is kept short and every part has a short introduction on its own. Chap. 2 presents my work on the LCDAs, and Chap. 3 is dedicated to the hidden bottom tetraquarks. In Chap. 4 I conclude and give an outlook over expected results and outline promising future works.

Various details can be found in the appendices. App. A contains a summary of used formulas and conventions. The details for the LCDAs and the tetraquarks can be found in App. B and C, respectively.

Chapter 1

HQET in the heavy-quark limit

The two topics in my thesis have in common, that both involve one or more bottom-quarks plus lighter ones combined in a hadronic bound state. Here I introduce the effective field-theory approach to describe such states. The arguments and formulas presented in this thesis are to some extent valid for all heavy charm and bottom-quarks (labeled c and b respectively). Since throughout my work I am only concerned with the latter ones, I refrain from introducing different notations for heavy-quark fields and discuss everything by explicitly referring to the b -quark. Note, that the top-quarks play a special role among the heavy-quarks: Due to its large mass the top-quark has an extremely short lifetime. In consequence it decays faster than the actual hadronization process. Accordingly, there are no top-quark bound states.

Naturally two or more energy scales are involved in the heavy-light-quark dynamics, the heavy-quark mass and the lower QCD scale. The *heavy-quark effective theory* or short HQET was developed to deal with scenarios of this type. It is a useful tool to handle heavy-quarks in an effective field theory approach. It is surprising what the few and simple derivations in this short chapter provide in insight in the field of heavy-flavor physics. The results discussed here will be needed throughout this thesis.

HQET is based on an expansion in the inverse heavy-quark mass $1/m_b$, or more precisely, in the dimensionless quantity Λ/m_b , where Λ is a characteristic hadronic energy scale in a certain problem, typically $\Lambda \simeq \mathcal{O}(\text{few hundred MeV})$. It is assumed, that the b -quark mass is sufficiently larger in comparison with all other present energy scales. In QCD bound states Λ is typically given by the confinement energy Λ_{QCD} or the confinement radius $1/\Lambda_{QCD}$. Sizes of hadronic states are usually of order 1 fm, which corresponds to $\Lambda_{QCD} \approx 200$ MeV. As one can see, in the bottom sector with $\Lambda/m_b \approx \mathcal{O}(1/10)$ an expansion in this parameter converges in general quite fast. Therefore I consider only the leading order in the heavy-quark expansion, in which $m_b \rightarrow \infty$, and hence the b -quark mass becomes a non-dynamical constant quantity. This approximation is called the *heavy-quark limit*. Neither in this chapter nor in the whole work I go beyond this approximation. For a textbook about this topic see for example [45].

The b -quark part of the QCD Lagrangian is given by

$$\mathcal{L}_{QCD} = \bar{Q}(i\not{D} - m)Q + \dots, \tag{1.0.1}$$

where Q denotes the heavy b -quark field, and the dots denote all other QCD interaction

terms, such as light-quark and gluonic interactions. The color $SU(3)$, abbreviated as $SU(3)_C$, covariant derivative is given by $D_\mu = (\partial_\mu - iA_\mu)$, where $A_\mu = g_s A_\mu^a t_a$ is the gluon field, g_s is the color charge, which is related to the strong coupling constant via $g_s^2/4\pi = \alpha_s$ and t_a are the generators of the $SU(3)_C$. The index a runs over the adjoint gluon representation from 1 to 8. The indices for the fundamental triplet quark representation are left implicit. Assuming as stated earlier, that all momenta are much smaller than m_b , the momentum p_b for a heavy-quark moving with velocity v is written as

$$p_b = m_b v + \tilde{p}, \quad \text{with } v^2 = 1, \quad (1.0.2)$$

in which \tilde{p} is the residual momentum with $|\tilde{p}^\mu| \ll m_b$, which vanishes in the heavy-quark limit. By choice of reference frame the b -quark is moving slowly with velocity v and hence this approximation violates Lorentz invariance. That this approximation works indeed well in practice can be seen at the meson mass spectrum, in which it is observed, that the meson mass of the heavy mesons is close to the constituent heavy-quark mass, which implies a slow moving heavy-quark. If convenient one can also consider the b -quark at rest with $v^\mu = (1, 0, 0, 0)$ and perform a Lorentz boost with velocity v afterwards (for the Lorentz boost see App. C.3). According to Eq. (1.0.2), the b -quark is on-shell in the heavy-quark limit because $|\tilde{p}|/m_b \rightarrow 0$ and hence the heavy b -quark field fulfills the non-relativistic on-shell condition

$$\not{p}Q = Q. \quad (1.0.3)$$

The lower spinor components of Q , which are the negative energy solutions, vanish since this equation projects out half of the components of the heavy-quark spinor, restricting it to be a particle without antiparticle component. This can easiest be seen choosing the rest frame $v^\mu = (1, \vec{0})$, in which Eq. (1.0.3) becomes

$$(\gamma_0 - \mathbb{1})Q = 0, \quad \text{with} \quad (1.0.4)$$

$$\gamma_0 - \mathbb{1} = -2 \begin{pmatrix} 0 & 0 & 0 & 0 \\ 0 & 0 & 0 & 0 \\ 0 & 0 & 1 & 0 \\ 0 & 0 & 0 & 1 \end{pmatrix} \quad \text{in the Dirac representation.} \quad (1.0.5)$$

Obviously the matrix kernel is two dimensional. Because particles and antiparticles have different parity and γ_0 is the parity operator in spinor space this equation expresses, that the antiparticle components of the heavy-quark spinor are projected out.

With the use of Eq. (1.0.2) the fermion propagator can be expanded in the inverse of the heavy-quark mass. In zeroth order the b -quark propagator is then given by

$$\frac{m_b + m_b \not{v} + \not{\tilde{p}}}{(m_b v + \tilde{p})^2 - m_b^2 + i\epsilon} = \frac{1 + \not{v}}{2} \frac{1}{\tilde{p} \cdot v + i\epsilon} + \mathcal{O}(1/m_b). \quad (1.0.6)$$

With the help of

$$\int_{-\infty}^{\infty} \frac{e^{-i\omega t}}{(-\omega - i\epsilon)^n} \frac{d\omega}{2\pi} = \frac{i^n}{\Gamma(n)} t^{n-1} \Theta(t), \quad (1.0.7)$$

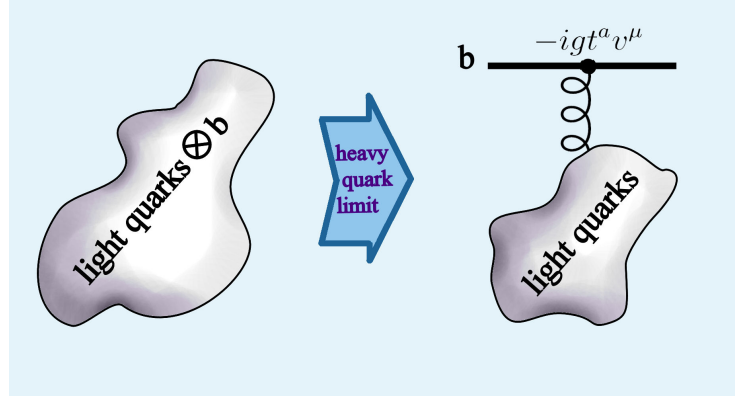


Figure 1.1: Schematic picture of the simplifications arising in the heavy-quark limit for a bound state containing a single b -quark. The heavy-quarks is put on-shell and the coupling to the light-quark cloud is independent of the heavy-quark spin.

the b -quark propagator in coordinate space is obtained:

$$i \langle T\{Q(x)\bar{Q}(0)\} \rangle = \frac{1+\psi}{2} \int dt \delta^4(x-vt), \quad (1.0.8)$$

and the b -quark behaves like a classical pointlike source moving with velocity v and Lorentz structure $(1+\psi)/2$.

The heavy-quark propagator provides enough information to determine the spin dependent interaction of the b -quark. By using the simple identity

$$\frac{1-\psi}{2} \gamma^\mu \frac{1-\psi}{2} = \frac{1-\psi}{2} v^\mu \frac{1-\psi}{2}, \quad (1.0.9)$$

which is present whenever a gluonic interaction is sandwiched between two b -quark propagators in the heavy-quark limit, the coupling of the b -quark and the gluon field can be simplified by

$$\begin{array}{c} \diagup \\ \diagdown \end{array} \begin{array}{c} \text{---} \\ \text{---} \\ \text{---} \end{array} \begin{array}{c} \mu a \\ \text{---} \\ \text{---} \end{array} \hat{=} i g t^a \gamma^\mu \longrightarrow i g t^a v^\mu \hat{=} \begin{array}{c} \diagup \\ \diagdown \end{array} \begin{array}{c} \text{---} \\ \text{---} \\ \text{---} \end{array} \begin{array}{c} \mu a \\ \text{---} \\ \text{---} \end{array}. \quad (1.0.10)$$

Throughout this work the heavy-quark is represented by a thick line. Eq. (1.0.10) is also true for external states because the on-shell condition (1.0.3) for the external fields allows for the insertion of the same projector. An equivalent statement is, that the heavy-quark spin can be rotated arbitrarily or switched off (superflavor symmetry). The simplifications arising from the Eqs. (1.0.3) and (1.0.10) are pictured in Fig. 1.1 for a hadronic bound state containing one b -quark.

The Lagrangian, describing the b -quark in the heavy-quark limit, which corresponds to the properties in Eq. (1.0.9) and (1.0.10) is given by

$$\mathcal{L}_{QCDv} = \bar{Q}_v i v \cdot D Q_v + \dots, \quad (1.0.11)$$

where the index v is a reminder of the Lorentz frame in which the Lagrangian is defined.

The simple expressions obtained in the heavy-quark limit, especially Eqs. (1.0.3) and (1.0.10), lead to far-reaching simplifications. Anticipatory of what is coming in the following chapters, let me name two of them: Due to the spin decoupling the number of twist ordered wave functions reduces by a factor of four (the degrees of freedom of the heavy-quark spinor), as will be shown in Chap. 2. The spin decoupling gives us an argument at hand, that there might be vector-like heavy-diquarks even though there is evidence, that they do not exist in the light-quark sector, which is discussed in Chap. 3.

Chapter 2

b -baryon LCDAs

In this chapter, I discuss the calculation of single bottom baryon *light-cone distribution amplitudes*, or short LCDAs. First I will give a short overview about the nature of the single bottom-baryons, in which context their LCDAs are needed and which role the LCDAs play in decay processes. Then I present the work I did together with Ahmed Ali and Alexander Parkhomenko. Our analysis is similar to the work of Ball, Braun and Gardi [46], in which the case of Λ_b -baryon is presented. We generalized their work to describe all ground state b -baryons, including higher spin states, and incorporated flavor $SU(3)$, or shorthand $SU(3)_F$, breaking effects by taking the mass of the s -quark into account. Both approaches, our and [46], are based on HQET in the heavy-quark limit and QCD sum-rules.

The b -baryons will be copiously produced at the LHC and their decays will be measured at the LHC b experiment. Of special interest are the decays in which the b -quark inside the baryon decays weakly and the baryon undergoes a transition to a different hadronic final state. These flavor changing decays may give new perspectives on the determination of the unitary triangle and therefore provide some hints on new physics beyond the standard model in the same fashion decays of heavy mesons did during the last decades. As is pointed out in [46], the advantage of baryons over mesons is the different spin assignment of its constituent quarks, which will provide new understanding of high energetic spin interactions. Our generalizations to the full ground state multiplets will provide new input for this analysis, and the calculated $SU(3)_F$ breaking effects might further be of interest for studying strange-quark properties. Especially the Ξ -resonances include three different mass quarks, the bottom, the strange and one light u or d quark are of relevance. They might give interesting insights on the nature of the strange-quark propagating in QCD background and give some hints on the validity of quark condensate models. Comparison with the kaon or B_s system will show to what extent the condensates are universal quantities.

First I introduce the framework of the LCDAs and discuss their definition by non-local operators in Sec. 2.1 and 2.2. In Sec. 2.3 and 2.4 I discuss the local limit of the operators and show how to restore Lorentz invariance, which is broken in the heavy-quark limit. The calculations of the correlation functions, which are defined as matrix elements of the non-local and local operators are performed subsequently in 2.5 followed by their renormalization in 2.7. At the end I present the results in 2.8. Tedious calculations and reviews of the used techniques for this chapter are sourced off to App. B for clearer reading.

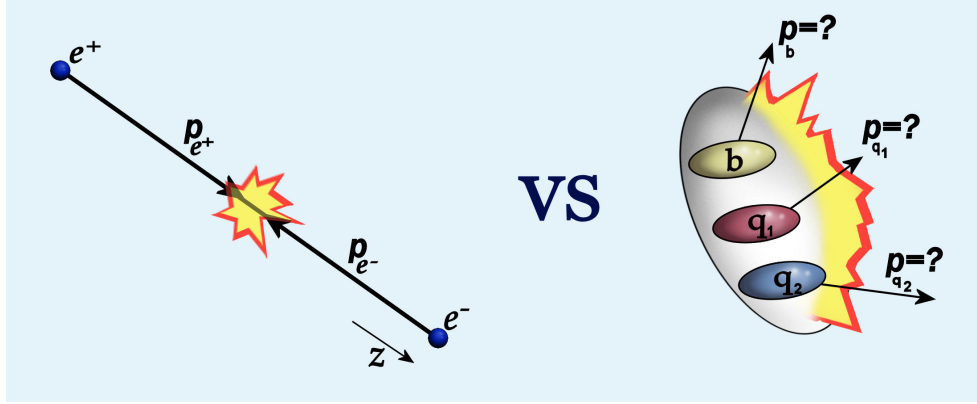


Figure 2.2: Fixed initial state kinematics of an e^+e^- accelerator on the left side compared with the decaying b -baryon with initial state momentum distribution provided by the LCDAs on the right side. The initial state kinematics for the former is trivial, while the initial state kinematics for the latter, *i.e.* the parton distributions, can only be obtained approximately.

2.1 A compendium of LCDAs

A b -baryon consists of three valence-quarks, a single bottom-quark and two light-quarks q , which are in this chapter representatives of the light-flavor $SU(3)_F$ group and can thus be an up, down or a strange-quark ($q = u, d, s$).

The b -quark inside the baryon can decay by coupling weakly to a W -boson, involving the elements of the CKM matrix V_{ub} or V_{cb} . In simplified words the weakly decaying b -baryons are small accelerators running at an energy region of a few GeV. While the e^+e^- machines have a very simple asymptotic kinematic (two almost massless fermions at fixed center of mass energy \sqrt{s} are moving towards each other along the beam axis with $p_{e^+} = (\sqrt{s}, 0, 0, \sqrt{s})/\sqrt{2}$ and $p_{e^-} = (\sqrt{s}, 0, 0, -\sqrt{s})/\sqrt{2}$), the baryons are more complicated. A schematic picture, in which the initial state kinematics of an e^+e^- accelerator is compared with the initial state kinematics of a weakly decaying b -baryon, is given in Fig. 2.2, in which the momenta p_i of the quarks which leave the baryon during its decay are not fixed as the momenta of the electrons and positrons in the storage rings. They are distributed in phase space with certain probabilities. To calculate the b -baryon decays, this probability distributions need to be known. The purpose of the *light-cone distribution amplitudes* is to provide these distributions. However, since they can be arbitrarily complicated, models such as LCDAs are to some extent limited, as will be discussed in the following.

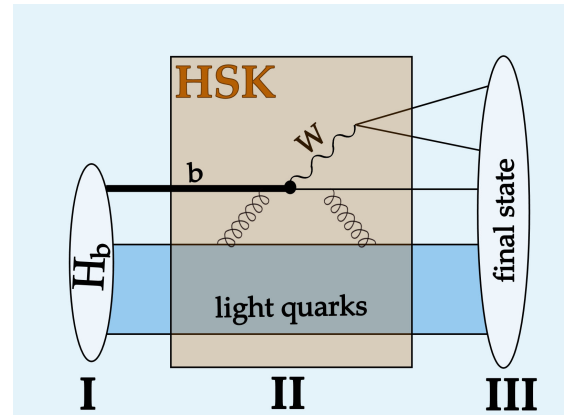


Figure 2.1: Weak decay of a heavy hadronic state I into a final hadronic bound state III. The interaction region II is perturbative and can be calculated on partonic level.

Since the binding energy is of order $\Lambda_{QCD} < 1\text{GeV}$, the hadronic bound states are non-perturbative objects. However, when the b -quark decays the energy is larger than the confinement scale, involving a perturbative part called *hard scattering kernel* or short HSK, see Fig. 2.1. The energy scale of the decay is given by the mass difference of the heavy b -quark and the lighter quark produced in its weak decay. For a b -quark decaying in a light-quark (u, d, s), the energy is approximately of the order of the b -quark mass $m_b \approx 4 - 5 \text{ GeV}$. For perturbation theory to be applicable at partonic level, the high energetic, or hard part, has to be separated from the low energy bound states, and the state has to be split in its partonic components. This means, that the incoming baryonic state $|H_b\rangle$ has to be rewritten in the partonic basis, *i.e.* the Fock-State basis

$$|H_b\rangle = \sum_I |P_I\rangle \langle P_I | H_b\rangle, \quad (2.1.1)$$

in which the formal sum over I includes summation and integration over all possible quantum numbers characterizing the states. The Fock state $|P_I\rangle$ depends on the partonic momenta and polarizations and is weighted by the probability (or wave function) $\langle P_I | H_b\rangle$ for finding the state $|P_I\rangle$. The process shown in Fig. 2.1 can thus formally be written as

$$|H_b\rangle = \sum_I \langle \text{final state} | \text{HSC} | P_I\rangle \langle P_I | H_b\rangle. \quad (2.1.2)$$

If there are hadronic particles left in the final state, a similar expansion in their Fock states needs to be performed, and the partonic amplitude, which includes the interaction described by the HSK, can be calculated using Feynman rules. The formal sum is performed afterwards, and thus the Feynman amplitude is convoluted with the wave functions.

A hadron consists of infinitely many partonic states, containing valence-quarks, sea-quarks, gluons and other elementary particles. Since one can not account for all of them, some approximation has to be made. The simplest possibility is to adopt the valence-quark approximation by taking into account only the valence-quark state $\langle P_0 | = \langle bqq |$, which is the lowest order term in the Fock state basis. Furthermore, the dominant contribution of the wave functions is originating from the part, where the light-quarks propagate near the light-cone (for a review see [47]_{Chap. 4}). In leading order in the expansion of the light-quarks in the vicinity of the light-cone, the quarks are aligned along a light-like direction n_μ ($n^2 = 0$) hence the ‘‘L’’ in LCDA. Choosing the b -quark to be in the origin of the coordinate frame, the dynamics is described by the projections t_i of the light-quark coordinates on the axes along n^μ , shown in Fig. 2.3.

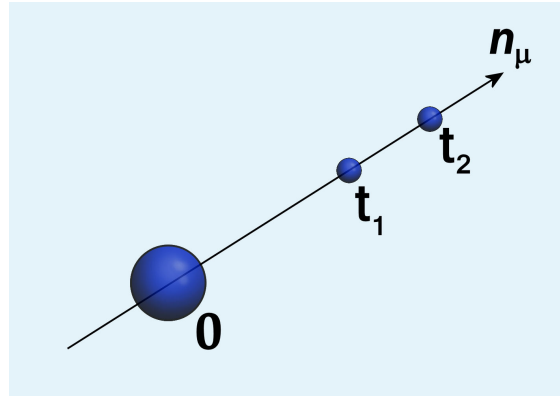


Figure 2.3: Lightcone approximation. n_μ is a light-like vector and t_1 and t_2 are the coordinate projections of the light-quark coordinates on the light-like axis. The origin coincides with the b -quark (big blue sphere). This constellation gives the dominant contribution to the wave function.

To calculate the LCDAs, one needs to give a meaning of the rather formal definition of the wave function in Eq. (2.1.1) in the valence-quark approximation

$$\langle P_0 | H_b \rangle = \langle q_1 q_2 b | H_b \rangle \quad (2.1.3)$$

in a quantitative way. However, it is not possible to use creation and annihilation operators to get hadron-to-vacuum transition matrix elements of the form

$$\langle q_1 q_2 b | H_b \rangle = \langle 0 | q_1(nt_1) q_2(nt_2) b(0) | H_b \rangle \quad (2.1.4)$$

in a straightforward manner. To ensure $SU(3)_C$ gauge invariance, gauge factors

$$E(x, y)^{i'}_i = P \left\{ e^{-ig_s \int_x^y dz^\mu A_\mu^c(z) t^{ci'}_i} \right\}, \quad (2.1.5)$$

the so called Wilson lines have to be included. In this expression P indicates path ordering, g_s is the strong coupling constant, n_μ is the above defined light-like vector, and A_μ is the gluon field. In the light-cone gauge with $A_+ = 0$ the Wilson lines vanish because they fulfill $E(t_i n, t_j n)^{i'}_i = \delta_i^{i'}$. The necessity of the Wilson lines can be easily understood in the language of gauge theory and its principle of locality. An object needs to be locally gauge invariant, here under the color $SU(3)_C$. If the baryon state is defined through non-local operators, one needs to take care, that the baryon is not defined at several spacetime points at the same time. The gauge links ensure that all colored objects are transported to the one spacetime point where the baryon is then properly defined. By convenience this will be the coordinate of the bottom-quark. Including index and coordinate structure, the operators are given by

$$\langle q_1 q_2 b | H_b \rangle = \epsilon^{ijk} \langle 0 | q_1(t_1 n)_{\alpha i'} q_2(t_2 n)_{\beta j'} b(0)_{\gamma k} E(t_1 n, 0)^{i'}_i E(t_2 n, 0)^{j'}_j | H_b \rangle, \quad (2.1.6)$$

where α, β and γ are spinor indices, i, i', \dots are color indices. For abbreviation, color indices and Wilson lines are henceforth left implicit.

In a nutshell one can say, that the LCDAs give the probability to find a certain given light-like coordinate distribution inside the baryon and are defined through the non-local light-ray operators in Eq. (2.1.6).

The heavy-quark limit is adopted for the following calculations, thus the mass of the heavy-quark is assumed to be arbitrary large. Thereby contributions proportional to $\frac{\Lambda_{QCD}}{m_b}$ are neglected, as discussed in Chap. 1. Two major simplifications arise in this limit. The heavy-quark can be set on mass-shell, moving with a constant velocity v_μ . Thus it becomes an external color source and obeys the non-relativistically normalized Dirac equation (1.0.3). The second important simplification arises due to the reason, that the spin dependent interactions of the light-quarks with the heavy quark enter with a factor $\frac{\Lambda_{QCD}}{m_b}$ and thus can be neglected, according to the heavy-quark spin symmetry in Eq. (1.0.10). In this way another half of the components of the heavy-quark spinor is projected out.

Without the heavy-quark limit the bound state of three quarks transforms under a representation of the $spin(3, 1)$. The $spin(3, 1)$ is given by the double covering of the spin group $SU(2) \oplus SU(2)$. Every fermion spinor is composed of two two-component Weyl spinors and transforms under the fundamental representation $\{0, \frac{1}{2}\} \oplus \{\frac{1}{2}, 0\}$. Hence, every

valence-quark transforms as a four component spinor. Because there are three valence-quarks, the third tensor product of the fundamental representation gives the multiplets of a three-quark state. In conclusion, the correlator

$$\langle 0 | q_{1\alpha} q_{2\beta} b_\gamma | H_b \rangle, \quad (2.1.7)$$

with spinor indices α , β and γ can be expanded in a $4^3 = 64$ dimensional covariant basis $C_{\alpha\beta\gamma}^I$ with $I = 1, \dots, 64$, which has been done in [48]. The present case simplifies in the heavy-quark limit, since, due to the discussed symmetries, all spinor degrees of freedom of the heavy-quark have been projected out. One finds, that the tensor product in the spinor space is in this limit merely a normal product of the light-quark system with the heavy-quark:

$$C_{\alpha\beta\gamma}^I \rightarrow B_{\alpha\beta}^J \times \psi_\gamma, \quad J = 1, \dots, 16. \quad (2.1.8)$$

Hence, the b -baryons are not characterized by the overall spin, but by the spin of the light-quark system. Therefore there are no spin 1/2 or spin 3/2, but scalar spin 0 or vector spin 1 b -baryons, see Fig. 1.1. The Lorentz structure of the baryon is equal to the structure of the product of an on-shell spinor ψ_γ with a light scalar meson ($s_l = 0$) in the case of Λ_b^0 and a vector meson ($s_l = 1$) in the case of Σ_b . The meson structure has already been discussed in [49].

The ground state $SU(3)_F$ baryon multiplets considered in this work are pictured in Fig. 2.4, in which the two different multiplets are characterized by the spin parity j^p of the light-quark system. In the state with $j^p = 0^+$ the spin wave-function is antisym-

metric, while Fermi statistics of the baryon state and antisymmetry in color space require antisymmetric flavor wave-function. This results in a baryonic state with isospin $I = 0$

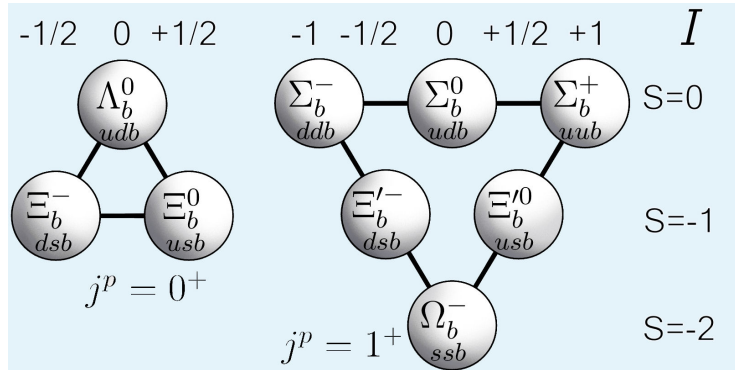


Figure 2.4: The $SU(3)_F$ flavor multiplets of the bottom-baryons. The flavor $SU(3)_F$ triplet with spin-parity $J^P = 1/2^+$ and scalar light-quark current ($j^p = 0^+$) is shown to the left, and the heavy-quark doublet with spin-parity ($J^P = 1/2^+$, $J^P = 3/2^+$) and vector light-quark current ($j^p = 1^+$) is shown to the right. Isospin and strangeness are given by I and S respectively.

constructed from the light u - and d -quarks which is called the Λ_Q -baryon (the overall spin-parity is $J^P = 1/2^+$). When the light-quark state has quantum numbers $j^p = 1^+$, the baryons come in doublets (with overall spin-parity $J^P = 1/2^+$, $J^P = 3/2^+$). The spin part for these baryons of the baryon wave-function is symmetric, which requires symmetry of the wave-function in flavor space. In the case of light u - and d -quarks this gives two degenerate states with isospin $I = 1$, which are called Σ_Q^- and Σ_Q^* -baryons. Inclusion of the s -quark increases the number of heavy baryons in the multiplet, characterized by strangeness S . If $S = -1$, there are two baryonic states Ξ_Q and Ξ_Q^* with $J^P = 1/2^+$ and

Ξ_Q^* -baryon with $J^P = 3/2^+$. For $S = -2$, the baryons with $J^P = 1/2^+$ and $J^P = 3/2^+$ are called Ω_Q and Ω_Q^* respectively.

To find an explicit Lorentz-invariant expression for the basis in (2.1.8), $B_{\alpha\beta}^J$ can be expanded in γ -matrices. The only Lorentz-invariant possibilities in the expansion are the metric $g_{\mu\nu}$ and the following antisymmetric tensors

tensor	degrees of freedom	
$\mathbb{1}$		1
γ_μ		4
$\gamma_{[\mu}\gamma_{\nu]}$	$= -i\sigma_{\mu\nu} = \frac{1}{2}\epsilon_{\mu\nu\rho\sigma}\sigma^{\rho\sigma}\gamma_5$	6
$\gamma_{[\mu}\gamma_\nu\gamma_{\rho]}$	$= -i\epsilon_{\mu\nu\rho\sigma}\gamma^\sigma\gamma_5$	4
$\gamma_{[\mu}\gamma_\nu\gamma_\rho\gamma_{\sigma]}$	$= -i\epsilon_{\mu\nu\rho\sigma}\gamma_5$	1

(2.1.9)

where the notation $\gamma_{[\mu}\gamma_{\nu]} = \frac{1}{2}(\gamma_\mu\gamma_\nu - \gamma_\nu\gamma_\mu)$, etc. has been adopted. Note, that the third (fourth) grade tensors are equal to the first (zeroth) grade tensors with opposite parity due to duality. In total 5 tensors $\mathbb{1}$, γ_μ , $\sigma_{\mu\nu}(\simeq \sigma_{\mu\nu}\gamma_5)$, $\gamma_\mu\gamma_5$ and γ_5 with combined $4^2 = 16$ degrees of freedom have to be taken into account in the expansion. The parity of each considered baryonic state needs to be positive, and the parity operator for a three-spinor object is obtained by acting on each spinor index with γ_0 :

$$B_{\alpha\beta}^J \times \psi_\gamma \xrightarrow{\text{parity}} (\gamma_0 \tilde{B}^J \gamma_0^T)_{\alpha\beta} \times (\gamma_0 \tilde{\psi})_\gamma = (\gamma_0 \tilde{B}^J \gamma_0)_{\alpha\beta} \times \psi_\gamma. \quad (2.1.10)$$

The tilde indicates the parity transformation. A more convenient basis is obtained by multiplying each element with the charge conjugation matrix C , which is in the Pauli-Dirac representation given by $C = i\gamma_2\gamma_0$. Hence, Eq. (2.1.7) can be expanded in the basis in (2.1.9) with unknown coefficient functions ϕ_i :

$$\langle 0 | q_{1\alpha} q_{2\beta} b_\gamma | H_b \rangle = \frac{1}{4} (\phi_1 C \gamma_5 + \phi_{2\mu} C \gamma_5 \gamma^\mu + \phi_{3\mu\nu} C \sigma^{\mu\nu} + \phi_{4\mu} C \gamma^\mu + \phi_5 C)_{\alpha\beta} \psi_\gamma. \quad (2.1.11)$$

By taking the trace and using the orthogonality of the matrices every coefficient function is defined by an interpolating operator. As example I show how the first coefficient function ϕ_1 is projected on its corresponding interpolating current:

$$\begin{aligned} \langle 0 | q_1 C \gamma_5 q_2 b_\gamma | H_b \rangle &= \frac{1}{4} (\gamma_5^T C^T)^{\beta\alpha} (\phi_1 C \gamma_5 + \phi_{2\mu} C \gamma_5 \gamma^\mu + \phi_{3\mu\nu} C \sigma^{\mu\nu} + \phi_{4\mu} C \gamma^\mu + \phi_5 C)_{\alpha\beta} \psi_\gamma, \\ &= \phi_1 \psi_\gamma, \end{aligned} \quad (2.1.12)$$

where the second and the fourth traces vanish because they include an odd number of γ matrices, the third because $\sigma^{\mu\nu}$ is antisymmetric and the last one because the trace of γ_5 is 0. In this way all of the basis elements are orthogonal with respect to each other and the Dirac structure can be moved to the light-quark currents, projecting out the corresponding coefficient function. According to (2.1.10) the light-quark currents have the following transformation properties:

$q_1 C \gamma_5 q_2$ scalar	$q_1 C \gamma_5 \gamma_\mu q_2$ vector	$q_1 C \sigma_{\mu\nu} q_2$ tensor	$q_1 C \gamma_\mu q_2$ pseudovector	$q_1 C q_2$ pseudoscalar
--------------------------------	---	---------------------------------------	--	-----------------------------

(2.1.13)

In summary the b -baryon in the approximations made here is composed of a scalar on-shell b -quark surrounded by off-shell light-quarks, moving on the light-cone. The latter are in spinor space the same objects as mesons. The wave functions giving the parton distributions on the light cone are according to Eq. (2.1.12) defined by corresponding matrix elements.

2.2 Nonlocal light-cone operators

The explicit form of the baryonic operators defined in (2.1.6) is derived in this section. The operators for the $j^P = 0^+$ triplet are known and given in [46]_{Eq. 1}. This section is about the sextet in Fig. 2.4.

According to the discussion in the previous section, the Rarita-Schwinger vector-spinor R^μ_γ describing the $j^P = 1^+$ baryon sextet can be written as a product $R^\mu_\gamma \rightarrow \varepsilon^\mu u_\gamma$ of the heavy-quark spinor u_γ and the polarization vector ε^μ of the light-quark system, described by Eq. (2.1.8) or Fig. 1.1. This is the effect of spin decoupling of light and heavy degrees of freedom in the heavy-quark limit. The properties of u_γ and ε^μ are shortly reviewed, while detailed information can be found in [50]_{Eqs. 2.12, 2.13}. Afterwards the baryonic currents are constructed.

The spin sum is given by

$$\sum_{i=1}^2 u^i \bar{u}^i = P_+ \quad \text{and} \quad \sum_{i=1}^3 \varepsilon_\mu^{*i} \varepsilon_\nu^i = -g_{\mu\nu} + v_\mu v_\nu, \quad (2.2.1)$$

with $P_+ = (1 + \not{v})/2$ and normalization

$$-g^{\mu\nu} \sum \text{Tr} [u \varepsilon_\mu^* \varepsilon_\nu \bar{u}] = 6, \quad (2.2.2)$$

which corresponds to the number of degrees of freedom (3 from the light-quark polarization vector, since it has to fulfill the transversality condition $v_\mu \varepsilon^\mu = 0$ leaving 3 degrees of freedom, times 2 from the heavy-quark on-shell spinor). The polarization vector is normalized as $\varepsilon^\mu \varepsilon_\mu^* = 1$.

The currents are non-local objects, aligned along a light-like direction n_μ , with coordinates $t_i n_\mu$ for the i -th quark. For simplicity the baryon is defined in the frame of the b -quark $Q_\gamma = Q(0)_\gamma$, and the Wilson lines are omitted. Their influence will be discussed whenever necessary. Including the light-cone coordinate dependencies one finds for the non-local light-cone operators, which define the LCDAs and were discussed in Sec. 2.1, that they can be written as

$$\langle 0 | q_1(t_1) C \Gamma^\mu q_2(t_2) \times Q_\gamma(0) | H_b \rangle = \sum_{i=1}^3 f_{H_b} \psi_i^\Gamma(t_1, t_2) \varepsilon^{(i)\mu} \times u_\gamma \quad (2.2.3)$$

in the heavy-quark limit. Here Γ^μ symbolizes all possible spinor structures allowed by Lorentz symmetry, H_b represents a baryon state of the sextet in Fig. 2.4, f_{H_b} is the baryonic decay constant and ψ_i^Γ are the distribution amplitudes corresponding to the current

defined by Γ^μ . The maximal number of independent structures is 16, as discussed in the previous section. Taking into account the currents in Eq. (2.1.13) and the two Lorentz vectors v^μ and n^μ , the maximal basis in Lorentz space is obtained. In total there are 8 linear independent structures, $n^\mu \mathbb{1}$, γ^μ , $n^\mu \not{v}$, $n^\mu \not{n}$, $-i\sigma^{\mu\nu}$, $-i\sigma^{\mu n}$, $-in^\mu \sigma^{nv}$ and $\epsilon^{\mu\nu\rho\sigma} \gamma_\rho \gamma_5$. The notation $n^\mu v^\nu \sigma_{\mu\nu} \equiv \sigma^{nv}$, etc. is used to shorten the expressions. The most general three-quark current in HQET is, corresponding to the Rarita-Schwinger vector-spinor, given by the direct product (*not* the spin tensor product, in which spin coupling terms like $q_1 C \sigma^{\mu\nu} q_2 (\gamma_\nu Q)_\gamma, \dots$ are present) of the light-quark current times the heavy-quark field Q .

Since the quarks are aligned along the light-like direction n_μ , it is convenient for the description of the quark dynamics to work in the light-cone basis, where a vector a_μ is decomposed as

$$a_\mu = \frac{1}{2}(a_- n_\mu + a_+ \bar{n}_\mu) + a_\mu^\perp, \quad (2.2.4)$$

in which $n_\mu = (1, 0, 0, -1)$ and $\bar{n}_\mu = (1, 0, 0, 1)$ are light-cone vectors with $n^2 = \bar{n}^2 = 0$, $n_\mu \bar{n}^\mu = 2$, and a_μ^\perp refers to the remaining two spacelike dimensions, which are perpendicular to both n_μ and \bar{n}_μ . The scalar product of two vectors a_μ and b_μ is given by

$$a_\mu b^\mu = \frac{1}{2}(a_+ b_- + a_- b_+) + a_\mu^\perp b^{\perp\mu}. \quad (2.2.5)$$

The coefficients of the decomposed kinematical vectors

$$\begin{aligned} v_\mu &= \frac{1}{2} \left(\frac{1}{v_+} n_\mu + v_+ \bar{n}_\mu \right), \\ \varepsilon_\mu &= \frac{1}{2} \varepsilon \left(\frac{1}{v_+} n_\mu - v_+ \bar{n}_\mu \right) + \varepsilon_{\perp\mu}, \end{aligned} \quad (2.2.6)$$

have been chosen in a way to fulfill the conditions $v^2 = 1$, $\varepsilon^\mu \varepsilon_\mu^* = 1$ and the transversality condition $v_\mu \varepsilon^\mu = 0$. By the choice of the coordinate frame, v_μ has no perpendicular components. Accordingly $\varepsilon_{\perp\mu}$ is called transversal and $\varepsilon_\mu^\parallel \equiv \varepsilon_\mu - \varepsilon_{\perp\mu}$ parallel polarization. They fulfill the conditions $\varepsilon_\mu^\parallel \varepsilon_\perp^\mu = 0$, $\varepsilon_{\parallel\mu} \varepsilon_\parallel^\mu = -\varepsilon^2$, $\varepsilon_{\perp\mu} \varepsilon_\perp^\mu = \varepsilon^2 - 1$ and $n_\mu \varepsilon^\mu = -\varepsilon v_+$. The scalar variable ε is the measure for the amount of parallel polarization.

Eq. (2.2.3) splits in linear independent parallel and transversal parts:

$$\langle 0 | q_1(t_1) \Gamma^\mu q_2(t_2) Q_\gamma | H_b \rangle = f_{H_b} (\psi_\parallel^\Gamma(t_1, t_2) \varepsilon_\parallel^\mu + \psi_\perp^\Gamma(t_1, t_2) \varepsilon_\perp^\mu) u_\gamma. \quad (2.2.7)$$

Thus the parallel operators

$$\begin{aligned} \frac{w^\mu}{v_+} \langle 0 | (q_1(t_1) C \not{n} q_2(t_2)) Q_\gamma | H_b \rangle &= \psi^n(t_1, t_2) f_{H_b}^{(2)} \varepsilon_\parallel^\mu u_\gamma, \\ i w^\mu \langle 0 | (q_1(t_1) C \sigma_{\bar{n}n} q_2(t_2)) Q_\gamma | H_b \rangle &= 2 \psi^{n\bar{n}}(t_1, t_2) f_{H_b}^{(1)} \varepsilon_\parallel^\mu u_\gamma, \\ w^\mu \langle 0 | (q_1(t_1) C q_2(t_2)) Q_\gamma | H_b \rangle &= \psi^\perp(t_1, t_2) f_{H_b}^{(1)} \varepsilon_\parallel^\mu u_\gamma, \\ -v_+ w^\mu \langle 0 | (q_1(t_1) C \not{\bar{n}} q_2(t_2)) Q_\gamma | H_b \rangle &= \psi^{\bar{n}}(t_1, t_2) f_{H_b}^{(2)} \varepsilon_\parallel^\mu u_\gamma, \end{aligned} \quad (2.2.8)$$

and transversal operators

$$\begin{aligned}
\frac{i}{v_+} \langle 0 | (q_1(t_1) C \sigma_{n\perp}^\mu q_2(t_2)) Q_\gamma | H_b \rangle &= \psi^{\perp n}(t_1, t_2) f_{H_b}^{(2)} \varepsilon_\perp^\mu u_\gamma, \\
\langle 0 | (q_1(t_1) C \gamma_\perp^\mu q_2(t_2)) Q_\gamma | H_b \rangle &= \psi^\perp(t_1, t_2) f_{H_b}^{(1)} \varepsilon_\perp^\mu u_\gamma, \\
i \langle 0 | (q_1(t_1) C \sigma_{\bar{n}n} \gamma_\perp^\mu q_2(t_2)) Q_\gamma | H_b \rangle &= 2\psi^{\perp 5}(t_1, t_2) f_{H_b}^{(1)} \varepsilon_\perp^\mu u_\gamma, \\
iv_+ \langle 0 | (q_1(t_1) C \sigma_{\bar{n}\perp}^\mu q_2(t_2)) Q_\gamma | H_b \rangle &= \psi^{\perp \bar{n}}(t_1, t_2) f_{H_b}^{(2)} \varepsilon_\perp^\mu u_\gamma,
\end{aligned} \tag{2.2.9}$$

can be identified. The following notations have been used, $\gamma_\perp^\mu = \gamma^\mu - \frac{1}{2}(\not{n}\bar{n}^\mu + \not{\bar{n}}n^\mu)$, $\{\gamma_\perp^\mu, \not{n}\} = \{\gamma_\perp^\mu, \not{\bar{n}}\} = 0$ with $\gamma_\parallel^\mu = -w^\mu \not{\psi}$, $\sigma_{n\perp}^\mu = \frac{i}{2}(\not{n}\gamma_\perp^\mu - \gamma_\perp^\mu \not{n})$. The vector $w^\mu = \frac{1}{2}(\frac{1}{v_+}n^\mu - v_+\bar{n}^\mu)$ is the only possible normalized combination of n^μ and v^μ , which fulfills the transversality condition $v_\mu w^\mu = 0$. All currents inherit this property from the polarization vector in the Rarita-Schwinger vector-spinor. Note, that there is no interpolating current involving γ_\parallel^μ , since $\gamma_\parallel^\mu = w^\mu \not{\psi}$. As a result such currents are linear combinations of the parallel currents defined in (2.2.8).

The twist is given by an expansion in v_+ (see for comparison [51]_{Eq. 2.5}). The leading, subleading and subsubleading twist is proportional to $1/v_+$, 1 and v_+ , respectively. Similar to the case of light vector mesons (see for example [49]_{Tab. 2}) one gets in the baryon case:

twist	2	3	4	
parallel polarization	ψ^n	$\psi^\parallel, \psi^{\bar{n}n}$	$\psi^{\bar{n}}$	(2.2.10)
transversal polarization	$\psi^{\perp n}$	$\psi^\perp, \psi^{5\perp}$	$\psi^{\perp \bar{n}}$	

The argument for the twist ordering is the following. Based on the choice of basis for v^μ , the orientation of the currents with respect to v induces a kinematical difference. The light-cone vectors \bar{n} and n differ only in their direction in their spacial coordinates along the z -direction. According to Eq. (2.2.6) $v^\mu = -(1/v_+ - v_+, 0, 0, 1/v_+ + v_+)/2$. Hence the characteristic feature is, with which three-velocity the baryon moves along the z -axis. In conclusion the importance (or twist) can be characterized by v_+ . However, this is not necessarily the conventional definition of “twist=dimension–spin”. To give a rough estimate by assuming, that the baryon moves with 0.5 times the light speed, where the kinetic energy of a particle is about 20% of its mass and can to some extent still be treated in a nonrelativistic way, see for example [45]_{p. 11}. In this case v_+ is approximately 0.6 and so the importance of the wave functions normalized with respect to leading twist, only concerning the parameter v_+ , is about 1, 0.6 and 0.4 for twist 2, 3 and 4.

The functions defined in (2.2.8) and (2.2.9) are normalized to give the corresponding decay constants $f_{H_b}^{(1)}$ and $f_{H_b}^{(2)}$ in the local limit, in which $\psi(0,0) \equiv 1$, which after Fourier transform ($t_i \rightarrow \omega_i$ and $\omega_1 = u\omega$, $\omega_2 = \bar{u}\omega$) leads to the following normalizations:

$$\int_0^\infty d\omega_1 \int_0^\infty d\omega_2 \psi(\omega_1, \omega_2) = \int_0^\infty \omega d\omega \int_0^1 du \psi(\omega, u) = 1. \tag{2.2.11}$$

Here ω_i are the light-like momenta of the light-quarks q_i , $\omega = \omega_1 + \omega_2$ is the total light-like momentum of the light-quark system and $u \in [0, 1]$, $\bar{u} = 1 - u$ are the momentum

fractions of the light-quarks. Eq. (2.2.11) indicates that the LCDAs are constructed in a way, such that the energy scale is given by the constants $f_{H_b}^{(1)}$ and $f_{H_b}^{(2)}$, while the coordinate dependencies are kept in the functions ψ . Hence the two decay constants are determined by the interpolating operators (2.2.8) and (2.2.9) in the local limit. Only two linear independent local operators survive in this limit as shown in the following section. Splitting the energy dependence from the coordinate dependencies leads to the advantage, that the decay constants can be calculated at higher orders than the more complicated distribution amplitudes. The decay constants $f_\Lambda \approx 0.03\text{GeV}^3$ and $f_\Sigma \approx 0.038\text{GeV}^3$ are known at NLO in the $SU(3)_F$ limit [52]_{p. 1, Tab. 2}, while the $SU(3)_F$ breaking effects are only known at LO. The decay constants $f_{H_b}^{(1)}$ and $f_{H_b}^{(2)}$ coincide approximately at the renormalization scale $\mu \approx 1 \text{ GeV}$ [46].

2.3 Local operators

The local interpolating operators, which will later on be used to approximate the baryon state in the sum rule calculations are given by the local limit of the operators defined in (2.2.8) and (2.2.9), see also [52]_{Eq. 2}. For example, the combination of the twist 2 and twist 4 matrix elements in local limit defines the decay constant $f_{H_b}^{(2)}$:

$$\begin{aligned} \frac{1}{2}(\psi^n(0,0) + \psi^{\bar{n}}(0,0))f_{H_b}^{(2)}\varepsilon_\parallel^\mu u_\gamma &= f_{H_b}^{(2)}\varepsilon_\parallel^\mu u_\gamma \\ &= \langle 0 | (q_1(0)C\gamma_\parallel^\mu q_2(0))Q_\gamma(0) | H_b \rangle. \end{aligned} \quad (2.3.1)$$

Finally, the only surviving gamma structures in the local limit are $\gamma_\perp^\mu C^{-1}$ and $\not{\psi}\gamma_\perp^\mu C^{-1}$ as transversal currents and $\gamma_\parallel^\mu C^{-1}$ and $\not{\psi}\gamma_\parallel^\mu C^{-1}$ as parallel ones. The most general local Interpolating current is then given by a linear combination:

$$\bar{J}_{\Gamma'\gamma}(x) = [\bar{q}_1(x)\Gamma'q_2(x)]\bar{Q}_\gamma(x), \quad (2.3.2)$$

where $\Gamma' = (A\mathbb{1} + B\not{\psi})\gamma_{\perp/\parallel}^\mu C^{-1}$ and $A \in [0, 1]$, $B = 1 - A$. Following [46], the arbitrariness in the choice of the local current, *i.e.* the variation in A , will later be adopted as an error estimate, and I will give the result for $A = 1/2$, which corresponds to a constituent quark model current that has maximal overlap with the ground state baryons in the constituent quark model picture, in which all quarks are on-shell [52]_{p. 5, Sec. 3.3}.

2.4 Switching heavy-quark spin on

The heavy-quark spin has no fixed direction in the heavy-quark limit and can be rotated at will. The heavy-quark vector-spinor $\psi\varepsilon^\mu u_\gamma$ is therefore neither transforming as a 3/2, nor a 1/2 quantity because Lorentz invariance is explicitly broken. One has to restore the proper Lorentz-invariant behavior by fixing the heavy-quark spinor with respect to the direction of the polarization vector ε_μ . This can be done by using the transformation properties of a spin 3/2 Rarita-Schwinger vector-spinor $R^{3/2\mu}_\gamma$ [50]_{Eq. 2.9} and [45]_{p. 10}:

$$(\psi R^{3/2\mu})_\gamma = R^{3/2\mu}_\gamma, \quad v_\mu R^{3/2\mu}_\gamma = 0, \quad (\gamma_\mu R^{3/2\mu})_\gamma = 0. \quad (2.4.1)$$

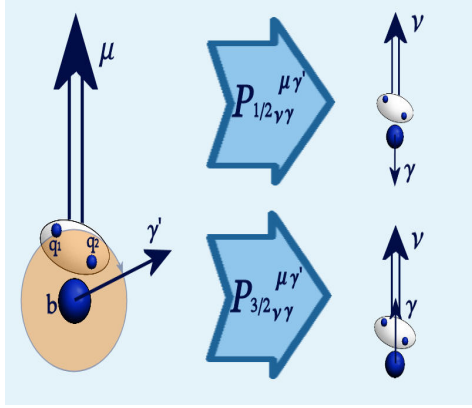


Figure 2.5: Action of the projectors in Eq. (2.4.2), which rotate the heavy-quark spin parallel to the light-quark spin to restore Lorentz invariance. The b -quark is indicated by the blue sphere and the light di-quark is indicated by the white oval.

Using [50]_{Eq. 2.10} I define

$$\begin{aligned} (P_{3/2})^\mu{}_{\nu\gamma}{}^{\gamma'} &= \left[\delta_\nu^\mu - \frac{1}{3}(\gamma^\mu + v^\mu)\gamma_\nu \right]_\gamma{}^{\gamma'}, \\ (P_{1/2})^\mu{}_{\nu\gamma}{}^{\gamma'} &= \left[\frac{1}{3}(\gamma^\mu + v^\mu)\gamma_\nu \right]_\gamma{}^{\gamma'}, \end{aligned} \quad (2.4.2)$$

which fulfill the projection operator conditions $P^2 = P$ and $P_{3/2} + P_{1/2} = 1$. The action of the projectors is depicted in Fig. 2.5. Now

$$\psi \varepsilon^\mu u_\gamma = \psi R^{3/2\mu}{}_\gamma + \psi R^{1/2\mu}{}_\gamma, \quad (2.4.3)$$

with

$$\begin{aligned} R^{3/2\mu}{}_\gamma &= \left(\left[\varepsilon^\mu - \frac{1}{3}(\gamma^\mu + v^\mu)\not{x} \right] u \right)_\gamma, \\ R^{1/2\mu}{}_\gamma &= \left(\left[\frac{1}{3}(\gamma^\mu + v^\mu)\not{x} \right] u \right)_\gamma. \end{aligned} \quad (2.4.4)$$

One can check that $R^{3/2\mu}{}_\gamma$ fulfills (2.4.1), and $R^{1/2\mu}{}_\gamma$ is a spin 1/2 spinor with normalization

$$-g_{\mu\nu} \sum \text{Tr} [\bar{R}^{3/2\mu} R^{3/2\nu}] = 4 \quad \text{and} \quad -g_{\mu\nu} \sum \text{Tr} [\bar{R}^{1/2\mu} R^{1/2\nu}] = 2, \quad (2.4.5)$$

corresponding to (2.2.2), where the 3/2 spinor gets 4 degrees of freedom and the 1/2 spinor gets 2. One should keep in mind, that this is a global rotation only to get the proper transformation properties. The rotation of the heavy-quark spin will not affect the following calculations, which are performed in the heavy-quark limit.

2.5 Correlation functions

Following the standard procedure of QCD Sum Rules, I calculate the matrix elements defined in (2.2.8) and (2.2.9) by approximating the baryonic state $|H_b\rangle$ by the local current defined in (2.3.2), *i.e.* $|H_b(x)\rangle \approx \bar{J}(x)|0\rangle$. Hence, the matrix elements in (2.1.6) are defined on partonic level. The corresponding correlation function is defined by $\Pi_{\Gamma\Gamma'\gamma\gamma'}(t_i, x) = i \langle 0 | O_{\Gamma\gamma}(t_1, t_2) \bar{J}_{\Gamma'\gamma'}(x) | 0 \rangle$, in which $O_{\Gamma\gamma}(t_1, t_2)$ can be any non-local operator defined in Eq. (2.2.8) and (2.2.9). The coefficient functions describe the propagation of the quarks inside the

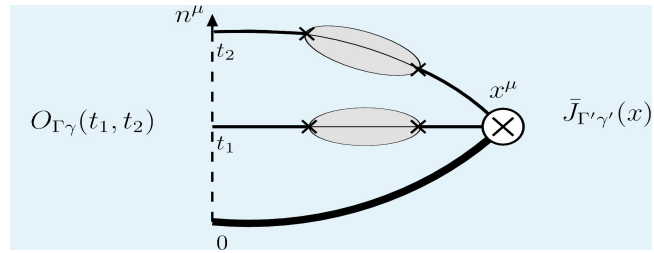


Figure 2.6: Correlation function in QCD background. The quarks move from point x in the QCD background (shaded regions) to the light-like direction described by n (dashed line). The b -quark is indicated by the thick black line.

baryon from point x to the light-cone,

which is parametrized through the light-quark projections t_i , pictured in Fig. 2.6. The double Fourier transform of the correlation function is then given by

$$\Pi_{\Gamma\Gamma'\gamma\gamma'}(\omega_1, \omega_2; E) = i \int_{-\infty}^{\infty} \frac{dt_1 t_2}{(2\pi)^2} e^{i(\omega_1 t_1 + \omega_2 t_2)} \int d^4x e^{-iEv \cdot x} \langle 0 | O_{\Gamma\gamma}(t_1, t_2) \bar{J}_{\Gamma'\gamma'}(x) | 0 \rangle. \quad (2.5.1)$$

Inserting and contracting the quark fields and performing the Fourier transformations yields

$$\Pi_{\Gamma\Gamma'}(\omega, u; E)_{\gamma\gamma'} = -i6 \int dt e^{-iEv \cdot x} \tilde{S}_{m=\infty}(x)_{\gamma\gamma'} \text{Tr} \left[\Gamma \tilde{S}_d(\bar{u}\omega, t) \Gamma' \tilde{S}_u^T(u\omega, t) \right]. \quad (2.5.2)$$

The propagators \tilde{S} , discussed later, are not free but describe the dynamical evolution of the valence-quarks within the low energetic QCD background of the baryon.

The correlation functions must be proportional to the Lorentz structure given by the spin sum (2.2.1), which will come out naturally, if the currents are defined correctly.

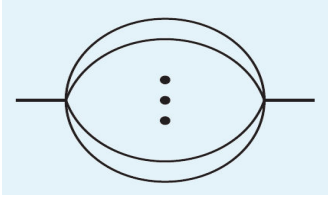


Figure 2.7: Topology of the sunrise type, which arise generically in the calculation of correlation functions of two local interpolating currents with n quark fields.

are given for the central value $A = B = 1/2$, $\Pi(\omega, u; E)$, and therefore the distribution functions $\psi(\omega, u)$ are the same for transversal and parallel polarization. The dependence of the correlation functions of A and B is due to our choice of set of linear independent operators for the non-local currents in (2.2.8) and (2.2.9). Rewriting the parallel currents by introducing a different basis, for example γ_{\parallel}^{μ} , would change the above described symmetry in A and B .

The heavy-quark spin structure can be seen directly. It is given by P_+ . The light-quark polarization is given implicit inside the trace by Γ and Γ' . For the transversal currents $\Pi_{\Gamma\Gamma'\gamma\gamma'}(\omega, u; E)$ it is given by $\Pi(\omega, u; E) \cdot (-g_{\mu\nu} + v_{\mu}v_{\nu} + \varepsilon_{\parallel\mu}\varepsilon_{\parallel\nu}/\varepsilon_{\parallel}^2) P_{+\gamma\gamma'}$ and consequently $\Pi_{\Gamma\Gamma'}(\omega, u; E)_{\gamma\gamma'}$ is equal to $-\Pi(\omega, u; E) \cdot (\varepsilon_{\parallel\mu}\varepsilon_{\parallel\nu}/\varepsilon_{\parallel}^2) P_{+\gamma\gamma'}$ for the parallel currents. In this sense the scalar functions $\Pi(\omega, u; E)$ are defined. They are identical for parallel and transversal polarizations up to different contributions of the local interpolating currents, which gives $\Pi_{\perp}(\omega, u; E)_{A,B} = \Pi_{\parallel}(\omega, u; E)_{B,A}$. Since the LCDAs

The correlation functions are evaluated in the following by using configuration space techniques, instead of working in the more common momentum space. The reason is, that the leading order sunrise-diagrams become very simple in coordinate space. Sunrise diagrams, depicted in Fig. 2.7, are certain types of $1 \rightarrow 1$ multi-loop self energy diagrams. For a review about the evaluation of diagrams of the sunrise type in coordinate space see [53]. The non-local diagrams, which are necessary for the calculation of the LCDAs, differ in principle from the sunrise type, because they do not involve two local interpolating currents, instead they are ripped open along a light-like line at the left side of the diagram pictured in Fig. 2.6. Hence a more correct term might be lacerated sunrise diagram. But despite the difference, configuration space techniques work pretty good for this kind of diagrams as well, as shown below.

in which the thin line corresponds to the light-quarks and the thick line corresponds to the b -quark. There is no b -quark condensate term, since it is suppressed by $1/m_b$ and hence vanishes in the heavy-quark limit. The sum rule reads

$$|f_{H_b}|^2 \psi_{H_b}^\Gamma e^{-\bar{\Lambda}_{H_b}/\tau} = \mathbb{B}[\Pi](\omega, u; \tau, s_0), \quad (2.5.9)$$

in which \mathbb{B} is the Borel transform, further explained in App. B.1, and s_0 is the momentum cutoff originating from the application of the quark-hadron duality. The QCD sum rules are further explained in App. B.2. The Borel transform can easily be applied together with the Fourier-Transform, since for a function $f(t)$

$$\mathbb{B} \left[\int e^{iEt} f(t) \right]_{E \rightarrow \tau} = if(i/\tau) \quad (2.5.10)$$

holds. As known, the Borel transform, given in Eq. (B.1.1), handles the UV-divergences automatically, making renormalization rather easy; as a short reminder, the renormalization condition is applied by adding a certain polynomial in E to remove the UV divergent terms, which vanishes due to the derivative of arbitrary order in E in the Borel transform.

The momentum cutoff is applied by cutting off the upper spectrum of the Laplace transform L^{-1} of the perturbative contributions, *i.e.*

$$f(\tau) \xrightarrow{L^{-1}} \int_0^\infty e^{-s/\tau} \tilde{f}(s) ds \xrightarrow{\text{cutoff}} \int_0^{s_0} e^{-s/\tau} \tilde{f}(s) ds. \quad (2.5.11)$$

One has to be careful, however, what one calls perturbative since there might be mixed perturbative and condensate contributions. Mixed contributions originate from diagrams, in which one light-quark is described by the low energy condensates and the other light-quark is described by the high energy perturbative propagator. We adopted the procedure of [46], and call a distribution perturbative, when at least one perturbative term is present. This procedure leads to plenty of incomplete Γ -functions, and it appears convenient to introduce the function

$$E_a(x) \equiv \frac{1}{\Gamma(a+1)} \int_0^x dt t^a e^{-t} = 1 - \frac{\Gamma(a+1, x)}{\Gamma(a+1)}, \quad (2.5.12)$$

in which $\Gamma(a+1, x) = \int_x^\infty dt t^a e^{-t}$ is the incomplete Γ -function. For $a = N \in \mathbb{N}$ this function is reduced to the well-known form

$$E_N(x) = 1 - e^{-x} \sum_{n=0}^N \frac{x^n}{n!}. \quad (2.5.13)$$

In practical numerical estimations it is also helpful to use the relation

$$E_a(x) = E_{a+1}(x) + \frac{x^{a+1} e^{-x}}{\Gamma(a+2)}, \quad (2.5.14)$$

obtained from (2.5.12) after integration by parts, connecting a negative value of the parameter a in $E_a(x)$ with a corresponding positive one.

Inserting the propagators (2.5.5) and (2.5.7) in Eq. (2.5.2) and performing the Borel and Fourier transform, the sum rules are obtained straightforward. I summarize our sum rule results, where the leading twist transverse result is given here as example:

$$\begin{aligned}
& f_{H_b}^{(2)} \left(A f_{H_b}^{(1)} + B f_{H_b}^{(2)} \right) \tilde{\psi}_2^{SR}(\omega, u) e^{-\bar{\Lambda}/\tau} = \\
& \frac{3\tau^4}{2\pi^4} [B\hat{\omega}^2 u\bar{u} + A\hat{\omega}(\hat{m}_2 u + \hat{m}_1 \bar{u})] E_1(2\hat{s}_\omega) e^{-\hat{\omega}} \\
& - \frac{\langle \bar{q}_1 q_1 \rangle \tau^3}{\pi^2} [A\hat{\omega}\bar{u} + B\hat{m}_2] f(2\tau\omega u) E_{2-a}(2\hat{s}_\kappa) e^{-\hat{\omega}} \\
& - \frac{\langle \bar{q}_2 q_2 \rangle \tau^3}{\pi^2} [A\hat{\omega}u + B\hat{m}_1] f(2\tau\omega\bar{u}) E_{2-a}(2\hat{s}_{\bar{\kappa}}) e^{-\hat{\omega}} \\
& + \frac{2B}{3} \langle \bar{q}_1 q_1 \rangle \langle \bar{q}_2 q_2 \rangle \tau^2 f(2\tau\omega u) f(2\tau\omega\bar{u}) E_{3-2a}(2\hat{s}_{\kappa\bar{\kappa}}) e^{-\hat{\omega}}, \tag{2.5.15}
\end{aligned}$$

in which $\hat{s}_\kappa = \hat{s}_\omega - \kappa/2$, $\hat{s}_{\bar{\kappa}} = \hat{s}_\omega - \bar{\kappa}/2$, $\hat{s}_{\kappa\bar{\kappa}} = \hat{s}_\omega - \kappa/2 - \bar{\kappa}/2$, and the short-hand notations

$$\kappa = \frac{\lambda}{2q_1\omega\tau}, \quad \bar{\kappa} = \frac{\lambda}{2\bar{q}_1\omega\tau} \tag{2.5.16}$$

are used. The parallel result is obtained by $A \leftrightarrow B$. All results of different twist can be found in App. B.5.

The QCD sum rules given in (B.5.1) can not be used in calculations directly. The main reason for this is, that the Sum Rules are build from a patchwork of different contributions, the perturbative and the condensate parts. They show neither smooth behavior, nor necessarily the correct asymptotic behavior, *i.e.* the asymptotic behavior of the perturbative contribution. As a consequence one has to propose model functions, which are then constrained by the sum rules. This is done in the next section.

2.6 The LCDA model

In the parametrization, in which the system is described by the total energy of the light-quark system ω and the momentum fractions u , the following arguments become manifest. The dynamics of the heavy-light system is described with the same formalism, which has proven well for the heavy-light meson dynamics. The dynamics of the light-light system is then described in the same way as the light-light mesons. In conclusion we choosed the multiplicative ansatz from [46]. In this approach the Gegenbauer polynomials C_n^η take

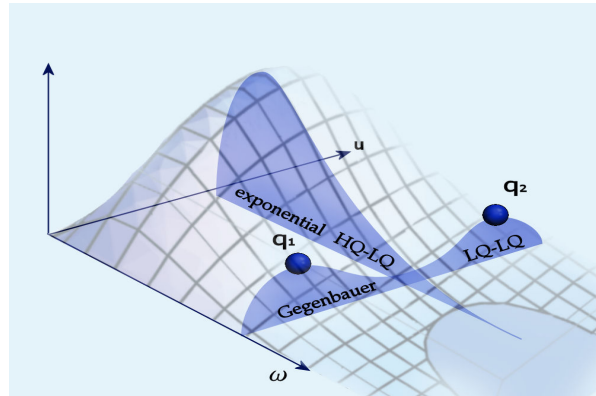


Figure 2.8: Model functions for the b -baryon LCDAs, composed of an exponential part for the heavy-light interaction and the Gegenbauer polynomials for the light-light interaction.

the light-quarks into account and an exponential factor characterizes the dynamic of the heavy-light system, as pictured in Fig. 2.8. It is more convenient to choose 3/2 Gegenbauer polynomials for twist 2 but 1/2 for the other twist functions. The first three polynomials are sufficient to account for the precision in this work. They are given by

$$C_0^\eta(x) = 1, \quad C_1^\eta(x) = 2\eta x, \quad C_2^\eta(x) = -x + 2\eta(1 + \eta)x^2. \quad (2.6.1)$$

To obtain the model fit, I calculate momentum fraction integrals (the moments), which are defined for an arbitrary function $f(\omega, u)$ as:

$$\langle f(\omega, u) \rangle_k^{HQ} \equiv \int_0^{2s_0} \omega d\omega \int_0^1 du f(\omega, u) \tilde{\psi}_k^{\text{SR}}(\omega, u). \quad (2.6.2)$$

The model functions for the LCDAs of different twist are:

$$\tilde{\psi}_2(\omega, u) = \omega^2 u(1-u) \sum_{n=0}^2 \frac{a_n}{\epsilon_n^4} \frac{C_n^{3/2}(2u-1)}{|C_n^{3/2}|} e^{-\omega/\epsilon_n}, \quad (2.6.3)$$

$$\tilde{\psi}_3(\omega, u) = \frac{\omega}{2} \sum_{n=0}^2 \frac{a_n}{\epsilon_n^3} \frac{C_n^{1/2}(2u-1)}{|C_n^{1/2}|} e^{-\omega/\epsilon_n}, \quad (2.6.4)$$

$$\tilde{\psi}_4(\omega, u) = \sum_{n=0}^2 \frac{a_n}{\epsilon_n^2} \frac{C_n^{1/2}(2u-1)}{|C_n^{1/2}|} e^{-\omega/\epsilon_n}, \quad (2.6.5)$$

in which the twist is indicated by the subscript numbers and $|C_n^\eta| = \sqrt{\int_0^1 du (C_n^\eta(2u-1))^2}$ with $|C_0^{3/2}|^2 = |C_0^{1/2}|^2 = 1$, $|C_1^{1/2}|^2 = 1/3$, $|C_2^{3/2}|^2 = 6$, $|C_1^{1/2}|^2 = 1/5$. The prefactors in front of the sums ($\omega^2 u(1-u)$, etc.) are determined by the corresponding perturbative part in order to give the correct asymptotic behavior (compare the B term in the first line in Eq. (B.5.1)). The moments of the functions (2.6.5), which are calculated with the use of (2.6.2), are listed in Tab. 2.6.1. In the construction of the models for the LCDAs, we

Table 2.6.1: Moments for the model functions

twist	$\langle 1 \rangle$	$\langle \omega^{-1} \rangle$	$\langle C_1^{3/2} \rangle$	$\langle \omega^{-1} C_1^{3/2} \rangle$	$\langle C_2^{3/2} \rangle$	$\langle \omega^{-1} C_2^{3/2} \rangle$
2	a_0	$a_0/3\epsilon_0$	$3a_1/5$	$a_1/5\epsilon_1$	$3a_2/7$	$a_2/7\epsilon_2$
twist	$\langle 1 \rangle$	$\langle \omega^{-1} \rangle$	$\langle C_1^{1/2} \rangle$	$\langle \omega^{-1} C_1^{1/2} \rangle$	$\langle C_2^{1/2} \rangle$	$\langle \omega^{-1} C_2^{1/2} \rangle$
3	a_0	$a_0/2\epsilon_0$	a_1	$a_1/2\epsilon_1$	a_2	$a_2/2\epsilon_2$
4	a_0	a_0/ϵ_0	a_1	a_1/ϵ_1	a_2	a_2/ϵ_2

have truncated the Gegenbauer expansion at the second non-asymptotic term and have taken the limit $s_0 \rightarrow \infty$ in the integral over ω . The change has negligible effect.

An example for the sum rules compared to the corresponding model fits is given in Fig. 2.9, in which one can see the patchwork of the different continuum and free parts of the propagators in Eq. (2.5.4). The moments

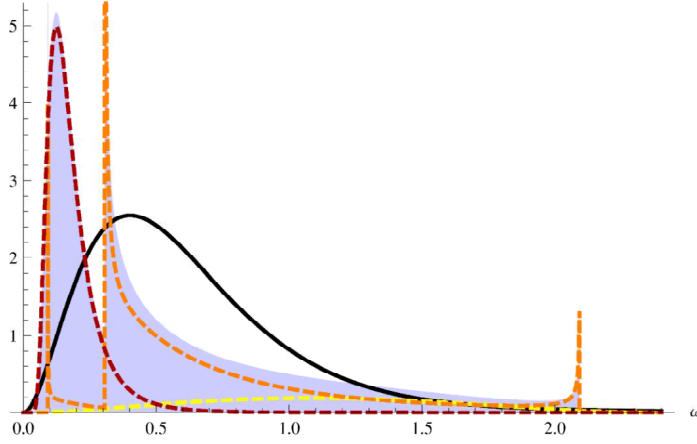


Figure 2.9: Example for sum rules and model fits. Shown is the twist 2 Σ contribution for ω at a value $u = 0.25$. The model fit is given by the solid, black line. The shaded region is the total sum rule contribution build of a perturbative part (yellow), two single condensate terms (orange) and a double condensate contribution (red).

$$\begin{aligned} \langle 1 \rangle &= 1 & \langle C_1^{3/2} / |C_1^{3/2}| \rangle &= 0.11^{+0.04}_{-0.03} & \langle C_2^{3/2} / |C_2^{3/2}| \rangle &= 0.33^{+0.17}_{-0.26} \\ \langle \omega^{-1} \rangle &= 1.54^{+0.58}_{-0.36} & \langle \omega^{-1} C_1^{3/2} / |C_1^{3/2}| \rangle &= 0.14^{+0.08}_{-0.05} & \langle \omega^{-1} C_2^{3/2} / |C_2^{3/2}| \rangle &= 0.24^{+0.21}_{-0.32} \end{aligned}, \quad (2.6.6)$$

and the model parameters

$$\begin{aligned} a_0 &= 1 & a_1 &= 0.18^{+0.07}_{-0.05} & a_2 &= 0.78^{+0.4}_{-0.62} \\ \varepsilon_0 &= 0.22^{+0.06}_{-0.06} & \varepsilon_1 &= 0.26^{+0.05}_{-0.03} & \varepsilon_2 &= 0.46^{+\infty}_{-0.09} \end{aligned}. \quad (2.6.7)$$

of twist 2 are given for Ξ (Ξ') as an example, in which the first moment is 1 by definition, see (2.2.11). The result for the other twists can be found in App. B.6.

The values we used for the calculation are

$$\begin{aligned} \langle \bar{q}q \rangle &= -(0.24 \text{ GeV})^3 & & \left[57 \right] \\ \langle \bar{s}s \rangle &= 0.8 \langle \bar{q}q \rangle & & \left[58 \right]_{\text{p. 9}}, \left[59 \right]_{\text{p. 261 ff}} \\ \lambda &= (0.4 \text{ GeV})^2 & & \left[46 \right]_{\text{p. 7}} \end{aligned}. \quad (2.6.8)$$

2.7 Renormalization

The LCDAs are defined via the Greens-Functions (2.2.8) and (2.2.9). Thus they are no physical quantities and have to obey renormalization group equations. The Greens functions define up to first order in g_s the non-local vertices:

$$\begin{aligned} \Gamma_{\gamma'\omega_1\omega_2} \begin{array}{c} \text{---} i\alpha k_{1+} \\ \text{---} j\beta k_{2+} \\ \text{---} k\gamma \end{array} &= -\epsilon_{ijk} \Gamma^{\alpha\beta} \mathbf{1}_{\gamma'} \delta(\omega_1 - k_{1+}) \delta(\omega_2 - k_{2+}), \\ \Gamma_{\gamma'\omega_1\omega_2} \begin{array}{c} \text{---} i\alpha k_{1+} \\ \text{---} \text{wavy} c\mu k_{4+} \\ \text{---} j\beta k_{2+} \\ \text{---} k\gamma \end{array} &= -g_s \epsilon_{ijk} t^{cl} i n^\mu \Gamma^{\alpha\beta} \mathbf{1}_{\gamma'} \frac{1}{k_{4+}} \\ &\quad \delta(\omega_2 - k_{2+}) (\delta(\omega_1 - k_{1+}) - \delta(\omega_1 - k_{4+} - k_{1+})) \end{aligned}. \quad (2.7.1)$$

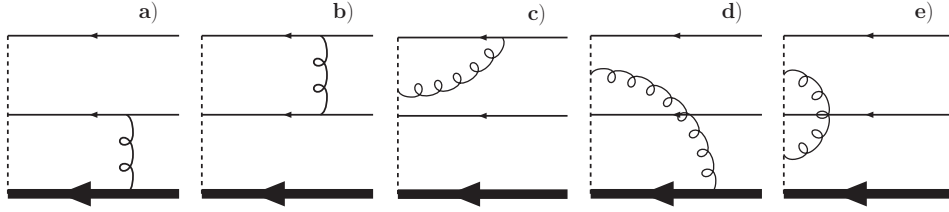


Figure 2.10: Types of diagrams for the non-local vertex renormalization. Each of the first four diagrams appears twice (one for each light-quark). The dashed line represents the Wilson line.

The vertex for the case, in which the gluon line is attached to the lower Wilson line is obtained by replacing $1 \leftrightarrow 2$. A detailed derivation of the vertices is presented in App. B.3.3. The expansion of the Greens-Functions in g_s corresponds to an expansion of the Wilson lines (2.1.5) in g_s . For the n -th order expansion there are in general n gluon-fields attached to the vertex, but for the calculations in this work one-loop calculations are sufficient, and additional vertices to the ones in Eq. (2.7.1) are not necessary. The evolution kernel at one-loop order is determined by the ultraviolet poles of the matrix elements of the bare operators. The types of diagrams which contribute to the kernel of the renormalization group equation up to one-loop order are given in Fig. 2.10. For leading twist (neglecting masses) the diagrams give the same contribution to the evolution equation of transverse and parallel twist. Furthermore they also give the same contribution for the $SU(3)_F$ triplet and sextet (Fig. 2.4), where only for the transversal functions diagram **b**) vanishes. This is due to some special properties of the Lorentz structures which define the currents and therefore the vertices. The $SU(3)_F$ triplet evolution equation has already been derived in [46]_{Eq. 13}. The calculations necessary for this section are rather lengthy and may obscure the main conclusions of this chapter. Hence, the detailed derivations of the renormalization group equations are hived off to App. B.4. Especially (B.4.8) shows the equality of the loop integrals for the triplet and parallel currents of the sextet in case of the leading twist and therefore also the equality of the evolution kernels. I will just sketch the derivation here and state the most important facts.

At one-loop order the diagrams shown in Fig. 2.10 involve at maximum two quarks in the loop and one ore more quarks are on-shell. Hence, the derivation of the evolution kernels is almost identical to the meson case. The heavy-light contributions, involving the b -quark and one light-quark, are similar to the heavy-light mesons [60] and the light-light contributions are similar to the light-light mesons [61]. Diagram **a**) is UV finite, as is also found in [60]. Diagram **e**) vanishes because the corresponding vertex is proportional to $n^\mu n^\nu$ and the gluon propagator is proportional to $g_{\mu\nu}$. The other diagrams are calculated at the end of App. B.4. The evolution equation for the leading twist reads [46]

$$\begin{aligned} \mu \frac{d}{d\mu} \psi_2(\omega_1, \omega_2; \mu) &= -\frac{\alpha_s(\mu)}{2\pi} \left(1 + \frac{1}{N_c}\right) \left[\int_0^\infty dk_{1+} \gamma^{\text{LN}}(\omega_1, k_{1+}; \mu) \psi_2(k_{1+}, \omega_2; \mu) \right. \\ &\quad \left. + \int_0^\infty dk_{2+} \gamma^{\text{LN}}(\omega_1, k_{2+}; \mu) \psi_2(\omega_1, k_{2+}; \mu) \right] \end{aligned}$$

$$- \int_0^1 dv V(u, v) \psi_2(v\omega, \bar{v}\omega; \mu) + \frac{3}{2} \psi_2(\omega_1, \omega_2; \mu) \Big], \quad (2.7.2)$$

in which

$$\gamma^{\text{LN}}(\omega, k_+; \mu) = \left(\ln \frac{\mu}{\omega} - \frac{5}{4} - \left[\frac{\omega}{k_+} \frac{\Theta(k_+ - \omega)}{k_+ - \omega} + \frac{\Theta(\omega - k_+)}{\omega - k_+} \right]_{\oplus} \right) \quad (2.7.3)$$

is taken from [60]_{Eq. 8} and

$$V(u, v) = \left[\frac{1-u}{1-v} \left(1 + \frac{1}{u-v} \right) \Theta(u-v) + \frac{u}{v} \left(1 + \frac{1}{v-u} \right) \Theta(v-u) \right]_+, \quad (2.7.4)$$

which is taken from [62]_{Eq. C17}. The “ \oplus ” and “ $+$ ” subtractions are defined via

$$\int_0^\infty dk_+ [\gamma(\omega, k_+)]_{\oplus} f(k_+) = \int_0^\infty dk_+ \gamma(\omega, k_+) (f(k_+) - f(\omega)),$$

$$[V(u, v)]_+ = V(u, v) - \delta(u-v) \int_0^1 dt V(t, v). \quad (2.7.5)$$

For small evolution steps, $\ln(\mu/\mu_0) \lesssim 1$, the differentiation with respect to μ in Eq. (2.7.2) is given by the linear approximation

$$\mu \frac{d}{d\mu} \psi_2(\omega_1, \omega_2; \mu) \approx \mu \frac{\psi_2(\omega_1, \omega_2; \mu) - \psi_2(\omega_1, \omega_2; \mu_0)}{\ln(\mu/\mu_0)}, \quad (2.7.6)$$

and the evolution of the distribution amplitudes can be calculated easily. In the following I give the parallel LCDAs as example. As will be shown, the effect of the renormalization is within the errors obtained from the variation of the two different local interpolating currents.

2.8 Results

The moments of the functions defined in (2.6.3, 2.6.4, 2.6.5), which are calculated using (2.6.2), are given in Tab. 2.6.1.

We used a strange-quark mass of $m_s = 0.128$ GeV and massless light-quarks, $m_{u/d} = 0$. The calculation is performed in the rest frame with $v_+ = 1$ at an energy scale of $\mu = 1$ GeV. The method of the non-local condensates, which involves the parameters λ and m_0^2 is not yet completely understood. Especially, since there is only one model parameter, the ratio $m_0 = \langle \bar{q} D^2 q \rangle / \langle \bar{q} q \rangle$ between the 5-dimensional and 3-dimensional local condensate, known. This parameter determines the center of the quark virtuality distribution in QCD background, but is not sufficient to determine the shape of the quark distribution. To determine the shape also yet unknown dimension 7 local condensates are needed. We took

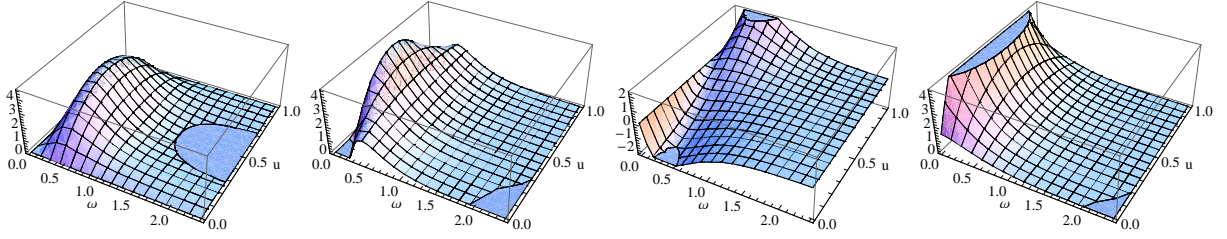


Figure 2.11: Model function ψ of Ξ . Shown is twist 2 (1st), symmetric twist 3 (2nd), antisymmetric twist 3 (3rd) and twist 4 (4th). They are given at an energy scale of $\mu = 1$ GeV.

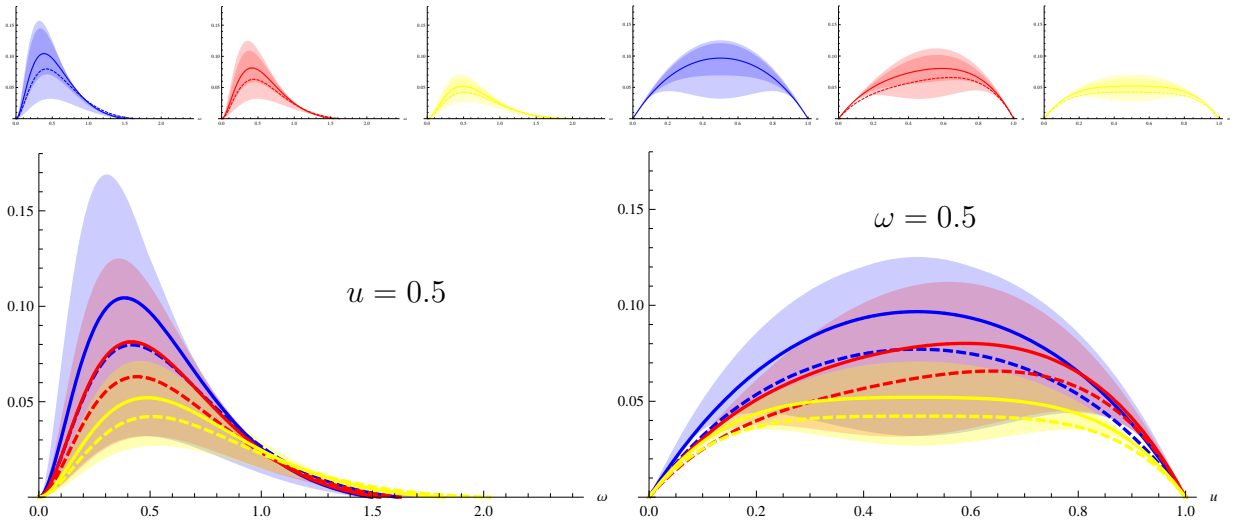


Figure 2.12: Twist 2 functions of Σ (blue), Ξ (red) and Ω (yellow) at energy scale $\mu = 1$ GeV (solid line) and energy scale $\mu = 2.5$ GeV (dashed line) including most conservative error $A \in [0, 1]$ in the two bottom plots (light shade). At the top, the distribution amplitudes for the baryons are listed separately, including the most conservative error (light shade) and the less conservative error $A \in [0.3, 0.7]$ (darker shade).

the shape parameter λ (2.6.8) as universal parameter, not influenced by either the baryon nor the mass of the propagating quark. For the strange-quark, where $m_{s_0} = \langle \bar{s}D^2s \rangle / \langle \bar{s}s \rangle$, the situation is more difficult since even dimension 5 condensates are not yet clearly understood. The value R , which is defined by $R \langle \bar{q}D^2q \rangle = \langle \bar{s}D^2s \rangle$, varies from $R \approx 0.8$ ([63]_{Eq. 15}, [59]_{Eq. 6.25}) which gives $m_0^2 \approx m_{s_0}^2$ to values around $R \approx 1.3$ ([64]_{Eq. 1}, [65]_{Tab. 1}, [66]_{Eq. 8}) which gives $1.7m_0^2 \approx m_{s_0}^2$. We took for our calculation $1.7m_0^2 \approx m_{s_0}^2$ since in this case the $SU(3)_F$ breaking effects appear already in the lower ω spectrum of the light-quark system as expected. The influence of the choice of R on the results is due to the already large uncertainties within error bars.

The corresponding LCDAs for Ξ (Ξ') are shown in Fig. 2.11. To give an overview over the tables of model parameters, I show the plots of the LCDAs in Figs 2.11 and 2.12.

Chapter 3

$[bq][\bar{b}\bar{q}]$ -tetraquarks

In this chapter I present my work concerning the hidden¹ bottom tetraquark states with valence-quark content $bq\bar{b}\bar{q}$, which was developed in collaboration with Ahmed Ali, Ishtiaq Ahmed, Muhammad Jamil Aslam and Satoshi Mishima.

First I introduce the tetraquarks as strongly bound four quark states, discuss their properties and give a roundup of other exotic hadrons, which are up to date studied by several groups. Afterwards I recall the tetraquark history, which has its roots in the mid seventies of the last century and point out their general relevance for modern QCD. The introductory chapters are partly based on our article [67] in *2physics.com* and the answers to some questions we have been asked during the preparation of the articles [68] and [69]. The introduction is followed by our work and split in several parts. Sec. 3.4 contains the calculation of $b\bar{b}$ -tetraquark masses by using the constituent quark model. The Isospin breaking, the production and the hadronic two-body decays for the most promising $b\bar{b}$ -tetraquark candidates, the $J^{PC} = 1^{--}$ states, are presented in Sec. 3.5 and 3.6. A fit to the inclusive BaBar data on R_b , to search for evidence for the $J^{PC} = 1^{--}$ tetraquark states is outlined in Sec. 3.7. The development of a dynamical model to explain the exclusive Belle data on the decay channels $\Upsilon(1S)\pi^+\pi^-$ and $\Upsilon(2S)\pi^+\pi^-$ can be found in Sec. 3.8, in which the model and the fit are presented in Sec. 3.8.1 and 3.8.2 respectively. The fit values and the model are used to provide specific predictions to verify our tetraquark interpretation, which are presented in Sec. 3.8.3.

3.1 What are tetraquarks?

A tetraquark, as depicted in Fig. 3.1, is a four-quark hadron consisting of a diquark $[qq]$ and an antidiquark $[\bar{q}\bar{q}]$. The diquarks and antidiquarks are themselves bound states in the sense, that they form distinguishable substructures inside a hadron. The former are composed of a quark pair and the latter of two antiquarks, shown in Fig. 3.2. Hence, the diquarks are not color singlets. They are bound by gluonic interactions inside the tetraquark, as opposed to the hadronic molecules, which are also four-quark states, explained at the end of this section. The tetraquark hadron is color neutral and can exist as a free particle. Tetraquarks enormously en-

¹The phrase “hidden” refers to the b -quark content ($b\bar{b}$) of the tetraquark, which has bottomness 0.

large the quark model of Gell-Mann and Zweig by the diquarks as new hadron constituents, adding new forms of hadronic interaction and a diversity of bound states, which are yet unexplored. So far the only existing known hadrons are either quark-antiquark ($q\bar{q}$), or three-quark (qqq) bound states, called mesons and baryons respectively. Hadrons with different valence-quark quantum numbers, such as tetraquarks, are termed exotics. However, all of these exotic states have so far been absent in experiments, and it is yet not clear if there exist any. The next section gives an impression of the intense search for clues which may (hopefully) lead to the discovery of exotic states and tetraquarks in particular.

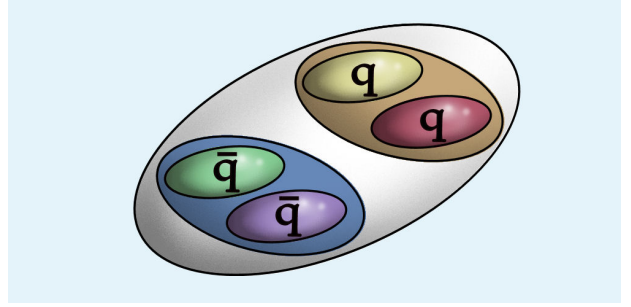


Figure 3.1: The tetraquark, composed of a diquark (orange) and an antidiquark (blue), which are themselves bound states of a quark qq (antiquark $\bar{q}\bar{q}$) pair.

In the pursuit of understanding the tetraquarks it is necessary to learn first about the properties of their constituents, the diquarks. The diquarks are, as building blocks of the tetraquarks, likewise important. They can also play a role in non-tetraquark scenarios. For example, they are relevant in the discussion of heavy ion collisions at RHIC and LHC in the framework of fragmentation functions, in which multi-quark configurations are important and in scenarios of color-superconductivity of cold, dense matter [70]. Another possible diquark scenario might be, that light diquarks are the mediators of forces, just like the pion exchange plays a crucial role in the binding of nucleons inside a nucleus. Though very speculative, it may well be that there is an underlying effective theory such as the very successful and well established chiral perturbation theory. However, to start exploring the putative rich field of research, it is important that the diquarks have well established footing in both theory and experiment. The tetraquarks are the most simple diquark scenarios. If the diquarks indeed open a new chapter in the story of strong interactions, the first pages will be dedicated to the tetraquarks, if their existence is confirmed.

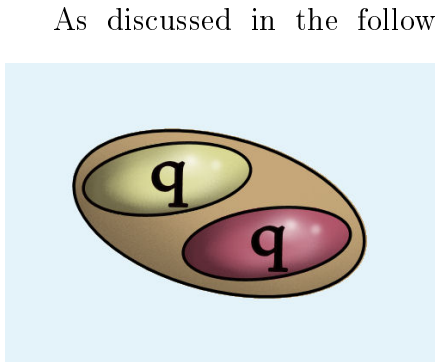


Figure 3.2: The color triplet diquark (orange), composed of two quarks (yellow and red).

As discussed in the following, diquarks turn out to be color triplets, possessing the same colors as the quarks. In general a bound state of two quarks transforms under the $SU(3)_C$ as $\mathbf{3} \otimes \mathbf{3} = \bar{\mathbf{3}} + \mathbf{6}$. However, there is good evidence from one gluon exchange models [2], that two quarks in a diquark with the color assignment $\mathbf{6}$ do not bind. The one gluon exchange models, as the name suggests, take into account the interchange of one gluon between two colored particles, as pictured in Fig. 3.3. All group-theoretical flows through the diagrams in $SU(N)$ gauge theories are in general independent of spacetime and factorize. This feature is for example used in the *large N expansion* for $SU(N)$ gauge theories. A nice way to calculate the color factors is provided by the diagrammatic *birdtrack* notation [71]. The

present diagram in Fig. 3.3 is, however, simple enough to be calculated by hand.

The color factor for the contribution corresponding to the diagram in Fig. 3.3 involves only the two $SU(N)$ generators t_{ij}^a . They are connected through a gluon by δ_b^a . The corresponding color structure is given by $t_{ij}^a t_{kl}^a$. Using the Fierz-identity for the generators of the $SU(N)$ gauge group leads to

$$t_{ij}^a t_{kl}^a = \frac{1}{2}(\delta_{il}\delta_{kj} - \frac{1}{N}\delta_{ij}\delta_{kl}). \quad (3.1.1)$$

The representation of a $SU(N)$ group is entirely defined through the permutation properties of the indices of the fundamental representation (this is also the reason, why the Young tableaux provides a proper description for $SU(N)$ representations). The dimension of the representation is obtained by counting the degrees of freedom. By rewriting expression (3.1.1) as

$$t_{ij}^a t_{kl}^a = -\frac{N+1}{2N}(\delta_{ij}\delta_{kl} - \delta_{il}\delta_{kj})/2 + \frac{N-1}{2N}(\delta_{ij}\delta_{kl} + \delta_{il}\delta_{kj})/2, \quad (3.1.2)$$

and by setting $N = 3$, the group theoretical property $\mathbf{3} \otimes \mathbf{3} = \bar{\mathbf{3}} + \mathbf{6}$ appears explicitly:

$$t_{ij}^a t_{kl}^a = -\frac{2}{3} \underbrace{(\delta_{ij}\delta_{kl} - \delta_{il}\delta_{kj})/2}_{\text{antisymmetric: projects } \bar{\mathbf{3}}} + \frac{1}{3} \underbrace{(\delta_{ij}\delta_{kl} + \delta_{il}\delta_{kj})/2}_{\text{symmetric: projects } \mathbf{6}}. \quad (3.1.3)$$

If the diquark transforms under the triplet, the color spinor is antisymmetric $\varepsilon_{jl} = -\varepsilon_{lj}$ and the normalized color spinor is given by $|\bar{\mathbf{3}}\rangle = \varepsilon_{jl}/\sqrt{\varepsilon^2}$ with $\varepsilon^2 = \varepsilon_{jl}\varepsilon_{jl}$ (similar the sextet is given by δ_{jl}). Thus

$$\langle \bar{\mathbf{3}} | t_{ij}^a t_{kl}^a | \bar{\mathbf{3}} \rangle = \frac{\varepsilon_{ik}}{\sqrt{\varepsilon^2}} \left(-\frac{2}{3}(\delta_{ij}\delta_{kl} - \delta_{il}\delta_{kj})/2 \right) \frac{\varepsilon_{jl}}{\sqrt{\varepsilon^2}} = -\frac{2}{3}. \quad (3.1.4)$$

In general the contribution of a diagram, in which two colored objects in a certain color configuration interchange one gluon is proportional to a group-theoretical factor, the discriminator I , which is defined by

$$I = \frac{1}{2}(C(D) - C(A) - C(B)), \quad (3.1.5)$$

in which A and B are the $SU(3)_C$ representations of two particles forming the state, which transforms under the representation D . The discriminator is the sum of the product of $SU(3)_C$ charges, where $C(X)$ is the Casimir invariant of representation X . For the $SU(3)_C$ representations it is listed in Tab. 3.1.1, in which Eq. (3.1.4) can be compared with the discriminator of the $\bar{\mathbf{3}}$ representation. Attractive forces

(like in electromagnetism, where positive times negative charges give negative and hence attractive contributions) exist for negative signs of I . The singlet case in Tab. 3.1.1, which corresponds to the binding of the $q\bar{q}$ pair inside the meson, is (of course) also attractive. Here one can see, that in this approximation the mesons transforming under $\mathbf{1}$ are bound twice as strong as the quarks in the diquark transforming under $\bar{\mathbf{3}}$.

According to the equations obtained in the one gluon exchange model approximation,

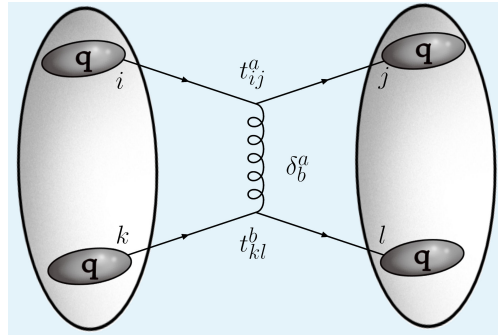


Figure 3.3: One gluon exchange model contribution to the binding of a quark-quark configuration.

Table 3.1.1: one gluon exchange model

$D = A \otimes B$	1	$\bar{\mathbf{3}}$	6	8
$C(D)$	0	4/3	10/3	3
I	-4/3	-2/3	1/3	1/6

hadron from a diquark and an antidiquark is very much the same as forming a meson, since both the quarks and the diquarks transform under the same triplet representation.

A diquark is, as discussed, similar to an antiquark in color space but inherently different in Minkowski space. Ground state diquarks can have two values of their spin quantum number, $s = 0$ and $s = 1$. In the first case they are called scalar or *good* diquarks and in the second case they are called vector or *bad* diquarks, shown in Fig. 3.4.

The overall quantum numbers of a tetraquark hadron are determined by the angular momenta and spins of the diquarks and antiquarks and by their possible orbital excitation. That *good* diquarks exist as bound states emerges from recent lattice QCD studies [72, 73] for the light-quark systems. On the other hand, no evidence is found on the lattice for an attractive diquark channel for the *bad* spin 1 diquarks involving light-quarks. In [73] the quark correlations inside the diquarks are probed. The result is depicted in Fig. 3.6. First they defined the interpolating currents, where the positive parity channels are $q^T C \gamma_5 q$ and $q^T C \gamma_5 \gamma_0 q$ with spin zero and $q^T C \gamma_i q$ and $q^T C \sigma_{0i} q$ with spin one, in which $\sigma_{\mu\nu} = (\gamma_\mu \gamma_\nu - \gamma_\nu \gamma_\mu)/2$. They are the same interpolating currents as the defined currents for the light-quark current in the definition of the LCDAs (2.1.13). The negative parity channels create states, which vanish in the non-relativistic limit and are excluded in quark models. These quark currents are studied by defining gauge-invariant two-density correlators:

$$C_\Gamma(\mathbf{r}_u, \mathbf{r}_d, t) = \langle 0 | J_\Gamma(\mathbf{0}, 2t) J_0^u(\mathbf{r}_u, t) J_0^d(\mathbf{r}_d, t) J_\Gamma^\dagger(\mathbf{0}, 0) | 0 \rangle, \quad (3.1.6)$$

where $J_0^f(\mathbf{r}, t) =: \bar{f}(\mathbf{r}, t) \gamma_0 f(\mathbf{r}, t) :$, $f = u, d$ and

$$J_\Gamma(x) = \epsilon^{abc} \left[u_a^T(x) C \Gamma d_b(x) \pm d_a^T(x) C \Gamma u_b(x) \right] s_c(x), \quad (3.1.7)$$

where the + (-) sign corresponds to the flavor symmetric (antisymmetric) combination, and s_c denotes the static-quark. Latin indices denote color.

In words, the color singlet operators in (3.1.6) are defined, then one quark is moved far away from the other two to test their interaction strength. The angle θ in the shown parametrization is defined by $r_{ud} = 2r \sin(\theta/2)$, where r_{ud} is the separation of the remaining quarks, as pictured in Fig. 3.6. The normalized correlation strength is plotted

the interaction in the sextet configuration **6** of the diquark is repulsive and the triplet **3** is attractive. Hence, only the diquarks having antitriplet color charges are phenomenologically relevant. In conclusion, the mechanism of forming a tetraquark

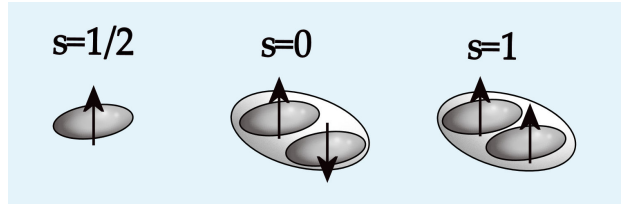


Figure 3.4: The *good* ($s=0$) and the *bad* ($s=1$) diquark spin assignments. This characterization holds, however, only for light diquarks.

with green triangles for the *bad* diquarks and black asterisks for the *good* diquarks. As is shown, they find no attraction for the former and increasing attraction for the latter case for decreasing quark distance. The measured attraction is similar to the case of quark attraction inside the mesons. In [73] both cases are compared. However, as the effective QCD Lagrangian is spin-independent in the heavy-quark limit, see Eq. (1.0.10), it is expected that the *bad* diquarks will also be in an attractive channel for $[cq]$ and $[bq]$ diquarks containing a charm or a bottom-quark. On account of this, both *good* and *bad* diquarks are considered in the following sections.

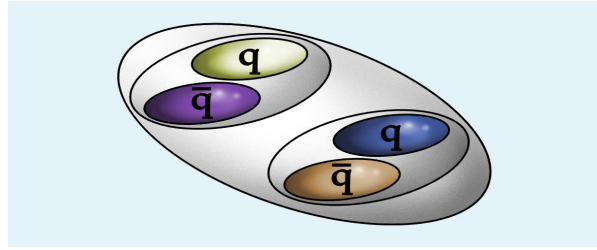


Figure 3.5: Hadronic molecule composed of two mesons (small white ovals)

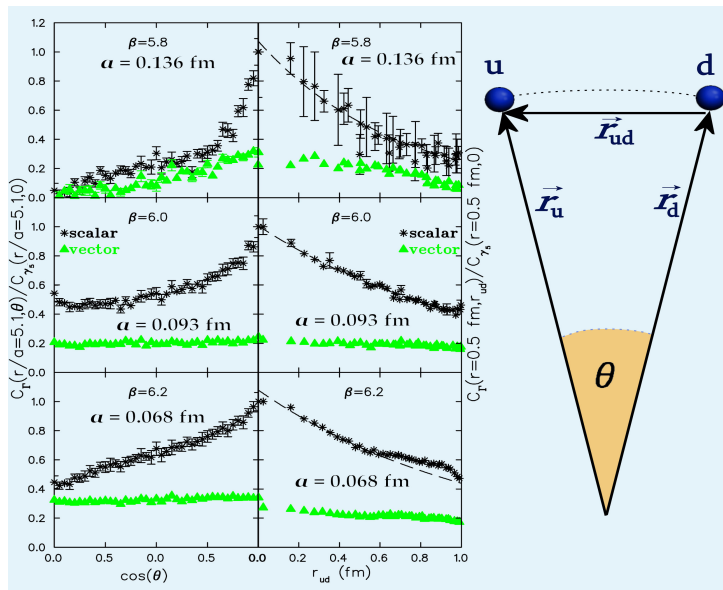


Figure 3.6: Evidence for the good light diquarks in lattice QCD. Figure taken from [73]. Left: $C_T(r/a = 5.1, \theta)/C_T(r/a = 5.1, 0)$ versus $\cos(\theta)$. Right: $C_T(r = 0.5 \text{ fm}, r_{ud})/C_T(r = 0.5 \text{ fm}, 0)$ versus r_{ud} , for the “good” (black asterisks) and “bad” (green filled triangles) diquarks at the lightest pion for three lattice spacings a .

quarks but also include one or more constituent gluons. The simplest are the hybrid $q\bar{q}g$ mesons and the glueballs gg and ggg , see Fig. 3.7.

The pentaquarks, pictured in Fig. 3.8, are baryons composed of four quarks and an antiquark. The four quarks bind to two diquarks. Pentaquarks are fermions and their decays follow the pattern of excited baryons, decaying for example in a lighter baryon and a meson. A pentaquark is always produced in association with another baryon (or antibaryon) to conserve the baryon quantum number. Experimental evidence for pentaquarks has disappeared in the meanwhile, which is discussed in the next section,

There are other exotic particles discussed in the framework of QCD. The most famous ones, the molecules, the hybrids and the pentaquarks are introduced below.

A seemingly close relative of the tetraquark is the hadronic molecule, shown in Fig. 3.5. Like the tetraquark it is composed out of four valence-quarks, but with an inherent difference: Hadronic molecules are not bound states of a diquark and an antiquark but of two mesons. The underlying physics is therefore very different. The composite mesons are color singlets and are bound by the exchange of intermediate light mesons, like baryons inside a nucleus.

The hybrids are bound states which do not consist entirely of

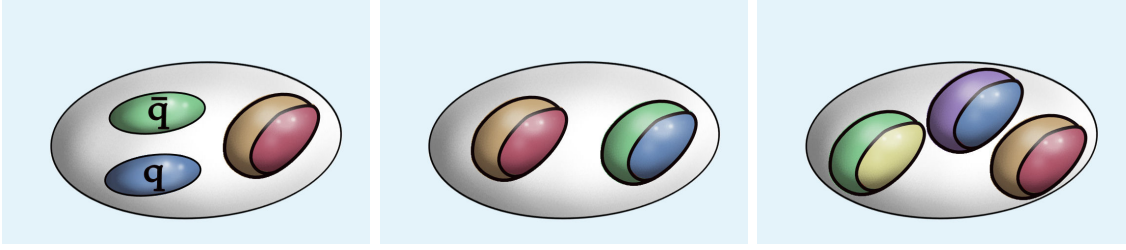


Figure 3.7: Exotic states, with the $q\bar{q}g$ -hybrid to the left, the gg -glueball in the middle and the ggg -glueball to the right. The gluons are adumbrated by the double colored objects.

including a historical abstract. On the theoretical side, simulations of pentaquarks on the lattice did not yield a clear signal of their existence and properties. Tetraquarks stand on much firmer experimental and theoretical footings than it is the case for pentaquarks. Probably, the latter are also present as bound states, but establishing this theoretically or experimentally is a formidable task.

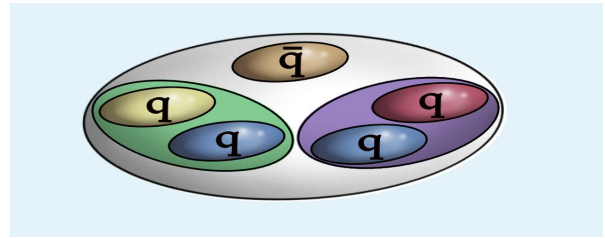


Figure 3.8: Pentaquark, composed of four quarks and one antiquark. The four quarks bind to two diquarks depicted in green and purple.

3.2 Tetraquarks: experimental evidence and history

The idea that diquarks and antidiquarks may play a fundamental role in hadron spectroscopy is rather old and goes back to the suggestions by Robert Jaffe and his collaborators over 30 years ago [74–76]. This suggestion was lying dormant for most of this period due to the lack of experimental evidence. More recently, diquarks were revived by Jaffe and Wilczek [76] in the context of exotic hadron spectroscopy, in particular that of pentaquark baryons, which now seem to have receded into oblivion. The story of the diquarks is still poorly treated because of the lacking evidence in data since several decades and the fatal setback in the pentaquark sector in the early part of this decade. However, diquarks as constituents of hadronic matter may eventually find their rightful place in particle physics, since the scientific case for the existence of tetraquarks recently got a boost by the discovery of new hadronic states with masses of typically 4 GeV. In the past several years, experiments at the two B-factories, BaBar and Belle, and at the Tevatron collider, CDF and D0, have discovered an impressive number of new hadronic states in the mass region of the charmonia [77]. These states, generically labeled as X , Y and Z , defy a conventional $c\bar{c}$ charmonium interpretation [2, 78]. Moreover, they are quite numerous, with 14 of them discovered by the last count, ranging in mass from the $J^{PC} = 1^{++}$ $X(3872)$, decaying into $D\bar{D}^*$, $J/\psi\pi^+\pi^-$, $J\psi\gamma$, to the $J^{PC} = 1^{--}$ $Y(4660)$, decaying into $\psi'\pi^+\pi^-$. There is also evidence for an $s\bar{s}$ bound state, $Y_s(2175)$ with the quantum numbers $J^{PC} = 1^{--}$, which was first observed by BaBar in the initial state radiation (ISR) process $e^+e^- \rightarrow \gamma_{\text{ISR}} f_0(980)\phi(1020)$, where $f_0(980)$ is the 0^{++} scalar state [79]. This was later confirmed by BES [80] and Belle [81].

Table 3.2.1: Summary of new states observed by Belle [84]

State	M [MeV]	Γ [MeV]	J^{PC}	Decay Modes	Production Modes	Also observed by
$Y_s(2175)$	2175 ± 8	58 ± 26	1^{--}	$\phi f_0(980)$	e^+e^- (ISR) $J/\psi \rightarrow \eta Y_s(2175)$	BaBar, BESII
$X(3872)$	3871.4 ± 0.6	< 2.3	1^{++}	$\pi^+\pi^- J/\psi,$	$B \rightarrow KX(3872), p\bar{p}$ $\gamma\gamma \rightarrow X(3872)$ $\gamma\gamma \rightarrow Z(3940)$	BaBar
$X(3915)$	3914 ± 4	28^{+12}_{-14}	$0/2^{++}$	$\gamma J/\psi, D\bar{D}^*$		CDF, D0,
$Z(3930)$	3929 ± 5	29 ± 10	2^{++}	$\omega J/\psi$		
$X(3940)$	3942 ± 9	37 ± 17	0^{2+}	$D\bar{D}^*$ (not $D\bar{D}$)	$e^+e^- \rightarrow J/\psi X(3940)$ $B \rightarrow KY(3940)$	BaBar
$Y(3940)$	3943 ± 17	87 ± 34	$?^{?+}$	or $\omega J/\psi$		
$Y(4008)$	4008^{+82}_{-49}	226^{+97}_{-80}	1^{--}	$\omega J/\psi$ (not $D\bar{D}^*$)	e^+e^- (ISR)	
$X(4160)$	4156 ± 29	139^{+113}_{-65}	0^{2+}	$\pi^+\pi^- J/\psi$	$e^+e^- \rightarrow J/\psi X(4160)$	
$Y(4260)$	4264 ± 12	83 ± 22	1^{--}	$D^*\bar{D}^*$ (not $D\bar{D}$)	e^+e^- (ISR)	BaBar, CLEO
$Y(4350)$	4361 ± 13	74 ± 18	1^{--}	$\pi^+\pi^- J/\psi$	e^+e^- (ISR)	BaBar
$X(4630)$	4634^{+9}_{-11}	92^{+41}_{-32}	1^{--}	$\pi^+\pi^- \psi'$	e^+e^- (ISR)	
$Y(4660)$	4664 ± 12	48 ± 15	1^{--}	$\Lambda_c^+ \Lambda_c^-$	e^+e^- (ISR)	
$Z(4050)$	4051^{+24}_{-23}	82^{+51}_{-29}	$?$	$\pi^\pm \chi_{c1}$	$B \rightarrow KZ^\pm(4050)$	
$Z(4250)$	4248^{+185}_{-45}	177^{+320}_{-72}	$?$	$\pi^\pm \chi_{c1}$	$B \rightarrow KZ^\pm(4250)$	
$Z(4430)$	4433 ± 5	45^{+35}_{-18}	$?$	$\pi^\pm \psi'$	$B \rightarrow KZ^\pm(4430)$	
$Y_b(10890)$	$10,890 \pm 3$	55 ± 9	1^{--}	$\pi^+\pi^- \Upsilon(1,2,3S)$	$e^+e^- \rightarrow Y_b$	

All these states are the subject of intense phenomenological studies. Three different frameworks have been suggested to accommodate them: (i) $D - D^*$ molecules [19, 24, 28]; (ii) $c\bar{c}g$ hybrids [33]; and (iii) tetraquarks [35, 36, 41], which are explained in the previous section. Of these hypotheses (i) and (iii) are the more popular ones. An example for a molecule candidate is the $X(3872)$. The motivation to explain this state, first observed by Belle [3] and later confirmed by CDF [4], D0 [5] and BaBar [6], as a hadronic molecule is that its mass is very close to the $D^0\bar{D}^{*0}$ threshold. Hence, the binding energy is small in this picture, implying that the hadronic molecules are not compact hadrons, in which case they would have typical sizes of $O(1)$ Fermi. But there are still caveats in this interpretation. The large size makes it unlikely that such a loosely bound state could be produced promptly (*i.e.* not from B decays, as seen by Belle and BaBar) in high energy hadron collisions, unless one tailors the wave functions to avoid this conclusion. In particular, Bignamini et al. [82] have estimated the prompt production cross section of $X(3872)$ at the Tevatron, assuming it as a $D^0\bar{D}^{*0}$ hadron molecule. Their upper bound on the cross section $p\bar{p} \rightarrow X(3872)+\dots$ is about two orders of magnitude smaller than the minimum production cross section from the CDF data [7], disfavoring the molecular interpretation of $X(3872)$. However, a dissenting estimate [83] yields a much larger cross section, invoking the charm-meson rescatterings. The discussion about the nature of $X(3872)$ and many other states is still ongoing. A summary of the newly discovered states observed by Belle and other experiments [84] mentioned above is presented in Tab. 3.2.1. For a recent theoretical review see [85].

Recently, the perception about the light scalar mesons, such as $f_0(600)$ or σ and $f_0(980)$ has changed. They are now interpreted as being dominantly tetraquark $[qq'][\bar{q}\bar{q}']$ states instead of the usual $q\bar{q}$ mesons [86]. In QCD, states are always organized in flavor multiplets, accompanied by their next kins. From the light-quark sector we have the following full $SU(3)_F$ nonet of tetraquark resonances [86], also shown in Fig. 3.9 (left):

$$\begin{aligned}
\sigma^{[0]} &= [ud][\bar{u}\bar{d}] & f_0^{[0]} &= \frac{[su][\bar{s}\bar{u}] + [sd][\bar{s}\bar{d}]}{\sqrt{2}} \\
\kappa &= [su][\bar{u}\bar{d}]; [sd][\bar{u}\bar{d}]; & a_0 &= \frac{[su][\bar{s}\bar{d}]; [sd][\bar{s}\bar{u}];}{\sqrt{2}} \\
& \quad (\text{+conjugate doublet}) & & \frac{[su][\bar{s}\bar{u}] - [sd][\bar{s}\bar{d}]}{\sqrt{2}}
\end{aligned} \tag{3.2.1}$$

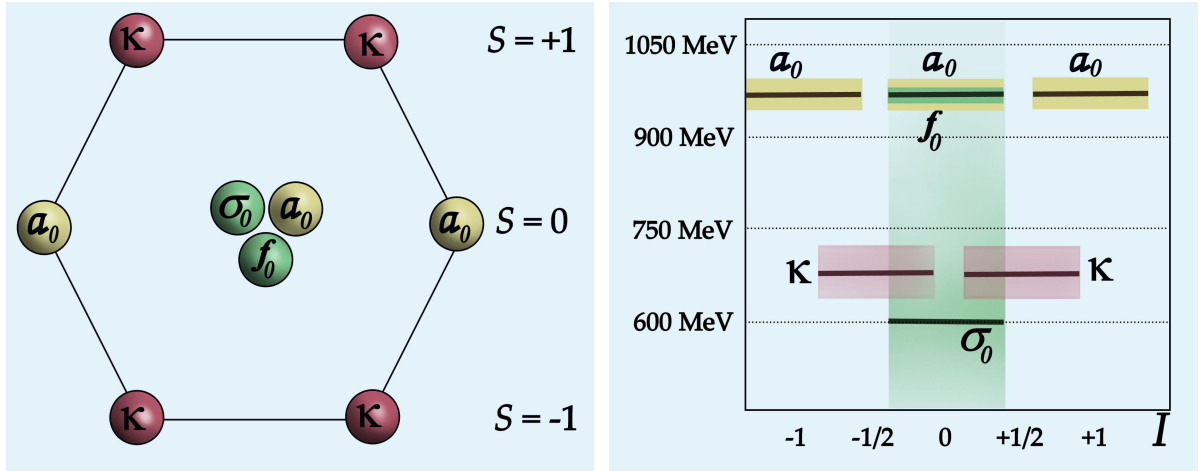


Figure 3.9: Light tetraquark nonet (left) and mass spectrum (right). The error bars are given by the semitransparent colors, yellow for the a_0 iso-triplet, red for the two conjugated κ iso-doublets and green for the two iso-scalars σ and $f_0(980)$. The mass values are taken from [77].

In the ordinary meson case, one would expect from the constituent quark model, that the masses of the $q\bar{q}$ nonet fall into a triangle. After s -quark mass-breaking, this triangle should arrange as shown in Fig. 3.10 (left), in which the expected masses for meson and tetraquark multiplets are compared. The iso-triplet contains the lowest lying states. The mass rises with increasing s -quark content for the iso-doublet and iso-singlet. The strongest experimental evidence favoring the existence of the light tetraquark nonet comes from the observed inverted mass spectrum. The measured triangle is indeed facing upside down as shown in Fig. 3.9 (right), which is in agreement with the expected constituent tetraquark mass spectrum in Fig. 3.10(right). Note, that the assigned error of the mass of the σ_0 is huge and even extend beyond the frame of the plot. In the PDG [77] it is listed with a mass ranging from 400 to 1200 MeV. There are several problems in its precise determination, originating mainly in the immense total decay width listed as $\Gamma = (600 - 1000)$ MeV. Thus there are threshold effects and overlaps with several other resonances and background terms. But also its unknown nature makes the analysis challenging, just to name some of the reasons why no value is currently fixed in the listings of the particle data group. In [87], however, the existence of the σ is established in a model-independent way using the dispersive representation of the partial wave amplitudes by Roy [88], also called Roy equations, which use the analytic properties of the scattering amplitudes at low energy scales. They have established the σ and $f_0(980)$ as poles, which are governed by the dynamics and interactions of the Goldstone bosons, the pions and kaons respectively. Their analysis yields a more precise value for the σ mass of $m_\sigma = 441^{+16}_{-8}$ MeV. The light scalar resonances also need to be accounted for in this work in the discussion of $Y_b^{(1)} \rightarrow \Upsilon(nS)PP'$ decays, in which $PP' = \pi^+\pi^-, K^+K^-$ or $\eta\pi^0$ are final state particles. In this work I use a mass of 478 MeV and a total decay width of 324 MeV for σ_0 , as determined by the E791 collaboration [89] from D^+ decays. The mass is very close to the one found by [87].

As mentioned, bound states in QCD are always accompanied by their next kins in the flavor multiplets. This should also hold to a certain extent for the heavier

quarks, especially in view of heavy-flavor symmetry. If a tetraquark can be composed of charm-quarks, it should also be possible to find them in the bottom sector. Till the end of 2009, there has been no tetraquark candidate observed in the hidden $b\bar{b}$ sector. In our work [43], [44] and [90], we presented the first evidence for tetraquarks in the bottom-quark sector - harbingers of an entirely new world of bound and open beauty hadrons. In our approach we interpreted the $Y_b(10890)$ state discovered by Belle [91], *i.e.* the last line in Tab. 3.2.1, as hidden bottom tetraquark. In the following this state is called $Y_b^{(1)}$. It is a P -wave $L = 1$ state composed of two *good* diquarks. One might ask the question, why there is so far only a single particle which provides evidence for the existence of tetraquarks in the $b\bar{b}$ sector, even though there should be a plethora of states present. While the lighter tetraquarks, including the charmed ones, can be produced in decays of heavier particles (such as weak B -decays), the bottom-quarks are lacking this possibility and have in general small production cross sections. The tetraquark $Y_b^{(1)}$ with spin-parity and charge conjugation assignment $J^{PC} = 1^{--}$, however, possesses the right quantum numbers to be directly produced in e^+e^- annihilation. If the e^+e^- production cross section is big enough, this could provide the desired opportunity for producing $b\bar{b}$ -tetraquarks experimentally.

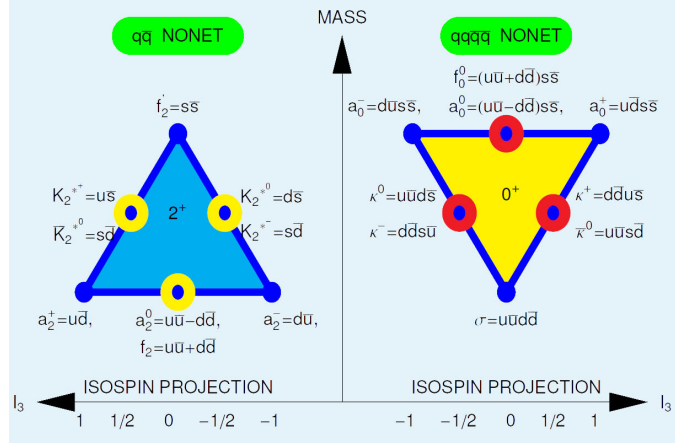


Figure 3.10: Comparison of the mass spectrum of tetraquark states (right) and mesons (left) expected from the constituent quark model.

3.3 Our work for tetraquarks in the bottom sector

In [43] we were able to identify tetraquark states, which can directly be produced in e^+e^- annihilation. Of these $Y_{[bu]}$ and $Y_{[bd]}$ with $J^{PC} = 1^{--}$ quantum numbers are estimated to have the right masses to be produced in the vicinity of the $\Upsilon(5S)$. The $Y_{[bq]}$ have the quark content $[bq][\bar{b}\bar{q}]$, in which $[bq]$ and $[\bar{b}\bar{q}]$ indicate the diquark and antidiquark respectively. The physical particles are called $Y_{[b,l]}$ and $Y_{[b,h]}$, for lighter and heavier, are mixed states. They have masses around 10.90 GeV, as will be shown in Sec. 3.4. We classified these states according to their J^{PC} quantum numbers and calculate the mass spectrum of the diquarks-antidiquarks $[bq][\bar{b}\bar{q}']$ with $q, q' = u, d, s$ and c in the ground and orbitally excited states by taking into account both *good* and *bad* diquarks. The resulting mass spectrum for the $0^{++}, 1^{++}, 1^{+-}, 1^{--}$ and 2^{++} states with valence diquark-antidiquark content $[bq][\bar{b}\bar{q}]$ ($q = u, d, s, c$) and the mixed states $[bd][\bar{b}\bar{s}]$ (and charge conjugates). The main focus of this work is as aforementioned on the $J^{PC} = 1^{--}$ states. To be specific, there are four neutral states $Y_{[bu]}^{(n)}$ ($n = 1, \dots, 4$) with the quark content ($[bu][\bar{b}\bar{u}]$) (which differ in their spin assignments) and another four $Y_{[bd]}^{(n)}$ with the quark content ($[bd][\bar{b}\bar{d}]$). These mass states are degenerate in the isospin symmetry limit for each n , and the notation is abbreviated as

$Y_b^{(n)}$. All four states have the quantum numbers $J^{PC} = 1^{--}$, but only the $Y_b^{(1)}$ is composed of only *good* diquarks. The $Y_b^{(2)}$ and $Y_b^{(3)}$ each contain one and the $Y_b^{(4)}$ two *bad* diquarks.

Isospin-breaking introduces a mass splitting and the mass eigenstates called $Y_{[b,l]}^{(n)}$ and $Y_{[b,h]}^{(n)}$ (for lighter and heavier of the two) become linear combinations of $Y_{[bu]}^{(n)}$ and $Y_{[bd]}^{(n)}$. Thus, $Y_{[b,l]}^{(n)} \equiv \cos\theta Y_{[bu]}^{(n)} + \sin\theta Y_{[bd]}^{(n)}$ and $Y_{[b,h]}^{(n)} \equiv -\sin\theta Y_{[bu]}^{(n)} + \cos\theta Y_{[bd]}^{(n)}$. The mass differences are estimated to be small, with $M(Y_{[b,h]}^{(n)}) - M(Y_{[b,l]}^{(n)}) = (7 \pm 2) \cos 2\theta$ MeV, where θ is a mixing angle. In Sec. 3.5 the calculation of the isospin breaking is explained.

The electromagnetic couplings of the tetraquarks $Y_{[b,l]}^{(n)}$ and $Y_{[b,h]}^{(n)}$ are calculated assuming that the diquarks have pointlike couplings with the photon, given by $eQ_{[bq]}$, where $e^2/(4\pi)$ is the electromagnetic fine structure constant α , and $Q_{[bq]} = +1/3$ for the $[bu]$ and $[bc]$ diquarks and $Q_{[bq]} = -2/3$ for the $[bd]$ and $[bs]$ diquarks. Because of this charge assignment, the electromagnetic couplings of the tetraquarks $Y_{[b,l]}^{(n)}$ and $Y_{[b,h]}^{(n)}$ depend on the mixing angle θ . To calculate the production cross sections $e^+e^- \rightarrow Y_{[b,l]}^{(n)} \rightarrow$ hadrons and $e^+e^- \rightarrow Y_{[b,h]}^{(n)} \rightarrow$ hadrons, one needs to calculate the partial widths $\Gamma_{ee}^{(n)}(Y_{[b,l]})$ and $\Gamma_{ee}^{(n)}(Y_{[b,h]})$ for decays into e^+e^- pair and the hadronic decay widths $\Gamma(Y_{[b,l]}^{(n)})$ and $\Gamma(Y_{[b,h]}^{(n)})$. For the $\Upsilon(nS)$, the leptonic decay widths are determined by the wave functions at the origin $\Psi_{b\bar{b}}(0)$. The tetraquark states are similar to the bottomonia for pointlike diquarks. To take into account the possibly larger hadronic size of the tetraquarks compared to that of the $b\bar{b}$ mesons, we modify the quarkonia potential, usually taken as a sum of linear (confining) and coulombic (short-distance) parts. For example, the Buchmüller-Tye $Q\bar{Q}$ potential [92] has the asymptotic forms $V(r) \sim k_{Q\bar{Q}} r$ (for $r \rightarrow \infty$) and $V(r) \sim 1/r \ln(1/\Lambda_{\text{QCD}}^2 r^2)$ (for $r \rightarrow 0$), where $k_{Q\bar{Q}}$ is the string tension and Λ_{QCD} is the QCD scale parameter. The bound state tetraquark potential $V_{Q\bar{Q}}(r)^2$ will differ from the Quarkonia potential $V_{Q\bar{Q}}(r)$ in the linear part, as the string tension in a diquark $k_{Q\bar{Q}}$ is expected to be different than the corresponding string tension $k_{Q\bar{Q}}$ in the $Q\bar{Q}$ mesons. However, as the diquarks-antidiquarks in the tetraquarks and the quarks-antiquarks in the mesons are in the same $(\mathbf{\bar{3}}, \mathbf{3})$ color representation, the Coulomb (short-distance) parts of the potentials are similar. Defining $\kappa = k_{Q\bar{Q}}/k_{Q\bar{Q}}$, κ is expected to have a value smaller than 1. A value of κ different from unity will modify the tetraquark wave functions $\Psi_{Q\bar{Q}}(0)$ from the corresponding ones of the bound $b\bar{b}$ systems, effecting the leptonic decay widths of the tetraquarks. The derivation of the leptonic decay width $\Gamma(Y_{[b,l]}^{(n)})$ and $\Gamma(Y_{[b,h]}^{(n)})$ is outlined in Sec. 3.5.

The hadronic decays of $Y_{[b,l]}^{(n)}$ and $Y_{[b,h]}^{(n)}$ are calculated by relating them to the corresponding decays of the $\Upsilon(5S)$, such as $\Upsilon(5S) \rightarrow B^{(*)}\bar{B}^{(*)}$, which we take from the PDG. It is assumed, that the form factors in the two set of decays ($Y_{[b,q]}$ and $\Upsilon(5S)$) are roughly (say up to a factor 2 or 3) related by κ , yielding the hadronic decay widths presented in Sec. 3.6. The results are related to the total decay width and give important hints for the searches in experimental data. Because the masses of the $Y_b^{(n)}$ are all above the Zweig allowed $B^{(*)}\bar{B}^{(*)}$ thresholds, the width is expected to be large.

Having specified the mass spectrum and our dynamical assumptions for the tetraquark decays, a theoretical analysis of the existing data from BaBar [93] on $R_b(s) = \sigma(e^+e^- \rightarrow$

²We shall use the symbol Q and \bar{Q} to denote a generic diquark and antidiquark, respectively. However, where the flavor content of the diquark is to be specified, we use the symbol $[bq]$, and $[\bar{b}\bar{q}]$ with $q = u, d, s, c$.

$b\bar{b})/\sigma(e^+e^- \rightarrow \mu^+\mu^-)$ is carried out in Sec. 3.7. The data were obtained during an energy scan of the $e^+e^- \rightarrow b\bar{b}$ cross section in the range of $\sqrt{s} = 10.54$ to 11.20 GeV. The question that is hoped to be answered in this analysis is: Are the kinematically allowed tetraquark states $Y_{[b,h]}^{(n)}$ and $Y_{[b,l]}^{(n)}$ visible in the BaBar energy scan of R_b ? To that end, the contributions of the lowest 1^{--} tetraquark states $Y_{[b,h]}$ and $Y_{[b,l]}$ to the hadronic cross sections $\sigma(e^+e^- \rightarrow Y_{[b,l]} \rightarrow \text{hadrons})$ and $\sigma(e^+e^- \rightarrow Y_{[b,h]} \rightarrow \text{hadrons})$, and hence the corresponding contributions $\Delta R_b(s)$ are calculated. Our fits in [43] of the BaBar R_b -data are consistent with the presence of a single state $Y_{[bq]}$ as a Breit-Wigner resonance with mass around 10.90 GeV and total width of about 30 MeV in addition to the $\Upsilon(5S)$ and $\Upsilon(6S)$. The quality of the fit with three Breit-Wigners is found to be better than the one obtained with just only $\Upsilon(5S)$ and $\Upsilon(6S)$ as reported by BaBar [93]. A closeup of the energy region around 10.90 GeV is necessary to confirm and resolve the structure reported by us. The isospin-induced mass difference between the two eigenstates $Y_{[b,h]}$ and $Y_{[b,l]}$ comes out as about 6 MeV, which is comparable to the BaBar center-of-mass energy step of 5 MeV. Hopefully this can be investigated in the near future by Belle. These results are presented in Sec. 3.7.

Our inference was that the BaBar data are consistent with the presence of additional $b\bar{b}$ states $Y_{[b,l]}$ and $Y_{[b,h]}$ with a mass of about 10.90 GeV and a decay width of about 30 MeV, beside the $\Upsilon(5S)$ and $\Upsilon(6S)$ resonances. This is insufficient to prove or disprove the existence of tetraquarks in the predicted region. It struck us that most of the enigmatic events in the Belle data, explained below, in the final states $\Upsilon(1S)\pi^+\pi^-$ and $\Upsilon(2S)\pi^+\pi^-$ are concentrated around 10.90 GeV, and hence we tentatively identified the states in our analysis of the R_b -scan with the state $Y_b(10890)$ in the Belle analysis shown in the last line of Tab. 3.2.1.

In December 2007, the Belle collaboration reported the first observation of the processes $e^+e^- \rightarrow \Upsilon(1S)\pi^+\pi^-$ and $e^+e^- \rightarrow \Upsilon(2S)\pi^+\pi^-$ near the peak of the $\Upsilon(5S)$ resonance at the center-of-mass energy \sqrt{s} of about 10.87 GeV [91,94]. The $\Upsilon(nS)$ states are called "bottomonia" - $b\bar{b}$ bound states of the bottom-quark and its antiparticle. In particular, the final states $\Upsilon(1S)\pi^+\pi^-$ and $\Upsilon(2S)\pi^+\pi^-$ arising from the production and decays of the lower bottomonia states, such as $\Upsilon(4S) \rightarrow \Upsilon(1S)\pi^+\pi^-$, have been studied in a number of experiments over the last thirty years and are theoretically well-understood in QCD [95–98].

The observed spin averaged $1 \rightarrow 3$ processes are in general characterized by the helicity angle θ and the invariant mass $m_{\pi\pi}$ as pictured in Fig. 3.11. This is also what was measured by the Belle group. Invariant mass refers to the absolute value of the sum of the outgoing particle momenta. For n outgoing particles with momenta k_i the invariant mass is defined by $m_{k_1\dots k_n} \equiv |\sum_i^n k_i|$. More about kinematics can be found in App. C.3. The invariant mass is a Lorentz-invariant quantity, but the helicity angle is frame dependent. It is defined as the angle between the pion and the $\Upsilon(nS)$ in the dipion rest frame. The differential

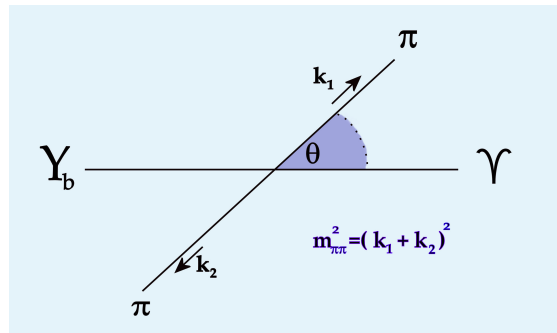


Figure 3.11: Kinematics of a (spin averaged) $1 \rightarrow 3$ process in the rest frame of the dipion system. The two independent variables in this frame are the helicity angle θ and the invariant mass $m_{\pi\pi}$.

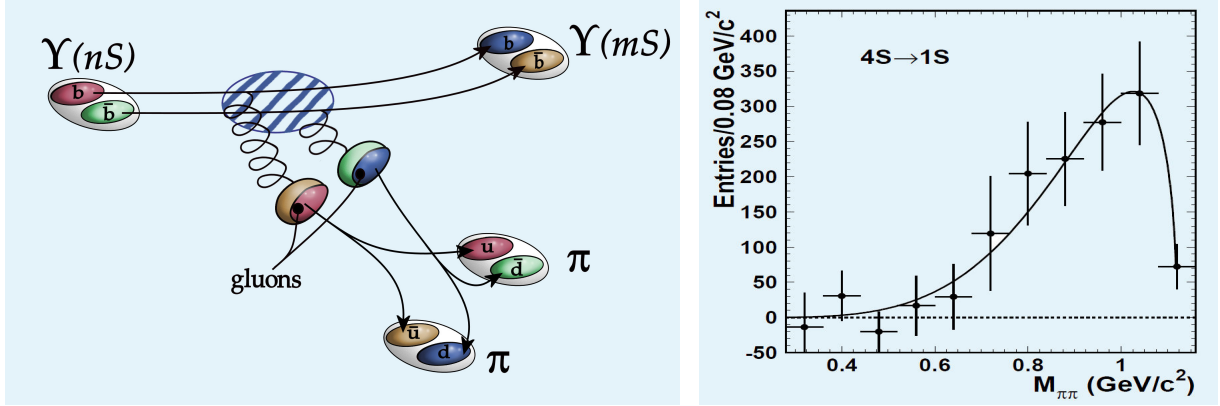


Figure 3.13: Underlying Zweig forbidden process for the $\Upsilon(nS) \rightarrow \Upsilon(mS)\pi^+\pi^-$ transition (left), in which $n > m$ such that the dipionic decay is kinematically allowed, and the corresponding invariant-mass spectrum for a typical decay $\Upsilon(4S) \rightarrow \Upsilon(1S)\pi^+\pi^-$ (right; frame taken from [99])

cross section is invariant under the interchange of π^+ and π^- in the isospin limit and hence symmetric in $\cos\theta$ distribution.

Belle measurements near the $\Upsilon(5S)$ did not fall in line with theoretical expectations [91,94]. Their data were enigmatic in that the partial decay widths for $\Upsilon(5S) \rightarrow \Upsilon(1S)\pi^+\pi^-$ and $\Upsilon(5S) \rightarrow \Upsilon(2S)\pi^+\pi^-$ were typically up to three orders of magnitude larger than anticipated in QCD [95–98]. The measured partial decay widths are listed in Tab. 3.3.1, in which the decay widths measured for the supposedly $\Upsilon(5S)$ state is highlighted in red.

The underlying process, pictured in Fig. 3.13 (left), describes the decays of the lower $\Upsilon(2S)$ - $\Upsilon(4S)$ decaying to $\Upsilon(2S)\pi^+\pi^-$ well and involves two gluon interactions. These processes are Zweig-forbidden and hence lead to small cross sections. In addition to the deviation of the measured cross sections from the expectations, the dipion invariant-mass distributions in these events were distinct different from theoretical expectations. The difference shows for example in the corresponding measurements for the $\Upsilon(4S)$ decays $\Upsilon(4S) \rightarrow \Upsilon(1S)\pi^+\pi^-$ undertaken previously by the Belle collaboration [99], shown in Fig. 3.13 (right). The measurements in question are robust, with the $\Upsilon(1S)\pi^+\pi^-$ and $\Upsilon(2S)\pi^+\pi^-$ channels having a significance of 20σ and 14σ [91,94], respectively. By comparing the expectations (shaded histograms and red line) with the measurements (crosses) given in Fig. 3.12 it is obvious that for the decays found near the $\Upsilon(5S)$, the hitherto working picture of the $\Upsilon(nS)$ decays is not valid.

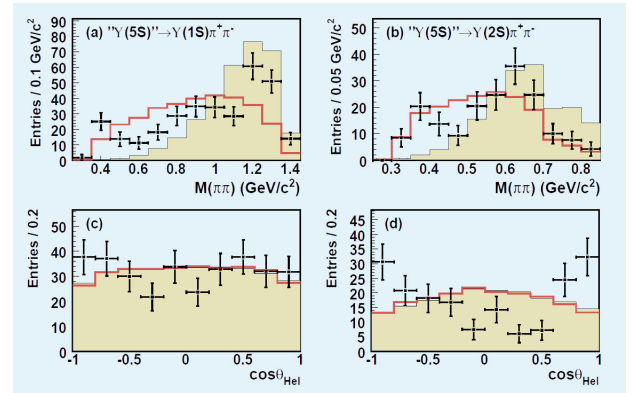


Figure 3.12: Measured spectra for the $\Upsilon(1S)\pi^+\pi^-$ and $\Upsilon(2S)\pi^+\pi^-$ channels (crosses; figures taken from [91]). The histograms (red curves) region is obtained from a Monte-Carlo simulation using the model of reference [95] (phase space model) described in Fig. 3.13.

Table 3.3.1: The total width Γ_{total} , and the partial width $\Gamma_{e^+e^-}$, $\Gamma_{\Upsilon(1S)\pi^+\pi^-}$ [91]_{Tab. II}.

Process	Γ_{total}	$\Gamma_{e^+e^-}$	$\Gamma_{\Upsilon(1S)\pi^+\pi^-}$
$\Upsilon(2S) \rightarrow \Upsilon(1S)\pi^+\pi^-$	0.032 MeV	0.612 keV	0.0060 MeV
$\Upsilon(3S) \rightarrow \Upsilon(1S)\pi^+\pi^-$	0.020 MeV	0.443 keV	0.0009 MeV
$\Upsilon(4S) \rightarrow \Upsilon(1S)\pi^+\pi^-$	20.5 MeV	0.272 keV	0.0019 MeV
$\Upsilon(5S) \rightarrow \Upsilon(1S)\pi^+\pi^-$	110 MeV	0.31 keV	0.59 MeV

To be precise, two aspects of the Belle data had to be explained: (a) the anomalously large partial decay rates and (b) the unexpected invariant-mass distributions of the dipions. A related and important issue is whether the puzzling events seen by Belle stem from the decays of the $\Upsilon(5S)$, or from another particle having a mass close to the mass of the $\Upsilon(5S)$. In the conventional quarkonium theory, there is no place for an additional $b\bar{b}$ resonance having the quantum numbers of $\Upsilon(5S)$.

Our interpretation [44] of the Belle data is that the anomalous $\Upsilon(1S)\pi^+\pi^-$ and $\Upsilon(2S)\pi^+\pi^-$ events are not caused by the production and decays of the $\Upsilon(5S)$, but rather by the production of a completely different hadron species, the above mentioned $Y_b^{(1)}$ tetraquark states, and their subsequent decays.

To pursue our theoretical hypothesis, we developed a dynamical theory to make quantitative predictions and undertake an analysis of the Belle data. The presented model can explain the larger decay rates for the transitions $Y_b^{(1)} \rightarrow \Upsilon(1S)\pi^+\pi^-$, $\Upsilon(2S)\pi^+\pi^-$, as well as the decays of $Y_b^{(1)}$ involving a recombination of the initial four quarks. This is exemplified below by the process $Y_{[bq]} = [bq][\bar{b}\bar{q}] \rightarrow (b\bar{b})(q\bar{q})$, with the subsequent projection $(b\bar{b}) \rightarrow \Upsilon(1S)$ and $(q\bar{q}) \rightarrow \pi^+\pi^-$. The model is further explained in Sec. 3.8.1.

The measured decay distributions, such as the dipion invariant-mass spectra, are also easily understood in terms of the affinity of the tetraquark states $Y_{[b,l]}$ and $Y_{[b,h]}$ to decay preferentially into $\Upsilon(1S)$ or $\Upsilon(2S)$ and lighter tetraquark states, like the light 0^{++} states $\sigma_0(600)$ and $f_0(980)$ as mentioned earlier. Hence, one expects a resonant structure in the dipion invariant mass, reflecting these and other known resonances allowed by phase space and angular momentum and parity conservation. In our model we were indeed able to perceive a clear indication for such intermediate resonance interchanges in the shape of the invariant-mass spectrum. In summary, the tetraquark interpretation of the $Y_b(10890)$ provides an excellent description of the decay distributions measured by Belle. The fit results are shown in Sec. 3.8.2.

Exciting and plausible as our explanation of the Belle and BaBar data is, a number of measurements are needed to confirm the tetraquark interpretation of the Belle anomaly. First and foremost two almost degenerate states $Y_{[b,l]}$ and $Y_{[b,h]}$, predicted in the tetraquark theory as members of an iso-doublet, have to be confirmed experimentally. We eagerly await the analysis of the new data which Belle is currently accumulating around the $\Upsilon(5S)$ region. Improved measurements of the cross section $e^+e^- \rightarrow b\bar{b}$ in dedicated energy scans, which will be carried out at the Super-B factories being planned at KEK and Frascati (Italy), may also greatly help in resolving this structure and perhaps establish other tetraquark resonances predicted in that region. If the higher and lower mass

eigenstates can be distinguished depends on the one hand on the suppression with respect to the background and the dominance of the enhanced contributions from the bottomonia resonances with masses in the same energy region. On the other hand it depend on the mixing between the flavor eigenstates $Y_{[bu]}$ and $Y_{[bd]}$. If there is no mixing ($\theta = 0$), the $Y_{[b,l]}$ state is even further suppressed with respect to $Y_{[b,l]}$ by a factor 1/4 (the squared ratio of the effective diquark charges). The inclusive (*i.e.* without specifying a single final state) data has therefore disadvantages and may not be more conclusive than the already analyzed BaBar data. There are, however, still unexplored exclusive (*i.e.* for a specific final state) channels. In our latest work [90] we utilized our fit to the data of the exclusive $Y_b^{(1)} \rightarrow \Upsilon(1S)\pi^+\pi^-$ channel to predict the size of the cross sections and the shapes for the exclusive channels $Y_b^{(1)} \rightarrow \Upsilon(1S)K^+K^-$ and $Y_b^{(1)} \rightarrow \Upsilon(1S)\eta\pi^0$. If the presented model in Sec. 3.8.1 is a proper description and the coupling to intermediate resonances is as predicted, the other exclusive channels should show the same feature. Another testable prediction in this framework is, that the ratio of the observed K^+K^- and $K^0\bar{K}^0$ should be 1. Currently we are preparing a forthcoming paper [100] in which further details about the correlations among the parameters and the cross sections will be presented. In Sec. 3.8.3 all our predictions are discussed in detail.

3.4 Mass spectrum of bottom diquark-antidiquark states

In this section I derive the hidden bottom tetraquark mass spectra in the framework of a simple constituent Hamiltonian model. See [41] for the application of the Hamiltonian model in the strange-tetraquark sector and [101] for the historical roots of the constituent quark models. The masses are the most easy accessible and moreover the first important input to any search for experimental evidence.

The mass spectrum of tetraquarks $[bq][\bar{b}\bar{q}']$ with $q = u, d, s$ and c can be described in terms of the constituent diquark masses, $m_{\mathcal{Q}}$, spin-spin interactions inside the single diquark, $H_{SS}^{(\mathcal{Q}\mathcal{Q})}$, spin-spin interactions between quark and antiquark belonging to two diquarks, $H_{SS}^{(\mathcal{Q}\bar{\mathcal{Q}})}$, spin-orbit interactions, H_{SL} , and purely orbital term, H_{LL} :

$$H = 2m_{\mathcal{Q}} + H_{SS}^{(\mathcal{Q}\mathcal{Q})} + H_{SS}^{(\mathcal{Q}\bar{\mathcal{Q}})} + H_{SL} + H_{LL}. \quad (3.4.1)$$

The Hamiltonian is diagonalized by a certain set of four quark states, which will be introduced later. Introducing the vector valued spin \mathbf{S} and angular momentum \mathbf{L} operators, the terms can be written as

$$\begin{aligned} H_{SS}^{(\mathcal{Q}\mathcal{Q})} &= 2(\mathcal{K}_{bq})_{\bar{3}}[(\mathbf{S}_b \cdot \mathbf{S}_q) + (\mathbf{S}_{\bar{b}} \cdot \mathbf{S}_{\bar{q}})], \\ H_{SS}^{(\mathcal{Q}\bar{\mathcal{Q}})} &= 2(\mathcal{K}_{b\bar{q}})(\mathbf{S}_b \cdot \mathbf{S}_{\bar{q}} + \mathbf{S}_{\bar{b}} \cdot \mathbf{S}_q) + 2\mathcal{K}_{b\bar{b}}(\mathbf{S}_b \cdot \mathbf{S}_{\bar{b}}) + 2\mathcal{K}_{q\bar{q}}(\mathbf{S}_q \cdot \mathbf{S}_{\bar{q}}), \\ H_{SL} &= 2A_{\mathcal{Q}}(\mathbf{S}_{\mathcal{Q}} \cdot \mathbf{L} + \mathbf{S}_{\bar{\mathcal{Q}}} \cdot \mathbf{L}), \\ H_{LL} &= B_{\mathcal{Q}} \frac{L_{\mathcal{Q}\bar{\mathcal{Q}}}(L_{\mathcal{Q}\bar{\mathcal{Q}}} + 1)}{2}. \end{aligned} \quad (3.4.2)$$

Here $m_{\mathcal{Q}}$ is the mass of the diquark $[bq]$, $L_{\mathcal{Q}\bar{\mathcal{Q}}}$ is the orbital excitation quantum number of the diquark and antidiquark,

$(\mathcal{K}_{bq})_{\bar{3}}$ accounts for the spin-spin interaction between the quarks inside the diquark and antidiquark, $\mathcal{K}_{q\bar{q}}$ are the couplings ranging from the quarks in the diquark to the antiquarks in the antidiquark, $A_{\mathcal{Q}}$ is the spin-orbit coupling of diquark and $B_{\mathcal{Q}}$ corresponds to the contribution of the total angular momentum of the diquark-antidiquark system. A schematic picture of the spin interactions is presented in Fig. 3.14. The overall factor of 2 is used customarily in the literature. A closer look on the spin interactions of Eq. (3.4.1) and (3.4.2) shows, that the spin part is composed of the spin interaction of each pairing of the quarks inside the tetraquark:

$$H_{SS} = \sum_{i<j} 2\mathcal{K}_{ij}(\mathbf{S}_i \cdot \mathbf{S}_j), \quad (3.4.3)$$

where the sum runs over the hadron constituents. The coefficient \mathcal{K}_{ij} depends on the flavor of the constituents i, j and on the particular color state of the pair. The color representation of the two quark system can be $\mathbf{3} \otimes \bar{\mathbf{3}} = \mathbf{1} \oplus \mathbf{8}$ for the quark-antiquark system and $\mathbf{3} \otimes \mathbf{3} = \bar{\mathbf{3}} \oplus \mathbf{6}$ for the quark-quark system (the antiquark-antiquark system is similar). In Sec. 3.1 it is argued, that the sextets are phenomenologically irrelevant.

For the calculation of the masses isospin symmetry is assumed, *i.e.* the iso-doublet consisting of the states

$$\begin{aligned} Y_{[bu]}^{(n)} &= [bu][\bar{b}\bar{u}] \quad \text{and} \\ Y_{[bd]}^{(n)} &= [bd][\bar{b}\bar{d}] \end{aligned} \quad (3.4.4)$$

are degenerate in mass for each n . Later, the isospin symmetry breaking effects in the masses will be calculated.

As mentioned, the Hamiltonian (3.4.1) needs to diagonalize the mass eigenstates. To accomplish this, the qualitative operator (3.4.1) needs to be cast in a mathematical form, and likewise the states. We use the non-relativistic notation $|S_{\mathcal{Q}}, S_{\bar{\mathcal{Q}}}; J\rangle$, where $S_{\mathcal{Q}}$ and $S_{\bar{\mathcal{Q}}}$ are the spin of diquark and antidiquark, respectively, and J is the total angular momentum. These states are then defined in terms of the direct product of the 2×2 matrices Γ^α in spinor space, which can be written in terms of the Pauli matrices as:

$$\Gamma^0 = \frac{\sigma_2}{\sqrt{2}}; \quad \Gamma^i = \frac{1}{\sqrt{2}}\sigma_2\sigma_i, \quad (3.4.5)$$

in which the former corresponds to the scalar and the latter to the vector diquark. The following tetraquark ground states are obtained:

$$\begin{aligned} |0_{\mathcal{Q}}, 0_{\bar{\mathcal{Q}}}; 0_J\rangle &= \frac{1}{2}(\sigma_2) \otimes (\sigma_2), \\ |1_{\mathcal{Q}}, 1_{\bar{\mathcal{Q}}}; 0_J\rangle &= \frac{1}{2\sqrt{3}}(\sigma_2\sigma^i) \otimes (\sigma_2\sigma^i), \end{aligned}$$

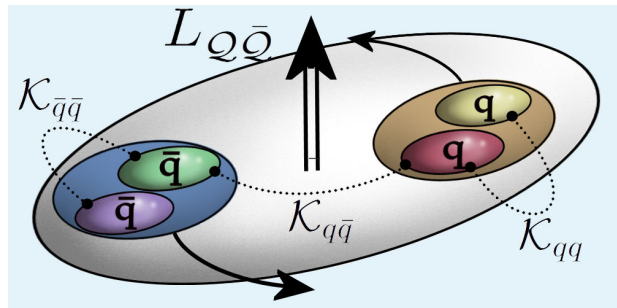


Figure 3.14: Schematic picture describing the meaning of the coefficients in the Hamiltonian (3.4.1). To illustrate the spin-orbit and purely orbital terms is beyond the scope of this simple picture.

Table 3.4.1: Constituent-quark masses derived from the $L = 0$ mesons and baryons.

Constituent mass [MeV]	q	s	c	b
Mesons	305	490	1670	5008
Baryons	362	546	1721	5050

Table 3.4.2: Spin-Spin couplings for quark-antiquark pairs in the color singlet state from the known mesons.

Spin-spin couplings	$q\bar{q}$	$s\bar{q}$	$s\bar{s}$	$c\bar{q}$	$c\bar{s}$	$c\bar{c}$	$b\bar{q}$	$b\bar{s}$	$b\bar{c}$	$b\bar{b}$
$(\mathcal{K}_{ij})_0$ [MeV]	318	200	129	71	72	59	23	23	20	36

$$\begin{aligned}
|0_{\mathcal{Q}}, 1_{\bar{\mathcal{Q}}}; 1_J\rangle &= \frac{1}{2} (\sigma_2) \otimes (\sigma_2 \sigma^i), \\
|1_{\mathcal{Q}}, 0_{\bar{\mathcal{Q}}}; 1_J\rangle &= \frac{1}{2} (\sigma_2 \sigma^i) \otimes (\sigma_2), \\
|1_{\mathcal{Q}}, 1_{\bar{\mathcal{Q}}}; 1_J\rangle &= \frac{1}{2\sqrt{2}} \varepsilon^{ijk} (\sigma_2 \sigma^j) \otimes (\sigma_2 \sigma^k).
\end{aligned} \tag{3.4.6}$$

Similar matrix representations exist for the spin operators. More about the explicit forms and calculations can be found in App. C.1.

The next step is the diagonalization of the Hamiltonian (3.4.1) by using the basis of states with definite diquark and antidiquark spin and total angular momentum. There are two different possibilities: The lowest lying states with $L_{\mathcal{Q}\bar{\mathcal{Q}}} = 0$ and the orbital excited higher mass states with $L_{\mathcal{Q}\bar{\mathcal{Q}}} = 1$, which are discussed below.

The parameters involved in the Hamiltonian (3.4.2) can be obtained from the known meson and baryon masses in the constituent quark model [101]. The derivation is straight forward. It is based on the assumption that the constants involved in the Hamiltonian are to a good approximation universal. This allows to resort to the known mesons and baryons and to derive the constants with their help. Namely, the spin interaction between two quarks can be obtained from the baryon mass spectrum, as the coefficients, say for example \mathcal{K}_{ud} , play a role in the calculation of the proton mass. The spin interaction between a quark and an antiquark can be obtained from the mesons and the orbital interactions can be estimated from the excited mesons and baryons and so on.

Using the entries in the PDG for hadron masses along with the assumption that the spin-spin interactions are independent of whether the quarks belong to a meson or a diquark, the results for diquark masses corresponding to X (3872) and Y (2175) were calculated in the literature [35, 41]. Here, this procedure is extended to the tetraquarks $[bq][\bar{b}\bar{q}]$. The constituent quark masses and the couplings \mathcal{K}_{ij} for the color singlet and antitriplet states are given in Tab. 3.4.1, 3.4.2 and 3.4.3. The 0 index indicates, that the quark and antiquark are in the singlet representation, which is the only accessible configuration from the mesons. The octet configuration is discussed later.

Table 3.4.3: Spin-Spin couplings for quark-quark pairs in color $\bar{3}$ state from the known baryons.

Spin-Spin couplings	qq	sq	cq	cs	ss	bq	bs	bc
$(\mathcal{K}_{ij})_{\bar{3}}[\text{MeV}]$	98	65	22	24	72	6	25	10

3.4.1 Lowest lying $[bq][\bar{b}\bar{q}]$ ground states with $L_{Q\bar{Q}} = 0$

The states can be classified in terms of the diquark and antidiquark spin, S_Q and $S_{\bar{Q}}$, total angular momentum J , parity P and charge conjugation C . The charge conjugation in terms of Pauli matrices is given by $C = i\sigma^2$, such that transposition works the same way as with Dirac matrices, $\sigma_i^T = C\sigma_i C$ and $\gamma_\mu^T = C\gamma_\mu C$ for Dirac matrices correspondingly. Considering both *good* and *bad* diquarks we have six possible states, which are listed below.

i. Two states with $J^{PC} = 0^{++}$:

$$\begin{aligned} |0^{++}\rangle &= |0_Q, 0_{\bar{Q}}; 0_J\rangle; \\ |0^{++'}\rangle &= |1_Q, 1_{\bar{Q}}; 0_J\rangle. \end{aligned} \quad (3.4.7)$$

ii. Three states with $J = 1$:

$$\begin{aligned} |1^{++}\rangle &= \frac{1}{\sqrt{2}} (|0_Q, 1_{\bar{Q}}; 1_J\rangle + |1_Q, 0_{\bar{Q}}; 1_J\rangle); \\ |1^{+-}\rangle &= \frac{1}{\sqrt{2}} (|0_Q, 1_{\bar{Q}}; 1_J\rangle - |1_Q, 0_{\bar{Q}}; 1_J\rangle); \\ |1^{+-'}\rangle &= |1_Q, 1_{\bar{Q}}; 1_J\rangle. \end{aligned} \quad (3.4.8)$$

All these states have positive parity, since both, the *good* and *bad* diquarks, have positive parity. They differ in the charge conjugation quantum number, the state $|1^{++}\rangle$ is even under charge conjugation, whereas $|1^{+-}\rangle$ and $|1^{+-'}\rangle$ are odd.

iii. One state with $J^{PC} = 2^{++}$:

$$|2^{++}\rangle = |1_Q, 1_{\bar{Q}}; 2_J\rangle. \quad (3.4.9)$$

For $L_{Q\bar{Q}} = 0$ the Hamiltonian (3.4.1) takes the form

$$\begin{aligned} H &= 2m_{[bq]} + 2(\mathcal{K}_{bq})_{\bar{3}}[(\mathbf{S}_b \cdot \mathbf{S}_q) + (\mathbf{S}_{\bar{b}} \cdot \mathbf{S}_{\bar{q}})] + 2\mathcal{K}_{q\bar{q}}(\mathbf{S}_q \cdot \mathbf{S}_{\bar{q}}) \\ &\quad + 2(\mathcal{K}_{b\bar{q}})(\mathbf{S}_b \cdot \mathbf{S}_{\bar{q}} + \mathbf{S}_{\bar{b}} \cdot \mathbf{S}_q) + 2\mathcal{K}_{b\bar{b}}(\mathbf{S}_b \cdot \mathbf{S}_{\bar{b}}). \end{aligned} \quad (3.4.10)$$

The diagonalization of the Hamiltonian (3.4.10) with the states defined above gives the eigenvalues, which are needed to estimate the masses of these states. For the 1^{++} and 2^{++} its eigenvalues are [35]

$$M(1^{++}) = 2m_{[bq]} - (\mathcal{K}_{bq})_{\bar{3}} + \frac{1}{2}\mathcal{K}_{q\bar{q}} - \mathcal{K}_{b\bar{q}} + \frac{1}{2}\mathcal{K}_{b\bar{b}}, \quad (3.4.11)$$

$$M(2^{++}) = 2m_{[bq]} + (\mathcal{K}_{bq})_{\bar{3}} + \frac{1}{2}\mathcal{K}_{q\bar{q}} + \mathcal{K}_{b\bar{q}} + \frac{1}{2}\mathcal{K}_{b\bar{b}}. \quad (3.4.12)$$

The coefficients \mathcal{K} are known, and the constituent diquark mass is obtained as follows. We took the Belle data [84] as input and identified the $Y_b(10890)$ with the lightest of the 1^{--} states, $Y_{[bq]}$, yielding a diquark mass

$$m_{[bq]} = 5.251 \text{ GeV}. \quad (3.4.13)$$

This procedure is analogous to what was done in [35], in which the mass of the diquark [cq] was fixed by using the mass of $X(3872)$ as input, yielding

$$m_{[cq]} = 1.933 \text{ GeV}. \quad (3.4.14)$$

It might look inconsistent to take the Belle data as input for the determination of the constituent quark mass and try in the following sections to prove that their observed state is indeed a tetraquark. But the mass in (3.4.13) does not appear from nowhere: Using heavy-quark symmetry the [bq] diquark mass can be obtained from the [cq] diquark mass in (3.4.14). In the heavy-quark limit the masses of the heavy-quarks are constant and equal to their constituent mass. In conclusion the [bq] diquark mass is given by

$$m_{[bq]} = m_{[cq]} + (m_b - m_c) \quad (3.4.15)$$

The mass difference $m_c - m_b \approx 3.33 \text{ GeV}$ is a well determined experimental quantity (see also Tab. 3.4.1) and one gets $m_{[bq]} = 5.267 \text{ GeV}$, yielding a difference with the mass in (3.4.13) of 16 MeV. This will be taken as an estimate of the theoretical error on $m_{[bq]}$, which then yields an uncertainty of about 30 MeV in the estimates of the tetraquark masses. Unfortunately, there is no consistent way to obtain well founded error estimates. Experience from other applications of the Hamiltonian models tells however, that the errors are usually some few 10 MeV. Thus the difference discussed above is well within errors.

The couplings corresponding to the spin-spin interactions have only been calculated for the color singlet and color antitriplet, as mentioned earlier. In Eq. (3.4.2), however, the quantities $\mathcal{K}_{q\bar{q}}$, $\mathcal{K}_{b\bar{q}}$ and $\mathcal{K}_{b\bar{b}}$ involve both color singlet and color octet couplings between the quarks and antiquarks in a $Q\bar{Q}$ system. For $\mathcal{K}_{b\bar{b}}$

$$\mathcal{K}_{b\bar{b}}([bq][\bar{b}\bar{q}]) = \frac{1}{3}(\mathcal{K}_{b\bar{b}})_0 + \frac{2}{3}(\mathcal{K}_{b\bar{b}})_8, \quad (3.4.16)$$

in which $(\mathcal{K}_{b\bar{b}})_0$ is reported in Tab. 3.4.2, $(\mathcal{K}_{b\bar{b}})_8$ can be derived from the one gluon exchange model, described in Sec. 3.1, by using the relation [35]

$$(\mathcal{K}_{b\bar{b}})_{\mathbf{X}} \sim (C^2(\mathbf{X}) - C^2(\mathbf{3}) - C^2(\bar{\mathbf{3}})), \quad (3.4.17)$$

with $C^2(\mathbf{X}) = 0, 4/3, 4/3, 3$ for $\mathbf{X} = \mathbf{1}, \mathbf{3}, \bar{\mathbf{3}}, \mathbf{8}$ respectively. The contributions are therefore proportional to the discriminator given in Tab. 3.1.1. Finally, Eq. (3.4.16) yields

$$\mathcal{K}_{b\bar{b}}([bq][\bar{b}\bar{q}]) = \frac{1}{4}(\mathcal{K}_{b\bar{b}})_0. \quad (3.4.18)$$

Using the values given in Eq. (3.4.13) and Tabs. 3.4.2 and 3.4.3, the masses for the hidden $b\bar{b}$ tetraquark states 1^{++} and 2^{++} states are:

$$M(1^{++}) = 10.533 \text{ GeV, for } q = u, d, \quad (3.4.19)$$

$$= 10.860 \text{ GeV, for } q = s, \quad (3.4.20)$$

$$= 13.222 \text{ GeV, for } q = c, \quad (3.4.21)$$

$$M(2^{++}) = 10.557 \text{ GeV, for } q = u, d, \quad (3.4.22)$$

$$= 10.921 \text{ GeV, for } q = s, \quad (3.4.23)$$

$$= 13.252 \text{ GeV, for } q = c. \quad (3.4.24)$$

For the corresponding 0^{++} and 1^{+-} tetraquark states, the Hamiltonian is not diagonal and we have the following 2×2 matrices:

$$M(0^{++}) = \begin{pmatrix} -3(\mathcal{K}_{bq})_{\bar{3}} & \frac{\sqrt{3}}{2}(\mathcal{K}_{q\bar{q}} + \mathcal{K}_{b\bar{b}} - 2\mathcal{K}_{b\bar{q}}) \\ \frac{\sqrt{3}}{2}(\mathcal{K}_{q\bar{q}} + \mathcal{K}_{b\bar{b}} - 2\mathcal{K}_{b\bar{q}}) & (\mathcal{K}_{bq})_{\bar{3}} - (\mathcal{K}_{q\bar{q}} + \mathcal{K}_{b\bar{b}} + 2\mathcal{K}_{b\bar{q}}) \end{pmatrix}, \quad (3.4.25)$$

$$M(1^{+-}) = \begin{pmatrix} -(\mathcal{K}_{bq})_{\bar{3}} + \mathcal{K}_{b\bar{q}} - \frac{(\mathcal{K}_{q\bar{q}} + \mathcal{K}_{b\bar{b}})}{2} & \mathcal{K}_{q\bar{q}} - \mathcal{K}_{b\bar{b}} \\ \mathcal{K}_{q\bar{q}} - \mathcal{K}_{b\bar{b}} & (\mathcal{K}_{bq})_{\bar{3}} - \mathcal{K}_{b\bar{q}} - \frac{(\mathcal{K}_{q\bar{q}} + \mathcal{K}_{b\bar{b}})}{2} \end{pmatrix}. \quad (3.4.26)$$

To estimate the masses of these two states, one has to diagonalize the above matrices. After doing this, the mass spectrum of the $b\bar{b}$ states is shown in Fig. 3.15.

3.4.2 Excited higher mass $[bq][\bar{b}\bar{q}]$ states with $L_{Q\bar{Q}} = 1$

I discuss now the orbital excited tetraquark states with $L_{Q\bar{Q}} = 1$, having both *good* and *bad* diquarks. This work is particularly focused on the 1^{--} multiplet. Using the basis vectors defined in reference [41] the mass shift due to the spin-spin interaction terms H_{SS} becomes:

$$\Delta M_{SS} = \begin{pmatrix} -3(\mathcal{K}_{bq})_{\bar{3}} & 0 & 0 \\ 0 - (\mathcal{K}_{bq})_{\bar{3}} - \mathcal{K}_{b\bar{q}} + (\mathcal{K}_{q\bar{q}} + \mathcal{K}_{b\bar{b}})/2 & 0 & 0 \\ 0 & 0 & -(\mathcal{K}_{bq})_{\bar{3}} - \mathcal{K}_{b\bar{q}} - (\mathcal{K}_{q\bar{q}} + \mathcal{K}_{b\bar{b}})/2 \end{pmatrix}. \quad (3.4.27)$$

The eigenvalues of the spin-orbit and angular momentum operators, given in Eq. (3.4.1), were calculated by Polosa et al. [41] and are summarized in Tab. 3.4.4.³

The Hamiltonian model yields for the masses of the eight tetraquark states $[bq][\bar{b}\bar{q}]$ ($q = u, d$) having the quantum numbers 1^{--} :

$$\begin{aligned} M_{Y_{[bq]}}^{(1)}(S_Q = 0, S_{\bar{Q}} = 0, S_{Q\bar{Q}} = 0, L_{Q\bar{Q}} = 1) &= 2m_{[bq]} + \lambda_1 + B_Q, \\ M_{Y_{[bq]}}^{(2)}(S_Q = 1, S_{\bar{Q}} = 0, S_{Q\bar{Q}} = 1, L_{Q\bar{Q}} = 1) &= 2m_{[bq]} + \Delta + \lambda_2 - 2A_Q + B_Q, \\ M_{Y_{[bq]}}^{(3)}(S_Q = 1, S_{\bar{Q}} = 1, S_{Q\bar{Q}} = 0, L_{Q\bar{Q}} = 1) &= 2m_{[bq]} + 2\Delta + \lambda_3 + B_Q, \end{aligned} \quad (3.4.28)$$

³The entry for a in the last row of Tab. 3.4.4 differs from the corresponding one in the first reference in [41], which is given as -2 , but this point has now been settled amicably in favor of the value given here.

Table 3.4.4: Eigenvalues of the spin-orbit and angular momentum operator in Eq. (3.4.1) for the states having $J = L_{Q\bar{Q}} + S_{Q\bar{Q}} = 1$.

$ S_Q, S_{\bar{Q}}, S_{Q\bar{Q}}, L_{Q\bar{Q}}\rangle$	$a(S_Q, S_{\bar{Q}}, S_{Q\bar{Q}}, L_{Q\bar{Q}})$	$b(s_Q, S_{\bar{Q}}, S_{Q\bar{Q}}, L_{Q\bar{Q}})$
$ 0, 0, 0, 1\rangle$	0	1
$ 1, 0, 1, 1\rangle$	-2	1
$ 1, 1, 2, 1\rangle$	-6	1
$ 1, 1, 1, 1\rangle$	-2	1
$ 1, 1, 0, 1\rangle$	0	1

$$M_{Y_{[bq]}^{(4)}}(S_Q = 1, S_{\bar{Q}} = 1, S_{Q\bar{Q}} = 2, L_{Q\bar{Q}} = 1) = 2m_{[bq]} + 2\Delta + \lambda_3 - 6A_Q + B_Q,$$

in which $\lambda_i (i = 1, 2, 3)$ are the diagonal elements of the matrix ΔM_{SS} given in Eq. (3.4.27) ($\lambda_1 = -18$ MeV, $\lambda_2 = 33$ MeV and $\lambda_3 = -56$ MeV). Note, that there are 16 electrically neutral self-conjugate 1^{--} tetraquark states $Y_{[bq]}^{(n)}$ with quark contents $[bq][\bar{b}\bar{q}]$, with $q = u, d, s$ or c , of which the two corresponding to $[bu][\bar{b}\bar{u}]$ and $[bd][\bar{b}\bar{d}]$, *i.e.* $Y_{[bu]}^{(n)}$ and $Y_{[bd]}^{(n)}$, are degenerate in mass due to the isospin symmetry. There are yet more electrically neutral $J^{PC} = 1^{--}$ states with the mixed light-quark content $[bd][\bar{b}\bar{s}]$ and their charge conjugates $[bs][\bar{b}\bar{d}]$. However, these mixed states don't couple directly to the photons, Z^0 or the gluon and are not of immediate interest in this work.

The numerical values of the coefficients corresponding to A_Q and B_Q are given in Tab. 3.4.4 and are labeled by a and b , respectively. The quantity Δ is the mass difference of the *good* and the *bad* diquarks

$$\Delta = m_Q(S_Q = 1) - m_Q(S_Q = 0). \quad (3.4.29)$$

In order to calculate the numerical values of these states one has to estimate Δ (the only unknown remaining constant in this calculation). Following Jaffe and Wilczek [2], the value of Δ for diquark $[bq]$ is $\Delta = 202$ MeV for $q = u, d, s$ and c -quarks. This value is, however, to be taken with caution. The value obviously ignores the mass differences of the different valence-quarks. The mass-breaking effects are very large and not well in agreement with the adopted heavy-quark limit and differ by a factor 4 from the mass difference of the ground state B -mesons and the excited B^* mesons, which is around 50 MeV. Naively one would expect them to be of the same order. In a recent work [102]_{Tab. II}, the diquark masses were calculated using the relativistic quark model. The diquark masses differ from the values used here by $O(50)$ MeV for $m_{[cq]}$ and by $O(100)$ MeV for $m_{[bq]}$. There is still some discussion needed in the determination of the constituent diquark mass. However, since the mass-breaking effect of the *good* and the *bad* diquark is taken into account in that work, it might be a better guideline. The findings for the mass-breaking Δ are given by 199 MeV, 121 MeV, 63 MeV and 22 MeV for $[qq]$, $[sq]$, $[cq]$ and $[bq]$ respectively. On the upside, however, the state $Y_b^{(1)}$ on which this work is focused only consists of the *good* diquarks and does not suffer from this uncertainties.

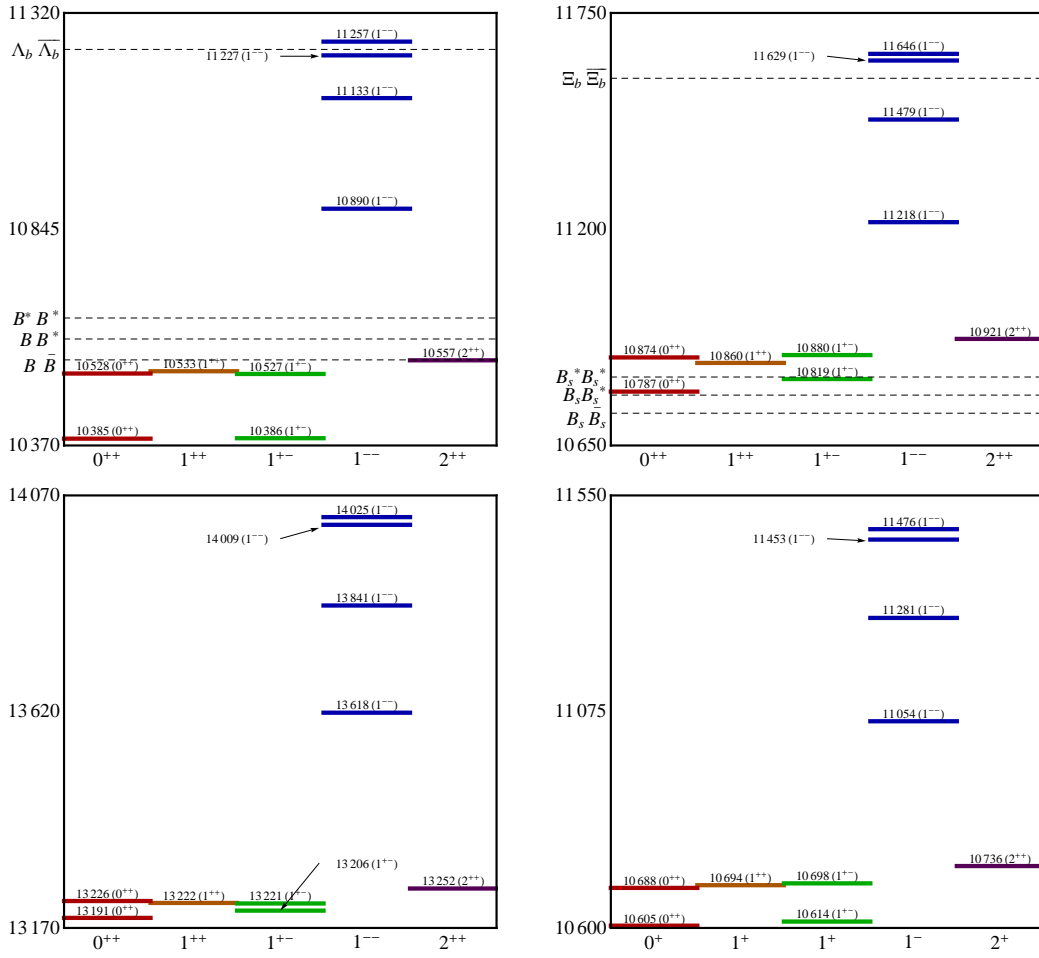


Figure 3.15: Tetraquark mass spectrum with the valence-quark content $[bq][\bar{b}\bar{q}]$ with $q = u, d$, assuming isospin symmetry (upper left frame), with $q = s$ (upper right frame), with $q = c$ (lower left frame), and for the mixed light-quark content $[bd][\bar{b}\bar{s}]$ (lower right frame). Some important decay thresholds are indicated by dashed lines. All masses are given in MeV.

The $S = 1$, $L = (0, 1)$ meson states B^* , B_1 (5721), B_2 (5747) are used to calculate the values of A_Q and B_Q which describe the orbital couplings of the excited states. They are:

$$\begin{aligned}
 A_Q &= 5 \text{ MeV, for } q = u, d, \\
 A_Q &= 3 \text{ MeV, for } q = s, c, \\
 B_Q &= 408 \text{ MeV, for } q = u, d, \\
 B_Q &= 423 \text{ MeV, for } q = s, c.
 \end{aligned} \tag{3.4.30}$$

Numerical values of the mass estimates for the states given in Eq. (3.4.28) are quoted in Tab. 3.4.2. Some of the entries, in particular $M_{Y^{(1)}}_{[bq]}$ ($q = u, d, s$), are comparable with the existing ones in references [103, 104].

Finally, the mass spectrum for the tetraquark states $[bq][\bar{b}\bar{q}]$ for $q = u, d, s, c$ with $J^{PC} = 0^{++}, 1^{++}, 1^{+-}, 1^{--}$ and 2^{++} states is plotted in Fig. 3.15 in the isospin-symmetry limit. The $b\bar{b}$ -tetraquark states with mixed light-quark content $[bd][\bar{b}\bar{s}]$ are also shown in

Table 3.4.5: Masses of the 1^{--} tetraquark states $M_{Y_{[bq]}^{(n)}}$ in GeV as computed from Eqs. (3.4.28), (3.4.29) and (3.4.30). The value $M_{Y_{[bq]}^{(1)}}$ (for $q = u, d$) is fixed to be 10.890 GeV, identifying this with the mass of the Y_b from Belle [84]

$M_{Y_{[bq]}^{(i)}}$	$q = u, d$	$q = s$	$q = c$	$q = d, \bar{q} = \bar{s}$
$M_{Y_{[bq]}^{(1)}}$	10.890	11.218	13.618	11.054
$M_{Y_{[bq]}^{(2)}}$	11.130	11.479	13.841	11.281
$M_{Y_{[bq]}^{(3)}}$	11.257	11.646	14.025	11.476
$M_{Y_{[bq]}^{(4)}}$	11.227	11.629	14.009	11.453

this figure. Of these the 1^{--} state $Y_{[bq]}^{(1)}$ (10.890), shown in the upper left frame in Fig. 3.15, is of central interest in this work. The mass $M_{Y_{[bq]}^{(1)}}$ is also in agreement with a later QCD sum rule estimate [105].

3.5 Isospin breaking and e^+e^- decay widths of the $J^{PC} = 1^{--}$ tetraquarks

In this section the isospin breaking effects of the $J^{PC} = 1^{--}$ tetraquarks are discussed and the partial decay widths $\Gamma_{ee}(Y_{[b,l]})$ and $\Gamma_{ee}(Y_{[b,h]})$ for the processes $Y_{[b,l]} \rightarrow e^+e^-$ and $Y_{[b,h]} \rightarrow e^+e^-$ are derived. The partial electronic width is needed to estimate the production of the Y_b states in e^+e^- annihilation processes and plays an important role. As mentioned earlier, all Y_b states are arranged in isospin doublets with quark content $[bu][\bar{b}\bar{u}]$ and $[bd][\bar{b}\bar{d}]$. The mass eigenstates are called $Y_{[b,l]}$ and $Y_{[b,h]}$ for the lighter and the heavier of the two. They are given by a linear superposition of the states defined in (3.4.4). Introducing a mixing angle θ they are generically defined by:

$$Y_{[b,l]} = \cos \theta Y_{[bu]} + \sin \theta Y_{[bd]} \quad \text{and} \quad Y_{[b,h]} = -\sin \theta Y_{[bu]} + \cos \theta Y_{[bd]}. \quad (3.5.1)$$

The isospin eigenstates are given by

$$Y_b^0 = (Y_{[bu]} + Y_{[bd]})/\sqrt{2} \quad \text{and} \quad Y_b^1 = (Y_{[bu]} - Y_{[bd]})/\sqrt{2}. \quad (3.5.2)$$

It is trivial to see, that for $\theta = -45^\circ$ $Y_{[b,l]} = Y_b^1$ and $Y_{[b,h]} = Y_b^0$, so that all general expressions are easily simplified for the isospin eigenstates. The isospin-invariant Hamiltonian model in the previous section needs to be extended by isospin breaking terms to yield the mass-breaking effects. Writing the quark eigenstates as $(Y_{[bu]}, Y_{[bd]})$ the mass-breaking matrix is defined as

$$\begin{pmatrix} 2m_u + \delta & \delta \\ \delta & 2m_d + \delta \end{pmatrix}, \quad (3.5.3)$$

in which δ is the contribution stemming from one gluon exchange quark annihilation diagrams, in which the light-quark pair annihilates to an intermediate gluon. The diagonal δ elements correspond to $u\bar{u} \rightarrow u\bar{u}$ and $d\bar{d} \rightarrow d\bar{d}$ and the off-diagonal terms describe the contribution $u\bar{u} \rightarrow d\bar{d}$ and $d\bar{d} \rightarrow u\bar{u}$. In the one gluon exchange models all contributions are identical. However, this contribution is assumed to be small compared with the breaking of the constituent quark mass m_u and m_d and will be neglected for mixing angles of $\theta \lesssim 30^\circ$ (the bigger the mixing, the more important are the annihilation diagrams). Then the isospin mass-breaking is given by⁴

$$M(Y_{[b,h]}) - M(Y_{[b,l]}) = (7 \pm 3) \cos(2\theta) \text{ MeV}. \quad (3.5.4)$$

The isospin mass-breaking is very small and experiments usually can not resolve this mass difference, though it may cause visible interference effects, which are, however, hard to handle on the theoretical side. Hence, in the analysis of the tetraquarks, this relation plays a minor role.

More interesting is another aspect of the mixing, namely the effects of the effective charge of the mixed constituent diquarks, which depends also on the mixing angle θ :

$$Q_{[b,l]} = \cos\theta Q_{[bu]} + \sin\theta Q_{[bd]} \quad \text{and} \quad Q_{[b,h]} = -\sin\theta Q_{[bu]} + \cos\theta Q_{[bd]}. \quad (3.5.5)$$

and

$$Q_b^0 = (Q_{[bu]} + Q_{[bd]})/\sqrt{2} \quad \text{and} \quad Q_b^1 = (Q_{[bu]} - Q_{[bd]})/\sqrt{2} \quad (3.5.6)$$

for the isospin eigenstate charges. Here $Q_{[bd]} = -2/3$ is the diquark charge in $Y_{bd} = [bd][\bar{b}\bar{d}]$ and $Q_{[bu]} = +1/3$ is the charge of the diquarks in $Y_{bu} = [bu][\bar{b}\bar{u}]$. For the P -wave tetraquark states, the decay width is given at LO in α_s by the generalized Van Royen-Weisskopf formulae

$$\Gamma(Y_i \rightarrow e^+e^-) = \frac{24\alpha_s^2 |Q_i|^2}{m_{Y_b}^4} \kappa^2 \left| R_{11}^{(1)}(0) \right|^2, \quad (3.5.7)$$

in which $R_{11}^{(1)}(0)$ is the first derivative of the radial wave function at the origin and i labels the basis ($i = [bu/bd], [bh/bl]$). The relation (3.5.7) is derived in App. C.2 after a short review of the bottomonia production, from where the derivation is borrowed. It rests upon the condition of approximately pointlike diquarks. As mentioned in Sec. 3.1 the tetraquarks are mainly strong bound states, and the pointlike diquarks are in color space almost identical to the quarks. Hence the close connection to the bottomonia family. The derivation of the Van Royen-Weisskopf formula involves an e^+e^- pair coupling to an intermediate off-shell photon, which couples to the diquark current and produces the diquark antidiquark pair at zero diquark distance (hence the behavior of the wave function at origin determines the overlap). The process is depicted in Fig. 3.16. We determined the wave functions for the P-state tetraquarks $[bd][\bar{b}\bar{d}]$ and $[bu][\bar{b}\bar{u}]$ from the corresponding wave functions for the P-state $b\bar{b}$ system by scaling the string tension

⁴The expression (3.5.4) differs from the one derived in [35], but there is consensus now on the expression given here.

in the linear part of the potential, as discussed earlier. As most potential models agree in their linear (confining) parts [92], and the linear part of the potential essentially determines the heavy Quarkonia wave functions, the uncertainty in $\Psi_{b\bar{b}}(0)$ from the underlying model is not a concern. We have used the QQ-onia package of [106], yielding $|R'(0)|^2 = 2.062 \text{ GeV}^5$ for the $b\bar{b}$ radial wave function, which we have used as normalization. The corresponding value for the tetraquark states $[bq][\bar{b}\bar{q}]$ is then calculated as $\Psi_{\mathcal{Q}\bar{\mathcal{Q}}}(0) \simeq \kappa \Psi_{b\bar{b}}(0)$. The constant parameter κ is introduced as a form factor to capture the differences between the bottom mesons and the

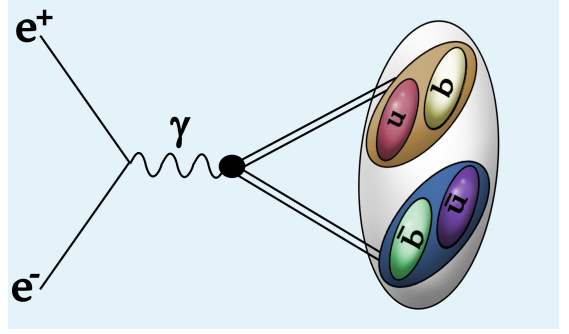


Figure 3.16: Schematic underlying process of the Van Royen-Weisskopf formula for tetraquarks with pointlike diquarks.

bottom tetraquarks as a first order approximation. Here κ reflects two effects, namely the size of the tetraquarks $Y_{[bu/bd]}$ compared to a typical hadronic bottomonia state, say, $\Upsilon(5S)$, and the effect of the nonzero size of the diquarks, since on the lattice, the diquarks exhibit typical sizes of $\mathcal{O}(1\text{fm})$, as discussed in Sec. 3.1. Hence κ is expected to be significantly smaller than 1. We expect that for all the P-states $Y_{[bu]}^{(n)}$ and $Y_{[bd]}^{(n)}$ the electronic widths will be constant to a good approximation.

With the formula (3.5.7) it is possible to determine the strength of the coupling in the effective Lagrangian

$$\mathcal{L}_{\text{eff}} = g_{e^+e^-Y_i}(Y_i)_\mu \bar{e}\gamma^\mu e, \quad (3.5.8)$$

which defines the effective vertex as

$$\begin{array}{c} e^+ \\ \nearrow \\ \bullet \\ \nwarrow \\ e^- \end{array} \begin{array}{c} \mu \\ \sim \\ Y_i \end{array} = ig_{e^+e^-Y_i}\gamma^\mu \quad (3.5.9)$$

and yields

$$\Gamma(Y_i \rightarrow e^+e^-) = \frac{m_{Y_b}}{12\pi} |g_{e^+e^-Y_i}|^2, \quad (3.5.10)$$

for the decay widths of Y_i . The effective couplings are defined in the same way as the effective charges for an arbitrary mixing angle by

$$\begin{aligned} g_{e^+e^-Y_{[b]}} &= \cos\theta g_{e^+e^-Y_{[bu]}} + \sin\theta g_{e^+e^-Y_{[bd]}}, \\ g_{e^+e^-Y_{[b]}} &= -\sin\theta g_{e^+e^-Y_{[bu]}} + \cos\theta g_{e^+e^-Y_{[bd]}}, \end{aligned} \quad (3.5.11)$$

and

$$\begin{aligned} g_{e^+e^-Y_b^0} &= (g_{e^+e^-Y_{[bu]}} + g_{e^+e^-Y_{[bd]}})/\sqrt{2}, \\ g_{e^+e^-Y_b^1} &= (g_{e^+e^-Y_{[bu]}} - g_{e^+e^-Y_{[bd]}})/\sqrt{2}. \end{aligned} \quad (3.5.12)$$

Some interesting relations can be derived with the above discussed formulas. In the following I state the most important of them. The ratio $\mathcal{R}_{ee}(Y_b)$ of $\Gamma_{ee}(Y_{[b,l]})$ and $\Gamma_{ee}(Y_{[b,h]})$ and hence also the production ratio is given by

$$\mathcal{R}_{ee}(Y_b) \equiv \frac{\Gamma_{ee}(Y_{[b,l]})}{\Gamma_{ee}(Y_{[b,h]})} = \frac{Q_l^2(\theta)}{Q_h^2(\theta)} = \left[\frac{1 - 2 \tan \theta}{2 + \tan \theta} \right]^2. \quad (3.5.13)$$

Since the total cross section $\sigma(e^+e^- \rightarrow (Y_{[b,l]}, Y_{[b,h]}) \rightarrow \text{hadrons})$ for the states $Y_{[b,l]}$ and $Y_{[b,h]}$, which are the physical relevant particles, are directly proportional to $\Gamma_{ee}(Y_{[b,l]})$ and $\Gamma_{ee}(Y_{[b,h]})$, the ratio $\mathcal{R}_{ee}(Y_b)$ is accessible from the experiment. The absolute values of the decay widths $\Gamma_{ee}(Y_{[b,l]})$ and $\Gamma_{ee}(Y_{[b,h]})$ are given by $\Gamma_{ee}(Y_i) \approx 0.2 \kappa^2 Q_i(\theta)^2 \text{ keV}$, where $Q_i(\theta)$ are the mixing angle weighted charges (3.5.5). The electronic decay width for the flavor eigenstates, which are approximately the mass eigenstates for small mixing angles θ , are given by

$$\Gamma_{ee}(Y_{[bu]}) \approx 10 \text{ eV} \quad \text{and} \quad \Gamma_{ee}(Y_{[bd]}) \approx 50 \text{ eV} \quad (3.5.14)$$

for a value of $\kappa = 1/2$. Compared to the electronic width $\Gamma_{ee}(Y_{[bd]}) = 310 \pm 70 \text{ eV}$ of $\Upsilon(5S)$, taken from [77], the tetraquarks are suppressed by one order of magnitude in the inclusive R_b -scans with respect to the bottomonia.

Comparing Eq. (3.5.10) with Eq. (3.5.7), we find the relations

$$|g_{e^+e^-Y_i}| = \frac{12\sqrt{2\pi} \alpha |Q_i| \kappa}{m_{Y_b}^{5/2}} \left| R_{11}^{(1)}(0) \right|. \quad (3.5.15)$$

The ratio of the couplings $g_{e^+e^-Y_b^0}$ and $g_{e^+e^-Y_b^1}$, which will be needed in the later sections is then given by

$$g_{e^+e^-Y_b^1}/g_{e^+e^-Y_b^0} = Q_1/Q_0 = -3. \quad (3.5.16)$$

We can compute the coupling of Y_b^0 to e^+e^- from Eq. (3.5.15):

$$g_{e^+e^-Y_i} \approx 8 \times 10^{-4} \kappa Q_i(\theta). \quad (3.5.17)$$

For the isospin eigenstates Y^0 and Y^1 and $\kappa = 1/2$ one finds

$$g_{e^+e^-Y^0} \approx 10^{-4} \quad \text{and} \quad g_{e^+e^-Y^1} \approx -3 \times 10^{-4}. \quad (3.5.18)$$

3.6 $Y_{[bq]}$ decay modes and total decay widths

In this section the dominant hadronic decays of the $L_{Q\bar{Q}} = 1$ states are discussed and the total decay width is estimated. All examined decays in this section are mediated through the strong interaction, thus isospin breaking is neglected. The calculations include only the two-body decays, $Y_{[bq]} \rightarrow B_q^{(*)} \bar{B}_q^{(*)}$, and when kinematically allowed also the decay $Y_{[bq]} \rightarrow \Lambda_b \bar{\Lambda}_b$. Their thresholds are indicated in Fig. 3.15. These decays are Zweig allowed and involve essentially quark rearrangements and the possible pop-up of a light $q\bar{q}$ pair to form the $\Lambda_b \bar{\Lambda}_b$ state. The decays $Y_{[bq]} \rightarrow \Upsilon(1S, 2S) \pi^+ \pi^-$ are also Zweig allowed. However,

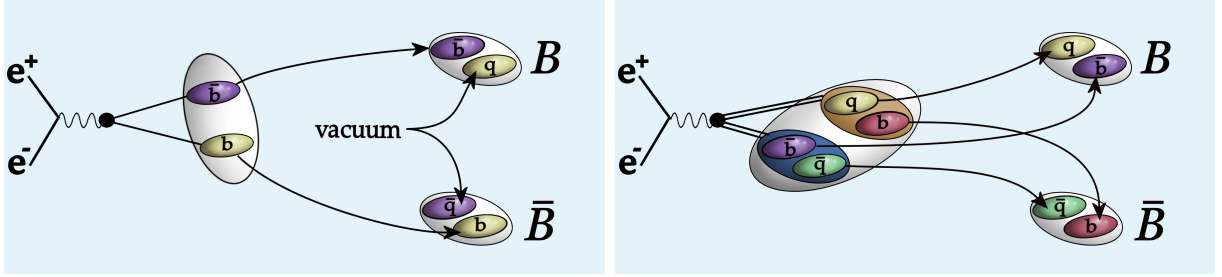


Figure 3.17: Comparison of the production and the subsequent decays of the $\Upsilon(5S)$ to the left and the tetraquark to the right. The production of the light-quark pair $q\bar{q}$ is produced in a strong process from the QCD background in the former and in the electromagnetic production process by the coupling to a virtual photon in the latter case.

they are kinematically suppressed and supposedly sub-dominant. Hence, they will be neglected in the calculation of the inclusive hadronic width. They are otherwise signature decays of the $Y_{[bq]}$ tetraquarks as discussed in the preceding Sec. 3.3. More about these three-body decays can be found in the following sections. It is assumed, that the Zweig allowed and kinematically augmented two-body decays are the dominant decay modes of the $Y_{[bq]}$ tetraquarks. Following this argument, the total decay width can be approximated by the sum of the partial decay widths of the two-body decays to a good approximation.

The vertices and the corresponding decay widths of the dominant decays are given below:⁵

$$\begin{aligned}
 B_q \bar{B}_q : & \quad 1^{--} \xrightarrow{\mu, q} \bullet \begin{array}{l} \nearrow k \\ \searrow l \end{array} \left. \begin{array}{l} 0^- \\ L=1 \\ 0^- \end{array} \right] \hat{=} F_{B_q \bar{B}_q} (k^\mu - l^\mu) \\
 & \quad \Rightarrow \Gamma_{B_q \bar{B}_q} = \frac{F_{B_q \bar{B}_q}^2 |\mathbf{k}|^3}{2M^2 \pi}, \\
 B_q \bar{B}_q^* : & \quad 1^{--} \xrightarrow{\mu, q} \bullet \begin{array}{l} \nearrow k \\ \searrow l \end{array} \left. \begin{array}{l} 0^- \\ L=1 \\ 1^- \end{array} \right] \hat{=} \frac{F_{B_q \bar{B}_q^*}}{M} \epsilon^{\mu\nu\rho\sigma} k_\rho l_\sigma \\
 & \quad \Rightarrow \Gamma_{B_q \bar{B}_q^*} = \frac{F_{B_q \bar{B}_q^*}^2 |\mathbf{k}|^3}{4M^2 \pi}, \\
 B_q^* \bar{B}_q^* : & \quad 1^{--} \xrightarrow{\mu, q} \bullet \begin{array}{l} \nearrow k \\ \searrow l \end{array} \left. \begin{array}{l} 1^- \\ L=1 \\ 1^- \end{array} \right] \hat{=} \begin{aligned} & F_{B_q^* \bar{B}_q^*} (g^{\mu\rho} (q+l)^\nu \\ & - g^{\mu\nu} (k+q)^\rho \\ & + g^{\rho\nu} (q+k)^\mu) \end{aligned} \\
 & \quad \Rightarrow \Gamma_{B_q^* \bar{B}_q^*} = \frac{F_{B_q^* \bar{B}_q^*}^2 |\mathbf{k}|^3 (48|\mathbf{k}|^4 - 104M^2|\mathbf{k}|^2 + 27M^4)}{2\pi(M^3 - 4|\mathbf{k}|^2 M)^2},
 \end{aligned} \tag{3.6.1}$$

⁵The second vertex involves the antisymmetric tensor due to parity conservation.

$$\begin{aligned}
\Lambda_b \bar{\Lambda}_b : \quad & \begin{array}{c} \begin{array}{c} \mu \\ \longleftarrow \\ \text{---} \\ \longrightarrow \\ \nu \end{array} \\ \bullet \\ \begin{array}{c} \nearrow k \\ \searrow l \end{array} \end{array} \begin{array}{c} \frac{1}{2}^+ \\ \alpha \\ \frac{1}{2}^+ \\ \beta \end{array} \quad \hat{=} \quad \left(F_{\Lambda_b \bar{\Lambda}_b} \gamma^\mu + \frac{2F'_{\Lambda_b \bar{\Lambda}_b}}{iM} q_\nu \sigma^{\nu\mu} \right)_{\alpha\beta} \\
\implies \Gamma_{\Lambda_b \bar{\Lambda}_b} = & \frac{3(F_{\Lambda_b \bar{\Lambda}_b}^2 + F'^2_{\Lambda_b \bar{\Lambda}_b})|\mathbf{k}|}{4\pi} - \frac{(F_{\Lambda_b \bar{\Lambda}_b}^2 + 2F'^2_{\Lambda_b \bar{\Lambda}_b})|\mathbf{k}|^3}{M^2\pi}.
\end{aligned}$$

The center-of-mass momentum $|\mathbf{k}|$ is given by

$$|\mathbf{k}| = \frac{\sqrt{M^2 - (M_1 + M_2)^2} \sqrt{M^2 - (M_1 - M_2)^2}}{2M}, \quad (3.6.2)$$

where M is the mass of the decaying particle and M_1, M_2 are the masses of the decay products. The matrix elements are obtained by multiplying the vertices in (3.6.1) by the polarization vectors. Thus the Lorentz-invariant matrix element for the decay $Y_{[b,q]} \rightarrow B_q \bar{B}_q$ is given by $\mathcal{M}_{B_q \bar{B}_q} = \varepsilon_\mu^{Y_{[b,q]}} F_{B_q \bar{B}_q} (k^\mu - l^\mu)$ and likewise for the other decays shown above. The decay constants F and F' are non-perturbative dynamical quantities, hard to estimate from first principles or in lattice QCD. In state of the art calculations experimental input is therefore still the first choice. We estimated the decay constants using the known two-body decays of a typical hadronic state with similar mass, the $\Upsilon(5S)$, which are described by the same vertices as given above [43]. Both Zweig allowed processes are pictured in Fig. 3.17. The nature of the production of the light-quark pair is the characteristic feature, which distinguishes both processes. The $\Upsilon(5S)$ is produced by coupling to the virtual photon, which couples to the e^+e^- current. Subsequently, the light-quark pair pops up from the QCD background of the $\Upsilon(5S)$. It is assumed, that the probability of the pop-up of a quark pair from the QCD vacuum is 1. The light-quark pair in the tetraquark decay process on the other hand is produced in the electromagnetic process by the coupling of the virtual photon to the pointlike diquarks. This is an important difference in our model and has far reaching consequences. It emerges whenever the production of the tetraquarks is taken into account. Since the quark pair is not specified, the $\Upsilon(5S)$ can decay to both charged and neutral mesons, whereas $[bu][\bar{b}\bar{u}]$ can only couple to charged and $[bd][\bar{b}\bar{d}]$ can only couple to neutral mesons, *i.e.* we used

$$\langle B^+ B^- | \hat{H} | Y_{[bu]} \rangle = \langle B^0 \bar{B}^0 | \hat{H} | Y_{[bd]} \rangle = \langle B^+ B^- | \hat{H} | \Upsilon(5S) \rangle = \langle B^0 \bar{B}^0 | \hat{H} | \Upsilon(5S) \rangle \quad (3.6.3)$$

and similar equations for the final states $B\bar{B}^*$ and $B^*\bar{B}^*$. This causes a suppression factor 2 in the total tetraquark decay width compared to the bottomonia. The different hadronic sizes of the bottomonia states and the tetraquarks $Y_{[bq]}$ are taken into account by the quantity κ , discussed earlier. We use the values for the partial decay widths for the decays $\Upsilon(5S) \rightarrow B\bar{B}, B\bar{B}^*, B^*\bar{B}^*$ from the PDG [77]. They are called Γ_{PDG} and are given in Tab. 3.6.2, yielding the coupling constants, called F_{PDG} , and the decay momentum $|\mathbf{k}|$. The full width of $\Upsilon(5S)$ is given by $\Gamma_{\text{tot}}[\Upsilon(5S)] = 110 \pm 13$ MeV. For the decays $Y_{[bq]}^{(i)} \rightarrow \Lambda_b \bar{\Lambda}_b$ and $Y_{[bs]}^{(i)} \rightarrow \Xi \bar{\Xi}$, we took $F_{\Lambda_b \bar{\Lambda}_b} = F'_{\Lambda_b \bar{\Lambda}_b} = 1.1_{-0.35}^{+0.3}$, and included a factor of 1/3 for the baryonic final state to take the creation of the additional $q\bar{q}$ pair from the vacuum into account. This is only a very bold guess, but for most (and more importantly for the relevant) states the mass is below the two-baryon threshold. I further remark,

that the estimates of F_{PDG} will be modified, if the total decay width $\Gamma_{\text{tot}}[\Upsilon(5S)]$ has a significantly lower value, as predicted by the BaBar R_b -analysis [93].

The input values for the masses used in our calculation are listed in Tab. 3.6.1. With this input, our estimates of the decay widths for $Y_{[bq]}^{(i)}$ are given in Tab. C.8.3. I give also the total decay widths (up to the factor κ^2) in Tab. 3.6.3. As seen in this table, the lowest lying 1^{--} states $Y_{[bq]}^{(1)}$ are expected to have decay widths of $O(20)$ MeV, for $\kappa^2 \simeq 0.5$. Admittedly this is a rather crude approximation and refined approaches will hopefully provide better estimates. However, the total decay width of $Y_{[bq]}^{(1)}$ are consistent with the measurements by Belle, if $Y_{[bq]}^{(1)}$ is identified with their $Y_b(10890)$, and moreover the Belle measurements are in agreement with a value of $\kappa \lesssim 1$. The higher 1^{--} states have much larger decay widths and will be correspondingly more difficult to find.

Table 3.6.1: Input masses taken from [77] in units of GeV.

hadron	mass	hadron	mass	hadron	mass
B	5.279	π	0.139	$\Upsilon(1S)$	9.46
B^*	5.325	Λ_b	5.62	$\Upsilon(4S)$	10.5794
B_s	5.366	Ξ_b	5.792	$\Upsilon(10860)$	10.865
B_s^*	5.412	K	0.4937	$\Upsilon(11020)$	11.019

Table 3.6.2: 2-body decays $\Upsilon(5S) \rightarrow B^{(*)}\bar{B}^{(*)}$, which we use as a reference, with the mass and the decay widths taken from [77], including the extracted values of the coupling constants F_{PDG} and the center of mass momentum $|\mathbf{k}|$.

process	$\Gamma_{\text{PDG}}[\text{MeV}]$	F_{PDG}	$ \mathbf{k} [\text{GeV}]$
$\Upsilon(10860) \rightarrow B \bar{B}$	< 13.2	< 2.15	1.3
$\Upsilon(10860) \rightarrow B \bar{B}^*$	$15.4_{-6.6}^{+6.6}$	$3.7_{-0.9}^{+0.7}$	1.2
$\Upsilon(10860) \rightarrow B^* \bar{B}^*$	48_{-11}^{+11}	$1_{-0.12}^{+0.13}$	1.0

Table 3.6.3: Total decay widths for the tetraquarks $Y_{[bq]}^{(i)}$ and $Y_{[bs]}^{(i)}$. The errors in the entries correspond to the errors in the decay widths in Tab. 3.6.2.

1^{--} Tetraquark	$\Gamma_{\text{tot}}/\kappa^2[\text{MeV}]$	1^{--} Tetraquark	$\Gamma_{\text{tot}}/\kappa^2[\text{MeV}]$
$Y_{[bq]}^{(1)}$	44 ± 8	$Y_{[bs]}^{(1)}$	88 ± 17
$Y_{[bq]}^{(2)}$	119 ± 24	$Y_{[bs]}^{(2)}$	184 ± 35
$Y_{[bq]}^{(3)}$	171 ± 33	$Y_{[bs]}^{(3)}$	267 ± 50
$Y_{[bq]}^{(4)}$	154 ± 30	$Y_{[bs]}^{(4)}$	258 ± 48

3.7 Analysis of the BaBar R_b energy scan

In this section I present our first (and simplest) attempt [43] to find experimental evidence for the $1^{--} Y_b^{(1)}$ and $Y_b^{(2)}$ tetraquarks from the R_b -scan performed by BaBar [93]. The findings are suggestive but not conclusive. Stronger evidence is presented from the analysis of $e^+e^- \rightarrow Y_b \rightarrow \Upsilon(1S)\pi^+\pi^-$, presented in the following Sec. 3.8.

In 2009 BaBar reported the $e^+e^- \rightarrow b\bar{b}$ cross section measured in a dedicated energy scan in the range 10.54 GeV and 11.20 GeV taken in steps of 5 MeV [93]. Their measurements are shown in Fig. 3.18 (left frame) together with the result of the BaBar fit, the details are described in their paper and were also made available to us. The ratio R_b is defined by the ratio of the cross section $\sigma(e^+e^- \rightarrow b\bar{b})$ and the cross section $\sigma(e^+e^- \rightarrow \mu^+\mu^-)$. Their fit model of the R_b -data contains the following ingredients: A flat component representing the $b\bar{b}$ -continuum states not interfering with resonant decays, called A_{nr} , added incoherently to a second flat component, called A_r , interfering with two relativistic Breit-Wigner resonances, having the amplitudes A_{10860} , A_{11020} and strong phases, ϕ_{10860} and ϕ_{11020} , respectively. Thus,

$$R_b \equiv \frac{\sigma(e^+e^- \rightarrow b\bar{b})}{\sigma(e^+e^- \rightarrow \mu^+\mu^-)} = |A_{nr}|^2 + |A_r + A_{10860}e^{i\phi_{10860}}BW(M_{10860}, \Gamma_{10860}) + A_{11020}e^{i\phi_{11020}}BW(M_{11020}, \Gamma_{11020})|^2, \quad (3.7.1)$$

with $BW(M, \Gamma) = 1/[(s - M^2) + iM\Gamma]$.

The one-resonance contribution of the amplitude $\mathcal{M}(ab \rightarrow cd)$ for a $2 \rightarrow 2$ process is given by [77]_{Eq. 2}

$$\mathcal{M}(ab \rightarrow cd) = \sum_{\lambda} \langle ab | r_{\lambda} \rangle T_r(m_{ab}) \langle r_{\lambda} | cd \rangle, \quad (3.7.2)$$

in which r labels the resonance. The sum runs over the resonance spin λ , and the function $T_r(m_{ab})$ is a dynamical quantity describing the r resonance pole of the S-matrix in the vicinity of $m_{ab} \approx m_r$, with m_r being the mass of the resonance. Different approaches such as the K-matrix formalism present types of models for this function. The Breit-Wigner form

$$T_r(m_{ab}) \propto \frac{1}{p_r^2 - m_r^2 + im_r\Gamma_r} \quad (3.7.3)$$

is the most handy example, in which Γ_r is the total decay width of the resonance r . The disadvantage of this parametrization is, however, that in the case of overlapping resonances the unitarity of the S-matrix is violated. Nevertheless, this model works well also in data analysis with overlapping contributions. The cross section is proportional to the squared amplitude and the terms given in (3.7.2), including terms modeling the background contribution, are added up with unknown complex coefficients in Eq. (3.7.1). The latter are merely proportionality factors and have no immediate physical meaning in this simple approach.

The BaBar results for the masses and widths of the $\Upsilon(5S)$ and $\Upsilon(6S)$ differ substantially from the corresponding PDG values [77], in particular for the total decay widths, which

are found to be 43 ± 4 MeV for the $\Upsilon(10860)$, as against the PDG value of 110 ± 13 MeV, and 37 ± 2 MeV for the $\Upsilon(11020)$, as compared to 79 ± 16 MeV in PDG. As the systematic errors from the various thresholds are not taken into account in the BaBar analysis, this mismatch needs further study. Their fit, shown in Fig. 3.18 (left frame), having a $\chi^2/\text{d.o.f.}$ of approximately 2 is not eminently impressive. In particular, the data points around 10.89 GeV and 11.2 GeV lie systematically above the fit. In our analysis of the BaBar data, we were able to reproduce these features, but also found, that the fit-quality can be improved somewhat at the expense of strong phases ϕ_{10860} and ϕ_{11020} , which come out different than the ones reported by BaBar [93]. I do not show this fit here as the resulting R_b -line-shape is close to the one shown in the BaBar publication and reproduced here.

We have repeated the fits of the BaBar R_b -data, modifying the fit model in Eq. (3.7.1) by taking two additional resonances into account, corresponding to the masses and widths of $Y_{[b,l]}$ and $Y_{[b,h]}$. Thus, formula (3.7.1) is extended by the terms

$$A_{Y_{[b,l]}} e^{i\phi_{Y_{[b,l]}}} BW(M_{Y_{[b,l]}}, \Gamma_{Y_{[b,l]}}) \quad \text{and} \quad A_{Y_{[b,h]}} e^{i\phi_{Y_{[b,h]}}} BW(M_{Y_{[b,h]}}, \Gamma_{Y_{[b,h]}}), \quad (3.7.4)$$

which interfere with the resonant amplitude A_r and the two resonant amplitudes for $\Upsilon(5S)$ and $\Upsilon(6S)$, shown in Eq. (3.7.1). We use the same non-resonant amplitude A_{nr} and A_r as in the BaBar analysis [93]. The resulting fit is shown in Fig. 3.18 (right frame) with resulting $\chi^2/\text{d.o.f.} = 88/67$. The $\chi^2/\text{d.o.f.}$ is better than that of the BaBar fit [93]. Values of the best-fit parameters are shown in Tab. 3.7.1, from where one sees, that the masses of the $\Upsilon(5S)$ and $\Upsilon(6S)$ and their respective full widths from our fit are almost identical to the values obtained by BaBar [93]. However, quite strikingly, a third resonances is seen in the R_b -line-shape at a mass of 10.90 GeV, tantalizingly close to the $Y_b(10890)$ -mass in the Belle measurement of the cross section for $e^+e^- \rightarrow Y_b(10890) \rightarrow \Upsilon(1S, 2S) \pi^+\pi^-$, and a width of about 28 MeV. In the region around 11.15 GeV, where the $Y_{[bq]}^{(2)}$ states are expected, our fits of the BaBar R_b -scan do not show a resonant structure. This can have several reasons. Foremost, the total decay width of $Y_{[bq]}^{(2)}$ is large. Considering, that the observed $Y_{[bq]}^{(1)}$ peak near the $\Upsilon(5S)$ is strongly suppressed compared with the $\Upsilon(5S)$ peak, a similar production ratio for the $Y_{[bq]}^{(2)}$ would mean, that the larger decay width will lead to even further suppression in its R_b -amplitude. As mentioned in Sec. 3.4 near Eq. (3.4.29), the $Y_{[bq]}^{(2)}$ contains one bad diquark. It may well be, that the calculated mass is overestimated. More precise calculations of the heavy-quark mass-breaking effect for the mass difference Δ of the $good$ and the bad diquarks could shift the mass of the $Y_{[bq]}^{(2)}$ downwards, in the extreme case even in the region of the $\Upsilon(6S)$. A Belle R_b -scan will greatly help to confirm the existence of the state $Y_{[bq]}$ visible in the analysis presented here.

The quantity $\mathcal{R}_{ee}(Y_b)$ in (3.5.13) is given by the ratio of the two amplitudes $A_{Y_{[b,l]}}$ and $A_{Y_{[b,h]}}$, which also fixes the mixing angle θ . From our fit, we get

$$\mathcal{R}_{ee}(Y_b) = 1.07 \pm 0.05, \quad (3.7.5)$$

yielding

$$\theta = -19 \pm 1^\circ \quad \text{and} \quad \Delta M = 5.6 \pm 2.8 \text{ MeV} \quad (3.7.6)$$

for the mixing angle and the mass difference between the eigenstates, respectively.

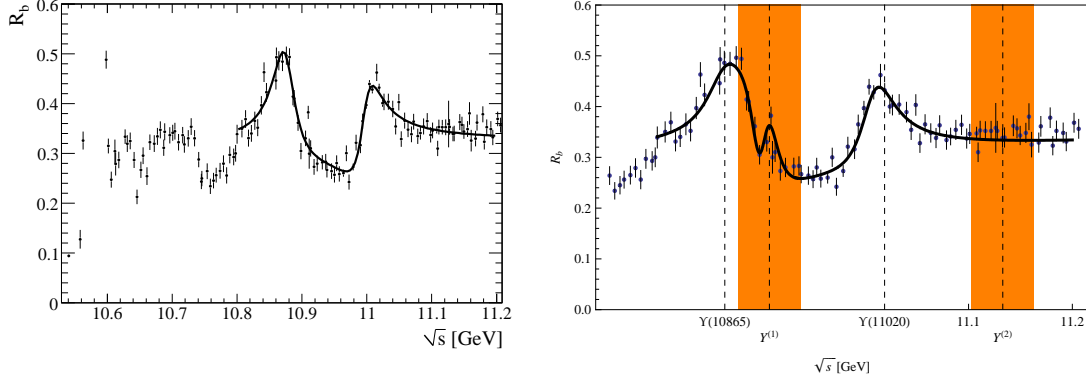


Figure 3.18: Measured R_b as a function of \sqrt{s} with the result of the fit with 2 Breit-Wigners described in [93] (left frame). Reprinted from Fig. 1 of B. Aubert *et al.* [93] [Copyright (2009) by the American Physical Society]. The result of the fit with 4 Breit-Wigners described in the text is shown in the right-hand frame, where we have indicated the location of the $\Upsilon(5S)$, $\Upsilon(6S)$ and the tetraquark state $Y_{[b,q]}$ (labeled as $Y^{(1)}$). The location of the next higher $J^{PC} = 1^{--}$ state $Y_{[b,q]}^{(2)}$ (labeled as $Y^{(2)}$) is also shown. The shaded bands around the mass of $Y^{(1)}$ and $Y^{(2)}$ reflect our theoretical uncertainty in the masses.

The R_b -analysis in the tetraquark picture can be used to determine κ . It can be obtained from the theoretically estimated total decay widths of the $Y_{[b,q]}$ states and the corresponding result from the R_b -fit.

$$\kappa = \sqrt{\frac{28 \pm 2}{44 \pm 8}} = 0.8 \pm 0.1, \quad (3.7.7)$$

which is in the expected ball park. For the mass eigenstates $Y_{[b,l]}$ and $Y_{[b,h]}$, the electronic widths $\Gamma_{ee}(Y_{[b,l]})$ and $\Gamma_{ee}(Y_{[b,h]})$ are given by $\Gamma_{ee}(\theta) = 0.2 \kappa^2 Q(\theta)^2$ keV, as already stated in Sec. 3.5. With the above determination of κ and θ we get

$$\Gamma_{ee}(Y_{[b,l]}) = 33 \pm 6 \text{ eV} \quad \text{and} \quad \Gamma_{ee}(Y_{[b,h]}) = 31 \pm 6 \text{ eV}. \quad (3.7.8)$$

Table 3.7.1: Fit values of the masses, decay widths and the strong phases ϕ .

	$M[MeV]$	$\Gamma[MeV]$	ϕ [rad.]
$\Upsilon(5S)$	10864 ± 5	46 ± 8	1.3 ± 0.3
$\Upsilon(6S)$	11007 ± 0.3	40 ± 2	0.88 ± 0.06
$Y_{[b,l]}$	$10900 - \Delta M/2 \pm 2$	28 ± 2	4.4 ± 0.2
$Y_{[b,h]}$	$10900 + \Delta M/2 \pm 2$	28 ± 2	1.9 ± 0.2

Table 3.8.1: Belle data at $\sqrt{s} \sim 10.87$ GeV [91].

channel	N_s	Σ	Eff.[%]	σ [pb]	\mathcal{B} [%]	Γ [MeV]
$\Upsilon(1S)\pi^+\pi^-$	325^{+20}_{-19}	20σ	37.4	$1.61 \pm 0.10 \pm 0.12$	$0.53 \pm 0.03 \pm 0.05$	$0.59 \pm 0.04 \pm 0.09$
$\Upsilon(2S)\pi^+\pi^-$	186 ± 15	14σ	18.9	$2.35 \pm 0.19 \pm 0.32$	$0.78 \pm 0.06 \pm 0.11$	$0.85 \pm 0.07 \pm 0.16$
$\Upsilon(3S)\pi^+\pi^-$	$10.5^{+4.0}_{-3.3}$	3.2σ	1.5	$1.44^{+0.55}_{-0.45} \pm 0.19$	$0.48^{+0.18}_{-0.15} \pm 0.07$	$0.52^{+0.20}_{-0.17} \pm 0.10$
$\Upsilon(1S)K^+K^-$	$20.2^{+5.2}_{-4.5}$	4.9σ	20.3	$0.185^{+0.048}_{-0.041} \pm 0.028$	$0.061^{+0.016}_{-0.014} \pm 0.010$	$0.067^{+0.017}_{-0.015} \pm 0.013$

3.8 Analysis of the Belle data on $e^+e^- \rightarrow Y_b \rightarrow \Upsilon(1S)(\pi^+\pi^-, K^+K^-, \eta\pi^0)$

In this section I discuss our analysis [44] and [90] of the Belle data taken near the $\Upsilon(5S)$ resonance at $\sqrt{s} \sim 10.87$ GeV. The Belle group reported results for the three-body final states $\Upsilon(1S)\pi^+\pi^-$, $\Upsilon(2S)\pi^+\pi^-$, $\Upsilon(3S)\pi^+\pi^-$ and $\Upsilon(1S)K^+K^-$ produced in e^+e^- annihilation [91]. Only the former two processes are statistically significant to adequately show the invariant-mass and helicity distributions. Of the latter two merely the total cross section is reported. The results are based on a data sample of 21.7 fb^{-1} . The measured cross sections are listed in Tab. 3.8.1, and the characteristic features of the data are presented in Sec. 3.3. We predict the dikaon invariant-mass spectrum as well as the $\eta\pi^0$ mass spectrum in the final states $\Upsilon(1S)K^+K^-$ and $\Upsilon(1S)\eta\pi^0$ by using the input from the fits to the $\Upsilon(1S)\pi^+\pi^-$ spectra. Note, that for $\Upsilon(1S)K^+K^-$ with a signal yield in the ballpark of 20 events, the invariant-mass spectrum is not yet measured, but it is promising, that the recent run of the Belle experiment in the first half of 2010 will improve the statistics sufficiently to make the spectrum available to the analysis of our predictions. Since two isospin states are contributing in this channel, as discussed later, the predictions might suffer from uncertainties in the cancellation of the different diagrams due to the conveyed strong interaction phases for the K^+K^- and $\eta\pi^0$ channels from the fit to the $\pi^+\pi^-$ spectra. However, this is not the case for the $\Upsilon(1S)\eta\pi^0$ channel. Because of the neutral final states the process can only be observed by the three-pion decay of the η meson, which is harder to detect compared with the charged decays $\Upsilon(1S)\pi^+\pi^-$ and $\Upsilon(1S)K^+K^-$. No data has been published for this process so far. We predicted the decay distributions and find, that the cross section for this process is large enough to justify a search.

The number of events N_s per bin, reported by Belle, are listed in Tab. C.8.1 and plotted in Fig. 3.12. To convert the signal yield N_s to cross sections in pb, the luminosity L , the detection efficiency Eff. and the branching ratio $B(\Upsilon(1S) \rightarrow \mu^+\mu^-)$ is needed (the events are selected if the invariant $\mu^+\mu^-$ mass is close to the mass of the $\Upsilon(1S)$, hence the necessity of the branching ratio $B(\Upsilon(1S) \rightarrow \mu^+\mu^-)$), where the detection efficiency Eff. is obtained in Monte-Carlo simulations. The correlations between the cross section and the signal yield N_s is then given by

$$\sigma(e^+e^- \rightarrow \Upsilon(1S)\pi^+\pi^-) = \frac{N_s}{L \times \text{Eff.} \times B(\Upsilon(1S) \rightarrow \mu^+\mu^-)} = \frac{(21700 \text{ pb})N_s}{0.374 \times 0.0248}. \quad (3.8.1)$$

The data is taken from reference [91], in which further information about the data selection can be found.

Mass-breaking of the heavy and light $Y_{[b,l]}$ and $Y_{[b,h]}$ is neglected in this section, and I work in the isospin basis with the two isospin components

$$Y_b^0 \equiv \frac{1}{\sqrt{2}}(Y_{[bu]} + Y_{[bd]}) \quad \text{with } I = 0, \quad Y_b^1 \equiv \frac{1}{\sqrt{2}}(Y_{[bu]} - Y_{[bd]}) \quad \text{with } I = 1. \quad (3.8.2)$$

The mass eigenstates are approximately $Y_{[bu]}$ and $Y_{[bd]}$ rather than the isospin eigenstates above, since the mixing between $Y_{[bu]}$ and $Y_{[bd]}$, arising from annihilation diagrams ($u\bar{u} \leftrightarrow d\bar{d}$), are suppressed as discussed in Sec. 3.5. Since the Y_b^I production in e^+e^- annihilation is considered, not all isospin breaking effects can be neglected. These effects are important in the coupling of the Y_b^I to the intermediate virtual photon. This is described in Sec. 3.5, in which it is derived, that the coupling is proportional to the effective constituent diquark charge Q_I of the Y_b^I .

To fit the data, we calculated the differential cross section of the $2 \rightarrow 3$ process $e^+e^- \rightarrow Y_b \rightarrow \Upsilon(nS)PP'$ at tree level, where P and P' can be one of the light meson final states in the above mentioned decays ($PP' = \pi^+\pi^-, K^+K^-, \eta\pi^0$). The topology and the kinematics of the process are shown in Fig. 3.19, in which the Y_b^I is in the s -channel. Two kind of contributions are accounted for, the resonant and non-resonant transitions. The former arise, when the Y_b^I decays in a two-body decay $Y_b^I \rightarrow R\Upsilon(nS)$ and subsequently the resonance R decays to the meson pair $R \rightarrow PP'$. In the following I take the Breit-Wigner ansatz, presented in Sec. 3.7 and Eq. (3.7.3) in particular, including also the Flatté formalism for the total decay width, which is discussed in App. C.4.2. The Flatté formalism is only used for resonances whose mass is close to a decay threshold compared with the total decay width. The resonant part comprises the resonance interchanges $e^+e^- \rightarrow Y_b \rightarrow \Upsilon(nS)[\sigma(600), f_0(980), a_0^0(980), f_2(1270)] \rightarrow \Upsilon(1S)PP'$. Since the quantum numbers of Y_b and $\Upsilon(nS)$ are $J^{PC} = 1^{--}$, those of the dipion system must be either 0^{++} or 2^{++} due to angular momentum and parity conservation, thus the above resonances include all contributions in the allowed kinematic region. In the following the notations for the resonances are abbreviated as σ , f_0 , a_0^0 and f_2 respectively (the upper index indicates the $I_3 = 0$ component of the iso-triplet a_0). Following t'Hooft et al. [86], we adopted a tetraquark interpretation of the light scalar mesons and ignored a supposedly tiny mixing between σ_0 and f_0 .

The non-resonating transitions are quark rearrangement processes, which can occur without forming intermediate states. This contributions are called continuum contributions, labeled by C . The amplitude factorizes however in the same way as in the resonant case in the sense, that those contributions can be kinematically interpreted as $Y_b \rightarrow \Upsilon(nS)C$ with the subsequent ‘‘decay’’ of the continuum $C \rightarrow PP'$. Hence in Fig. 3.19 \mathcal{T} stands for any of the aforementioned contributions C or R . The different types of contributions are pictured in Fig. 3.20. This contribution is not stemming from poles in the S-matrix as the resonances and needs a different model, which we adopted from [95].

The model and the different contributions are described in the following.

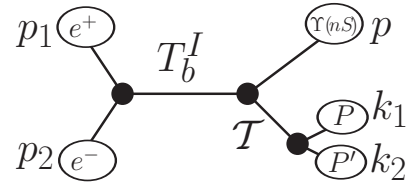


Figure 3.19: Topology and kinematics of the observed $2 \rightarrow 3$ processes $e^+e^- \rightarrow Y_b \rightarrow \Upsilon(nS)PP'$. The momenta are assigned to the final particle states as shown.

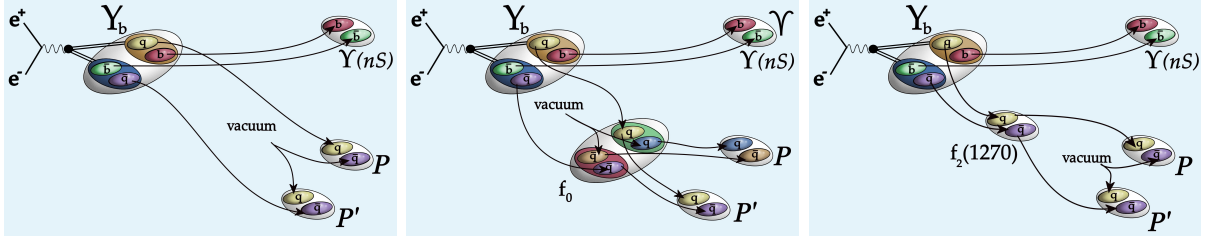


Figure 3.20: Zweig allowed quark rearrangement diagrams contributing to the model for the cross section $\sigma(e^+e^- \rightarrow Y_b \rightarrow \Upsilon(nS)PP')$. The continuum contribution is pictured to the left, the scalar tetraquark resonance interchange is given in the middle and the $f_2(1270)$ meson interchange to the right.

3.8.1 Model for the process $e^+e^- \rightarrow Y_b \rightarrow \Upsilon(nS)PP'$

First I sketch the derivation of the differential cross section $d\sigma(e^+e^- \rightarrow Y_b \rightarrow \Upsilon(nS)PP')$ (shorthand $d\sigma_{PP'}$). Afterwards I introduce the couplings, which are involved in the resonant decay and the continuum couplings. The values for the input parameters, which are used in this section can be found in Tab. C.8.2.

The differential cross section $d\sigma_{PP'}$ is given by

$$d\sigma_{PP'} = \frac{(2\pi)^4}{2s} \frac{1}{4} \sum_{\lambda_{e^+}, \lambda_{e^-}, \lambda_{\Upsilon}} \left| \sum_{\mathcal{T}, I, \lambda_{Y_b}} \mathcal{M}_{\mathcal{T}, \lambda_{Y_b}}^I \right|^2 d\Phi_3(p_1 + p_2; p, k_1, k_2), \quad (3.8.3)$$

in which the invariant amplitude

$$\mathcal{M}_{\mathcal{T}, \lambda_{Y_b}}^I \hat{=} \begin{array}{c} \diagup \quad \diagdown \\ \quad \quad Y_b^I \\ \diagdown \quad \diagup \\ \quad \quad \mathcal{T} \end{array} \quad (3.8.4)$$

has mass dimension -1 , and the sum over \mathcal{T} runs over the resonant and continuum contributions. It is summed over the polarizations λ_i of the final and averaged over the spin λ_{e^+} and λ_{e^-} of the initial state particles.

Each PP' channel receives specified contributions depending on the isospin of PP' and the kinematically allowed region for the invariant mass $M_{PP'} \in [m_P + m_{P'}, \sqrt{s} - m_{\Upsilon(1S)}]$, in which $I = 0$ for $\pi^+\pi^-$, $I = 0, 1$ for K^+K^- , and $I = 1$ for $\eta\pi^0$, since the $\Upsilon(1S)$ is an isospin 0 state, and the following resonances contribute to each process:

$$\begin{array}{ll} \sigma, f_0 \text{ and } f_2 & \text{for } PP' = \pi^+\pi^-, \\ f_0, a_0^0 \text{ and } f_2 & \text{for } PP' = K^+K^-, \\ a_0^0 & \text{for } PP' = \eta\pi^0. \end{array} \quad (3.8.5)$$

The contributions for the different final states are listed in Fig. 3.21. Because Y_b^I is in the s -channel, the amplitude in (3.8.3) factorizes in the product of the amplitudes for $e^+e^- \rightarrow Y_b^I$ and $Y_b^I \rightarrow \Upsilon(nS)\mathcal{T}$ and splits explicitly in a production and a decay part:

$$\mathcal{M}_{\mathcal{T}, \lambda_{Y_b}}^I = \sum_{\lambda_{Y_b^I}} \mathcal{M}(e^+e^- \rightarrow Y_b^I) \frac{1}{s - m_{Y_b}^2 + im_R \Gamma_{Y_b}} \mathcal{M}(Y_b^I \rightarrow \Upsilon(nS)\mathcal{T}).$$

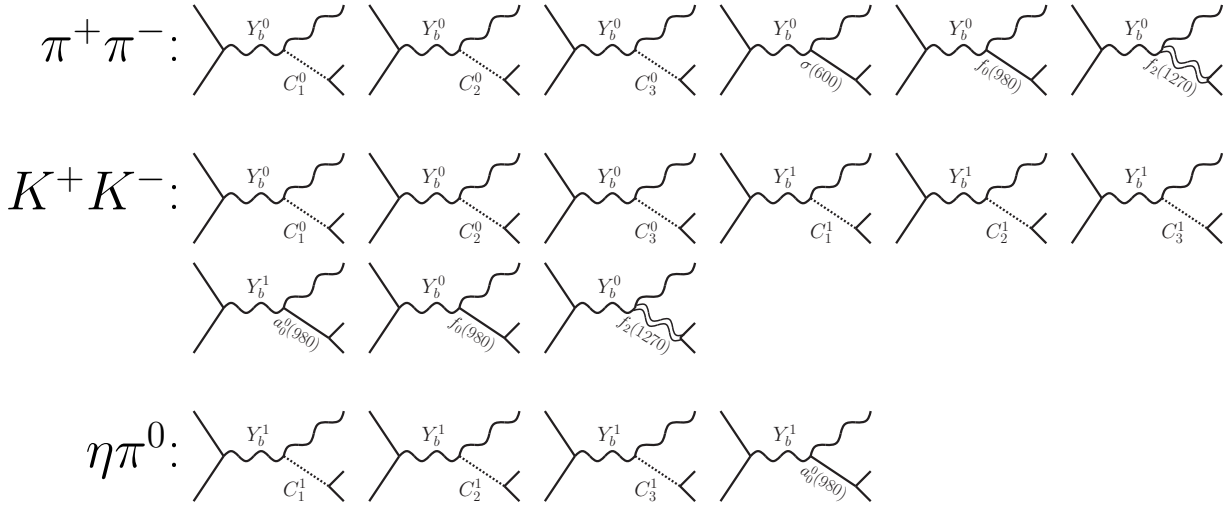


Figure 3.21: Diagrams contributing to the different channels $e^+e^- \rightarrow \Upsilon(nS)PP'$, with PP' being the above listed meson pairs $\pi^+\pi^-$, K^+K^- and $\eta\pi^0$. Note, that the continuum part, labeled by C , in this notation do not denote propagators. They are to be understood in the sense of Eq. (3.8.19).

$$\cong \sum_{\lambda_{Y_b^I}} \left[\text{Diagram} \right] \times \frac{1}{s - m_{Y_b}^2 + im_R \Gamma_{Y_b}} \times \left[\text{Diagram} \right] \quad (3.8.6)$$

This is valid under the assumption, that the process is dominated by the interchange of the intermediate Y_b^I resonance, as described in Eq. (3.7.2).

The calculations in this section are performed with the use of helicity amplitudes without the use of the polarization sums of the external states. However, the polarization of the internal state Y_b^I can be summed over. The product of $\epsilon_{Y_b}^{*\delta}$ in the production amplitude and $\epsilon_{Y_b}^\nu$ in the decay amplitude gives the usual polarization sum in a vector-boson propagator, after summing over the helicity λ_{Y_b} of the Y_b^I resonance: $\sum_{\lambda_{Y_b}} \epsilon_{Y_b}^\nu(\lambda_{Y_b}) \epsilon_{Y_b}^{*\delta}(\lambda_{Y_b}) = -g^{\nu\delta} + q^\nu q^\delta / q^2$. The momentum-dependent term vanishes in the calculations due to the on-shell condition. The external polarization vectors satisfy the transversality condition and only the metric part remains. I define therefore the production and decay amplitudes as

$$\begin{aligned} \mathcal{M}_\mu^{\text{prd}} \epsilon_{Y_b}^\mu(\lambda_{Y_b}) &\equiv \mathcal{M}(e^+e^- \rightarrow Y_b^I), \\ \mathcal{M}_\nu^{\text{dec}} \epsilon_{Y_b}^\nu(\lambda_{Y_b}) &\equiv \mathcal{M}(Y_b^I \rightarrow \Upsilon(nS)\mathcal{T}) \end{aligned} \quad (3.8.7)$$

respectively. Thus yielding

$$\begin{aligned} d\sigma_{PP'} &= \sum_{\mathcal{T}, I} \sum_{\lambda_{e^+}, \lambda_{e^-}} \frac{(2\pi)^4}{2s} \frac{1}{4} \frac{dM_{PP'}^2}{2\pi} d\Phi_2(p_1 + p_2; p, k_1 + k_2) d\Phi_2(p_R; k_1, k_2) \\ &\quad \mathcal{M}_\mu^{\text{prd}} \mathcal{M}_\nu^{\text{prd}*} \frac{1}{(s - m_{Y_b}^2)^2 + m_{Y_b}^2 \Gamma_{Y_b}^2} \sum_{\lambda_Y} \mathcal{M}^{\text{dec}} \mu \mathcal{M}^{\text{dec} \nu*}. \end{aligned} \quad (3.8.8)$$

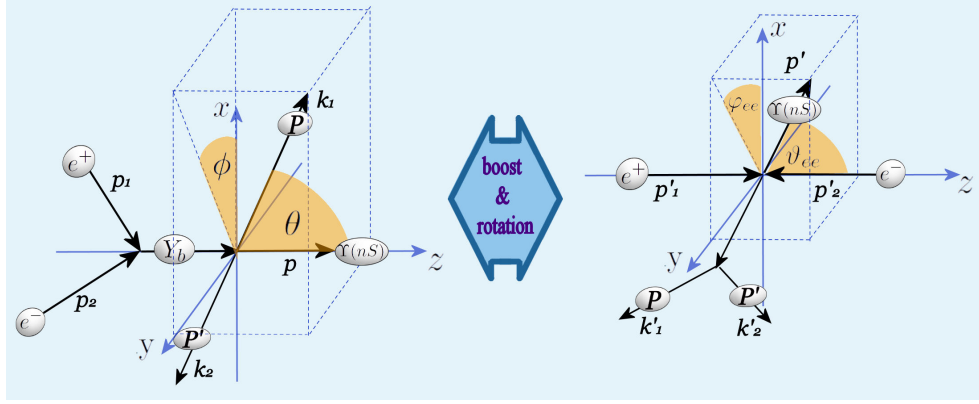


Figure 3.22: $e^+e^- \rightarrow \Upsilon(1S)\pi^+\pi^-$ in the rest frame of the dipion (left) and in the rest frame of the e^+e^- pair (right).

Here the phase space factor $d\Phi_3(p_a + p_b; p_c, p_1, p_2)$ is split in the two-body phase spaces in the e^+e^- and $\pi^+\pi^-$ rest frame, further described in App. C.3, where also details of the phase space parametrization can be found.

A $2 \rightarrow 3$ process is in general described by 6 independent variables, in which the center of mass energy \sqrt{s} is fixed. The 5 independent final state integration variables are in the present case $M_{PP'}$, $\cos\theta$, ϕ , $\cos\vartheta_{ee}$ and φ_{ee} . The parametrization is described in Fig. 3.22 and the variables are defined in two different frames, the e^+e^- rest frame and the PP' rest frame. The subscript ee indicates definition in the former and no subscript definition in the latter frame. Both frames are correlated by a rotation by ϑ_{ee} and φ_{ee} , and a boost along the $k_1 + k_2$ direction. The boost is described in Eq. C.3.14. The two particle phase space $d\Phi_2$ is given in Eq. (C.3.7).

The production and decay amplitudes are separately discussed in the following. The coupling $g_{e^+e^-Y_b^I}$ between $e^+e^-Y_b^I$ was already introduced in Sec. 3.5 in the discussion of the production process through intermediate virtual photons, described by the Van Royen-Weisskopf formula. The effective couplings of the resonances are in a similar way defined by the effective Lagrangians

$$\mathcal{L} = g_{SPP'}(\partial_\mu P)(\partial^\mu P') S + g_{Y_b^I \Upsilon(nS) S} Y_{b\mu}^I \Upsilon^\mu S, \quad (3.8.9)$$

for the scalar tetraquark resonances S , while those for the f_2 meson are defined through

$$\mathcal{L} = 2g_{f_2 PP'}(\partial_\mu P)(\partial_\nu P') f_2^{\mu\nu} + g_{Y_b^I \Upsilon(nS) f_2} Y_{b\mu}^I \Upsilon_\nu f_2^{\mu\nu}, \quad (3.8.10)$$

in which $f_2^{\mu\nu}$ denotes the f_2 meson field. The Lagrangians give rise to the vertices, which are

$$\begin{array}{c}
\begin{array}{ccccccc}
\begin{array}{c} e^+ \\ \mu \\ e^- \end{array} \begin{array}{c} \text{---} \\ \bullet \\ \text{---} \end{array} \begin{array}{c} \mu \\ Y_b^I \end{array} \begin{array}{c} \text{---} \\ \bullet \\ \text{---} \end{array} \begin{array}{c} \mu \\ Y_b^I \end{array} \begin{array}{c} \nu \\ S \end{array} \begin{array}{c} \text{---} \\ \bullet \\ \text{---} \end{array} \begin{array}{c} \mu \\ Y_b^I \end{array} \begin{array}{c} \nu \\ \Upsilon(nS) \end{array} \begin{array}{c} \text{---} \\ \bullet \\ \text{---} \end{array} \begin{array}{c} \mu \\ Y_b^I \end{array} \begin{array}{c} \nu \\ \Upsilon(nS) \end{array} \begin{array}{c} \text{---} \\ \bullet \\ \text{---} \end{array} \begin{array}{c} k_1 \\ P \end{array} \begin{array}{c} \text{---} \\ \bullet \\ \text{---} \end{array} \begin{array}{c} k_2 \\ P' \end{array} \begin{array}{c} \text{---} \\ \bullet \\ \text{---} \end{array} \begin{array}{c} \mu\nu \\ f_2 \end{array} \begin{array}{c} \text{---} \\ \bullet \\ \text{---} \end{array} \begin{array}{c} k_1 \\ P \end{array} \begin{array}{c} \text{---} \\ \bullet \\ \text{---} \end{array} \begin{array}{c} k_2 \\ P' \end{array} \end{array} \quad (3.8.11) \\
\begin{array}{ccccccc}
ig_{e^+e^-Y_b^I} \gamma^\mu & ig_{Y_b^I \Upsilon(nS) S} g_{\mu\nu} & ig_{Y_b^I \Upsilon(1S) f_2} g_{\mu\rho} g_{\nu\sigma} & -ig_{SPP'} k_1 \cdot k_2 & ig_{f_2 PP'} \frac{1}{2} \times \\
& & & & (k_1 - k_2)_\mu (k_1 - k_2)_\nu
\end{array}
\end{array}$$

for $m_P = m_{P'}$, where the data for $\Gamma(f_2 \rightarrow \pi\pi) = (3/2)\Gamma(f_2 \rightarrow \pi^+\pi^-)$ and $\Gamma(f_2 \rightarrow K\bar{K}) = 2\Gamma(f_2 \rightarrow K^+K^-)$, and $m_{f_2} = 1275$ MeV are taken from PDG [77]. The other inputs for the pseudo-scalar mesons and the $\Upsilon(1S)$ are also taken from PDG. The Flatté model is detailed in App. C.4.2, and the f_2 contribution is further described in App. C.4.3.

The continuum contributions describe the Zweig allowed quark rearrangement diagrams in Fig. 3.20 (left). Our continuum parametrization is described in detail in App. C.4.1 and was taken from [95]. It is similar to the model describing the ordinary $\Upsilon(nS)$ decays like the one shown for $\Upsilon(4S)$ in Fig. 3.13 (right). In total one finds the following three types of contributions

$$\begin{aligned}
\begin{array}{c} \nu \\ \Upsilon(nS) \\ \text{---} \\ \bullet \\ \text{---} \\ Y_b^0 \quad \mu \\ \text{---} \\ \bullet \\ C_1^0 \\ \text{---} \\ P \\ \text{---} \\ P' \end{array} & : & g_{\mu\nu} \mathcal{M}_1^C(M_{PP'}^2), \\
\begin{array}{c} \nu \\ \Upsilon(nS) \\ \text{---} \\ \bullet \\ \text{---} \\ Y_b^0 \quad \mu \\ \text{---} \\ \bullet \\ C_2^0 \\ \text{---} \\ P \\ \text{---} \\ P' \end{array} & : & g_{\mu\nu} \mathcal{M}_2^C(M_{PP'}^2) \left(\cos^2 \theta - \frac{1}{3} \right), \\
\begin{array}{c} \nu \\ \Upsilon(nS) \\ \text{---} \\ \bullet \\ \text{---} \\ Y_b^0 \quad \mu \\ \text{---} \\ \bullet \\ C_3^0 \\ \text{---} \\ P \\ \text{---} \\ P' \end{array} & : & (k_{1\mu}k_{2\nu} + k_{2\mu}k_{1\nu}) \mathcal{M}_3^C(M_{PP'}^2), \tag{3.8.19}
\end{aligned}$$

of which the last one is suppressed by the heavy-quark mass.

After the introduction of the phase space parametrization and the explicit form of the amplitudes, the differential cross section $d\sigma_{PP'}$ is calculated. The production amplitude is the same for all diagrams in Fig. 3.21 and is given by the effective coupling of the Y_b^I to the e^+e^- current described by the vertex in (3.8.11). It is given by

$$M_\mu^{\text{prd}} = g_{e^+e^-Y_b^I} [\bar{v}_e(p_1, \lambda_1) \gamma_\mu u_e(p_2, \lambda_2)] \tag{3.8.20}$$

The coupling constant is related to the Van Royen-Weisskopf formula, described in Sec. 3.5, in which an approximate value is given in Eq. (3.5.17). The decay amplitude is obtained similar to the production amplitude by using the vertices and propagators in Eqs. (3.8.11) to (3.8.19).

Choosing explicit expressions for the electron spinors and the $\Upsilon(nS)$ polarization vector, which are listed in App. C.3, every diagram is proportional to a helicity factor, which can be explicitly calculated. The helicity factor takes only the direct dependence on the external polarization vectors and spinors of the amplitude into account, further outlined in App. C.5, and contains therefore the full angular dependence. The simplest of them, namely the one corresponding to the scalar resonance exchange, is given as example. The corresponding diagram reads

$$\mathcal{M} = \frac{k_1 \cdot k_2 \ g_{SPP'} \ g_{Y_b^0 \Upsilon(1S)S} \ g_{e^+e^-Y_b^I}}{[s - m_{Y_b}^2 + im_{Y_b} \Gamma_{Y_b}][M_{PP'}^2 - m_S^2 + im_S \Gamma_S]} \times \mathcal{H}_1^C \cong \begin{array}{c} Y_b^I \\ \diagup \quad \diagdown \\ \quad \quad R \end{array}, \tag{3.8.21}$$

with helicity factor

$$\mathcal{H}_1^C \equiv \epsilon_{\Upsilon}^{*\mu}(\lambda_{\Upsilon}) g_{\mu\nu} [\bar{v}_e(p_1, \lambda_1) \gamma^{\nu} u_e(p_2, \lambda_2)]. \quad (3.8.22)$$

The structure is very simple because the decay matrix element $\mathcal{M}^{\text{dec } \mu}$ is only proportional to the polarization vector $\epsilon_{\Upsilon}^{*\mu}$ of $\Upsilon(nS)$. After the insertion of the polarization vectors and spinors, listed in App. C.3, Eq. (3.8.22) yields

$$\mathcal{H}_1^C = \begin{cases} -\sqrt{2\pi s}(1 + \cos(\vartheta_{ee})) e^{\pm i\varphi_{ee}} Y_0^0(\theta, \phi) & \text{for } \{\lambda_{e^+}, \lambda_{e^-}, \lambda_{\Upsilon}\} = \left\{ \pm\frac{1}{2}, \pm\frac{1}{2}, \pm 1 \right\}, \\ \pm\sqrt{2\pi s} \frac{\sqrt{2}(q \cdot p)}{\sqrt{s} m_{\Upsilon}} \sin(\vartheta_{ee}) e^{\pm i\varphi_{ee}} Y_0^0(\theta, \phi) & \text{for } \{\lambda_{e^+}, \lambda_{e^-}, \lambda_{\Upsilon}\} = \left\{ \pm\frac{1}{2}, \pm\frac{1}{2}, 0 \right\}, \\ -\sqrt{2\pi s}(1 - \cos(\vartheta_{ee})) e^{\pm i\varphi_{ee}} Y_0^0(\theta, \phi) & \text{for } \{\lambda_{e^+}, \lambda_{e^-}, \lambda_{\Upsilon}\} = \left\{ \pm\frac{1}{2}, \pm\frac{1}{2}, \mp 1 \right\}, \\ 0 & \text{otherwise.} \end{cases} \quad (3.8.23)$$

The spherical harmonics $Y_l^m(\theta, \phi)$ are given in App. A.3. The helicity decomposition is described in App. C.5, in which the factors for all different helicity contributions are given in Eq. (C.5.7).

The Belle data on the differential cross sections $d\sigma_{PP'}/dM_{PP'}$ and $d\sigma_{PP'}/d\cos\theta$ in Fig. 3.12 is described by the invariant mass $M_{PP'}$ and the helicity $\cos\theta$ respectively. To obtain the differential cross sections, the variables ϑ_{ee} , ϕ and φ_{ee} have to be integrated out:

$$\frac{d^2\sigma}{dM_{PP'} d\cos\theta} = \int_0^{2\pi} d\phi \int_{-1}^1 d\cos\vartheta_{ee} \int_0^{2\pi} d\varphi_{ee} \frac{\lambda^{1/2}(s, m_{\Upsilon}^2, M_{PP'}^2) \lambda^{1/2}(M_{PP'}^2, m_P^2, m_{P'}^2)}{256(2\pi)^5 s^2 M_{PP'}} \sum_{\lambda_{e^+}, \lambda_{e^-}, \lambda_{\Upsilon}, \mathcal{I}, I} M_{\mu}^{\text{prd}} M_{\nu}^{\text{prd}*} \mathcal{M}^{\text{dec } \mu} \mathcal{M}^{\text{dec } \nu*}, \quad (3.8.24)$$

in which $\lambda(x, y, z) \equiv (x - y - z)^2 - 4yz$. The integration over $M_{PP'}$ or $\cos\theta$ is performed subsequently. The integration around the beam axis, described by φ_{ee} , is trivial and yields an overall factor 2π . The integration over the other angles can be performed analytically. It is helpful, that the differential cross section in (3.8.24) is a polynomial in the trigonometric functions of the angles. Here I just give the final result:

$$\begin{aligned} \frac{d^2\sigma_{PP'}}{dM_{PP'} d\cos\theta} = & \frac{\lambda^{1/2}(s, m_{\Upsilon}^2, M_{PP'}^2) \lambda^{1/2}(M_{PP'}^2, m_P^2, m_{P'}^2)}{384\pi^3 s M_{PP'} [(s - m_{Y_b}^2)^2 + m_{Y_b}^2 \Gamma_{Y_b}^2]} \left\{ \left(1 + \frac{(q \cdot p)^2}{2s m_{\Upsilon}^2} \right) |\mathcal{S}|^2 \right. \\ & + 2 \text{Re} \left[\mathcal{S}^* \left(\mathcal{D}' + \frac{(q \cdot p)^2}{2s m_{\Upsilon}^2} \mathcal{D}'' \right) \right] \left(\cos^2\theta - \frac{1}{3} \right) \\ & + |\mathcal{D}|^2 \sin^2\theta \left(\sin^2\theta + 2 \left(\frac{(q^0)^2}{s} + \frac{(p^0)^2}{m_{\Upsilon}^2} \right) \cos^2\theta \right) \\ & \left. + \left(|\mathcal{D}'|^2 + \frac{(q \cdot p)^2}{2s m_{\Upsilon}^2} |\mathcal{D}''|^2 \right) \left(\cos^2\theta - \frac{1}{3} \right)^2 \right\}, \end{aligned} \quad (3.8.25)$$

The S-wave amplitude for the PP' system, \mathcal{S} , and the D-wave amplitudes, \mathcal{D} , \mathcal{D}' and \mathcal{D}'' , are the sums over possible isospin states

$$\mathcal{M} = \sum_I \mathcal{M}_I \quad \text{for } \mathcal{M} = \mathcal{S}, \mathcal{D}, \mathcal{D}', \mathcal{D}'' \quad (3.8.26)$$

The $I = 0$ amplitudes are given by the combinations of the resonance amplitudes, \mathcal{M}_0^S and $\mathcal{M}_0^{f_2}$, and the non-resonating continuum amplitudes, \mathcal{M}_0^{1C} , \mathcal{M}_0^{2C} and \mathcal{M}_0^{3C} :

$$\begin{aligned}\mathcal{S}_0 &= \mathcal{M}_0^{1C} + (k_1 \cdot k_2) \sum_S \mathcal{M}_0^S + \frac{2|\mathbf{k}|^2}{3} \mathcal{M}_3^C(M_{PP'}), \quad \mathcal{D}_0 = |\mathbf{k}|^2 (\mathcal{M}_0^{f_2} + \mathcal{M}_3^C(M_{PP'})), \\ \mathcal{D}'_0 &= \mathcal{M}_0^{2C} - \mathcal{D}_0, \quad \mathcal{D}''_0 = \mathcal{M}_0^{2C} + \frac{2q^0 p^0}{(q \cdot p)} \mathcal{D}_0,\end{aligned}\quad (3.8.27)$$

where S runs over possible $I = 0$ scalar resonances in Eq. (3.8.5). Similarly, the $I = 1$ amplitudes are given by

$$\mathcal{S}_1 = \frac{g_{e^+e^-Y_b^1}}{g_{e^+e^-Y_b^0}} \left[\mathcal{M}_1^{1C} + (k_1 \cdot k_2) \mathcal{M}_1^{a_0} \right], \quad \mathcal{D}_1 = 0, \quad \mathcal{D}'_1 = \mathcal{D}''_1 = \frac{g_{e^+e^-Y_b^1}}{g_{e^+e^-Y_b^0}} \mathcal{M}_1^{2C}, \quad (3.8.28)$$

in which the dimensionless couplings $g_{e^+e^-Y_b^0}$ and $g_{e^+e^-Y_b^1}$ are defined via the Lagrangian (3.5.8). The continuum amplitudes in Eq. (3.8.27) are written in terms of the two form factors A , B and C as

$$\begin{aligned}\mathcal{M}_0^{1C}(M_{PP'}^2) &= \frac{2A}{f_P f_{P'}} (k_1 \cdot k_2) + \frac{B}{f_P f_{P'}} \frac{3(q^0)^2 k_1^0 k_2^0 - |\mathbf{q}|^2 |\mathbf{k}|^2}{3s}, \\ \mathcal{M}_0^{2C}(M_{PP'}^2) &= -\frac{B}{f_P f_{P'}} \frac{|\mathbf{q}|^2 |\mathbf{k}|^2}{s}, \\ \mathcal{M}_0^{3C}(M_{PP'}^2) &= \frac{C}{f_P f_{P'}},\end{aligned}\quad (3.8.29)$$

in which $f_{P^{(\prime)}}$ is the decay constant of $P^{(\prime)}$. Using SU(3) symmetry the relations

$$\begin{aligned}\mathcal{M}_0^{1C,2C,3C}(\Upsilon(1S)K^+K^-) &= (\sqrt{3}/2) \mathcal{M}_0^{1C,2C,3C}(\Upsilon(1S)\pi^+\pi^-), \\ \mathcal{M}_1^{1C,2C,3C}(\Upsilon(1S)K^+K^-) &= \mathcal{M}_0^{1C,2C,3C}(\Upsilon(1S)K^+K^-), \\ \mathcal{M}_1^{1C,2C,3C}(\Upsilon(1S)\eta\pi^0) &= \sqrt{2} \mathcal{M}_1^{1C,2C,3C}(\Upsilon(1S)K^+K^-)\end{aligned}\quad (3.8.30)$$

are assumed. The continuum contributions are explicitly defined in the PP' rest frame. The variables q^0 , p^0 , k_1^0 , k_2^0 , $|\mathbf{q}|$ and $|\mathbf{k}|$ are given in terms of $s \equiv q^2 = (p_1 + p_2)^2$ and $M_{PP'}^2 \equiv (k_1 + k_2)^2$ by

$$\begin{aligned}q^0 &= \frac{s - m_\Upsilon^2 + M_{PP'}^2}{2M_{PP'}}, \quad p^0 = q^0 - M_{PP'} = \frac{s - m_\Upsilon^2 - M_{PP'}^2}{2M_{PP'}}, \\ |\mathbf{q}|^2 &= (q^0)^2 - s = (p^0)^2 - m_\Upsilon^2, \quad k_1^0 = \sqrt{|\mathbf{k}|^2 + m_P^2}, \quad k_2^0 = \sqrt{|\mathbf{k}|^2 + m_{P'}^2}, \\ |\mathbf{k}|^2 &= \frac{M_{PP'}^2}{4} \left(1 - \frac{(m_P + m_{P'})^2}{M_{PP'}^2} \right) \left(1 - \frac{(m_P - m_{P'})^2}{M_{PP'}^2} \right),\end{aligned}\quad (3.8.31)$$

in which $M_{PP'}^2 = (k_1 + k_2)^2 = (k_1^0 + k_2^0)^2$. Note, that this set of equations simplifies for the $\pi^+\pi^-$ and K^+K^- case since the light meson masses are identical. Only the $\eta\pi^0$ case has a more complicated kinematics.

The differential cross section $d\sigma/dM_{PP'}$ is obtained by analytically integrating (3.8.25) over $\cos\theta$. One finds:

$$\frac{d\sigma_{PP'}}{dM_{PP'}} = \frac{\lambda^{1/2}(s, m_\Upsilon^2, M_{PP'}^2) \lambda^{1/2}(M_{PP'}^2, m_P^2, m_{P'}^2)}{192\pi^3 s M_{PP'} [(s - m_{Y_b}^2)^2 + m_{Y_b}^2 \Gamma_{Y_b}^2]} \left\{ \left(1 + \frac{(q \cdot p)^2}{2s m_\Upsilon^2} \right) |\mathcal{S}|^2 \right\} \quad (3.8.32)$$

$$+ \frac{4}{15} |\mathcal{D}|^2 \left(2 + \left(\frac{(q^0)^2}{s} + \frac{(p^0)^2}{m_\Upsilon^2} \right) \right) + \frac{4}{45} \left(|\mathcal{D}'|^2 + \frac{(q \cdot p)^2}{2sm_\Upsilon^2} |\mathcal{D}''|^2 \right) \Bigg\},$$

To obtain the differential cross section $d\sigma_{PP'}/d\cos\theta$, the integration over $M_{PP'}$ of the differential cross section given in (3.8.25) needs to be performed numerically. In this case it is helpful, that the formula is a simple polynomial in the fitting parameters (the coupling constants) and $\cos\theta$ of maximal fourth degree, *i.e.* the differential cross section

$$\frac{d\sigma_{PP'}}{d\cos\theta} = \int_{P+P'}^{\sqrt{s}-m_{\Upsilon(ns)}} dM_{PP'} \frac{d^2\sigma_{PP'}}{dM_{PP'} d\cos\theta} \quad (3.8.33)$$

has the form

$$= \frac{1}{384\pi^3 s [(s - m_{Y_b}^2)^2 + m_{Y_b}^2 \Gamma_{Y_b}^2]} (\mathcal{C}_0 + \mathcal{C}_2 \cos^2\theta + \mathcal{C}_4 \cos^4\theta), \quad (3.8.34)$$

in which \mathcal{C}_0 , \mathcal{C}_2 and \mathcal{C}_4 are functions of the fitting parameters. This polynomial expansion and the numerical integration of the coefficient functions can be easily automatized.

The model functions (3.8.32) and (3.8.33) are used in the following to perform a fit to the Belle data for $PP' = \pi^+\pi^-$ and to subsequently use the obtained fitting parameters as input to predict the spectra for $PP' = K^+K^-, \eta\pi^0$. The Dalitz plot for the differential cross section $d\sigma_{PP'}/M_{\Upsilon P}^2/M_{P'P'}^2$ is also given below, in which the invariant mass for the $\Upsilon(1S)P$ system is given in terms of the helicity angle via

$$\begin{aligned} M_{\Upsilon P}^2 &= m_\Upsilon^2 + m_P^2 + \frac{1}{2M_{PP'}^2} (s - M_{PP'}^2 - m_\Upsilon^2) (M_{PP'}^2 + m_P^2 - m_{P'}^2) \\ &\quad - \frac{1}{2M_{PP'}^2} \cos\theta \sqrt{\lambda(s, M_{PP'}^2, m_\Upsilon^2) \lambda(M_{PP'}^2, m_P^2, m_{P'}^2)}. \end{aligned} \quad (3.8.35)$$

3.8.2 Fit to the $\Upsilon(1S)\pi^+\pi^-$ data

Here I discuss our fit to the Belle data [90], using the modeled differential cross sections in Eqs. (3.8.32) and (3.8.33). The experimental data, the input parameters and the Flatté couplings, which are needed for this section are listed in Tabs. C.8.1 and C.8.2. Although \mathcal{M}_3^C is suppressed by the heavy-quark mass compared to the other continuum terms \mathcal{M}_1^C and \mathcal{M}_2^C , the interference between \mathcal{M}_3^C and the f_2 contribution may be significant. However, we found in the fit, that the contribution is negligible even for allowing arbitrary large couplings in the fit. Due to this reasons, we set the continuum term \mathcal{M}_3^C to zero, which moreover results in more stable fits. The spectra are normalized by the measured cross section $d\tilde{\sigma}_{\pi^+\pi^-}/dM_{\pi\pi}$ and $d\tilde{\sigma}_{\pi^+\pi^-}/d\cos\theta$, where

$$\tilde{\sigma}_{\pi^+\pi^-} \equiv \sigma_{\Upsilon(1S)\pi^+\pi^-} / \sigma_{\Upsilon(1S)\pi^+\pi^-}^{\text{Belle}} \quad \text{with} \quad \sigma_{\Upsilon(1S)\pi^+\pi^-}^{\text{Belle}} = 1.61 \pm 0.16 \text{ pb [91]}. \quad (3.8.36)$$

With assuming SU(3) symmetry for the $Y_b^0 \Upsilon(1S) R$ couplings in Eq. (3.8.11), *i.e.*, setting $g_{Y_b^0 \Upsilon(1S) \sigma} = g_{Y_b^0 \Upsilon(1S) f_0}$, one finds 7 free fitting parameters:

$$A' \equiv A |g_{e^+e^- Y_b^0}|, \quad B' \equiv B |g_{e^+e^- Y_b^0}|,$$

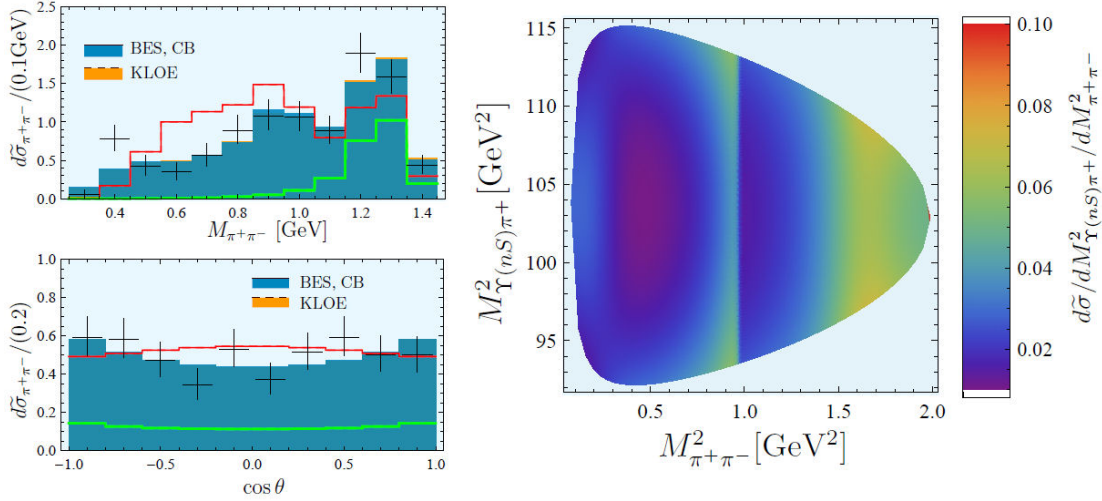


Figure 3.23: Fit results for the model for the process $e^+e^- \rightarrow Y_b \rightarrow \Upsilon(1S)\pi^+\pi^-$ for different Flatté couplings BES, CB (solid, blue, $\chi^2/\text{d.o.f.} = 21.5/15$) and KLOE (dashed, orange, $\chi^2/\text{d.o.f.} = 21.9/15$). To the left, the $M_{\pi^+\pi^-}$ (upper left) and $\cos\theta$ (lower left) spectra are shown. To the right the Dalitz plot is shown for the BES, CB values. The shaded histograms represent the binned model fits to the measured spectrum, which is given by the black crosses. The red lines show the contributions without the continuum terms, and the green lines show the contribution from only $f_2(1270)$. The fits for the different input parameters are almost identical, and the KLOE fits are almost covered by the BES, CB fits.

$$\begin{aligned}
g'_{Y_b^0\Upsilon(1S)\sigma} &\equiv g_{Y_b^0\Upsilon(1S)\sigma}|g_{e^+e^-Y_b^0}|, & \varphi_\sigma, \\
g'_{Y_b^0\Upsilon(1S)f_0} &\equiv g_{Y_b^0\Upsilon(1S)f_0}|g_{e^+e^-Y_b^0}|, & \varphi_{f_0}, \\
g'_{Y_b^0\Upsilon(1S)f_2} &\equiv g_{Y_b^0\Upsilon(1S)f_2}|g_{e^+e^-Y_b^0}|, & \varphi_{f_2}.
\end{aligned} \tag{3.8.37}$$

With 12 and 10 degrees of freedom in the $M_{PP'}$ and $\cos\theta$ spectrum respectively, the number of degrees of freedom in the fit is $\text{d.o.f.} = (12 + 10) - 7 = 15$.

With these inputs, we have performed a large number of fits (typically $O(5000)$) of the Belle data with the tetraquark theory predictions. The resultant best fit is fairly good, with $\chi^2/\text{d.o.f.} = (15.1 + 6.4)/15 = 21.5/15$ for the BES and CB input in Eq. (3.8.17), which corresponds to a p -value of 0.12. The first (second) summand in χ^2 is the χ^2 -value obtained from the fit to the $M_{PP'}$ ($\cos\theta$) spectrum. The corresponding best fit using the KLOE data is very similar, having a $\chi^2/\text{d.o.f.} = (15.4 + 6.5)/15 = 21.9/15$, yielding a p -value of 0.11. The best fits using the BES, CB and KLOE data are presented in Fig. 3.23 and the corresponding fit values of the parameters are listed in Tab. 3.8.2. The fits were performed with ROOT which was implemented in a C++ program and checked with Mathematica, using a self-made fitting routine. The p -value, the χ^2 method and the fitting procedure are further explained in App. C.7.

I note, that the resonance contribution represented by the red curve (only resonant contributions) and the green curve (f_2 contribution) in Fig. 3.23 dominate the $M_{\pi^+\pi^-}$ spectrum, supporting our dynamical model in the decay $Y_b \rightarrow \Upsilon(1S)\pi^+\pi^-$. Sufficient data may provide enough statistics to undertake an analysis in the end-region of $M_{\pi^+\pi^-}$ to probe the angular distribution of $f_2 \rightarrow \pi^+\pi^-$, although the shape in the helicity spectrum is not very distinctive. However, it might be possible, that the different partial wave contributions

Table 3.8.2: Best fit parameters of the fit to the $\Upsilon(1S)\pi^+\pi^-$ spectrum, yielding $\chi^2/\text{d.o.f.} = 21.5/15$ for BES, CB and $\chi^2/\text{d.o.f.} = 21.9/15$ for KLOE input. Here A' and B' are dimensionless, $g'_{Y_b^0\Upsilon(1S)f_0}$ and $g'_{Y_b^0\Upsilon(1S)f_2}$ are given in units of MeV, and the angles are in units of rad.

	A'	B'	$g'_{Y_b^0\Upsilon(1S)f_0}$	$g'_{Y_b^0\Upsilon(1S)f_2}$	φ_σ	φ_{f_0}	φ_{f_2}
BES, CB	0.000079	-0.00020	0.318	0.439	0.36	-2.76	-0.46
KLOE	0.000079	-0.00020	0.327	0.424	0.42	-2.49	-0.32

of f_2 enter the partial cross section with different strength, which may lead to a more pronounced shape. This possibility was not taken into account and needs experimental scrutiny.

Using the measured cross section given in (3.8.36), the partial decay width for $Y_b \rightarrow \Upsilon(1S)\pi^+\pi^-$ can be computed:

$$\begin{aligned} \Gamma(Y_b^I \rightarrow \Upsilon(1S)\pi^+\pi^-) &\approx \frac{m_{Y_b}\Gamma_{Y_b}^2}{|g_{e^+e^-Y_b^I}|^2} \sigma(e^+e^- \rightarrow Y_b^I \rightarrow \Upsilon(1S)\pi^+\pi^-), \\ &= 4.1 \left(\frac{\Gamma_{Y_b}}{30 \text{ MeV}} \right)^2 \left(\frac{10^{-4}}{|g_{e^+e^-Y_b^I}|} \right)^2 \text{ MeV}, \end{aligned} \quad (3.8.38)$$

where $s = m_{Y_b}^2$ has been assumed. With Eq. (3.5.17) one finds for a total decay width of approximately 30 MeV

$$\Gamma(Y_b^I \rightarrow \Upsilon(1S)\pi^+\pi^-) \approx 0.5 \frac{1}{\kappa^2 Q_I^2} \text{ MeV}. \quad (3.8.39)$$

Thus the physical states $Y_{[bu/bd]}$ have a partial decay width $\Gamma(Y_{[bu/bd]} \rightarrow \Upsilon(1S)\pi^+\pi^-)$ of $\mathcal{O}(1)$ MeV.

3.8.3 Predictions for $e^+e^- \rightarrow \Upsilon(1S)K^+K^-$ and $e^+e^- \rightarrow \Upsilon(1S)\eta\pi^0$

Here I present our predictions for the decays, in which $PP' = K^+K^-$ and $PP' = \eta\pi^0$. These channels are suppressed by phase space compared with the $\pi^+\pi^-$ case. However, isospin $I = 1$ diagrams contribute in both channels (in the $\eta\pi^0$ channel only the $I = 1$ amplitudes are important). Because of the ratio $g_{e^+e^-Y_b^1}/g_{e^+e^-Y_b^0} = -3$ due to the different effective diquark charges, as shown in Eq. (3.5.16), these channels receive an enhancement. Thus the total cross section is larger than naively expected.

I approximate $f_\eta = f_\pi$ in the numerical analysis, as explained further in App. C.6. The normalized $M_{K^+K^-}$ and $M_{\eta\pi^0}$ distributions, calculated with the best-fit parameters in Tab. 3.8.2, are shown in Fig. 3.24 and Fig. 3.25, respectively. In these figures the red (black) curves show the dimeson invariant-mass spectra from the resonant (total) contribution. Since these spectra are dominated by the scalars $f_0 + a_0^0$ and a_0^0 for the K^+K^- and $\eta\pi^0$ channel respectively, there is a strong correlation between the two cross sections. This is shown in Fig. 3.26, where the ratio of the normalized cross sections $\tilde{\sigma}_{K^+K^-}$ and $\tilde{\sigma}_{\eta\pi^0}$ (red dots) are plotted. The shown ratios result from our fits and satisfy $\chi^2/\text{d.o.f.} < 1.6$ (corresponding to $\chi^2/\text{d.o.f.} \lesssim \chi_{\min}^2 + 1$). The current Belle measurement $\tilde{\sigma}_{K^+K^-} = 0.11_{-0.03}^{+0.04}$ [91] is shown as a shaded (blue) band on this figure. Our model is in agreement

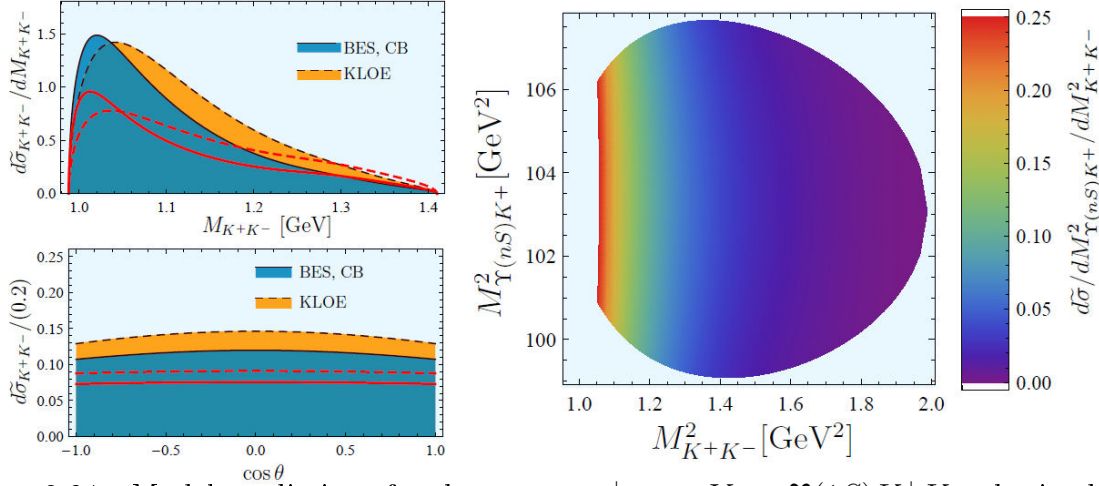


Figure 3.24: Model predictions for the process $e^+e^- \rightarrow Y_b \rightarrow \Upsilon(1S)K^+K^-$ obtained from the fit to the dipion spectra for different Flatté couplings BES, CB (solid, blue) and KLOE (dashed, orange). To the left, the M_{K+K^-} (upper left) and $\cos\theta$ (lower left) spectra are shown. The shaded curves represent the model predictions, and the red lines show the contributions without the continuum terms. To the right the Dalitz plot is shown for the BES, CB values.

with the Belle measurement, though there is a tendency in the fits to yield larger values for $\tilde{\sigma}_{K+K^-}$. The predictions will be further tested as and when the cross section $\tilde{\sigma}_{\eta\pi^0}$ is measured.

Errors are very difficult to quantify. The usual errors, calculated for example by ROOT, are only given for one local minimum of the fit parameters, in which the variation within $\chi^2_{min} + 1$ is taken into account. These errors are very small since other local minima, which yield different fit values, are ignored. Taking all minima in the given χ^2 range into account seems to be a reasonable choice. However, the entity of minima returned by the program strongly depends on the fitting routine and moreover non-minima configurations might yield larger errors. As can be seen in Fig. 3.26, the errors are sizable and certainly larger than the variation due to the different input parameters from BES, CB and KLOE. In conclusion, noticing, that we have neglected the SU(3)-breaking effects, the normalized cross section is in the region $1.0 \leq \tilde{\sigma}_{\eta\pi^0} \leq 2.0$.

Finally, I note that the states $\Upsilon(1S)K^+K^-$ and $\Upsilon(1S)K^0\bar{K}^0$ are produced by the underlying mechanism $e^+e^- \rightarrow Y_{[bu]} \rightarrow \Upsilon(1S)K^+K^-$ and $e^+e^- \rightarrow Y_{[bd]} \rightarrow \Upsilon(1S)K^0\bar{K}^0$. Hence, a firm prediction is

$$\frac{\sigma_{\Upsilon(1S)K^+K^-}}{\sigma_{\Upsilon(1S)K^0\bar{K}^0}} = \frac{Q_{[bu]}^2}{Q_{[bd]}^2} = \frac{1}{4}. \quad (3.8.40)$$

This relation is valid under the assumption that the diquarks are pointlike. In terms of the mass eigenstates, we predicted $\sigma_{\Upsilon(1S)K^+K^-} = \sigma_{\Upsilon(1S)K_S K_S}$. Using the same argument for the two-body final states B^+B^- and B^0, \bar{B}^0 , and taking into account, that the $\Upsilon(5S)$ also contributes to this decay channel with an enhanced production rate, which is given by $\Gamma(\Upsilon(5S) \rightarrow e^+e^-) = 0.31 \pm 0.07$ keV, one finds

$$\frac{\sigma_{B^+B^-}}{\sigma_{B^0\bar{B}^0}} \approx 1 - \frac{0.2}{\kappa^2 + 0.27}. \quad (3.8.41)$$

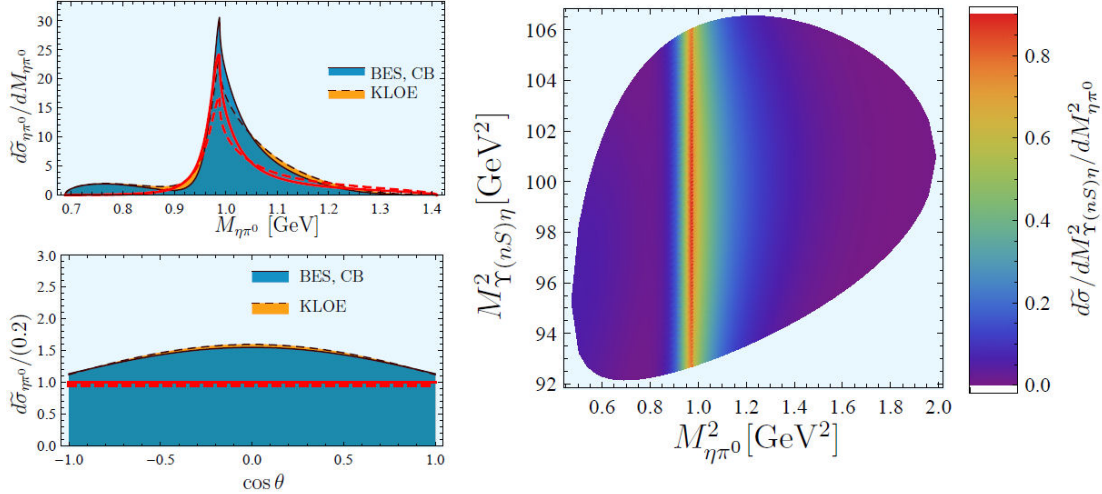


Figure 3.25: Model predictions for the process $e^+e^- \rightarrow Y_b \rightarrow \Upsilon(1S)\eta\pi^0$ obtained from the fit to the dipion spectra for different Flatté couplings BES, CB (solid, blue) and KLOE (dashed, orange). To the left, the $M_{\eta\pi^0}$ (upper left) and $\cos\theta$ (lower left) spectra are shown. The shaded curves represent the model predictions, and the red lines show the contributions without the continuum terms. To the right the Dalitz plot is shown for the BES, CB values.

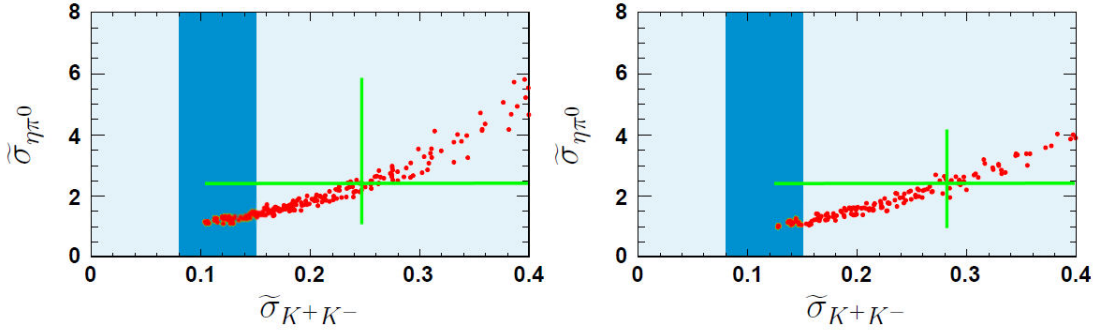


Figure 3.26: Predictions for the correlations of the total cross sections $\sigma(e^+e^- \rightarrow \Upsilon(1S)K^+K^-)$ and $\sigma(e^+e^- \rightarrow \Upsilon(1S)\eta\pi^0)$ obtained from the fit to the dipion spectra for different Flatté couplings BES, CB (left) and KLOE (right). Shown are the best fits of $\mathcal{O}(5000)$ fits, which satisfy $\chi^2 < \chi^2_{min} + 1$. The shaded blue band shows the current Belle measurement $\tilde{\sigma}_{K^+K^-} = 0.11^{+0.04}_{-0.03}$ [91]. The best fit is indicated by the green cross, in which the bars correspond to the spread in the predictions for the cross sections.

The dimeson channel $B^0\bar{B}^0$ has therefore a 10% enhanced production rate compared to B^+B^- for $\kappa^2 = 0.5$ when the background production is well-accounted for.

Chapter 4

Conclusions and outlook

In this chapter I summarize the results of the work on the b -baryon LCDAs and the $[bq][\bar{b}\bar{q}]$ -tetraquarks, presented in my thesis, and give an outlook of promising future projects and relevant experimental results anticipated in the near future, which may decide the fate of the hidden bottom tetraquarks.

LCDAs

In Chap. 2, I presented the LCDAs of single-bottom-baryons, derived in collaboration with Ahmed Ali and Alexander Parkhomenko. We aim to publish our results in early 2011. As shown in Fig. 2.4 we were able to obtain the LCDAs for the entire ground state multiplets of the single-bottom-baryons, thereby generalizing the work of Ball, Braun and Gardi [46]. We accounted for the mass-breaking effects due to the strange-quark mass and calculated the evolution of the LCDAs with the use of renormalization group equations, obtained from the one-loop renormalization of the non-local light-cone operators, given in Eqs. (2.2.8) and (2.2.9), which define the LCDAs. The decay constants f_{H_b} , which are local objects and have been determined for the different hadronic states at LO and NLO [52]_{p. 1, Tab. 2} are also taken into account. The resulting LCDAs are plotted in Figs. 2.11 and 2.12, in which the evolution from $\mu = 1$ GeV to $\mu = 2.5$ GeV and our error estimates are also shown. We find, that the $SU(3)_F$ breaking effects are of order 10 percent. The sources for the $SU(3)_F$ breaking are the strange-quark mass $m_s \approx 128$ MeV, the borel parameter τ , the momentum cutoff s_0 and the non-local condensates. The difference coming from the non-local condensates has its origin in the difference of the local condensates of dimension 3 and 5. We used $\langle \bar{s}s \rangle \approx 0.8 \langle \bar{u}u \rangle$ [58]_{p. 9} and $\langle : \bar{s}D^2s : \rangle \approx 1.3 \langle : \bar{q}D^2q : \rangle$. The latter one is, as already mentioned, not well determined. However, the mass-breaking effects appear in the lower part of the energy spectrum in the region of the constituent s -quark mass, as expected.

The major problem in using the LCDAs are the large errors of the model parameters. Even though the $SU(3)_F$ breaking effects appear to be quite large at some momenta, they are within the conservative error bars of the massless case, as is the evolution to the energy scale $\mu = 2.5$ GeV. The errors are obtained by varying the parameter A , which drives the linear superposition of the two local interpolating currents, defined in Eq. (2.3.2). For

$A = 0$, the baryon is approximated by the first interpolating current and by varying A from 0 to 1. Eventually the first current vanishes and the baryon is interpolated by the second current. The most conservative error estimate is then obtained by varying A in the full possible range $[0, 1]$. Reducing the variation of A to the less conservative range $[0.3, 0.7]$ results in a variation of the distribution amplitudes of roughly the same size as the evolution to $\mu = 2.5$ GeV.

In the calculations of the baryonic properties, like form factors, weak and strong decays, a better parametrization of the local interpolating currents, which are the roots of the large errors in Fig. 2.12 and our results presented in the Tabs. B.6.1 to B.6.6 in App. B.6 in Sec. 2.3, is desirable. The same applies also to the LCDAs of the Λ_b -baryon introduced in [46]. An attempt to improve this derivation and to reduce the effects of the interpolating currents, for the use in calculations of the weak-baryon decays and for the derivation of the baryonic form factors, is currently undertaken by Ahmed Ali, Aoife Bharucha, Wei Wang, Yuming Wang and myself. Once this is accomplished, the work may pave the way for many other interesting analysis, such as the calculation of semileptonic and purely hadronic two-body decays of the b -baryon in improved factorization methods. This will be necessary, since the LHCb experiment will measure many baryonic decay modes with improved statistics and higher precision, thus longing for better theoretical predictions. To what extent the LCDAs provide enough precision to accomplish those tasks, and in which areas further improvement is needed, will become clear in the future.

Tetraquarks

My work in the $[bq][\bar{b}\bar{q}]$ -tetraquark sector is outlined in Chap. 3. Due to its exploratory nature some of the results need an elaborated discussion, as given below. In collaboration with Ahmed Ali, Ishtiaq Ahmed and Muhammad Jamil Aslam [43], I calculated the hidden bottom tetraquark masses in a constituent Hamiltonian quark model and estimated the hadronic two-body partial decay widths for the 1^{--} iso-doublet states, labeled $Y_b^{(n)}$, as discussed in Sec. 3.4 to 3.7. Our results for the tetraquark mass spectra and the two-body partial decay widths are shown in Fig. 3.15 and Tab. C.8.1 respectively. We introduced a specific hadronic size parameter κ , taking into account the larger sizes of the hidden bottom tetraquarks compared to the typical sizes of the bottomonia states in the same energy region. We expect the tetraquarks to be larger in size due to a weaker string tension and the non-zero diquark size and estimate κ to lie in the range $1/2 < \kappa < 1$. For $Y_b^{(1)}$ we obtained a total decay width of $\Gamma(Y_b^{(1)}) \approx \kappa^2 40$ MeV, which indicates that the tetraquark hadrons have a similar (but slightly larger) hadronic size compared to $\Upsilon(5S)$, which has a total decay width roughly within a factor 2. An open issue in the mass calculations for the tetraquark states involving the *bad* diquarks is the little-known *bad* diquark mass. Those calculations should be updated once the mass splitting (3.4.29) between the heavy *good* and *bad* diquarks is known more precisely, as discussed in Sec. 3.4.2. The $Y_b^{(1)}$ is however only composed of *good* diquarks and is therefore not affected by this uncertainty. Also in the mass estimate, the smallness of the spin coupling parameter $K_{bq} = 6$ MeV, listed in Tab. 3.4.3, is puzzling, since it is found to be surprisingly small compared to $K_{bs} = 25$ MeV and $K_{bc} = 10$ MeV. Usually we would expect increasing spin coupling for decreasing light-quark mass, as suggested by the heavy-quark effective theories. Since we fixed our diquark mass to reproduce the mass $m_{Y_b^{(1)}} = 10.89$ GeV found by the Belle group according to

Eq. (3.4.28) our estimated constituent diquark mass of $m_{[bq]} \approx 5.251$ GeV in (3.4.13) will shift upwards, yielding even better agreement with the constituent diquark mass [35], as discussed in Sec. 3.4.1. The resulting change of the tetraquark masses (of all but the $Y_b^{(1)}$ mass) will be within our error estimates of $\mathcal{O}(30$ MeV).

Since the hidden bottom tetraquarks, unlike their lighter relatives in the charm and light-quark sector are too heavy to be produced in B -meson decays, we focus on 1^{--} tetraquarks (and $Y_b^{(1)}$ in particular), which have the right quantum numbers to be produced directly in the e^+e^- annihilation processes. Ahmed Ali, Satoshi Mishima and I were able to calculate the Van Royen-Weisskopf formula for the 1^{--} tetraquark states. This formula is a crucial input to estimate the e^+e^- production rates. We showed, that under the assumption of pointlike diquarks, the $Y_b^{(n)}$ states can be produced in e^+e^- reactions with sufficient statistics. I presented our result in Sec. 3.5, in which the partial electronic decay widths are estimated to be of $\mathcal{O}(50$ eV).

Knowing these important tetraquark characteristics, we undertook a fit to the $e^+e^- \rightarrow b\bar{b}$ cross section between $\sqrt{s} = 10.54$ and 11.20 GeV, measured by BaBar [93], and presented a case for the observation of the hidden $b\bar{b}$ -tetraquark states. The fit with good $\chi^2/\text{d.o.f.} = 88/67$ is plotted in Fig. 3.18 and the fit values are listed in Tab. 3.7.1. Our analysis is compatible with a $J^{PC} = 1^{--}$ state $Y_{[bq]}(10900)$ having a width of about 30 MeV. We were able to identify a suppressed resonant structure near the $\Upsilon(5S)$ peak for the lowest 1^{--} tetraquark state $Y_b^{(1)}$ but not for the higher state $Y_b^{(2)}$ consisting of a *good* and a *bad* diquark, whose mass is also estimated to be in the energy range of the measured BaBar data. This is not very surprising, as discussed in Sec. 3.7, especially due to the little-known *bad* diquark. The suppression by one order of magnitude in the electronic decay width of the $Y_b^{(n)}$, compared to the $\Upsilon(5S)$, directly leads to a suppression in an inclusive energy scan, which is the main reason for the challenge in their discovery in the inclusive data on R_b . We also found additional fits with similar $\chi^2/\text{d.o.f.}$, which do not show the resonant structure seen in Fig. 3.18 (right frame). Thus the BaBar R_b -fit is suggestive but not conclusive. Finer energy steps may be able to resolve the structure seen at this mass in terms of two mass eigenstates, split by about 6 MeV, and a Belle R_b -scan might help to confirm the existence of the state $Y_{[bq]}$ visible in the analysis presented in Sec. 3.7. As the decays $Y_{[bq]} \rightarrow B_s^{(*)}\bar{B}_s^{(*)}$ are not allowed, restricting the final states in R_b to the $B_q^{(*)}\bar{B}_q^{(*)}$ ($q = u, d$), into which $Y_{[bq]}$ decay, will also reduce the background to the $Y_{[bq]}$ signal. It is important to check that the characteristics of $Y_{[bq]}$ (mass, full width and electronic width) match those of the Y_b , measured in the exclusive process $e^+e^- \rightarrow Y_b \rightarrow \Upsilon(1S, 2S) \pi^+\pi^-$. This may solve one of the outstanding mysteries in the $\Upsilon(nS)$ physics, though this issue might have to wait for the higher precision and increased statistics of the next-generation B-factories, the SuperB in Frascati and the Super Belle in Japan.

The energy resolution of the e^+e^- accelerators is usually of the order of 5 MeV, making a search for nearby overlapping resonances in inclusive data cumbersome. Interference effects might be visible, but on the theoretical side the modeling of three overlapping resonances in the $\Upsilon(5S)$ region, namely $\Upsilon(5S)$ and the mass eigenstates $Y_{[bl]}^{(1)}$ and $Y_{[bh]}^{(1)}$, is sophisticated. This is a topic which might be addressed in future works, also in combination with a simultaneous fit to the \sqrt{s} scan of the Belle group [94]_{Fig. 2} for the exclusive data for the production $e^+e^- \rightarrow \Upsilon(nS)\pi^+\pi^-$. It is not clear if one can sufficiently account for the resonance overlap and the possibility of fitting exclusive and inclusive cross

sections simultaneously, especially regarding the suppression of the tetraquark resonance in the inclusive data due to the rare production. Together with Ahmed Ali and Satoshi Mishima, I am currently investigating this possibility. The conclusion thus far is, that the most promising approach to gain evidence for the hidden bottom tetraquarks is found in the analysis of the exclusive measurements in e^+e^- production for a tetraquark composed of *good* diquarks, due to the bottomonia and background pollution in the inclusive decays. Thus the hidden bottom tetraquark case will most likely be decided in the exclusive transitions $e^+e^- \rightarrow Y_b^{(1)} \rightarrow \text{hadrons}$.

The exclusive three-body final states $\Upsilon(1S)(\pi^+\pi^-, K^+K^-, \eta\pi^0)$ are studied in Sec. 3.8. We were able to develop a model, presented in Sec. 3.8.1, which describes the e^+e^- production of the final states via $Y_b^{(1)}$ tetraquark resonance interchange in the s -channel. The model fit to the invariant-mass and helicity spectra, measured by Belle for the process $e^+e^- \rightarrow Y_b^{(1)} \rightarrow \Upsilon(1S)\pi^+\pi^-$, yields good results with $\chi^2/\text{d.o.f} \approx 1.5$, discussed in Sec. 3.8.2. The fits are manifestly dominated by the exchange of the meson $f_2(1270)$ and intermediate light 0^{++} resonances, which are, very probably, tetraquarks themselves (see Sec. 3.2). Using the knowledge of the values for the couplings of the intermediate resonances and the strength of the continuum contributions, we predicted the spectra for the processes $e^+e^- \rightarrow Y_b^{(1)} \rightarrow \Upsilon(1S)(K^+K^-, \eta\pi^0)$ and the resulting total cross sections, normalized to the experimental cross section $\sigma(e^+e^- \rightarrow \Upsilon(1S)\pi^+\pi^-)$. We are in agreement with the reported ratio $\sigma(e^+e^- \rightarrow \Upsilon(1S)\pi^+\pi^-)/\sigma(e^+e^- \rightarrow \Upsilon(1S)K^+K^-) = 0.11_{-0.03}^{+0.04}$, measured by Belle. The definite predictions made for the spectra of these channels, shown in Figs. 3.24 and 3.25 are characteristically different from what has been seen in the prominent $\Upsilon(nS)$ decays and show a clear resonant shape, which should be visible even for reduced signal yield. The spectra for the $\Upsilon(1S)(K^+K^-, \eta\pi^0)$ states and the cross section for $\Upsilon(1S)\eta\pi^0$ are yet not available from experiments due to low statistics. This will improve once the data taken by Belle during the first half of 2010 is made public. The predicted appearance of the resonances in the measured spectra will be a clear indication in favor of our tetraquark interpretation. Sufficient data may provide also enough statistics to undertake an analysis in the end-region of $M_{\pi^+\pi^-}$ to probe the angular distribution of $f_2 \rightarrow \pi^+\pi^-$.

Another test for the tetraquark picture is the ratio $\sigma_{\Upsilon(1S)K^+K^-}/\sigma_{\Upsilon(1S)K^0\bar{K}^0} = Q_{[bu]}^2/Q_{[bd]}^2 = 1/4$ and in terms of the mass eigenstates $\sigma_{\Upsilon(1S)K^+K^-} = \sigma_{\Upsilon(1S)K_S K_S}$. This is a distinctive feature in the tetraquark picture under the assumptions of pointlike diquarks and the tetraquark dominance in the three-body decays. This peculiarity is not present for the bottomonia states, since the light-quark pairs for the final states are produced in the isospin-invariant strong interaction, while for the tetraquarks, they are produced in the e^+e^- production, thus breaking isospin invariance, which is also the case for the B^+B^- and B^0, \bar{B}^0 two-body production rates. These decays are, however, overlaid by the production via $\Upsilon(5S)$, which leads to a suppression of the charged B^+B^- production. We predict a 10% increased production rate of the B^0, \bar{B}^0 compared with B^+, B^- when the background contributions are well-accounted for. In conclusion, the distributions, cross sections, and correlations presented here and published in [44] and [90] are crucial tests of the underlying tetraquark hypothesis in the $b\bar{b}$ sector and go well beyond what has been proposed in the literature to understand the nature of the $Y_b(10890)$ state. If the tests support our inference, the $Y_b^{(1)}$ state will be the first tetraquark in the bottom sector.

The future projects concerning the studies of the hidden bottom tetraquarks will depend on the outcome of the analysis of the Belle data. If the measurements are in agreement with our predictions, several topics need further and improved calculations, and yet others might be valuable if the matter remains undecided. For the latter case, the production of tetraquarks at the LHC, which will be measured at the LHC*b*-experiment, is an interesting task. It will open the door to appraise the tetraquark hypothesis with the high statistics data provided by the LHC in the near future. However, the production process through proton-proton collisions is more involved, than the e^+e^- production observed at BaBar or Belle and requires for example the use of Monte-Carlo techniques.

If the tetraquark picture is proven to be correct, the computation of tetraquark masses with the use of QCD-sum-rules at next-to-leading order will be an interesting extension of the constituent quark model calculations. Also the parton distributions of the tetraquarks will be necessary to enhance the accuracy in the calculations of tetraquark decay rates. Several approaches are possible, for example the generalization of the well-known quarkonium models or a calculation in the framework of QCD-sum-rules. In the former, the simplest first step might be a product ansatz in the diquark-diquark wave functions and the quark-quark (antiquark-antiquark) wave functions. The study of the wave functions will become especially important, if the approximation of pointlike diquarks is found to be inadequate.

If the existence of the constituents of the tetraquarks, the diquarks and antidiquarks, is confirmed and well established in all quark sectors, effective methods to describe their dynamics need to be developed, which will open an entire new field in the theory of strong interactions. Similar to pion exchange between the baryons in a nucleus they could be mediators of forces and provide crucial input to different multiquark scenarios such as fragmentation functions in heavy-ion collisions.

Concluding, our predictions will be scrutinized soon in the existing and the forthcoming Belle data to which we look forward. The analysis will hopefully decide the fate of the bottom tetraquarks, pointing out future research directions in this field.

Appendix A

Summary of definitions and useful relations

I use the metric in the “mostly minus” convention

$$g_{\mu\nu} = g^{\mu\nu} = \begin{pmatrix} 1 & 0 & 0 & 0 \\ 0 & -1 & 0 & 0 \\ 0 & 0 & -1 & 0 \\ 0 & 0 & 0 & -1 \end{pmatrix}. \quad (\text{A.0.1})$$

The Pauli matrices are defined as

$$\sigma^1 = \begin{pmatrix} 0 & 1 \\ 1 & 0 \end{pmatrix}, \quad \sigma^2 = \begin{pmatrix} 0 & -i \\ i & 0 \end{pmatrix}, \quad \sigma^3 = \begin{pmatrix} 1 & 0 \\ 0 & -1 \end{pmatrix}. \quad (\text{A.0.2})$$

In the *Weyl* or *chiral* basis the Dirac matrices are given by

$$\gamma^\mu = \begin{pmatrix} 0 & \sigma^\mu \\ \bar{\sigma}^\mu & 0 \end{pmatrix}, \quad \gamma^5 = \begin{pmatrix} -1 & 0 \\ 0 & 1 \end{pmatrix} \quad (\text{A.0.3})$$

with $\sigma^\mu = (1, \boldsymbol{\sigma})$ and $\bar{\sigma}^\mu = (1, -\boldsymbol{\sigma})$, and the charge conjugation in the same basis is given by

$$C = i\gamma_2\gamma_0 = \begin{pmatrix} -1 & 0 & 0 & 0 \\ 0 & 1 & 0 & 0 \\ 0 & 0 & -1 & 0 \\ 0 & 0 & 0 & 1 \end{pmatrix}. \quad (\text{A.0.4})$$

The free propagator of a massive scalar particle with mass m in D -dimensional (Euclidean) space-time [53]_{eq 7} is given by

$$D(x, m) = \frac{1}{(2\pi)^D} \int \frac{e^{i(p \cdot x)} d^D p}{p^2 + m^2} = \frac{(mx)^\lambda K_\lambda(mx)}{(2\pi)^{\lambda+1} x^{2\lambda}} \quad (\text{A.0.5})$$

with $D = 2\lambda + 2$ and $K_\lambda(z)$ is the modified Bessel function of the second kind

$$K_\lambda(z) = \frac{\pi I_{-\lambda}(z) - I_\lambda(z)}{2 \sin(\pi\lambda)}, \quad \Gamma(\lambda)\Gamma(1-\lambda) = \frac{\pi}{\sin(\pi\lambda)}, \quad (\text{A.0.6})$$

in which

$$I_\lambda(z) = \left(\frac{z}{2}\right)^\lambda \sum_{k=0}^{\infty} \frac{(z^2/4)^k}{k! \Gamma(\lambda + k + 1)} \quad (\text{A.0.7})$$

is the modified Bessel function of the first kind.

A.1 The Dirac field

Using the formalism developed in the canonical quantization method, where a fermionic (antifermionic) field Ψ ($\bar{\Psi}$) in one variable t can be expanded as [112]_{p. 58}

$$\begin{aligned} \Psi(t)_\alpha &= \int \frac{dp}{2\pi} \frac{1}{\sqrt{2E_p}} \sum_s (a_p^s u_\alpha^s(p) e^{-ipt} + b_p^{s\dagger} v_\alpha^s(p) e^{ipt}), \\ \bar{\Psi}(t)_\alpha &= \int \frac{dp}{2\pi} \frac{1}{\sqrt{2E_p}} \sum_s (a_p^{s\dagger} \bar{u}_\alpha^s(p) e^{ipt} + b_p^s \bar{v}_\alpha^s(p) e^{-ipt}), \end{aligned} \quad (\text{A.1.1})$$

in which $a_p^{s\dagger}$ ($b_p^{s\dagger}$) creates a fermion (antifermion). The similar expression holds for the expansion in three space-time coordinates:

$$\Psi(\mathbf{x})_\alpha = \int \frac{d^3p}{(2\pi)^3} \frac{1}{\sqrt{2E_{\mathbf{p}}}} \sum_s (a_{\mathbf{p}}^s u_\alpha^s(\mathbf{p}) e^{-i\mathbf{x}\cdot\mathbf{p}} + b_{\mathbf{p}}^{s\dagger} v_\alpha^s(\mathbf{p}) e^{i\mathbf{x}\cdot\mathbf{p}}), \quad (\text{A.1.2})$$

and similar for $\bar{\Psi}$. A fermion is created from the vacuum by

$$|p, s\rangle \equiv \sqrt{2E_{\mathbf{p}}} a_{\mathbf{p}}^{s\dagger} |0\rangle \quad (\text{A.1.3})$$

with momentum \mathbf{p} and energy $E_{\mathbf{p}}$. The index s refers to the spinor basis spanned by $u_\alpha^s(\mathbf{p})$. The creation and annihilation operators obey the well known anticommutation relations

$$\{a_{ip}^{f_1 r}, a_{jq}^{f_2 s\dagger}\} = 2\pi\delta(p-q)\delta^{rs}\delta_{ij}\delta^{f_1 f_2} \quad \text{or} \quad \{a_{ip}^{f_1 r}, a_{jq}^{f_2 s\dagger}\} = (2\pi)^3\delta(\mathbf{p}-\mathbf{q})^{(3)}\delta^{rs}\delta_{ij}\delta^{f_1 f_2}, \quad (\text{A.1.4})$$

in which f_i indicates the type of the particle. In the following these and color indices will be omitted.

For three dimensions, the spinors are in the chiral basis given by

$$u_s(\mathbf{p}) = \begin{pmatrix} \sqrt{\mathbf{p}\cdot\boldsymbol{\sigma}}\xi^s \\ \sqrt{\mathbf{p}\cdot\bar{\boldsymbol{\sigma}}}\xi^s \end{pmatrix}, \quad v_s(\mathbf{p}) = \begin{pmatrix} \sqrt{\mathbf{p}\cdot\boldsymbol{\sigma}}\eta^s \\ -\sqrt{\mathbf{p}\cdot\bar{\boldsymbol{\sigma}}}\eta^s \end{pmatrix} \quad s = 1, 2, \quad (\text{A.1.5})$$

in which $\eta^s = -i\sigma^2(\xi^s)^*$. By choice of basis $\xi^1 = (1, 0)^T$ and $\xi^2 = (0, 1)^T$. The two vectors denote spin up and spin down along the z -axis respectively. Both spinors can

combine to spin 1 or spin 0, in which the symmetric combinations gives the former and the antisymmetric combination gives the latter multiplet:

$$\eta_\beta^{r\dagger} \xi_\alpha^s = \begin{cases} -\frac{1}{\sqrt{2}} \begin{pmatrix} 1 & 0 \\ 0 & 1 \end{pmatrix}_{\alpha\beta} = -\frac{1_{\alpha\beta}}{\sqrt{2}} & \{0, 0\} \text{ for } \frac{[(1,2)-(2,1)]}{\sqrt{2}} \\ \hline \begin{pmatrix} 0 & 1 \\ 0 & 0 \end{pmatrix}_{\alpha\beta} = -\frac{\mathbf{n} \cdot \boldsymbol{\sigma}_{\alpha\beta}}{\sqrt{2}} & \{1, 1\} \text{ for } (1, 1) \text{ with } \mathbf{n} = -\frac{\hat{e}_x + i\hat{e}_y}{\sqrt{2}} \\ -\frac{1}{\sqrt{2}} \begin{pmatrix} 1 & 0 \\ 0 & -1 \end{pmatrix}_{\alpha\beta} = -\frac{\mathbf{n} \cdot \boldsymbol{\sigma}_{\alpha\beta}}{\sqrt{2}} & \{1, 0\} \text{ for } \frac{[(1,2)+(2,1)]}{\sqrt{2}} \text{ with } \mathbf{n} = \hat{e}_z \\ \begin{pmatrix} 0 & 0 \\ -1 & 0 \end{pmatrix}_{\alpha\beta} = -\frac{\mathbf{n} \cdot \boldsymbol{\sigma}_{\alpha\beta}}{\sqrt{2}} & \{1, -1\} \text{ for } (2, 2) \text{ with } \mathbf{n} = \frac{\hat{e}_x - i\hat{e}_y}{\sqrt{2}} \end{cases}, \quad (\text{A.1.6})$$

in which the parenthesis (a, b) correspond to the spinor polarizations ($s = a, r = b$), and $\{S, s_z\}$ gives the spin multiplet S and the spin projection along the z -axis s_z . The vector \mathbf{n} with $|\mathbf{n}|^2 = 1$ is a polarization vector of the spin 1 ground state formed by the two fermions.

The fermionic propagator in coordinate space is obtained from Eq. (A.0.5) by differentiation with respect to x^μ :

$$S_F(x-y) = \int \frac{d^4 p}{(2\pi)^4} \frac{e^{-ip \cdot (x-y)} (\not{p} + m)}{p^2 - m^2 + i\epsilon} = \left(\frac{\not{x} - \not{y}}{|x-y|^5} + \frac{m}{|x-y|^3} \right) I_1(m|x-y|) \quad (\text{A.1.7})$$

with first order mass corrections

$$S(x) = \frac{i}{2\pi^2} \frac{\not{x}}{x^4} - \frac{m}{4\pi x^2} \quad (\text{A.1.8})$$

The heavy-quark propagator in coordinate space [112]_{p. 177 ff} reads

$$i \langle T \{ h_v(x) \bar{h}_v(0) \} \rangle = \frac{1 + \not{v}}{2} \int dt \delta^4(x - vt), \quad (\text{A.1.9})$$

which is obtained from Eq. (1.0.9) with the help of

$$\int_{-\infty}^{\infty} \frac{e^{-i\omega t}}{(-\omega - i\epsilon)^n} \frac{d\omega}{2\pi} = \frac{i^n}{\Gamma(n)} t^{n-1} \Theta(t) \quad \text{and} \\ \int_0^{\infty} e^{i\omega t} t^n dt = \frac{(-i)^{n+1} \Gamma(n+1)}{(-\omega - i\epsilon)^{n+1}}. \quad (\text{A.1.10})$$

A.2 The gluon field

The vector gauge field $A^\mu(tz)^{i'}$ in one coordinate can be expanded similar to the Eqs. (A.1.2) [112]_{p. 123}:

$$A_\mu^l{}_{i'}(t) = \int \frac{dp}{2\pi} \frac{1}{\sqrt{2E_p}} \sum_{r,c} (A_p^{cr} \epsilon_\mu^r(p) t^{cl}{}_{i'} e^{-ipt} + A_p^{cr\dagger} \epsilon_\mu^{r*}(p) t^{cl}{}_{i'} e^{ipt}), \quad (\text{A.2.1})$$

in which ϵ_μ^r is the basis of polarization vectors where $r = 0, \dots, 3$, and $A_p^{rc\dagger}$ (A_p^{rc}) is the creation (annihilation) operator, which creates (annihilates) a gluon with momentum p , polarization r and color c . They obey

$$[A_p^{rc}, A_q^{sc'\dagger}] = 2\pi\delta(p-q)\delta^{rs}\delta^{cc'}. \quad (\text{A.2.2})$$

Since the gluon transforms as gauge field under the adjoint representation, which is the $\mathbf{8}_{SU(3)_c}$, the index c runs from 1 to 8. The eight matrices $t^{ci'}$ are the generators of $SU(3)$ and the indices i, i' are the color indices of the fundamental representations $\mathbf{3}_{SU(3)_c}$ and $\bar{\mathbf{3}}_{SU(3)_c}$.

A.3 Spherical harmonics

The spherical harmonics $Y_l^m(\theta, \varphi)$ with angular momentum quantum number l and projection to the z-axis m up to $l = 2$ are given by:

$$Y_0^0(\theta, \varphi) = \sqrt{\frac{1}{4\pi}}, \quad \text{spin 0}$$

$$\begin{aligned} Y_1^{+1}(\theta, \varphi) &= -\frac{1}{2}\sqrt{\frac{3}{2\pi}}\sin\theta e^{i\varphi} = -\frac{1}{2}\sqrt{\frac{3}{\pi}}\frac{x+iy}{\sqrt{2}r}, \\ Y_1^0(\theta, \varphi) &= \frac{1}{2}\sqrt{\frac{3}{\pi}}\cos\theta = \frac{1}{2}\sqrt{\frac{3}{\pi}}\frac{z}{r}, \\ Y_1^{-1}(\theta, \varphi) &= \frac{1}{2}\sqrt{\frac{3}{2\pi}}\sin\theta e^{-i\varphi} = \frac{1}{2}\sqrt{\frac{3}{\pi}}\frac{x-iy}{\sqrt{2}r}, \end{aligned} \quad \text{spin 1}$$

$$\begin{aligned} Y_2^0(\theta, \varphi) &= \sqrt{\frac{5}{16\pi}}(3\cos^2\theta - 1), \\ Y_2^{\pm 1}(\theta, \varphi) &= \mp\sqrt{\frac{15}{8\pi}}\sin\theta\cos\theta e^{\pm i\varphi}, \\ Y_2^{\pm 2}(\theta, \varphi) &= \sqrt{\frac{15}{32\pi}}\sin^2\theta e^{\pm 2i\varphi}. \end{aligned} \quad (\text{A.3.1})$$

Here the spin 1 triplet is given in two coordinate systems, spherical coordinates and Cartesian coordinates with $x = r\sin\theta\cos\varphi$, $y = r\sin\theta\sin\varphi$ and $z = r\cos\theta$. This parametrization makes the definition of the polarization vectors $\epsilon^{(m)}$ of a spin 1 state apparent:

$$\epsilon^{(m)} = \{\epsilon^{(m=+1)}, \epsilon^{(m=0)}, \epsilon^{(m=-1)}\} = \left\{ -\frac{\mathbf{e}_x + i\mathbf{e}_y}{\sqrt{2}}, \mathbf{e}_z, \frac{\mathbf{e}_x - i\mathbf{e}_y}{\sqrt{2}} \right\}. \quad (\text{A.3.2})$$

Thus by defining $\hat{x}^i \equiv x^i/r$, the spin 1 triplet can be written in terms of the polarization vector as

$$Y_1^m(\theta, \varphi) = \frac{1}{2}\sqrt{\frac{3}{\pi}}\hat{\mathbf{x}} \cdot \epsilon^{(m)}, \quad (\text{A.3.3})$$

and the wave function for a P -wave state with principal quantum number n and spin projection m can be written as

$$\Psi_{n1m}(\mathbf{x}) = \frac{1}{2} \sqrt{\frac{3}{\pi}} \hat{\mathbf{x}} \cdot \boldsymbol{\epsilon}^{(m)} R_{n1}(r) = \psi_{n1}^i(\mathbf{x}) \epsilon_i^{(m)}, \quad \text{with} \quad \psi_{n1}^i(\mathbf{x}) \equiv \frac{1}{2} \sqrt{\frac{3}{\pi}} \hat{x}^i R_{n1}(r). \quad (\text{A.3.4})$$

Some useful relations are further:

$$\begin{aligned} \int_0^{2\pi} d\varphi Y_0^{0*}(\theta, \varphi) Y_0^0(\theta, \varphi) &= \frac{1}{2}, \\ \int_0^{2\pi} d\varphi Y_0^{0*}(\theta, \varphi) Y_2^0(\theta, \varphi) &= \frac{3\sqrt{5}}{4} \left(\cos^2 \theta - \frac{1}{3} \right), \\ \int_0^{2\pi} d\varphi Y_2^{0*}(\theta, \varphi) Y_2^0(\theta, \varphi) &= \frac{45}{8} \left(\cos^2 \theta - \frac{1}{3} \right)^2, \\ \int_0^{2\pi} d\varphi Y_2^{\pm 1*}(\theta, \varphi) Y_2^{\pm 1}(\theta, \varphi) &= \frac{15}{4} \sin^2 \theta \cos^2 \theta, \\ \int_0^{2\pi} d\varphi Y_2^{\pm 2*}(\theta, \varphi) Y_2^{\pm 2}(\theta, \varphi) &= \frac{15}{16} \sin^4 \theta, \end{aligned} \quad (\text{A.3.5})$$

and in general the normalization

$$\int_{-1}^1 d\cos \theta \int_0^{2\pi} d\varphi Y_\ell^{m*}(\theta, \varphi) Y_{\ell'}^{m'}(\theta, \varphi) = \delta_{\ell\ell'} \delta_{mm'} \quad (\text{A.3.6})$$

holds.

A.4 Master integrals for renormalization

In $D = 4 - 2\epsilon$ dimensions the master integrals are given as follows:

$$\begin{aligned} I_1(\Delta) &= \int \frac{d^{D-2}l}{i(2\pi)^{D-2}} \frac{1}{l^2 - \Delta} = -\frac{1}{4\pi} \Gamma(\epsilon) \left(\frac{1}{\Delta} \right)^\epsilon, \\ I_2(\Delta) &= \int \frac{d^{D-2}l}{i(2\pi)^{D-2}} \frac{l^2}{l^2 - \Delta} = \frac{1}{4\pi} (1 - \epsilon) \Gamma(-1 + \epsilon) \left(\frac{1}{\Delta} \right)^{-1+\epsilon}, \\ I_3(\Delta) &= \int \frac{d^{D-2}l}{i(2\pi)^{D-2}} \frac{1}{(l^2 - \Delta)^2} = \frac{1}{4\pi} \Gamma(1 + \epsilon) \left(\frac{1}{\Delta} \right)^{1+\epsilon} \quad \text{UV finite}, \\ I_4(\Delta) &= \int \frac{d^{D-2}l}{i(2\pi)^{D-2}} \frac{l^2}{(l^2 - \Delta)^2} = -\frac{1}{4\pi} (1 - \epsilon) \Gamma(\epsilon) \left(\frac{1}{\Delta} \right)^\epsilon = (1 - \epsilon) I_1, \\ I_5(\Delta) &= \int \frac{d^{D-2}l}{i(2\pi)^{D-2}} \frac{l^4}{(l^2 - \Delta)^2} = \frac{i}{4\pi} (1 - \epsilon)(2 - \epsilon) \Gamma(\epsilon - 1) \left(\frac{1}{\Delta} \right)^{\epsilon-1}, \\ I_6(\Delta) &= \int \frac{d^{D-2}l}{i(2\pi)^{D-2}} \frac{l_\mu l_\nu}{(l^2 - \Delta)^2} = -\frac{i g_{\mu\nu}}{8\pi} \Gamma(\epsilon) \left(\frac{1}{\Delta} \right)^\epsilon = \frac{g_{\mu\nu}}{2} I_1, \\ J_1(\Delta) &= \int_0^\infty \frac{dx}{(x + \Delta)^{1+\epsilon}} = \frac{\Gamma(\epsilon)}{\Delta^\epsilon}, \end{aligned}$$

$$J_2(\Delta) = \int_0^\infty \frac{x dx}{(x + \Delta)^{1+\epsilon}} = \frac{\Gamma(\epsilon - 1)}{\Delta^{\epsilon-1}}, \quad (\text{A.4.1})$$

and

$$\int_0^\infty \frac{t^{x-1} dt}{(\Delta + t)^{x+y}} = \frac{1}{\Delta^y} \int_0^\infty \frac{t^{x-1} dt}{(1+t)^{x+y}} = \frac{1}{\Delta^y} \frac{\Gamma(x)\Gamma(y)}{\Gamma(x+y)}. \quad (\text{A.4.2})$$

Several quantities above can be expanded in a series in ϵ for epsilon close to 0:

$$\frac{1}{\epsilon \Delta^\epsilon} = \frac{1}{\epsilon} - \log(\Delta) + \frac{1}{2} \log^2(\Delta) \epsilon + O(\epsilon^2) \quad (\text{A.4.3})$$

$$\Gamma(\epsilon) = \frac{1}{\epsilon} - \gamma + O(\epsilon) \quad \left(\frac{1}{\Delta}\right)^\epsilon = 1 - \epsilon \log \Delta \quad (\text{A.4.4})$$

and

$$\Gamma(x) = \frac{(-1)^n}{n!} \left(\frac{1}{x+n} - \gamma_E + 1 + \dots + \frac{1}{n} + \mathcal{O}(x+n) \right) \quad (\text{A.4.5})$$

near $x = -n$, in which γ_E is the Euler constant.

Feynman parameters are useful to rewrite the integrations in terms of the master integrals. They are defined by:

$$\frac{1}{A_1 \dots A_n} = \int_0^1 dx_1 \dots dx_n \delta\left(\sum x_i - 1\right) \frac{(n-1)!}{[x_1 A_1 + \dots x_n A_n]^n}. \quad (\text{A.4.6})$$

Appendix B

b-baryon LCDAs

This appendix contains several calculations and detailed explanations necessary for the discussion of the LCDAs in Chap. 2. The order of the sections follows the order of the appearance of the corresponding topics in the main work.

B.1 The Borel transform

The Borel transform $E \rightarrow \tau$ is defined as

$$\mathbb{B}[f(E)](\tau) = \lim_{\substack{n \rightarrow \infty \\ E \rightarrow \infty \\ E/n = \tau}} \frac{E^{n+1}}{n!} \left(-\frac{d}{dE} \right)^n f(E), \quad (\text{B.1.1})$$

such that

$$\begin{aligned} \mathbb{B} \left[\int_0^\infty dt e^{\pm it(-i\epsilon + \Omega + E)} \frac{1}{t^x} \right] &= \lim_{\substack{n \rightarrow \infty \\ E \rightarrow \infty \\ E/n = \tau \\ \epsilon \rightarrow 0}} \int_0^\infty dt \frac{i^n e^{\pm t(\epsilon + i(\Omega + E))} t^{n-x} E^{n+1}}{n!}, \\ &= i^{\pm(-x+1)} e^{-\frac{\Omega}{\tau} \tau^x}, \\ &= \frac{i^{\pm(-x+1)}}{\Gamma(x)} \int_\Omega^\infty ds e^{-\frac{s}{\tau}} (s - \Omega)^{x-1}. \end{aligned} \quad (\text{B.1.2})$$

The definition of the Borel transform in Eq. (B.1.1) is equivalent to the inverse Laplace transform. However, in the former form it becomes apparent, that the Borel transform handles the regularization of the correlation functions in Sec. 2.5 automatically, since the renormalization is applied by subtracting polynomials in E , which vanish due to the derivative of arbitrary large order. Applying the Borel transform to the sum rules, the contributions of states heavier than the ground state are exponentially suppressed. Introducing the cutoff after the application of the Borel transform, which is needed for the sum rule calculations one finds:

$$\frac{i^{\pm(-x+1)}}{\Gamma(x)} \int_\Omega^{s_0} ds e^{-\frac{s}{\tau}} (s - \Omega)^{x-1} = \frac{i^{\pm(-x+1)}}{\Gamma(x)} e^{-\frac{\Omega}{\tau} \tau^x} \left(\Gamma(x) - \Gamma\left(x, \frac{s_0 - \Omega}{\tau}\right) \right) \quad (\text{B.1.3})$$

B.2 QCD sum rules

The QCD sum rules provide a framework of techniques to gain access to the non-perturbative interaction regime $\alpha_s \gtrsim 1$, in which the energy scale is of order of the binding scale Λ_{QCD} . The characteristics of the hadron ground states can be calculated with this type of calculations. Together with lattice QCD it is among the most famous working tools in this field. An elaborated review was introduced by Colangelo and Khodjamirian [47]. Here I sketch the working principles of the QCD sum rules briefly.

The correlation function (2.5.1), defined by two interpolating operators, is given by

$$\Pi(q^2, t_1, t_2) = i \int d^4x e^{iq \cdot x} \langle 0 | O_{\Gamma\gamma}(t_1, t_2) \bar{J}_{\Gamma'\gamma'}(x) | 0 \rangle. \quad (\text{B.2.1})$$

In the heavy-quark limit, discussed in Chap. 1, the *b*-quark is moving on-shell with velocity *v*. The origin of the coordinate frame is chosen to coincide with the *b*-quark, when it is annihilated by the non-local operator $O_{\Gamma\gamma}(t_1, t_2)$. Because the *b*-quark moves as classical particle along a straight line along \mathbf{v} , at a time *t* it will be at point \mathbf{x} . Thus *t* is defined by $x_\mu = tv_\mu$ (a resting *b*-quark is also produced in the origin by the local interpolating current). The Fourier transform in time defines the energy *E*. Thus Eq. (B.2.1) simplifies to

$$\Pi(E, t_1, t_2) = i \int dt e^{iEt} \langle 0 | O_{\Gamma\gamma}(t_1, t_2) \bar{J}_{\Gamma'\gamma'}(t) | 0 \rangle. \quad (\text{B.2.2})$$

With some mathematical transformations, shown below, the correlation function $\Pi(E)$ can be rewritten in form of a hadronic dispersion relation and by using the operator product expansion. These two formulations are then used to derive the sum rule.

Using the analytic continuation of the correlation function $\Pi(E)$ on the contour plotted in Fig. B.1 one gets

$$\begin{aligned} \Pi(E, t_1, t_2) &= \frac{1}{2\pi i} \int_C dz \frac{\Pi(z, t_1, t_2)}{z - E} \\ &= \frac{1}{2\pi i} \int_{|z|=R} dz \frac{\Pi(z, t_1, t_2)}{z - E} + \frac{1}{2\pi i} \int_0^R dz \frac{\Pi(z + i\epsilon) - \Pi(z - i\epsilon)}{z - E}. \end{aligned} \quad (\text{B.2.3})$$

The correlation function at any point *E* (green cross) is linked to the hadronic dispersion relation (brown shades) for the on-shell states, pictured in Fig. B.1. The first term vanishes at $R = \infty$ and according to the Schwarz reflection principle:

$$\Pi(E, t_1, t_2) = \frac{1}{\pi} \int_0^\infty ds \frac{\text{Im}(\Pi(s, t_1, t_2))}{s - E - i\epsilon}, \quad (\text{B.2.4})$$

where the hadronic bound states lie on the positive real axis. The lowest bound state is indicated in the density plot in Fig. B.1 by the vertical line and the red cross. In general, there are a couple of such discrete bound states, which blend into the hadronic

continuum (brown shade) at some higher excitation energy. In the sum of discrete states, every contribution is accompanied by a delta function $\delta(E_n - s)$. The first term in the sum, which corresponds to the ground state can be extracted by shifting the integration boundary upwards to $s_0 > \bar{\Lambda}$. This gives the hadronic dispersion relation

$$\Pi(E, t_1, t_2) = \frac{|f|^2 \Psi(t_1, t_2)}{\bar{\Lambda} - E} + \int_{s_0 > \bar{\Lambda}}^{\infty} ds \frac{\text{Im}(\Pi(s, t_1, t_2))}{s - E}. \quad (\text{B.2.5})$$

The perturbative contribution can not account for the soft contributions of the partons, which are interacting with the QCD vacuum. Those vacuum fields induce long-distant effects, while the short distance is described by the perturbative contributions. Thus the correlation function is, as described in Sec. 2.5, calculated with the use of the propagators in the QCD background.

In summary one finds two formulations of the correlation function:

$$\begin{aligned} \text{hadronic} & \\ \text{dispersion} & : \quad \Pi(E, t_1, t_2) = \frac{|f_{H_b}|^2 \Psi(t_1, t_2)}{\bar{\Lambda} - E} + \int_{s_0}^{\infty} ds \frac{\text{Im}(\Pi(s, t_1, t_2))}{s - E} \\ \text{relation} & \\ \text{operator} & \\ \text{product} & : \quad \Pi(E, t_1, t_2) = \frac{1}{\pi} \int ds \frac{\text{Im}(\langle O_{\Gamma} \bar{J} \rangle^{\text{pert}} + \langle O_{\Gamma} \bar{J} \rangle^{\text{cond}})(s)}{s - E} \\ \text{expansion} & \end{aligned} \quad (\text{B.2.6})$$

The spectral density includes the low lying ground state, higher excitations and the continuum. The parameter s_0 cuts off the higher excitations and the continuum, since we are only interested in the pure ground state. The quark-hadron duality is applied via assuming the approximate equality of the perturbative contributions and the density for $s > s_0$:

$$\int_{s_0}^{\infty} ds \frac{\rho(s)}{s - E} \approx \frac{1}{\pi} \int_{s_0}^{\infty} ds \frac{\text{Im}(\langle O_{\Gamma} \bar{J} \rangle^{\text{pert}})(s)}{s - E}, \quad (\text{B.2.7})$$

in which $\bar{\Lambda} = m_{H_b} - m_b$ is the effective mass of the baryon. One has to be very careful, what one calls perturbative, since there might be mixed perturbative and condensate contributions (*i.e.* diagrams in which one light-quark is described by the low energy condensates and the other light-quark is described by the high energy perturbative propagator). We adopted the procedure of [46], and call a distribution perturbative, when at least one perturbative term is present. Inserting the quark hadron duality one gets:

$$\frac{|f_{H_b}|^2 \Psi(t_1, t_2)}{\bar{\Lambda} - E} = \frac{1}{\pi} \int_0^{s_0} ds \frac{\text{Im}(\langle O_{\Gamma} \bar{J} \rangle^{\text{pert}})}{s - E} + \frac{1}{\pi} \int_0^{\infty} ds \frac{\text{Im}(\langle O_{\Gamma} \bar{J} \rangle^{\text{cond}})}{s - E} \quad (\text{B.2.8})$$

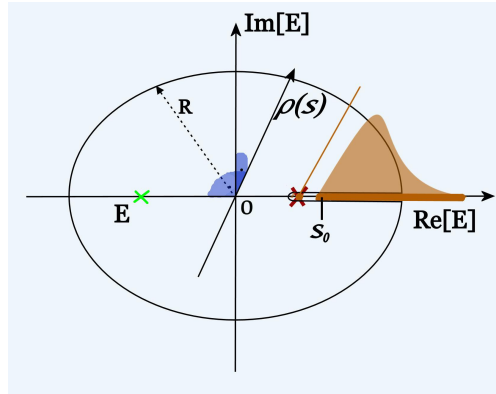


Figure B.1: Density and contour. The Correlation function $\Pi(E, t_1, t_2)$ in the complex plane at any point E (green cross) is linked to the on-shell hadronic thresholds (brown shades).

The application of the Borel transform with $\mathbb{B} \left[\frac{1}{A-E} \right] (E \rightarrow \tau) = -e^{-\frac{A}{\tau}}$ results in the sum rule to determine the desired wave functions $\Psi(t_1, t_2)$:

$$|f_{H_b}|^2 \Psi(t_1, t_2) e^{-\frac{\Lambda}{\tau}} = \frac{1}{\pi} \int_0^{s_0} ds e^{-\frac{s}{\tau}} \text{Im}(\langle \langle O_\Gamma \bar{J} \rangle \rangle^{pert}) + \frac{1}{\pi} \int_0^\infty ds e^{-\frac{s}{\tau}} \text{Im}(\langle \langle O_\Gamma \bar{J} \rangle \rangle^{cond}). \quad (\text{B.2.9})$$

B.3 Non-local vertex calculations

The explicit calculations to derive the vertex expressions corresponding to the operators defined in Eq. (2.2.3) are performed in this section. The first step is to expand the Wilson lines in (2.1.5) up to first order in the coupling g_s :

$$P \circ \left\{ e^{ig_s \int_0^{t_1} dt n_\mu A^\mu(tn)^{i'}_i} \right\} \approx \mathbb{1}^{i'}_i + ig_s \int_0^{t_1} dt n_\mu A^\mu(tn)^{i'}_i. \quad (\text{B.3.1})$$

Setting $g_s = 0$ the zeroth order operator

$$O_\Gamma^{(0)} = \epsilon^{ijk} \left[u_{i\alpha}(t_1) \Gamma^{\alpha\beta} d_{j\beta}(t_2) \right] b_{k\gamma}(0) \quad (\text{B.3.2})$$

is obtained. The first order matrix element in g_s reads

$$O_\Gamma^{(1)} = \epsilon^{i'j'k'} \left[u_{l\alpha}(t_1) ig_s \int_0^{t_1} dt n_\mu A^\mu(tn)^l_{i'} \Gamma^{\alpha\beta} d_{j'\beta}(t_2) \right] b_{k'\gamma}(0). \quad (\text{B.3.3})$$

The following results are similar to the ones given in [51]_{Fig. 3}.

B.3.1 Vertex calculations lowest order in g_s

Calculating

$$\langle 0 | O_\Gamma^{(0)} | u(k_{1+})^{s_1} d(k_{2+})^{s_2} b(E)^{s_3} \rangle \quad (\text{B.3.4})$$

to lowest order in perturbation theory gives the vertex corresponding to $O_\Gamma^{(0)}$, defined in Eq. (B.3.2). Using the Eqs. (B.3.2) to (B.3.4) and the anticommutation relations of the creation and annihilation operators one finds

$$\begin{aligned} & \langle 0 | O_\Gamma^{(0)} | u(k_{1+})^{s_1} d(k_{2+})^{s_2} b(E)^{s_3} \rangle \\ &= \langle 0 | \epsilon^{i'j'k'} \left[u_{i'\alpha}(t_1) \Gamma^{\alpha\beta} d_{j'\beta}(t_2) \right] b_{k'\gamma}(0) \sqrt{2^3 E_{k_{1+}} E_{k_{2+}} E_E} a_{ik_{1+}}^{u s_1 \dagger} a_{jk_{2+}}^{d s_2 \dagger} a_{kE}^{b s_3 \dagger} | 0 \rangle, \\ &= \langle 0 | \epsilon^{i'j'k'} \left[\int \frac{dp_1}{2\pi} \frac{1}{\sqrt{2E_{p_1}}} \sum_{r_1} a_{i'p_1}^{u r_1} u_\alpha^{r_1}(p_1) e^{-ip_1 t_1} \right. \\ & \quad \left. \int \frac{dp_2}{2\pi} \frac{1}{\sqrt{2E_{p_2}}} \sum_{r_2} a_{j'p_2}^{d r_2} u_\beta^{r_2}(p_2) e^{-ip_2 t_2} \right] \Gamma^{\alpha\beta} \end{aligned}$$

$$\int \frac{dp_3}{2\pi} \frac{1}{\sqrt{2E_{p_3}}} \sum_{r_3} \begin{matrix} b^{r_3} & b^{r_3} \\ a_{k'p_3} & u_\gamma \end{matrix} (p_3) \sqrt{2^3 E_{k_{1+}} E_{k_{2+}} E_E} \begin{matrix} u^{s_1 \dagger} & d^{s_2 \dagger} & b^{s_3 \dagger} \\ a_{ik_{1+}} & a_{jk_{2+}} & a_{kE} \end{matrix} |0\rangle. \quad (\text{B.3.5})$$

Using now the anti commutation relations (A.1.4), Eq. (B.3.5) yields

$$\begin{aligned} &= -\langle 0 | \epsilon^{i'j'k'} \left[\int dp_1 \sum_{r_1} \delta(p_1 - k_{1+}) \delta^{r_1 s_1} \delta_{ii'} u_\alpha^{r_1} (p_1) e^{-ip_1 t_1} \right. \\ &\quad \left. \int dp_2 \sum_{r_2} \delta(p_2 - k_{2+}) \delta^{r_2 s_2} \delta_{jj'} u_\beta^{r_2} (p_2) e^{-ip_2 t_2} \right] \Gamma^{\alpha\beta} \\ &\quad \left. \int dp_3 \sum_{r_3} \delta(p_3 - E) \delta^{r_3 s_3} \delta_{kk'} u_\gamma^{r_3} (p_3) |0\rangle, \right. \\ &= -\epsilon^{ijk} \left[u_\alpha^{s_1} (k_{1+}) e^{-ik_{1+} t_1} \Gamma^{\alpha\beta} u_\beta^{s_2} (k_{2+}) e^{-ik_{2+} t_2} \right] u_\gamma^{s_3} (E). \end{aligned} \quad (\text{B.3.6})$$

The vertex for the operator $O_\Gamma^{(0)}$ defined in Eq. (B.3.2) can be identified as

$$= -\epsilon_{ijk} e^{-i(k_{2+} t_2 + k_{1+} t_1)} \Gamma^{\alpha\beta} \mathbf{1}_{\gamma'}^\gamma. \quad (\text{B.3.7})$$

Simplifying and performing the Fourier transform for the coordinate projections $t_i \rightarrow \omega_i$ leads to

$$\Gamma^{\gamma' \omega_1 \omega_2} \begin{array}{l} \text{---} i\alpha k_{1+} \\ \text{---} j\beta k_{2+} \\ \text{---} k\gamma \end{array} = -\epsilon_{ijk} \Gamma^{\alpha\beta} \mathbf{1}_{\gamma'}^\gamma \delta(\omega_1 - k_{1+}) \delta(\omega_2 - k_{2+}). \quad (\text{B.3.8})$$

B.3.2 Vertex calculations first order in g_s

Here the first order vertex defined by the operator in (B.3.3) is calculated. The matrix element reads:

$$\begin{aligned} &\langle 0 | O_\Gamma^{(1)} | u(t_1)^{s_1} g(t_1)^{cs_3} d(k_{2+})^{s_2} b(E)^{s_3} \rangle \\ &= \langle 0 | \epsilon^{i'j'k'} \left[\int \frac{dp_1}{2\pi} \frac{1}{\sqrt{2E_{p_1}}} \sum_{r_1} \begin{matrix} u^{r_1} & u^{r_1} \\ a_{i'p_1} & u_\alpha \end{matrix} (p_1) e^{-ip_1 t_1} \right. \\ &\quad \left. \int_0^{t_1} dt_4 n^\mu \int \frac{dp_4}{2\pi} \frac{1}{\sqrt{2E_{p_4}}} \sum_{r_4, c'} A_{p_4}^{c' r_4} \epsilon_\mu^{r_4} (p_4) t^{c' i'} e^{-ip_4 t_4} \right. \\ &\quad \left. \int \frac{dp_2}{2\pi} \frac{1}{\sqrt{2E_{p_2}}} \sum_{r_2} \begin{matrix} d^{r_2} & d^{r_2} \\ a_{j'p_2} & u_\beta \end{matrix} (p_2) e^{-ip_2 t_2} \right] \Gamma^{\alpha\beta} \\ &\quad \left. \int \frac{dp_3}{2\pi} \frac{1}{\sqrt{2E_{p_3}}} \sum_{r_3} \begin{matrix} b^{r_3} & b^{r_3} \\ a_{k'p_3} & u_\gamma \end{matrix} (p_3) \right. \\ &\quad \left. \sqrt{2^4 E_{k_{1+}} E_{k_{2+}} E_E E_{k_{4+}}} \begin{matrix} u^{s_1 \dagger} & d^{s_2 \dagger} & b^{s_3 \dagger} \\ a_{ik_{1+}} & a_{jk_{2+}} & a_{kE} \end{matrix} A_{k_{4+}}^{s_4 c \dagger} |0\rangle, \right. \end{aligned}$$

B.4 Renormalization of the b -baryon LCDAs

This part of the appendix contains the discussion of the calculations necessary for Sec. 2.7. After some general remarks, I derive the equality of the leading twist evolution equations for the triplet and the parallel currents of the sextet in Fig. 2.4. This information is sufficient to perform the evolution of the b -baryon LCDAs, following [46]. Then I calculate the corresponding diagrams to provide some deeper insight in the formalism. Since the ultraviolet behavior is of interest for the renormalization group equations, the isospin limit is adopted in this chapter. The evolution equation for the leading twist distribution amplitude $\psi^I(t_1, t_2)$, defined in Eq. (2.2.8), is calculated at leading order in this work. The leading order evolution equation is derived by identifying the ultraviolet singularities of the vertices at one-loop order, pictured in Fig. 2.10.

The propagators and vertices for the quarks and the gluon are given by

$$\begin{aligned}
 \longrightarrow &= i\frac{\not{p}}{p^2+i\epsilon} + O(m), & \longrightarrow &= iP_+\frac{1}{p.v+i\epsilon}, \\
 \overset{\mu}{\text{-----}}\overset{\nu}{\text{-----}} &= -i\frac{g^{\mu\nu}}{p^2+i\epsilon}, & \text{---} &= it^a g_s \gamma^\mu, & \text{---} &= ig_s t^a v^\mu,
 \end{aligned} \tag{B.4.1}$$

in which the light-quark propagator is given up to first order in its mass, and the heavy-quark is described in the heavy-quark limit, see Chap. 1. The vertices defined by the non-local operators in (2.2.8) and (2.2.9) are derived in App. B.3.3 and given in Eq. (B.3.8) and (B.3.11). Some helpful relations and definitions for the following calculations are:

$$\begin{aligned}
 \{\gamma_\perp^\mu, \not{n}\} &= \{\gamma_\perp^\mu, \not{\bar{n}}\} = 0, & g_{\perp\mu\nu} &= g_{\mu\nu} - n^\mu \bar{n}^\nu / 2 - n^\nu \bar{n}^\mu / 2, \\
 \{\gamma_\perp^\mu, \gamma_\perp^\nu\} &= 2g_\perp^{\mu\nu}, & \gamma_\perp^\mu \gamma_{\perp\mu} &= 2.
 \end{aligned} \tag{B.4.2}$$

The loop integration over the loop momentum α is performed in light-cone coordinates, and the integrand is transformed via

$$\int \frac{d^D\alpha}{i(2\pi)^D} \rightarrow \int \frac{d^{D-2}\alpha_\perp d\alpha_+ d\alpha_-}{2i(2\pi)^D}. \tag{B.4.3}$$

Some important scalar products in the following evaluations are:

$$\alpha^2 = \alpha_\perp^2 + \alpha_+ \alpha_-, \quad \alpha.v = (\alpha_+ + \alpha_-)/2, \quad \not{\alpha} = \not{\alpha}_\perp + (\alpha_+ \not{n} + \alpha_- \not{\bar{n}})/2. \tag{B.4.4}$$

In zeroth order in m , the denominator will only depend on α_\perp^2 and thus be symmetric in α_\perp . In consequence all nominators $\propto \alpha_\perp^\mu$ vanish. The master integrals are defined in App. A.4. In the following, Feynman parameters (A.4.6) are used to rewrite the integrals in terms of the master integrals. The residue theorem will also be needed in the following chapters. For isolated single pole c of a complex function $f(z)$ the residue is given by

$$\text{Res}(f, c) = \lim_{z \rightarrow c} (z - c) f(z), \tag{B.4.5}$$

And the integral of the function along a path γ in counterclockwise direction, enclosing n isolated poles c_i is given by

$$\oint_\gamma dz f(z) = 2\pi i \sum_i^n \text{Res}(f, c_i). \tag{B.4.6}$$

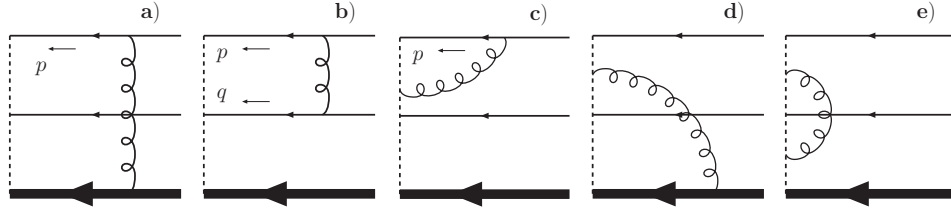


Figure B.2: Diagrams for the non-local vertex renormalization. Each of the first four diagrams appears twice (one for each light-quark). The dashed line represents the Wilson line.

Reversing the integration direction results in an overall minus sign.

B.4.1 Lorentz structure of the one-loop diagrams

The leading twist structures are $C\gamma_5\not{n}$ for the $j^P = 0^+$ multiplet [46], $w^\mu C\not{n}$ for the parallel components and $iC\sigma_{n\perp}^\mu = -\frac{1}{2}C(\not{n}\gamma_\perp^\mu - \gamma_\perp^\mu\not{n}) = C\gamma_\perp^\mu\not{n}$ for the transversal currents in the $j^P = 1^+$ multiplet given in Eqs. (2.2.8) and (2.2.9). The most important feature of this leading twist gamma structures $\tilde{\Gamma}_I$ is given by the condition $\not{n}\tilde{\Gamma}_I = \tilde{\Gamma}_I\not{n} = 0$, as will become clear later in this section.

Prior to the evaluation of the diagrams shown in Fig. 2.10, the general features of the Lorentz structures are discussed. What is meant by Lorentz structures needs some further specification: Everything which carries Lorentz indices and does not belong to the trivial Lorentz structure of the heavy-quark is accounted for (v^μ in the heavy-quark vertex, \not{n} in the light-quark propagator, etc.). The loop momenta are generically labeled as shown in Fig. B.2. Namely, the quark q_1 has loop momentum p and the quark q_2 has loop momentum q . The first diagram, explicitly shown in Fig. B.3, is given as example, including the projector P_+ for the b -quark, which is left implicit in the following. Following Feynman rules, the corresponding structures are v^ν (heavy-quark vertex), P_+ (heavy-quark propagator), Γ (non-local vertex), \not{n} (light-quark propagator), γ^μ (light-quark vertex) and $g_{\mu\nu}$ (gluon propagator):

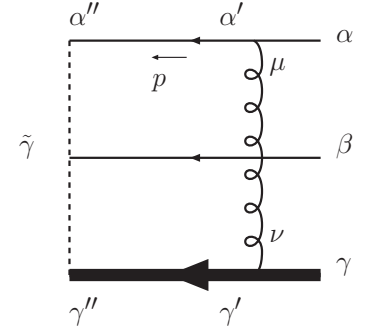


Figure B.3: Example diagram with explicitly shown spinor and Lorentz indices.

$$\begin{aligned} v^\nu(P_+)\gamma''_{\gamma'}\mathbf{1}_{\gamma'}\mathbf{1}_{\tilde{\gamma}}\gamma''_{\tilde{\gamma}}\Gamma^{\alpha'\beta}\not{n}_{\alpha''}(\gamma^\mu)_{\alpha'}^\alpha g_{\mu\nu} &= (P_+)\tilde{\gamma}_{\gamma'}\Gamma^{\alpha'\beta}(\not{n}\not{n})_{\alpha''}^\alpha, \\ &= (P_+)\tilde{\gamma}_{\gamma'}(\not{n}^T\not{n}^TC\tilde{\Gamma}_I)^{\alpha\beta}, \end{aligned} \quad (\text{B.4.7})$$

in which a tilde on the Γ implies, that the charge conjugation, which is always present in the definition of the currents (compare Eq. (2.2.8) and (2.2.9)) has been extracted, *i.e.* $\tilde{\Gamma} \equiv -C\Gamma$. Note, that the heavy-quark spin, described by the spinor indices γ and $\tilde{\gamma}$, is passed through the diagram unchanged as described in Chap. 1.

Using the vertices in Eq. (B.3.8), (B.3.11) and (B.4.1) and applying the Feynman rules,

omitting color and using $\gamma_\mu^T = C\gamma_\mu C$, the following Dirac structures are derived:

$$\begin{array}{c|c|c|c|c}
 \text{diag. a)} & \text{diag. b)} & \text{diag. c)} & \text{diag. d)} & \text{diag. e)} \\
 \psi^T \not{p}^T C \tilde{\Gamma}_I & \gamma^{\mu T} \not{p}^T C \tilde{\Gamma}_I \not{q} \gamma_\mu & \not{p}^T \not{p}^T C \tilde{\Gamma}_I & n^\mu v_\mu C \tilde{\Gamma}_I & n^\mu n_\mu \\
 = & = & = & = & = \\
 C \psi \not{p} \tilde{\Gamma}_I & C \gamma^\mu \not{p} \tilde{\Gamma}_I \not{q} \gamma_\mu & C \not{p} \tilde{\Gamma}_I & C \tilde{\Gamma}_I & 0 \\
 = & = & = & = & = \\
 p_+ \Gamma_I & -2\alpha_\perp^2 \Gamma_I \text{ or } 0 & 2p_+ \Gamma_I & \Gamma_I & 0
 \end{array} , \quad (\text{B.4.8})$$

where the derivations for the last line are given below for the only non-trivial case **b)**. The last diagram vanishes because the vertex is proportional to n^μ and hence vanishes when connected by a gluon line.

The loop momenta are specified as shown in Fig. B.4. Thus the Lorentz structure of diagram **b)** reads:

$$\begin{aligned}
 C \gamma^\mu \not{p} \tilde{\Gamma}_I \not{q} \gamma_\mu &= C \gamma^\mu (q_+ \not{\not{p}}/2 + \not{\not{q}}) \tilde{\Gamma}_I (p_+ \not{\not{p}}/2 - \not{\not{q}}) \gamma_\mu \\
 &= C \gamma^\mu ((q_+ + \alpha_+) (p_+ - \alpha_+) \not{\not{p}} \tilde{\Gamma}_I \not{\not{p}}/4 - \not{\not{q}}_\perp \tilde{\Gamma}_I \not{\not{q}}_\perp) \gamma_\mu.
 \end{aligned} \quad (\text{B.4.9})$$

The term $\not{\not{p}} \tilde{\Gamma}_I \not{\not{p}}$ is finite since the integration is performed over $d^{D-2} \alpha_\perp$, and the denominator is proportional to α_\perp^4 . For the loop integration I conclude:

$$\begin{aligned}
 C \gamma^\mu \not{p} \tilde{\Gamma}_I \not{q} \gamma_\mu &= -C \gamma^\mu \not{\not{q}}_\perp \tilde{\Gamma}_I \not{\not{q}}_\perp \gamma_\mu \\
 &= -C \gamma_\perp^\mu \not{\not{q}}_\perp \tilde{\Gamma}_I \not{\not{q}}_\perp \gamma_{\perp\mu}.
 \end{aligned} \quad (\text{B.4.10})$$

For the structure $C \gamma_5 \not{p}$ of the $j^p = 0^+$ triplet this leads to

$$C \gamma^\mu \not{p} \tilde{\Gamma}_I \not{q} \gamma_\mu = -C \tilde{\Gamma}_I \gamma_\perp^\mu \not{\not{q}}_\perp \gamma_{\perp\mu} = -2\alpha_\perp^2 C \tilde{\Gamma}_I. \quad (\text{B.4.11})$$

Obviously this is the same for the parallel currents with $\Gamma = w^\mu C \not{p}$. For the transversal currents with $\Gamma = C \gamma_\perp^\mu \not{p}$ Eq. (B.4.12) reads:

$$\begin{aligned}
 C \gamma^\mu \not{p} \tilde{\Gamma}_I \not{q} \gamma_\mu &= -C \gamma_\perp^\mu \not{\not{q}}_\perp \gamma_\perp^\nu \not{\not{q}}_\perp \gamma_{\perp\mu} = C \not{p} \gamma_\perp^\mu \not{\not{q}}_\perp \gamma_\perp^\nu \not{\not{q}}_\perp \gamma_{\perp\mu} \\
 &= C \not{p} \gamma_\perp^\mu (-\gamma_\perp^\nu \alpha_\perp^2 + 2\alpha_\perp^\nu \not{\not{q}}_\perp) \gamma_{\perp\mu} \\
 &= C \not{p} (-\alpha_\perp^2 (-\gamma_\perp^\nu \gamma_\perp^\mu + 2g_\perp^{\mu\nu}) + 2\alpha_\perp^\nu (-\not{\not{q}}_\perp \gamma_\perp^\mu + 2\alpha_\perp^\mu)) \gamma_{\perp\mu} \\
 &= C \not{p} (-\alpha_\perp^2 (-2\gamma_\perp^\nu + 2\gamma_\perp^\nu) + 2\alpha_\perp^\nu (-2\not{\not{q}}_\perp + 2\not{\not{q}}_\perp)) \\
 &= 0,
 \end{aligned} \quad (\text{B.4.12})$$

and hence this diagram does not contribute to the evolution of the transversal currents.

In the following the results in (B.4.8) are used to calculate the loop diagrams. The loop integral is given in units of $C_F \alpha_s / 4\pi$ ($\varepsilon_{ij'k} t_{i'i}^a t_{j'j}^a = -C_F \varepsilon_{ijk} / 2$, etc.), and the kinematics are described in Fig. B.4.

diag **a)**: This diagram was calculated in [51]_{Eq. 3.7}. I will just show in this part, that the diagram is finite for the leading twist.

$$\mathcal{D}_a = 4\Gamma \delta(\omega_2 - k_{2+}) \int \frac{d^{D-2} \alpha_\perp d\alpha_+ d\alpha_-}{2(2\pi)^{D-2}} \frac{\delta(k_{1+} - \alpha_+)}{[\alpha_\perp^2 + \alpha_+ \alpha_- + i\epsilon]}$$

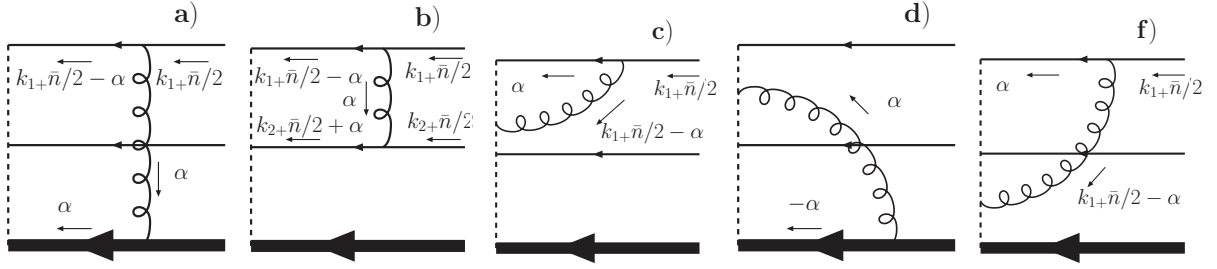


Figure B.4: Momentum assignment for the one-loop calculations. The loop integration is parametrized by the loop momentum α .

$$\frac{\delta(\omega_1 - k_{1+} + \alpha_+)}{[(\alpha_+ + \alpha_-)/2 + i\epsilon][\alpha_\perp^2 + \alpha_- (\alpha_+ - k_{1+}) + i\epsilon]} \quad (\text{B.4.13})$$

After integrating over α_+ , which is trivial due to the delta function, two possible pole structures arise: $\Theta(k_{1+} - \omega_1)$ with closing around $\alpha_- = (\alpha_\perp^2 + i\epsilon)/\omega_1$ and $\Theta(\omega_1 - k_{1+})$ with closing around $\alpha_- = -(k_{1+} - \omega_1 + i\epsilon)$.

$$\begin{aligned} \mathcal{D}_a = & -i16\pi\Gamma\delta(\omega_2 - k_{2+})\omega_1 \int \frac{d^{D-2}\alpha_\perp}{2(2\pi)^{D-2}} \left[\frac{\omega\Theta(k_{1+} - \omega_1)}{k_{1+}[\alpha_\perp^2 + i\epsilon][\alpha_\perp^2 + \omega_1(k_{1+} - \omega_1) + i\epsilon]} \right. \\ & \left. + \frac{\Theta(\omega_1 - k_{1+})}{[\alpha_\perp^2 - (k_{1+} - \omega_1)^2 + i\epsilon][\alpha_\perp^2\omega_1(k_{1+} - \omega_1) + i\epsilon]} \right] \end{aligned} \quad (\text{B.4.14})$$

Note, that the lower contour integration needs to be integrated clockwise, hence the contribution is negative. Obviously the integrand is proportional to $1/\alpha_\perp^4$ for large momenta. Hence the contribution is UV finite.

diag **b**): This diagram was calculated in [62]_{Eq. C16}. Using the propagators and vertices in (B.4.1) and the Lorentz structure $-2\alpha_\perp^2\Gamma$, which is already calculated in (B.4.8), one finds:

$$\begin{aligned} \mathcal{D}_b = & -(4\pi)^2\Gamma \int \frac{d^{D-2}\alpha_\perp d\alpha_+ d\alpha_-}{2(2\pi)^D} \frac{\delta(\omega_1 - k_{1+} - \alpha_+)\alpha_\perp^2}{[\alpha_\perp^2 + \alpha_+\alpha_- + i\epsilon]} \\ & \frac{\delta(\omega_2 - k_{2+} + \alpha_+)\alpha_\perp^2}{[\alpha_\perp^2 + \alpha_+\alpha_- + k_{1+}\alpha_- + i\epsilon][\alpha_\perp^2 + \alpha_+\alpha_- - k_{2+}\alpha_- + i\epsilon]} \end{aligned} \quad (\text{B.4.15})$$

There are two possibilities for which the integral is non-zero, namely $\Theta(\alpha_+)\Theta(k_{2+} - \alpha_+)$ and $\Theta(-\alpha_+)\Theta(k_{1+} + \alpha_+)$ with poles at

$$\alpha_- = -\frac{\alpha_\perp^2 + i\epsilon}{\alpha_+ - k_{2+}} \quad \text{and} \quad \alpha_- = -\frac{\alpha_\perp^2 + i\epsilon}{\alpha_+ + k_{1+}} \quad (\text{B.4.16})$$

respectively. Closing the contour upwards for the former and downwards for the latter case one obtains

$$\mathcal{D}_b = 2(4\pi)\Gamma \int \frac{d^{D-2}\alpha_\perp d\alpha_+}{2i(2\pi)^{D-2}} \delta(\omega_1 - k_{1+} - \alpha_+)\delta(\omega_2 - k_{2+} + \alpha_+)$$

$$\left(\frac{\Theta(\alpha_+) \Theta(k_{2+} - \alpha_+) (\alpha_+ - k_{2+})}{k_{2+} (k_{1+} + k_{2+}) [\alpha_\perp^2 + i\epsilon]} + \frac{\Theta(-\alpha_+) \Theta(k_{1+} + \alpha_+) (\alpha_+ + k_{1+})}{k_{1+} (k_{1+} + k_{2+}) [\alpha_\perp^2 + i\epsilon]} \right). \quad (\text{B.4.17})$$

The integration over the transverse loop momentum α_\perp is trivial and divergent with $1/\epsilon$. The formula is given in App. (A.4). After removing finite and infrared terms, Eq. (B.4.17) yields

$$\mathcal{D}_b = -\frac{1}{\epsilon} \Gamma \int d\alpha_+ \delta(\omega_1 - k_{1+} - \alpha_+) \delta(\omega_2 - k_{2+} + \alpha_+) \left(\frac{\Theta(\alpha_+) \Theta(k_{2+} - \alpha_+) (\alpha_+ - k_{2+})}{k_{2+} (k_{1+} + k_{2+})} + \frac{\Theta(-\alpha_+) \Theta(k_{1+} + \alpha_+) (\alpha_+ + k_{1+})}{k_{1+} (k_{1+} + k_{2+})} \right) \quad (\text{B.4.18})$$

The last integration is independent on the choice of the delta functions in the integrand. They will in both choices simply give the overall (lightlike) momentum conservation $\omega_2 + \omega_1 = k_{2+} + k_{1+}$:

$$\mathcal{D}_b = -\frac{1}{\epsilon} \Gamma \delta(\omega_2 + \omega_1 - k_{2+} - k_{1+}) \left(-\frac{\Theta(\omega_1 - k_{1+}) \omega_2}{k_{2+} (k_{1+} + k_{2+})} + \frac{\Theta(-\omega_1 + k_{1+}) \omega_1}{k_{1+} (k_{1+} + k_{2+})} \right). \quad (\text{B.4.19})$$

Following the works [62, 113] and [46], the parametrization $k_{1+} = v\omega$, $k_{2+} = (1-v)\omega$, $\omega_1 = u\omega$ and $\omega_2 = (1-u)\omega$ with $\omega = \omega_1 + \omega_2 = k_{1+} + k_{2+}$ are introduced for comparison:

$$\mathcal{D}_b = -\frac{1}{\omega\epsilon} \Gamma \delta(\omega - k_{1+} - k_{2+}) \left(\frac{\Theta(u-v)(1-u)}{1-v} + \frac{\Theta(v-u)u}{v} \right). \quad (\text{B.4.20})$$

diag **c**): This diagram was calculated in [62]_{Eq. C.16} and [60]_{Eq. 3.8}. Here I adopt the parametrization of the latter and show the equality with the former at the end. Using the propagators and vertices in (B.4.1) and the Lorentz structure $2p_+\Gamma$ in Eq. (B.4.8), one finds:

$$\mathcal{D}_c = 8\Gamma \delta(\omega_2 - k_{2+}) \int \frac{d^{D-2}\alpha_\perp d\alpha_+ d\alpha_-}{2(2\pi)^{D-2}} \frac{\alpha_+}{k_{1+} - \alpha_+} \frac{\delta(\omega_1 - \alpha_+) - \delta(\omega_1 - k_{1+})}{[\alpha_\perp^2 + \alpha_+ \alpha_- + i\epsilon][\alpha_\perp^2 + \alpha_+ \alpha_- - k_{1+} \alpha_- + i\epsilon]}. \quad (\text{B.4.21})$$

The only pole in α_- enclosed by the upper contour is given by $\alpha_- = -(\alpha_\perp^2 + i\epsilon)/(\alpha_+ - k_{1+})$ for $\alpha_+ > 0$ and $\alpha_+ < k_{1+}$. Using the theorem of residues yields:

$$\mathcal{D}_c = -16\pi\Gamma \delta(\omega_2 - k_{2+}) \int \frac{d^{D-2}\alpha_\perp d\alpha_+}{2i(2\pi)^{D-2}} \frac{\alpha_+}{k_{1+} - \alpha_+} \frac{(\delta(\omega_1 - \alpha_+) - \delta(\omega_1 - k_{1+})) \Theta(k_{1+} - \alpha_+)}{[\alpha_\perp^2 - i\epsilon]}. \quad (\text{B.4.22})$$

With the help of the master integrals in App. A.4 one finds, after ignoring finite and infrared terms:

$$\mathcal{D}_c = 2\frac{\Gamma}{\epsilon} \delta(\omega_2 - k_{2+}) \int_0^{k_{1+}} \frac{\alpha_+}{k_{1+}} \frac{\alpha_+}{k_{1+} - \alpha_+} (\delta(\omega_1 - \alpha_+) - \delta(\omega_1 - k_{1+})) \quad (\text{B.4.23})$$

The final integration yields:

$$\mathcal{D}_c = \Gamma \frac{2}{\epsilon} \delta(\omega_2 - k_{2+}) \left(\frac{\omega_1}{k_{1+}} \frac{\Theta(k_{1+} - \omega_1)}{k_{1+} - \omega_1} - \delta(\omega_1 - k_{1+}) \int_0^\infty \alpha_+ \frac{\alpha_+}{\omega_1} \frac{\Theta(\omega_1 - \alpha_+)}{\omega_1 - \alpha_+} \right). \quad (\text{B.4.24})$$

Note, that from [62]_{Eq. C17} the corresponding part of this diagram reads

$$\frac{u\Theta(v-u)}{v(v-u)} - \delta(u-v) \int du' \frac{u'}{v(v-u')} \Theta(u'-v) \quad (\text{B.4.25})$$

which can be rewritten in the same form of Eq. (B.4.24) by setting $u\omega = \omega_1$, etc. as

$$\frac{\omega_1 \Theta(k_{1+} - \omega_1)}{k_{1+}(k_{1+} - \omega_1)} - \delta(\omega_1 - k_{1+}) \int d\alpha_+ \frac{\alpha_+}{k_{1+}(k_{1+} - \alpha_+)} \Theta(\alpha_+ - k_{1+}). \quad (\text{B.4.26})$$

The change of dimensionality is due to the fact, that in the evolution equations this kernel is convoluted with the wave function. Hence the integral measure needs to be transformed accordingly.

diag **d**): This diagram was calculated in [60]_{Eq. 3.10} and later corrected in [51]_{Eq. 8}. According to the previous section the Lorentz structure Γ is trivial for this diagram. One finds:

$$\begin{aligned} \mathcal{D}_d &= (4\pi)^2 \Gamma \delta(\omega_2 - k_{2+}) \int \frac{d^{D-2} \alpha_\perp d\alpha_+ d\alpha_-}{2(2\pi)^D} \frac{1}{\alpha_+} \\ &\quad \frac{\delta(\omega_1 - k_{1+}) - \delta(\omega_1 - \alpha_+ - k_{1+})}{[\alpha_\perp^2 + \alpha_+ \alpha_- + i\epsilon][\alpha_+ + \alpha_- - i\epsilon]}. \end{aligned} \quad (\text{B.4.27})$$

The poles of the diagram are at

$$\alpha_- = -\alpha_+ + i2\epsilon \quad \text{and} \quad \alpha_- = -\frac{\alpha_\perp^2 + i\epsilon}{\alpha_+}. \quad (\text{B.4.28})$$

The integral vanishes for $a_+ < 0$. Taking this into account by including the theta function $\Theta(a_+)$ and closing the contour upwards, enclosing the pole $\alpha_- = -\alpha_+ + i2\epsilon$, Eq. (B.4.27) yields

$$\begin{aligned} \mathcal{D}_d &= \frac{i(4\pi)^2}{2\pi} \Gamma \delta(\omega_2 - k_{2+}) \int \frac{d^{D-2} \alpha_\perp d\alpha_+}{2(2\pi)^{D-2}} \Theta(a_+) \\ &\quad \frac{\delta(\omega_1 - k_{1+}) - \delta(\omega_1 - \alpha_+ - k_{1+})}{\alpha_+ [\alpha_\perp^2 - \alpha_+^2 + i\epsilon]}. \end{aligned} \quad (\text{B.4.29})$$

The α_\perp integration can easily be performed by using the dimensional regularization. The master integral $I_1(\Delta)$ is given in App. A.4 and the equation yields, remembering the mass scale μ , which ensures the correct dimensionality in the dimensional regularization [114]:

$$\mathcal{D}_d = \Gamma(\epsilon) \Gamma \delta(\omega_2 - k_{2+})$$

$$\int_0^\infty d\alpha_+ (\delta(\omega_1 - k_{1+}) - \delta(\omega_1 - \alpha_+ - k_{1+})) \frac{1}{\alpha_+} \left(\frac{\mu}{\alpha_+} \right)^{2\epsilon}. \quad (\text{B.4.30})$$

The delta function, which includes α_+ , is readily calculated. The first integral is split in the integration region

$$\begin{aligned} \mathcal{D}_d = & \Gamma(\epsilon)\Gamma\delta(\omega_2 - k_{2+}) \left\{ \delta(\omega_1 - k_{1+}) - \frac{\Theta(\omega_1 - k_{1+})}{\omega_1 - k_{1+}} \right. \\ & \left. + \left[\int_0^\omega \frac{d\alpha_+}{\alpha_+} \left(\frac{\mu}{\alpha_+} \right)^{2\epsilon} + \int_\omega^\infty \frac{d\alpha_+}{\alpha_+} \left(\frac{\mu}{\alpha_+} \right)^{2\epsilon} \right] \right\}. \end{aligned} \quad (\text{B.4.31})$$

Using the master integrals in App. A.4 one gets

$$\begin{aligned} \mathcal{D}_d = & -\Gamma(\epsilon)\Gamma\delta(\omega_2 - k_{2+}) \left\{ -\delta(\omega_1 - k_{1+})\Gamma(2\epsilon) \left(\frac{\mu}{\omega_1} \right)^{2\epsilon} \right. \\ & \left. + \frac{\Theta(\omega_1 - k_{1+})}{\omega_1 - k_{1+}} - \delta(\omega_1 - k_{1+}) \int_0^\infty d\alpha_+ \frac{\Theta(\omega_1 - \alpha_+)}{\omega_1 - \alpha_+} \right\}. \end{aligned} \quad (\text{B.4.32})$$

The first term can be expanded via

$$\Gamma(\epsilon)\Gamma(2\epsilon) \left(\frac{\mu}{\omega_1} \right)^{2\epsilon} = \frac{1}{2\epsilon^2} + \frac{1}{\epsilon} \log \frac{\mu}{\omega_1} \quad (\text{B.4.33})$$

diag **f**): The Lorentz structure is the same as that of diagram **c**).

$$\begin{aligned} \mathcal{D}_f = & 2\Gamma \int \frac{d^{D-2}\alpha_\perp d\alpha_+ d\alpha_-}{(2\pi)^{D-2}} \frac{\alpha_+}{k_{1+} - \alpha_+} \\ & \frac{\delta(\omega_1 - \alpha_+) (\delta(\omega_2 - k_{2+}) - \delta(\omega_2 - \alpha_+ - k_{2+}))}{[\alpha_\perp^2 + \alpha_+ \alpha_- + i\epsilon] [\alpha_\perp^2 + \alpha_+ \alpha_- - \alpha_- k_{1+} + i\epsilon]}. \end{aligned} \quad (\text{B.4.34})$$

The contribution is given in units of $C_F \alpha_s / 4\pi$. The integration over α_+ is trivial. Hence, the non-zero contribution is coming from $\omega_1 - k_{1+} < 0$ and the pole when the contour is closed in the upper plane is $\alpha_- = -(\alpha_\perp^2 + i\epsilon) / (\omega_1 - k_{1+})$. Thus leading to

$$\mathcal{D}_f = -4\pi\Gamma \int \frac{d^{D-2}\alpha_\perp}{i(2\pi)^{D-2}} \frac{\omega_1 \Theta(k_{1+} - \omega_1)}{k_{1+} - \omega_1} \frac{\delta(\omega_2 - k_{2+}) - \delta(\omega_2 - \omega_1 - k_{2+})}{[\alpha_\perp^2 - i\epsilon]} \frac{1}{k_{1+}}. \quad (\text{B.4.35})$$

With the master integrals of App. A.4 one gets

$$\mathcal{D}_f = -\frac{1}{\epsilon} \Gamma \frac{\omega_1 \Theta(k_{1+} - \omega_1)}{k_{1+} - \omega_1} \frac{1}{k_{1+}} (\delta(\omega_2 - k_{2+}) - \delta(\omega_2 - \omega_1 - k_{2+})). \quad (\text{B.4.36})$$

B.5 QCD sum rule results

Sum rule results for all twists. Here the transverse result is given. The parallel result is obtained by $A \leftrightarrow B$.

$$\begin{aligned}
f_{H_b}^{(2)} \left(A f_{H_b}^{(1)} + B f_{H_b}^{(2)} \right) \tilde{\psi}_2^{SR}(\omega, u) e^{-\bar{\Lambda}/\tau} = & \quad (B.5.1) \\
& \frac{3\tau^4}{2\pi^4} [B\hat{\omega}^2 u\bar{u} + A\hat{\omega}(\hat{m}_2 u + \hat{m}_1 \bar{u})] E_1(2\hat{s}_\omega) e^{-\hat{\omega}} \\
& - \frac{\langle \bar{q}_1 q_1 \rangle \tau^3}{\pi^2} [A\hat{\omega}\bar{u} + B\hat{m}_2] f(2\tau\omega u) E_{2-a}(2\hat{s}_\kappa) e^{-\hat{\omega}} \\
& - \frac{\langle \bar{q}_2 q_2 \rangle \tau^3}{\pi^2} [A\hat{\omega}u + B\hat{m}_1] f(2\tau\omega\bar{u}) E_{2-a}(2\hat{s}_{\bar{\kappa}}) e^{-\hat{\omega}} \\
& + \frac{2B}{3} \langle \bar{q}_1 q_1 \rangle \langle \bar{q}_2 q_2 \rangle \tau^2 f(2\tau\omega u) f(2\tau\omega\bar{u}) E_{3-2a}(2\hat{s}_{\kappa\bar{\kappa}}) e^{-\hat{\omega}},
\end{aligned}$$

$$\begin{aligned}
f_{H_b}^{(2)} \left(A f_{H_b}^{(1)} + B f_{H_b}^{(2)} \right) \tilde{\psi}_4^{SR}(\omega, u) e^{-\bar{\Lambda}/\tau} = & \quad (B.5.2) \\
& \frac{3\tau^4}{2\pi^4} [B E_3(2\hat{s}_\omega) + A(\hat{m}_1 + \hat{m}_2) E_2(2\hat{s}_\omega)] e^{-\hat{\omega}} \\
& - \frac{\langle \bar{q}_1 q_1 \rangle \tau^3}{\pi^2} [A E_{3-a}(2\hat{s}_\kappa) + B\hat{m}_2 E_{2-a}(2\hat{s}_\kappa)] f(2\tau\omega u) e^{-\hat{\omega}} \\
& - \frac{\langle \bar{q}_2 q_2 \rangle \tau^3}{\pi^2} [A E_{3-a}(2\hat{s}_{\bar{\kappa}}) + B\hat{m}_1 E_{2-a}(2\hat{s}_{\bar{\kappa}})] f(2\tau\omega\bar{u}) e^{-\hat{\omega}} \\
& + \frac{2B}{3} \langle \bar{q}_1 q_1 \rangle \langle \bar{q}_2 q_2 \rangle \tau^2 f(2\tau\omega u) f(2\tau\omega\bar{u}) E_{3-2a}(2\hat{s}_{\kappa\bar{\kappa}}) e^{-\hat{\omega}},
\end{aligned}$$

$$\begin{aligned}
f_{H_b}^{(1)} \left(A f_{H_b}^{(1)} + B f_{H_b}^{(2)} \right) \tilde{\psi}_{3s}^{SR}(\omega, u) e^{-\bar{\Lambda}/\tau} = & \quad (B.5.3) \\
& \frac{3\tau^4}{4\pi^4} \{ [A\hat{\omega} + B(\hat{m}_1 + \hat{m}_2)] E_2(2\hat{s}_\omega) + B\hat{\omega}(\hat{m}_2 u + \hat{m}_1 \bar{u}) E_1(2\hat{s}_\omega) \} e^{-\hat{\omega}} \\
& - \frac{\langle \bar{q}_1 q_1 \rangle \tau^3}{2\pi^2} [B E_{3-a}(2\hat{s}_\kappa) + (B\hat{\omega}\bar{u} + 2A\hat{m}_2) E_{2-a}(2\hat{s}_\kappa)] f(2\tau\omega u) e^{-\hat{\omega}} \\
& - \frac{\langle \bar{q}_2 q_2 \rangle \tau^3}{2\pi^2} [B E_{3-a}(2\hat{s}_{\bar{\kappa}}) + (B\hat{\omega}u + 2A\hat{m}_1) E_{2-a}(2\hat{s}_{\bar{\kappa}})] f(2\tau\omega\bar{u}) e^{-\hat{\omega}} \\
& + \frac{2A}{3} \langle \bar{q}_1 q_1 \rangle \langle \bar{q}_2 q_2 \rangle \tau^2 f(2\tau\omega u) f(2\tau\omega\bar{u}) E_{3-2a}(2\hat{s}_{\kappa\bar{\kappa}}) e^{-\hat{\omega}},
\end{aligned}$$

$$\begin{aligned}
f_{H_b}^{(1)} \left(A f_{H_b}^{(1)} + B f_{H_b}^{(2)} \right) \tilde{\psi}_{3\sigma}^{SR}(\omega, u) e^{-\bar{\Lambda}/\tau} = & \quad (B.5.4) \\
& \frac{3\tau^4}{4\pi^4} \{ [A\hat{\omega}(u - \bar{u}) + B(\hat{m}_1 - \hat{m}_2)] E_2(2\hat{s}_\omega) + B\hat{\omega}(\hat{m}_2 u - \hat{m}_1 \bar{u}) E_1(2\hat{s}_\omega) \} e^{-\hat{\omega}} \\
& - \frac{B\langle \bar{q}_1 q_1 \rangle \tau^3}{2\pi^2} [E_{3-a}(2\hat{s}_\kappa) - \hat{\omega}\bar{u} E_{2-a}(2\hat{s}_\kappa)] f(2\tau\omega u) e^{-\hat{\omega}}
\end{aligned}$$

$$+ \frac{B \langle \bar{q}_2 q_2 \rangle \tau^3}{2\pi^2} [E_{3-a}(2\hat{s}_{\bar{\kappa}}) - \hat{\omega} u E_{2-a}(2\hat{s}_{\bar{\kappa}})] f(2\tau\omega\bar{u}) e^{-\hat{\omega}},$$

where $\hat{s}_{\kappa} = \hat{s}_{\omega} - \kappa/2$, $\hat{s}_{\bar{\kappa}} = \hat{s}_{\omega} - \bar{\kappa}/2$, $\hat{s}_{\kappa\bar{\kappa}} = \hat{s}_{\omega} - \kappa/2 - \bar{\kappa}/2$, and the short-hand notations

$$\kappa = \frac{\lambda}{2q_1\omega\tau}, \quad \bar{\kappa} = \frac{\lambda}{2\bar{q}_1\omega\tau} \quad (\text{B.5.5})$$

are used.

B.6 Numerical results for the LCDAs

Here I present a summary of our numeric results. The moments for Λ (Σ), Ξ (Ξ') and Ω are listed in Tab. B.6.1, B.6.2 and B.6.3. The model for Λ (Σ), Ξ (Ξ') and Ω parameters are listed in Tab. B.6.4, B.6.5 and B.6.6

Table B.6.1: Λ (Σ) with $s_0 = 1.2$ [52] and $\tau = 0.6$ [46]_{p. 6}

twist	$\langle 1 \rangle$	$\langle \omega^{-1} \rangle$	$\langle C_1^{3/2} / C_1^{3/2} \rangle$	$\langle \omega^{-1} C_1^{3/2} / C_1^{3/2} \rangle$	$\langle C_2^{3/2} / C_2^{3/2} \rangle$	$\langle \omega^{-1} C_2^{3/2} / C_2^{3/2} \rangle$
2	1	$1.71_{-0.51}^{+0.86}$	—	—	$0.37_{-0.22}^{+0.17}$	$0.2_{-0.55}^{+0.32}$
twist	$\langle 1 \rangle$	$\langle \omega^{-1} \rangle$	$\langle C_1^{1/2} / C_1^{1/2} \rangle$	$\langle \omega^{-1} C_1^{1/2} / C_1^{1/2} \rangle$	$\langle C_2^{1/2} / C_2^{1/2} \rangle$	$\langle \omega^{-1} C_2^{1/2} / C_2^{1/2} \rangle$
3s	1	$2.2_{-0.37}^{+0.65}$	—	—	$-0.09_{-0.07}^{+0.03}$	$-0.7_{-0.57}^{+0.32}$
3 σ	—	—	1	$1.61_{-0.29}^{+0.23}$	—	—
4	1	$2.84_{-0.45}^{+0.88}$	—	—	$-0.24_{-0.04}^{+0.08}$	$-0.92_{-0.35}^{+0.18}$

Table B.6.2: Ξ (Ξ') with $s_0 = 1.2$ [52] and $\tau = 0.6$ [46]_{p. 6}

twist	$\langle 1 \rangle$	$\langle \omega^{-1} \rangle$	$\langle C_1^{3/2} / C_1^{3/2} \rangle$	$\langle \omega^{-1} C_1^{3/2} / C_1^{3/2} \rangle$	$\langle C_2^{3/2} / C_2^{3/2} \rangle$	$\langle \omega^{-1} C_2^{3/2} / C_2^{3/2} \rangle$
2	1	$1.54_{-0.36}^{+0.58}$	$0.11_{-0.03}^{+0.04}$	$0.14_{-0.05}^{+0.08}$	$0.33_{-0.26}^{+0.17}$	$0.24_{-0.32}^{+0.21}$
twist	$\langle 1 \rangle$	$\langle \omega^{-1} \rangle$	$\langle C_1^{1/2} / C_1^{1/2} \rangle$	$\langle \omega^{-1} C_1^{1/2} / C_1^{1/2} \rangle$	$\langle C_2^{1/2} / C_2^{1/2} \rangle$	$\langle \omega^{-1} C_2^{1/2} / C_2^{1/2} \rangle$
3s	1	$2_{-0.24}^{+0.38}$	$0.12_{-0.02}^{+0.03}$	$0.13_{-0.05}^{+0.09}$	$-0.1_{-0.01}^{+0.01}$	$-0.52_{-0.28}^{+0.17}$
3 σ	$-0.07_{-0.04}^{+0.07}$	$-0.19_{-0.14}^{+0.19}$	1	$1.53_{-0.21}^{+0.15}$	$0.11_{-0.08}^{+0.03}$	$0.2_{-0.2}^{+0.15}$
4	1	$2.62_{-0.32}^{+0.54}$	$0.13_{-0.01}^{+0.02}$	$0.13_{-0.06}^{+0.09}$	$-0.21_{-0.6}^{+0.1}$	$-0.7_{-0.1}^{+0.05}$

Table B.6.3: Ω with $s_0 = 1.4$ and $\tau = 0.4$

twist	$\langle 1 \rangle$	$\langle \omega^{-1} \rangle$	$\langle C_1^{3/2} / C_1^{3/2} \rangle$	$\langle \omega^{-1} C_1^{3/2} / C_1^{3/2} \rangle$	$\langle C_2^{3/2} / C_2^{3/2} \rangle$	$\langle \omega^{-1} C_2^{3/2} / C_2^{3/2} \rangle$
2	1	$1.29_{-0.19}^{+0.25}$	—	—	$0.32_{-0.24}^{+0.19}$	$0.26_{-0.22}^{+0.17}$
twist	$\langle 1 \rangle$	$\langle \omega^{-1} \rangle$	$\langle C_1^{1/2} / C_1^{1/2} \rangle$	$\langle \omega^{-1} C_1^{1/2} / C_1^{1/2} \rangle$	$\langle C_2^{1/2} / C_2^{1/2} \rangle$	$\langle \omega^{-1} C_2^{1/2} / C_2^{1/2} \rangle$
3s	1	$1.69_{-0.07}^{+0.08}$	—	—	$-0.06_{-0.04}^{+0.03}$	$-0.32_{-0.12}^{+0.1}$
3 σ	—	—	1	$1.33_{-0.12}^{+0.1}$	—	—
4	1	$2.29_{-0.14}^{+0.17}$	—	—	$-0.15_{-0.03}^{+0.05}$	$-0.43_{-0.01}^{+0.01}$

Table B.6.4: Λ (Σ) with $s_0 = 1.2$ and $\tau = 0.6$. The error of $+\infty$ is not a problem since it just represents the case, where $a_2 = 0$ and the second Gegenbauer polynomial vanishes.

twist	ε_0	ε_1	ε_2	a_0	a_1	a_2
2	$0.2_{-0.07}^{+0.08}$	—	$0.62_{-0.24}^{+\infty}$	1	—	$0.87_{-0.87}^{+0.52}$
3s	$0.23_{-0.05}^{+0.04}$	—	$0.07_{-0.01}^{+0.005}$	1	—	$-0.09_{-0.07}^{+0.03}$
3 σ	—	$0.31_{-0.04}^{+0.07}$	—	—	1	—
4	$0.35_{-0.08}^{+0.07}$	—	$0.26_{-0.13}^{+0.12}$	1	—	$-0.24_{-0.04}^{+0.08}$

Table B.6.5: Ξ (Ξ') with $s_0 = 1.2$ and $\tau = 0.6$. The error of $+\infty$ is not a problem since it just represents the case, where $a_2 = 0$ and the second Gegenbauer polynomial vanishes.

twist	ε_0	ε_1	ε_2	a_0	a_1	a_2
2	$0.22_{-0.06}^{+0.06}$	$0.26_{-0.03}^{+0.05}$	$0.46_{-0.09}^{+\infty}$	1	$0.18_{-0.05}^{+0.07}$	$0.78_{-0.78}^{+0.4}$
3s	$0.25_{-0.04}^{+0.03}$	$0.45_{-0.1}^{+0.18}$	$0.09_{-0.02}^{+0.04}$	1	$0.12_{-0.02}^{+0.03}$	$-0.1_{-0.01}^{+0.01}$
3 σ	$0.17_{-0.17}^{+0.12}$	$0.33_{-0.03}^{+0.38}$	$0.28_{-0.28}^{+0.2}$	$-0.07_{-0.04}^{+0.07}$	1	$0.11_{-0.11}^{+0.08}$
4	$0.38_{-0.06}^{+0.05}$	$1.02_{-0.33}^{+0.6}$	$0.3_{-0.17}^{+0.12}$	1	$0.13_{-0.01}^{+0.02}$	$-0.21_{-0.06}^{+0.1}$

Table B.6.6: Ω with $s_0 = 1.4$ and $\tau = 0.4$

twist	ε_0	ε_1	ε_2	a_0	a_1	a_2
2	$0.26_{-0.04}^{+0.04}$	—	$0.42_{-0.02}^{+0.25}$	1	—	$0.76_{-0.57}^{+0.43}$
3s	$0.3_{-0.02}^{+0.01}$	—	$0.1_{-0.02}^{+0.01}$	1	—	$-0.06_{-0.04}^{+0.03}$
3 σ	—	$0.38_{-0.03}^{+0.03}$	—	—	1	—
4	$0.44_{-0.03}^{+0.03}$	—	$0.34_{-0.11}^{+0.08}$	1	—	$-0.15_{-0.03}^{+0.05}$

Appendix C

Tetraquarks

This appendix contains several calculations and detailed explanations necessary for the discussion of the hidden bottom tetraquarks in Chap. 3. The order of the sections corresponds to the appearance of the topic in the main work.

C.1 Tetraquark interpolating currents

In this section I give a short overview over the properties of the $L = 0$ tetraquark interpolating operators and the calculations in which they are involved.

Interpolating operators play in general an important role in QCD, see for example the derivation of the non-local baryonic interpolating operators in Sec. 2.2 and the definition of the local interpolating operators in Sec. 2.3. Opposed to the relativistic interpolating operators in Sec. 2.2 and 2.3, the tetraquark operators are given in the non-relativistic limit and are defined by Pauli matrices. A generalization to Dirac matrices is, however, straightforward, and in principle the interpolating operators given here can be used in tetraquark sum rule mass calculations as was already done by several groups.

The states which are obtained with the help of the matrices

$$\Gamma^0 = \frac{\sigma_2}{\sqrt{2}} \quad \text{and} \quad \Gamma^i = \frac{1}{\sqrt{2}} \sigma_2 \sigma_i, \quad (\text{C.1.1})$$

and defined in (3.4.6). They can be understood in the following way. A state $|S_{\mathcal{Q}}, S_{\bar{\mathcal{Q}}}; J\rangle$ with diquark spin $S_{\mathcal{Q}}$, antidiquark spin $S_{\bar{\mathcal{Q}}}$ and total angular momentum J is given by

$$|S_{\mathcal{Q}}, S_{\bar{\mathcal{Q}}}; J\rangle = |\Gamma, \Gamma' J\rangle = (b\Gamma q)(\bar{b}\Gamma' \bar{q}) |0\rangle, \quad (\text{C.1.2})$$

in which Γ and Γ' can be Γ^0 or Γ^i . The Γ and Γ' define the interpolating operators of the diquark and the antidiquark inside the tetraquark, where the matrix Γ^0 defines a *good* and Γ^i defines a *bad* diquark. The spins of the diquark and antidiquark combine to give the overall spin of the tetraquark. For example the antisymmetric doubly-bad combination defines the $J = 1$ ground state tetraquark via $|1_{\mathcal{Q}}, 1_{\bar{\mathcal{Q}}}; 1_J\rangle = \frac{1}{2\sqrt{2}} \varepsilon^{ijk} (b\sigma_2 \sigma^j q) \otimes (\bar{b}\sigma_2 \sigma^k \bar{q}) |0\rangle$ or, as abbreviated in Chap. 3 by leaving the quark fields and the vacuum state implicit, by $\frac{1}{2\sqrt{2}} \varepsilon^{ijk} (\sigma_2 \sigma^j) \otimes (\sigma_2 \sigma^k)$. The spin operators \mathbf{S}_q in Eq. (3.4.2) act on every quark q .

In the definition (C.1.2) the spin operators can act on the b -quark, which stands on the left, or the lighter quarks, which stand on the right. Since \mathbf{S}_q are vector valued two by two matrices, there is only one normalized possible definition in terms of Pauli matrices, namely $\mathbf{S}_q = \frac{1}{2}\boldsymbol{\sigma}$. Their action on the tetraquark states is defined by

$$\begin{aligned} \mathbf{S}_b |\Gamma, \Gamma'; J\rangle &= \left| \frac{1}{2}\boldsymbol{\sigma}^T \Gamma, \Gamma'; J \right\rangle, & \mathbf{S}_q |\Gamma, \Gamma'; J\rangle &= \left| \Gamma \frac{1}{2}\boldsymbol{\sigma}, \Gamma'; J \right\rangle, \\ \mathbf{S}_{\bar{b}} |\Gamma, \Gamma'; J\rangle &= \left| \Gamma, \frac{1}{2}\boldsymbol{\sigma}^T \Gamma'; J \right\rangle, & \mathbf{S}_{\bar{q}} |\Gamma, \Gamma'; J\rangle &= \left| \Gamma, \Gamma' \frac{1}{2}\boldsymbol{\sigma}; J \right\rangle. \end{aligned} \quad (\text{C.1.3})$$

With the so defined operators the action of the Hamiltonian on the states is given, and one can diagonalize the operator defined in (3.4.1) and (3.4.2) to determine the mass eigenvalues. To give an explicit example, the $q\bar{q}$ spin term, which is acting on the $|1, 0; 1\rangle$ state, is derived below.

$$\begin{aligned} \mathbf{S}_q \cdot \mathbf{S}_{\bar{q}} |1, 0; 1\rangle &= \frac{1}{8} (\sigma_2 \sigma^j \sigma_i) \otimes (\sigma_2 \sigma^i), \\ &= -\frac{i}{8} \varepsilon^{jki} (\sigma_2 \sigma_k) \otimes (\sigma_2 \sigma_i) + \frac{1}{8} (\sigma_2) \otimes (\sigma_2 \sigma^j), \\ &= -\frac{i\sqrt{2}}{4} |1, 1; 1\rangle + \frac{1}{4} |0, 1; 1\rangle. \end{aligned} \quad (\text{C.1.4})$$

C.2 Derivation of the Van Royen-Weisskopf formula

The Van Royen-Weisskopf formula yields the leptonic e^+e^- decay width of a two-body valence-quark state, described by a wave function $\psi(\mathbf{x})$, where \mathbf{x} is the relative coordinate of the two quarks. They are (as probability distributions) normalized to 1,

$$\int d^3x \psi^*(\mathbf{x}) \psi(\mathbf{x}) = 1. \quad (\text{C.2.1})$$

It is convenient to separate the wave function by using angular coordinates as

$$\Psi_{nlm}(\mathbf{x}) = R_{nl}(r) Y_{lm}(\theta, \phi), \quad (\text{C.2.2})$$

in which $R_{nl}(r)$ is the radial part and $Y_{lm}(\theta, \phi)$ is the angular momentum part. The function for each state is described by the principal quantum number n , the angular momentum quantum number l and its projection m to the z -axis. The Schrödinger wave function is obtained by Fourier transform:

$$\tilde{\psi}(\mathbf{k}) = \int d^3x e^{-i\mathbf{k}\cdot\mathbf{x}} \psi(\mathbf{x}). \quad (\text{C.2.3})$$

The underlying dynamics to derive the Van Royen-Weisskopf formula, pictured in Fig. C.1, can be described as follows. The coordinate dependence of the constituents

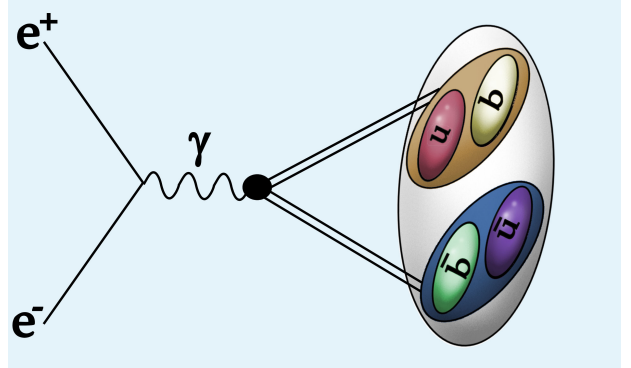


Figure C.1: Schematic underlying process of the Van Royen-Weisskopf formula for tetraquarks with pointlike diquarks.

of the state are distributed with a certain probability, given by the wave function. If the constituents are close enough, they can annihilate to a virtual photon. The decay is therefore dominated by the behavior of the wave function near the origin. The virtual photon subsequently decays to the lepton pair. The coupling to the photon is an electroweak process and involves the charge Q_I of the constituents of the bound state. Thus the partial electronic width is in this approximation proportional to Q_I^2 , where Q_I refers to the effective diquark charge given in Eq. (3.5.5) and (3.5.12). Note, that it is necessary in this section, that the diquarks are pointlike. At present there is no proper tetraquark wave function available which could be used as input.

The Van Royen-Weisskopf formula was originally developed for the heavy-quarkonia family. Several potential models such as [92] were derived well over thirty years ago to derive the quarkonia radial wave functions. An important instance to carry the methods used for the bottomonia over to the tetraquark case is, that the quarkonia are to first order strongly bound objects. Since the diquarks $[bq]$ are pointlike color triplets and moreover have in the constituent quark model to a good approximation the same mass as the b -quark, both derivations are very similar. Because plenty of work has already been done for the heavy-quarkonia, they are discussed first.

C.2.1 Heavy $q\bar{q}$ -quarkonia

As aforementioned, the wave functions give the probability distributions of the quarks inside the meson. See also [112]_{Sec. 5.3} for further information. In the valence-quark approximation a meson $|\mathcal{M}\rangle$ is formally described by

$$\int_k |q(\mathbf{k})\bar{q}(-\mathbf{k})\rangle \langle q(\mathbf{k})\bar{q}(-\mathbf{k})| M\rangle, \quad (\text{C.2.4})$$

in which $\langle q(\mathbf{k})\bar{q}(-\mathbf{k})| \mathcal{M}\rangle \hat{=} \tilde{\psi}(\mathbf{k})$, omitting color and spinor indices, and the integration is performed over the relative momentum \mathbf{k} . This equation is similar to Eq. (2.1.1), describing the b -baryon wave functions. The spinor structure specifies the meson multiplet, compare Sec. 2.1 and 2.2 for the baryons. The simplest spin singlet $J^P = 0^+$ configuration 1S_0 is given by

$$|{}^1S_0\rangle = \sqrt{\frac{M}{3}} \int \frac{d^3k}{(2\pi)^3 2m} \tilde{\psi}(\mathbf{k}) \mathbb{1}^{\alpha\beta} |q_\alpha(\mathbf{k})\bar{q}_\beta(-\mathbf{k})\rangle, \quad (\text{C.2.5})$$

$$= \sqrt{\frac{M}{3}} \int \frac{d^3k}{(2\pi)^3 2m} \tilde{\psi}(\mathbf{k}) a_\alpha^\dagger(\mathbf{k}) \mathbb{1}^{\alpha\beta} b_\beta^\dagger(-\mathbf{k}) |0\rangle, \quad (\text{C.2.6})$$

in which quark-annihilation and creation operators are used. The Notation ${}^{2S+1}L_J$ is used, in which the upper left index is the spin representation, the lower right index refers to the total angular momentum and the capital letter indicates the orbital excitation (S, P, D, \dots). The meson ground state with $J^P = 1^-$ is given by

$$|{}^3S_1\rangle = \sqrt{\frac{M}{3}} \int \frac{d^3k}{(2\pi)^3 2m} \tilde{\psi}(\mathbf{k}) \mathbf{n} \cdot \boldsymbol{\sigma}^{\alpha\beta} |q_\alpha(\mathbf{k})\bar{q}_\beta(-\mathbf{k})\rangle, \quad (\text{C.2.7})$$

in which \mathbf{n} is the polarization vector of the meson with $\mathbf{n} \cdot \mathbf{n}^* = 1$. The simplest excited and also the most interesting state in this section is the spin 0 P -wave meson 1P_1 :

$$|{}^1P_1\rangle = \sqrt{\frac{M}{3}} \int \frac{d^3k}{(2\pi)^3 2m} \tilde{\psi}_i(\mathbf{k}) \cdot n^i \mathbf{1}^{\alpha\beta} |q_\alpha(\mathbf{k}) \bar{q}_\beta(-\mathbf{k})\rangle, \quad (\text{C.2.8})$$

with $\tilde{\psi}(\mathbf{k})$ being a vector valued function. The 1P_1 state has quantum numbers 1^{+-} for the quarkonia, with $P = (-1)^{L+1}$ and $C = (-1)^{L+S}$, and has therefore no coupling to photons. The tetraquark 1P_1 state, discussed later, on the other hand has quantum numbers 1^{--} with $P = (-1)^L$ and $C = (-1)^L$. The factor $\sqrt{3}$ comes from the normalization in color space. The color structure for all mesons is trivial included by a delta function in color space. The meson states $|\mathcal{M}\rangle$ shown above are normalized to $\langle \mathcal{M} | \mathcal{M} \rangle = 2M$. The spin structure in terms of polarization vectors and Pauli matrices can be found in Eq. (A.1.6).

The decay of the heavy-quarkonia is described by $q(k)\bar{q}(k') \rightarrow e^-(p)e^+(p')$, where the kinematics is in the center of mass frame given by $k^\mu = (E_{\mathbf{k}}, \mathbf{k})$, $k'^\mu = (E_{\mathbf{k}}, -\mathbf{k})$, $p^\mu = (E_{\mathbf{p}}, \mathbf{p})$ and $p'^\mu = (E_{\mathbf{p}}, -\mathbf{p})$. The one photon exchange amplitude is given by

$$i\mathcal{M}(q\bar{q} \rightarrow e^-e^+) = \frac{ie^2 Q_e Q_b}{M^2} [\bar{u}_e(p)\gamma_\mu v_e(p')] [\bar{v}_b(k')\gamma^\mu u_b(k)]. \quad (\text{C.2.9})$$

The electrons are massless with $k^2 = k'^2 = 0$ and in the heavy-quark limit, discussed in Chap. 1, one finds $|\mathbf{p}| \approx E_{\mathbf{p}} = E_{\mathbf{k}} \approx m_b \gg |\mathbf{k}|$. Thus the b -quarks are on-shell, the mass is constant and the spinors defined in (A.1.5) are in the chiral basis given by

$$u_b(\mathbf{k}) = \begin{pmatrix} \sqrt{\mathbf{k} \cdot \boldsymbol{\sigma}} \xi \\ \sqrt{\mathbf{k} \cdot \bar{\boldsymbol{\sigma}}} \xi \end{pmatrix} \approx \sqrt{m_b} \begin{pmatrix} \xi \\ \xi \end{pmatrix}, v_b(\mathbf{k}') = \begin{pmatrix} \sqrt{\mathbf{k}' \cdot \boldsymbol{\sigma}} \eta \\ -\sqrt{\mathbf{k}' \cdot \bar{\boldsymbol{\sigma}}} \eta \end{pmatrix} \approx \sqrt{m_b} \begin{pmatrix} \eta \\ -\eta \end{pmatrix}. \quad (\text{C.2.10})$$

The heavy-quark current in Eq. (C.2.9) simplifies to

$$[\bar{v}_b(k')\gamma^\mu u_b(k)] \approx -2m_b \eta^\dagger \sigma^\mu \xi \text{ for } \mu = 1, 2, 3 \text{ and } 0 \text{ for } \mu = 0, \quad (\text{C.2.11})$$

in which the explicit form of the Dirac matrices in the chiral representation is given in Eq. (A.0.3). With Eq. (A.1.6) one readily obtains

$$[\bar{v}_b(k')\gamma^\mu u_b(k)] \approx 2m_b \text{Tr} \left[\frac{\mathbf{n}\boldsymbol{\sigma}}{\sqrt{2}} \sigma^\mu \right] \text{ for } \mu = 1, 2, 3 \text{ and } 0 \text{ for } \mu = 0. \quad (\text{C.2.12})$$

The spin 0 part vanishes automatically because the b -quark current transforms as a vector, and hence the scalar part has no coupling to intermediate photons. The Lorentz structure in Eq. (C.2.12) is the same as for the $|{}^3S_1\rangle$ state defined in (C.2.7). This statement is tautological to some extent, because the state was constructed to exhibit that transformation property, but it points out the role of the wave function as probability function of the momentum distributions, *i.e.* it shows the actuality, that up to normalization $\langle e^-e^+ | {}^3S_1 \rangle \hat{=} \int d^3k \bar{\psi}(\mathbf{k}) \langle e^-e^+ | q(\mathbf{k}) \bar{q}(-\mathbf{k}) \rangle$. Thus the amplitude for the decay is given by

$$i\mathcal{M}({}^3S_1 \rightarrow e^-e^+) \approx \frac{ie^2 Q_e Q_b}{M^2} \sqrt{3M} \int \frac{d^3k}{(2\pi)^3} \bar{\psi}(\mathbf{k}) \text{Tr} [\mathbf{n}\boldsymbol{\sigma}\sigma^\mu] [\bar{u}_e(p)\gamma_\mu v_e(p')],$$

$$= \frac{2ie^2 Q_e Q_b \sqrt{3M}}{M^2} \psi(0) n^i [\bar{u}_e(p) \gamma_i v_e(p')], \quad (\text{C.2.13})$$

in which the calculation of the color factors have not been shown. According to Eq. (C.2.12) the b -quark vector current does not depend on \mathbf{k} in the heavy-quark limit, and the Fourier transform of the Schrödinger wave function in (C.2.13) yields the wave function in coordinate space times $\delta(x)$. Thus the wave function is taken at the origin. Averaging over the spin of the initial states and summing over those of the final state, the squared matrix element with the non-relativistic polarization sum $\sum_\lambda n_\lambda^{*i} n_\lambda^j = \delta^{ij}$ becomes

$$\begin{aligned} \frac{1}{2} \sum_{\text{spin}} |\mathcal{M}(^3S_1 \rightarrow e^+ e^-)|^2 &\approx \frac{4e^4 Q_e^2 Q_b^2}{M^3} |\psi(0)|^2 \delta^{ij} \text{Tr} [\not{p} \gamma_i \not{p}' \gamma_j], \\ &= \frac{4e^4 Q_e^2 Q_b^2}{M^3} |\psi(0)|^2 [3(E_p^2 + |\mathbf{p}|^2) - 2|\mathbf{p}|^2], \\ &\approx \frac{256\pi^2 \alpha^2 Q_b^2}{M} |\psi(0)|^2 = \frac{64\pi \alpha^2 Q_b^2}{M} |R(0)|^2. \end{aligned} \quad (\text{C.2.14})$$

The factorization in Eq. (C.2.2) has been used in the last step. The partial leptonic decay width is readily obtained:

$$\Gamma(^3S_1 \rightarrow e^+ e^-) = \frac{|\mathbf{p}|}{8\pi M^2} \frac{1}{3} |\mathcal{M}|^2 \approx \frac{4\alpha^2 Q_b^2}{M^2} |R_{n0}(0)|^2. \quad (\text{C.2.15})$$

This is the famous Van Royen-Weisskopf formula for the 3S_1 bottomonium. The unknown quantity, the radial wave function at origin, is derived with the help of potential model, such as the Buchmüller-Tye potential [92]. Numerical tools to solve the corresponding Schrödinger equations are also available, see for example the QQ-onia package from [106].

C.2.2 Heavy $Q\bar{Q}$ -tetraquarks

The wave functions of the heavy tetraquarks states for pointlike diquarks \mathcal{Q} with $\mathcal{Q} = [bq]$ are given in a similar way to the wave functions of the heavy-quarkonia. The difference is the spin assignment of the constituents. For scalar diquarks one finds for the 1^{--} state:

$$|^1P_1\rangle = \sqrt{2M} \int \frac{d^3k}{(2\pi)^3 2m} \tilde{\psi}_{n1m}^i n_i^{(m)}(\mathbf{k}) \frac{\delta^{ab}}{\sqrt{3}} \left| \mathcal{Q}^a(\mathbf{k}) \bar{\mathcal{Q}}^b(-\mathbf{k}) \right\rangle, \quad (\text{C.2.16})$$

in which the color indices a, b are given explicitly, to show the analogy with the quarkonia in color space, see for comparison Eq. (C.2.8). It is immanent for this derivation, that the sextet is negligible, as stated in Sec. 3.1. The polarization vector $\mathbf{n}^{(m)}$ satisfies $|\mathbf{n}^{(m)}|^2 = 1$ for all spin polarizations m , see also Eq. (A.3.4) for further details to the wave function and its polarization. The decay amplitude is accordingly given by

$$i\mathcal{M}(^1P_1[Q\bar{Q}] \rightarrow e^+ e^-) = \frac{\sqrt{2M} \delta_b^a \delta_b^a}{\sqrt{3}} \int \frac{d^3k \tilde{\psi}_{n1}^i(\mathbf{k}) n_i^{(m)}}{(2\pi)^3 2m_{\mathcal{Q}}} \frac{ie^2 Q_e Q_{\mathcal{Q}}}{M^2} [\bar{u}_e(p) \gamma_\mu v_e(p')] (k - k')^\mu, \quad (\text{C.2.17})$$

where, due to the dependence of the vertex on the momenta $(k - k')^\mu$, integrals of the type

$$\int \frac{d^3k k_j}{(2\pi)^3} \tilde{\Psi}_{n1m}(\mathbf{k}) = \int \frac{d^3k k_j}{(2\pi)^3} \int d^3x e^{-i\mathbf{k}\cdot\mathbf{x}} \psi_{n1m}(\mathbf{x}) = -i \int d^3x \delta^{(3)}(\mathbf{x}) \frac{\partial}{\partial x^j} \Psi_{n1m}(\mathbf{x})$$

$$= -i \frac{\partial}{\partial x^j} \Psi_{n1m}(\mathbf{x}) \Big|_{\mathbf{x}=0} \quad (\text{C.2.18})$$

appear. Using the explicit form of the wave function in Eq. (A.3.4), and recalling, that the radial wave function of a state with angular momentum quantum number l is proportional to r^l for $r \rightarrow 0$, one finds after expanding the radial wave function in a polynomial in r with coefficients $R_{n1}^{(p)}$:

$$-\frac{i}{2} \sqrt{\frac{3}{\pi}} \frac{\partial}{\partial x^j} \left(\sum_{p=0}^{\infty} \frac{1}{p!} R_{n1}^{(p)}(0) r^p \frac{\mathbf{x} \cdot \boldsymbol{\epsilon}^{(m)}}{r} \right) \Big|_{\mathbf{x}=0} \xrightarrow{r \rightarrow 0} -\frac{i}{2} \sqrt{\frac{3}{\pi}} \frac{\partial}{\partial x^j} \left(R_{n1}^{(1)}(0) r \frac{\mathbf{x} \cdot \boldsymbol{\epsilon}^{(m)}}{r} \right) \Big|_{\mathbf{x}=0}. \quad (\text{C.2.19})$$

Thus finally

$$\int \frac{d^3 k k_j}{(2\pi)^3} \tilde{\Psi}_{n1m}(\mathbf{k}) = -i \frac{\partial}{\partial x^j} \Psi_{n1m}(\mathbf{x}) \Big|_{\mathbf{x}=0} = -i \epsilon_j^{(m)} \sqrt{\frac{3}{4\pi}} R_{n1}^{(1)}(0). \quad (\text{C.2.20})$$

With Eq. (C.2.20) one can calculate the amplitude in (C.2.17):

$$i\mathcal{M}(^1P_1[Q\bar{Q}] \rightarrow e^+e^-) = \frac{3e^2 Q_e Q_Q}{M^3} \sqrt{\frac{2M}{\pi}} [\bar{u}_e(p) \gamma_j v_e(p')] (n^{(m)})^j R_{n1}^{(1)}(0). \quad (\text{C.2.21})$$

The squared amplitude is obtained in the heavy-quark limit

$$\begin{aligned} \frac{1}{3} \sum_{m, \lambda_{e^+}, \lambda_{e^-}} |\mathcal{M}(^1P_1[Q\bar{Q}] \rightarrow e^+e^-)|^2 &= \frac{6e^4 Q_Q^2}{\pi M^5} \text{Tr}[\not{p} \gamma_j \not{p}' \gamma_k] \sum_m n^{(m)*j} n^{(m)*k} |R_{n1}^{(1)}(0)|^2, \\ &= \frac{384\pi\alpha^2 Q_Q^2}{M^3} |R_{n1}^{(1)}(0)|^2, \end{aligned} \quad (\text{C.2.22})$$

in which the sum runs over the final state polarization m and the electron spins λ_{e^+} and λ_{e^-} . The tetraquark leptonic decay width is then given by

$$\Gamma(^1P_1[Q\bar{Q}] \rightarrow e^+e^-) = \frac{|\mathbf{p}|}{8\pi M^2} \frac{1}{3} \sum_{m, \lambda_{e^+}, \lambda_{e^-}} |\mathcal{M}|^2 = \frac{24\alpha^2 Q_Q^2}{M^4} |R_{n1}^{(1)}(0)|^2. \quad (\text{C.2.23})$$

This is the partial decay width for the tetraquark states in the pointlike diquark approximation. It plays a central role in our works and in this thesis.

C.3 Kinematics and phase space

In this part I give an introduction to the recursive phase space parametrization. The recursive n -body phase space is build of $n - 1$ two-body phase spaces, which are in the chosen parametrization not Lorentz invariant. The first nontrivial case is the $2 \rightarrow 3$ process in which the general case becomes apparent, as becomes clear in the following. I start with some remarks on the general $2 \rightarrow n$ case and get into detail with the $2 \rightarrow 3$ process, concentrating on the recursive parametrization.

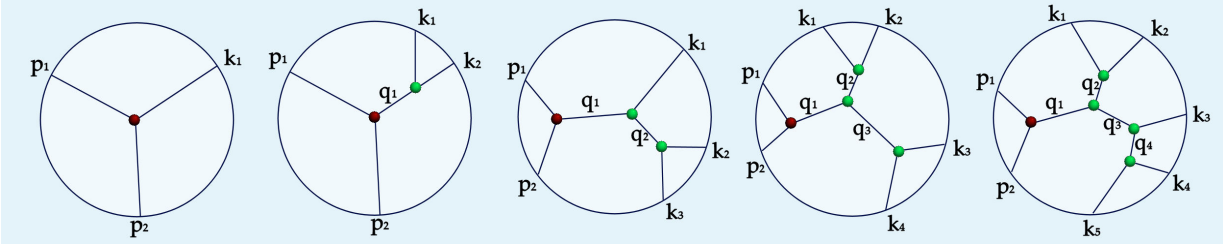


Figure C.2: The n -body phase space for $n \leq 5$. Each green dot corresponds to a two-body phase space and the red dot corresponds to the initial-state phase space.

The phase space for the final state particles of a $2 \rightarrow n$ process, in which two particles collide in a beam, can be parametrized by

$$\#\text{d.o.f}(2 \rightarrow n) = 3n - 4 \quad (\text{C.3.1})$$

independent variables. The dependence of one parameter, the rotation along the beam axis, is trivial. For a $2 \rightarrow 2$ process for example, the two independent final state variables are t and ϕ (the Mandelstam variable and the rotation around the beam axis respectively). Processes are usually characterized by the final state variables, while the initial state variables (like the center of mass energy \sqrt{s}) are assumed to be constant input parameters. Compared, the $1 \rightarrow m$ process has $3m - 4$ independent final state variables. Detailed information on the different cases can be found in Ref. [115], while here I concentrate on the former.

The differential n -body phase space is given by

$$d\Phi_n(p_1 + p_2; k_1, \dots, k_n) = \delta^{(4)}\left(p_1 + p_2 - \sum_{i=1}^n k_i\right) \prod_{i=1}^n \frac{d^3 k_i}{(2\pi)^3 2E_i}, \quad (\text{C.3.2})$$

in which k_i are the outgoing momenta, p_i are the incoming momenta and $E_i = k_{i0}$ are the energies of the outgoing particles. Inserting the delta function $d^4 q \delta^{(4)}(q - \sum_{i=1}^j k_i)$, one can construct a recurrence relation and rewrite Eq. (C.3.2) in the form

$$d\Phi_n(p_1 + p_2; k_1, \dots, k_n) = d\Phi_j(q; k_1, \dots, k_j) d\Phi_{n-j+1}(p_1 + p_2; q, k_{j+1}, \dots, k_n) (2\pi)^3 dq^2, \quad (\text{C.3.3})$$

which defines the new differential *internal* momentum q . The diagrams in Fig. C.2 can be understood as a diagrammatic realization of the recurrence relation in Eq. (C.3.3), in which the recurrence relation is used to describe the full phase space by adequate combinations of two-body phase spaces. The term two-body phase space is, however, slightly misleading, since the corresponding phase space has in general only the form of the two-body phase space (a more accurate denotation might be two-momentum phase space). To every green dot corresponds such a phase space and an internal momentum q_i . The first internal momentum is always given by $q_1 = p_1 + p_2$ with $q_1^2 = s$, yielding the (constant) squared center of mass energy. The red dot corresponds to the initial-state particles which play a special role, because their kinematics is constrained by the beam pipe. The $n = 1$ case is obviously fully determined. Every additional final-state particle introduces a new green dot and therefore three new degrees of freedom to the phase-space integral, as given in Eq. (C.3.1). The lines in the diagrams in Fig. C.2 correspond *only* to the choice of parametrization *not*

to a Feynman diagrammatic notation, as will become clear in the following, *i.e.* the lines do not necessarily correspond to particle exchange. I stress this to avoid confusion, since the diagrams can look exactly the same and in the case presented in Sec. 3.8.1 they do indeed. Usually one is always keen to choose the phase space parametrization to reflect the propagator structure of the Feynman diagrams, since equations tend to adopt a simpler form in this case. Using Eqs. (C.3.2) and (C.3.3), the three-particle phase space (third diagram in Fig. C.2) is given by

$$\begin{aligned} d\Phi_3(p_1 + p_2; k_1, k_2, k_3) &= \delta^{(4)}(p_1 + p_2 - k_1 - k_2 - k_3) \frac{d^3 k_1}{(2\pi)^3 2k_1^0} \frac{d^3 k_2}{(2\pi)^3 2k_2^0} \frac{d^3 k_3}{(2\pi)^3 2k_3^0}, \\ &= d\Phi_2(p_1 + p_2; k_1, q_2) d\Phi_2(q_2; k_2, k_3) (2\pi)^3 dq_2^2, \end{aligned} \quad (\text{C.3.4})$$

where $(k_2 + k_3)^2 = q_2^2$. Note, that each two-body phase space $d\Phi_2$ in the last line is Lorentz invariant.

The diagrams in Fig. C.2 have a supplemental use if one interprets the length of the inner lines with momenta q_i as the value of 3-momentum \mathbf{q}_i exchanged. By choice of coordinate frame one can always choose a particular frame, in which the i th line has zero length ($\mathbf{q}_i = 0$). In this case two green dots (or the red and the first green dot) are contracted and eventually coincide (indicated by a blue dot) and 2 pairs of the 4 attached momenta are in a back-to-back configuration. This frame may then be described by the invariant mass and two angles, pictured in Fig. C.3 (left), in which the two-body phase space takes the form

$$d\Phi_2(q_i + q_j; q_k, q_l) = \frac{\sqrt{\lambda((q_i + q_j)^2, q_k^2, q_l^2)}}{8(q_i + q_j)^2} d\phi d \cos \theta \quad (\text{C.3.5})$$

with kinematical function

$$\lambda(x, y, z) \equiv (x - y - z)^2 - 4yz. \quad (\text{C.3.6})$$

Every of the $n - 1$ blue dots defines such a center of mass frame, and the four-vectors described in one frame are connected through $n - 2$ sets of Lorentz boost and rotations, *i.e.* the transformations to change the coordinate system from one rest frame to another. The $2 \rightarrow 2$ case is trivial in the sense, that only one contraction is possible. It is usually most convenient to choose the laboratory frame (e^+e^- rest frame) for calculating the cross section. This is the reason for the initial statement, that the $2 \rightarrow 3$ process is the first non-trivial case, in which boost and rotations are indispensable, since two contractions are necessary to divide the phase space of the differential cross section in two-body phase spaces. The two possible contractions for the $2 \rightarrow 3$ case are pictured in Fig. C.3 (right).

As an example I give the phase space parametrization needed in Sec. 3.8 explicitly below. In this work the process $e^+(p_1)e^-(p_2) \rightarrow \Upsilon(nS)(p)P(k_1)P'(k_2)$ is parametrized. The momenta are assigned to the particles as shown above and in Fig. C.4 (deviating slightly from the above definitions, to match the equations in Sec. 3.8). Here Fig. C.4 is the more explicit version of Fig. C.3 (right) for this process. In this case the interchange of the intermediate resonances coincides with the third diagram in Fig. C.2. Note, that in an equivalent way I could also have chosen the two-body phase space of $\Upsilon(nS)$ and P instead of P and P' , in which the Feynman diagrams for resonance interchange would deviate from the third diagram in Fig. C.2.

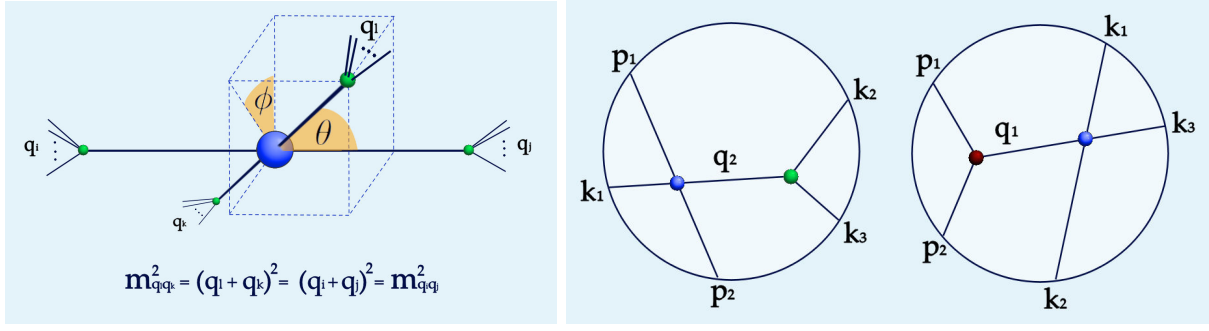


Figure C.3: Left frame: Two particle phase space. The blue dot corresponds to the rest frame with $\mathbf{q}_k + \mathbf{q}_l = 0$ holds for the 3-momenta. In this frame the kinematics is described by two angles ϕ and θ and the Lorentz-invariant quantity m_{q_i, q_j}^2 . The lines at the green dots indicate, that the momenta $q_{i,j,k}$ are given by the sum of the attached external momenta (for example $q_2 = k_2 + k_3$ in the right diagram of the right frame, etc..). Right frame: Example for the contractions of the $2 \rightarrow 3$ process of Fig. C.2, defining two rest frames. Two rotations (by θ and ϕ) and one boost connects both frames.

Choosing the e^+e^- rest frame for $d\Phi_2(p_1 + p_2; p, q)$ and the PP' rest frame for $d\Phi_2(q; k_1, k_2)$, one gets

$$\begin{aligned}
d\Phi_2(p_1 + p_2; p, q) &= d\Phi_2(p'_1 + p'_2; p', q') = \delta^{(4)}(p'_1 + p'_2 - p' - q') \frac{d^3 p'}{(2\pi)^3 2p^{0'}} \frac{d^3 q'}{(2\pi)^3 2q^{0'}} \\
&= \frac{\lambda^{1/2}(s, m_\Upsilon^2, M_{PP'}^2)}{512\pi^6 s} d\cos\vartheta_{ee} d\varphi_{ee}, \\
d\Phi_2(q; k_1, k_2) &= \delta^{(4)}(q - k_1 - k_2) \frac{d^3 k_1}{(2\pi)^3 2k_1^0} \frac{d^3 k_2}{(2\pi)^3 2k_2^0} \\
&= \frac{\lambda^{1/2}(M_{PP'}^2, m_P^2, m_{P'}^2)}{512\pi^6 M_{PP'}^2} d\cos\theta d\phi, \tag{C.3.7}
\end{aligned}$$

in which $s = (p_1 + p_2)^2$, and the primed momenta are defined in the e^+e^- rest frame. Thus the complete three-body phase space reads:

$$\begin{aligned}
d\Phi_3(p_1 + p_2; p, k_1, k_2) &= \frac{\lambda^{1/2}(s, m_\Upsilon^2, M_{PP'}^2)}{512\pi^6 s} \frac{\lambda^{1/2}(M_{PP'}^2, m_P^2, m_{P'}^2)}{512\pi^6 M_{PP'}^2} \\
&\times d\cos\theta d\phi d\cos\vartheta_{ee} d\varphi_{ee} (2\pi)^3 dM_{PP'}^2. \tag{C.3.8}
\end{aligned}$$

In the following I give the phase-space parametrization in full detail for the process $e^+e^- \rightarrow \Upsilon(1S)PP'$, in which P and P' are scalar mesons. Electron masses are neglected and the shorthand notation $\sin(\alpha) \equiv s_\alpha$ and $\cos(\alpha) \equiv c_\alpha$ is used.

The dipion rest frame: The z -axis is chosen to be in the direction of the momenta for Y_b and $\Upsilon(1S)$, and the momenta of e^+ and e^- are in the x - z plane, as shown in Fig. C.4 (left). In this frame the momenta read:

$$p_1^\mu = \frac{1}{2} \left(q^0 - |\mathbf{q}|c_{\vartheta_{ee}}, \sqrt{s}s_{\vartheta_{ee}}, 0, |\mathbf{q}| - q^0c_{\vartheta_{ee}} \right),$$

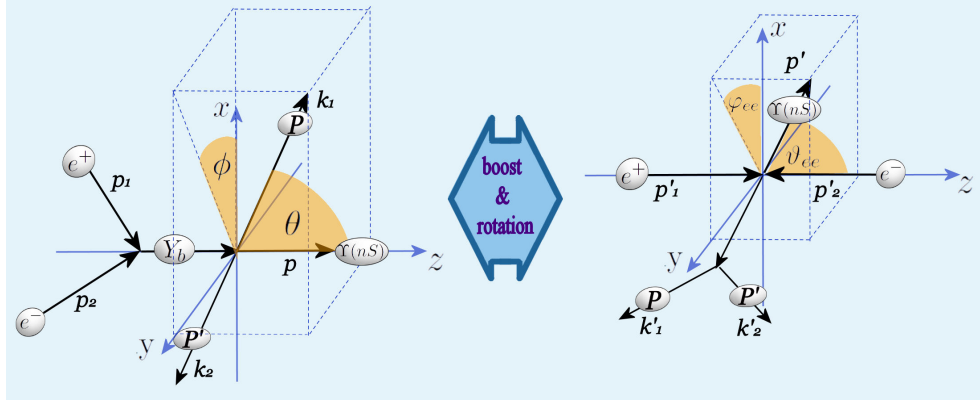


Figure C.4: Explicit picture of the two right figures in Fig. C.3 for the process $e^+(p_1)e^-(p_2) \rightarrow \Upsilon(nS)(p)P(k_1)P'(k_2)$ in the rest frame of PP' (left) and in the rest frame of the e^+e^- pair (right).

$$\begin{aligned}
p_2^\mu &= \frac{1}{2} (q^0 + |\mathbf{q}|c_{\vartheta_{ee}}, -\sqrt{s}s_{\vartheta_{ee}}, 0, |\mathbf{q}| + q^0c_{\vartheta_{ee}}), \\
q^\mu &= (q^0, 0, 0, |\mathbf{q}|), \\
p^\mu &= (p^0, 0, 0, |\mathbf{q}|), \\
k_1^\mu &= (k_1^0, |\mathbf{k}|s_\theta c_\phi, |\mathbf{k}|s_\theta s_\phi, |\mathbf{k}|c_\theta), \\
k_2^\mu &= (k_2^0, -|\mathbf{k}|s_\theta c_\phi, -|\mathbf{k}|s_\theta s_\phi, -|\mathbf{k}|c_\theta),
\end{aligned} \tag{C.3.9}$$

in which the angle ϑ_{ee} is defined in the rest frame of the e^+e^- pair, as shown in Fig. C.4 (right). The variables q^0 , p^0 , k_1^0 , k_2^0 , $|\mathbf{q}|$ and $|\mathbf{k}|$ are given in terms of $s \equiv q^2 = (p_1 + p_2)^2$ and $M_{PP'}^2 \equiv (k_1 + k_2)^2$ by

$$\begin{aligned}
q^0 &= \frac{s - m_\Upsilon^2 + M_{PP'}^2}{2M_{PP'}}, & p^0 &= q^0 - M_{PP'} = \frac{s - m_\Upsilon^2 - M_{PP'}^2}{2M_{PP'}}, \\
|\mathbf{q}|^2 &= (q^0)^2 - s = (p^0)^2 - m_\Upsilon^2, \\
k_1^0 &= \sqrt{|\mathbf{k}|^2 + m_P^2} = \frac{M_{PP'}}{2} \sqrt{1 + \frac{(2M_{PP'}^2 + m_P^2 - m_{P'}^2)(m_P^2 - m_{P'}^2)}{M_{PP'}^4}}, \\
k_2^0 &= \sqrt{|\mathbf{k}|^2 + m_{P'}^2} = \frac{M_{PP'}}{2} \sqrt{1 + \frac{(2M_{PP'}^2 + m_{P'}^2 - m_P^2)(m_{P'}^2 - m_P^2)}{M_{PP'}^4}}, \\
|\mathbf{k}|^2 &= \frac{M_{PP'}^2}{4} \left(1 - \frac{(m_P + m_{P'})^2}{M_{PP'}^2}\right) \left(1 - \frac{(m_P - m_{P'})^2}{M_{PP'}^2}\right),
\end{aligned} \tag{C.3.10}$$

in which $M_{PP'}^2 = (k_1 + k_2)^2 = (k_1^0 + k_2^0)^2$. The polarization vectors for the outgoing $\Upsilon(1S)$ are given by

$$\epsilon_\Upsilon^{*\mu}(\lambda_\Upsilon = 0) = \frac{1}{m_\Upsilon} (|\mathbf{q}|, 0, 0, p^0), \quad \epsilon_\Upsilon^{*\mu}(\lambda_\Upsilon = \pm 1) = \frac{1}{\sqrt{2}} (0, \mp 1, i, 0) \tag{C.3.11}$$

for the longitudinal and transverse polarizations, respectively.

The e^+e^- rest frame: The z -axis is chosen to be in the direction of the momenta for e^+ and e^- , as shown in Fig. C.4 (right):

$$\begin{aligned} p'^\mu &= \left(\frac{(q \cdot p)}{\sqrt{s}}, \frac{|\mathbf{q}|M_{PP'}}{\sqrt{s}} s_{\vartheta_{ee}} c_{\varphi_{ee}}, \frac{|\mathbf{q}|M_{PP'}}{\sqrt{s}} s_{\vartheta_{ee}} s_{\varphi_{ee}}, \frac{|\mathbf{q}|M_{PP'}}{\sqrt{s}} c_{\vartheta_{ee}} \right), \\ p_1'^\mu &= \left(\frac{\sqrt{s}}{2}, 0, 0, -\frac{\sqrt{s}}{2} \right), \quad p_2'^\mu = \left(\frac{\sqrt{s}}{2}, 0, 0, \frac{\sqrt{s}}{2} \right), \quad q'^\mu = (\sqrt{s}, \mathbf{0}), \end{aligned} \quad (\text{C.3.12})$$

in which the primes represent the momenta in the e^+e^- rest frame. The polarization vectors for the outgoing $\Upsilon(1S)$ are given by

$$\begin{aligned} \epsilon_{\Upsilon}^{*\mu}(\lambda_{\Upsilon} = 0) &= \frac{1}{m_{\Upsilon}} \left(\frac{|\mathbf{q}|M_{PP'}}{\sqrt{s}}, \frac{(q \cdot p)}{\sqrt{s}} s_{\vartheta_{ee}} c_{\varphi_{ee}}, \frac{(q \cdot p)}{\sqrt{s}} s_{\vartheta_{ee}} s_{\varphi_{ee}}, \frac{(q \cdot p)}{\sqrt{s}} c_{\vartheta_{ee}} \right), \\ \epsilon_{\Upsilon}^{*\mu}(\lambda_{\Upsilon} = \pm 1) &= \frac{1}{\sqrt{2}} (0, \mp c_{\vartheta_{ee}} c_{\varphi_{ee}} - i s_{\varphi_{ee}}, \mp c_{\vartheta_{ee}} s_{\varphi_{ee}} + i c_{\varphi_{ee}}, \pm s_{\vartheta_{ee}}). \end{aligned} \quad (\text{C.3.13})$$

Both frames: The momenta $p_{1,2}$ for the e^\pm in the PP' rest frame are obtained from the corresponding momenta in the e^+e^- rest frame via a rotation and a subsequent boost:

$$p_{1,2}^\mu = \Lambda^\mu{}_\nu \mathcal{R}^\nu{}_\sigma p_{1,2}^{\prime\sigma}, \quad (\text{C.3.14})$$

in which the boost and rotation matrices Λ and \mathcal{R} are given by

$$\begin{aligned} \mathcal{R}^\mu{}_\nu &= \begin{pmatrix} 1 & 0 & 0 & 0 \\ 1 & \cos(-\vartheta_{ee}) & 0 & \sin(-\vartheta_{ee}) \\ 0 & 0 & 1 & 0 \\ 0 & -\sin(-\vartheta_{ee}) & 0 & \cos(-\vartheta_{ee}) \end{pmatrix} \begin{pmatrix} 1 & 0 & 0 & 0 \\ 0 & \cos(-\varphi_{ee}) & -\sin(-\varphi_{ee}) & 0 \\ 0 & \sin(-\varphi_{ee}) & \cos(-\varphi_{ee}) & 0 \\ 0 & 0 & 0 & 1 \end{pmatrix}, \\ \Lambda^\mu{}_\nu &= \begin{pmatrix} q^0/\sqrt{s} & 0 & 0 & |\mathbf{q}|/\sqrt{s} \\ 0 & 1 & 0 & 0 \\ 0 & 0 & 1 & 0 \\ |\mathbf{q}|/\sqrt{s} & 0 & 0 & q^0/\sqrt{s} \end{pmatrix}. \end{aligned} \quad (\text{C.3.15})$$

The scalar products of the above momenta are given by

$$\begin{aligned} p_1^2 &= p_2^2 = 0, \quad q^2 = s, \quad p^2 = m_{\Upsilon}^2, \quad k_1^2 = k_2^2 = m_{\pi}^2, \\ p_1 \cdot p_2 &= p_1 \cdot q = p_2 \cdot q = \frac{s}{2}, \\ p_1 \cdot p &= \frac{1}{2} (q^0 p^0 - |\mathbf{q}|^2 + M_{PP'} |\mathbf{q}| c_{\vartheta_{ee}}), \quad p_2 \cdot p = \frac{1}{2} (q^0 p^0 - |\mathbf{q}|^2 - M_{PP'} |\mathbf{q}| c_{\vartheta_{ee}}), \\ p_1 \cdot k_1 &= \frac{1}{2} \left[\frac{M_{PP'}}{2} (q^0 - |\mathbf{q}| c_{\vartheta_{ee}}) - \sqrt{s} |\mathbf{k}| s_{\vartheta_{ee}} s_{\theta} c_{\phi} - (|\mathbf{q}| - q^0 c_{\vartheta_{ee}}) |\mathbf{k}| c_{\theta} \right], \\ p_1 \cdot k_2 &= \frac{1}{2} \left[\frac{M_{PP'}}{2} (q^0 - |\mathbf{q}| c_{\vartheta_{ee}}) + \sqrt{s} |\mathbf{k}| s_{\vartheta_{ee}} s_{\theta} c_{\phi} + (|\mathbf{q}| - q^0 c_{\vartheta_{ee}}) |\mathbf{k}| c_{\theta} \right], \\ p_2 \cdot k_1 &= \frac{1}{2} \left[\frac{M_{PP'}}{2} (q^0 + |\mathbf{q}| c_{\vartheta_{ee}}) + \sqrt{s} |\mathbf{k}| s_{\vartheta_{ee}} s_{\theta} c_{\phi} - (|\mathbf{q}| + q^0 c_{\vartheta_{ee}}) |\mathbf{k}| c_{\theta} \right], \\ p_2 \cdot k_2 &= \frac{1}{2} \left[\frac{M_{PP'}}{2} (q^0 + |\mathbf{q}| c_{\vartheta_{ee}}) - \sqrt{s} |\mathbf{k}| s_{\vartheta_{ee}} s_{\theta} c_{\phi} + (|\mathbf{q}| + q^0 c_{\vartheta_{ee}}) |\mathbf{k}| c_{\theta} \right], \end{aligned}$$

$$\begin{aligned}
q.p &= q^0 p^0 - |\mathbf{q}|^2 = \frac{s + m_\Upsilon^2 - M_{PP'}^2}{2}, \\
q.k_1 &= \frac{q^0 M_{PP'}}{2} - |\mathbf{q}||\mathbf{k}|c_\theta, & q.k_2 &= \frac{q^0 M_{PP'}}{2} + |\mathbf{q}||\mathbf{k}|c_\theta, \\
p.k_1 &= \frac{p^0 M_{PP'}}{2} - |\mathbf{q}||\mathbf{k}|c_\theta, & p.k_2 &= \frac{p^0 M_{PP'}}{2} + |\mathbf{q}||\mathbf{k}|c_\theta, \\
k_1.k_2 &= \frac{M_{PP'}^2}{2} - m_P^2 - m_{P'}^2,
\end{aligned} \tag{C.3.16}$$

and

$$\begin{aligned}
\epsilon_\Upsilon^*(\pm 1).k_1 &= -\epsilon_\Upsilon^*(\pm 1).k_2 = \pm \frac{|\mathbf{k}|}{\sqrt{2}} s_\theta e^{\mp i\phi}, \\
\epsilon_\Upsilon^*(0).k_1 &= \frac{1}{m_\Upsilon} \left(\frac{|\mathbf{q}|M_{PP'}}{2} - p^0 |\mathbf{k}|c_\theta \right), \\
\epsilon_\Upsilon^*(0).k_2 &= \frac{1}{m_\Upsilon} \left(\frac{|\mathbf{q}|M_{PP'}}{2} + p^0 |\mathbf{k}|c_\theta \right).
\end{aligned} \tag{C.3.17}$$

C.4 Background and resonance contributions

In this part of the appendix I explain the separate contributions in the determination of the cross section of the process $e^+e^- \rightarrow Y_b \rightarrow \Upsilon(nS)PP'$, which is undertaken in Sec. 3.8.1. In simplified words, this section gives an overview over the invariant mass $M_{PP'}$ behavior of the continuum and resonant contributions and the next Sec. C.5, "helicity amplitudes", deals with the angular distributions.

C.4.1 Continuum contribution

The underlying process for the continuum contribution in terms of quark-rearrangement diagrams is shown in Fig. C.5. The general form of the amplitude for $V'(q, \epsilon_{Y_b}) \rightarrow$

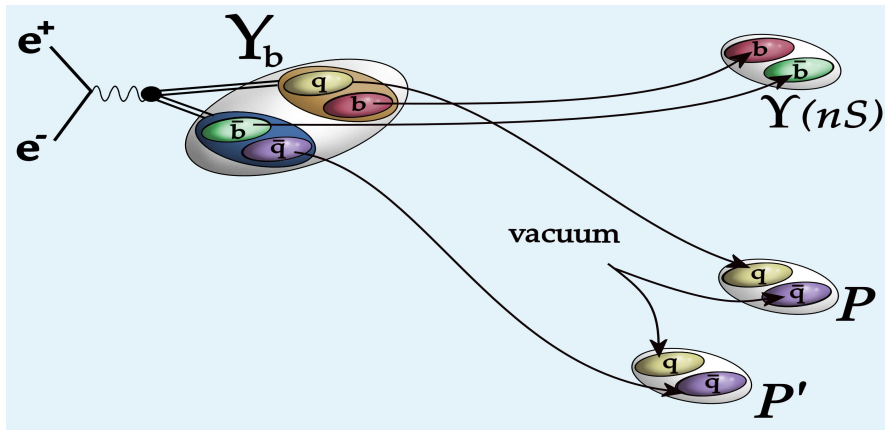


Figure C.5: Schematic diagram of the Zweig allowed continuum quark rearrangement, in which one light-quark pair pops up from the QCD background.

$V(p, \epsilon_\Upsilon)\pi(k_1)\pi(k_2)$ in the soft-pion limit was derived with PCAC (“Partially Conserved Axial Current” hypothesis) by Brown and Cahn [95]. In the soft-pion limit, *i.e.* in the lowest order in the pion momentum expansion, the amplitude is given in the non-relativistic form as [116]

$$\begin{aligned} \mathcal{M}(V' \rightarrow V\pi\pi) = f_\pi^{-2} \left\{ (\epsilon_{Y_b} \cdot \epsilon_\Upsilon^*) [2Ak_1 \cdot k_2 + BE_1E_2 + \lambda m_\pi^2] \right. \\ \left. + C [(\epsilon_{Y_b} \cdot k_1)(\epsilon_\Upsilon^* \cdot k_2) + (\epsilon_{Y_b} \cdot k_2)(\epsilon_\Upsilon^* \cdot k_1)] \right\}, \end{aligned} \quad (\text{C.4.1})$$

in which E_1 and E_2 are the energies of the two pions in the rest frame of the initial state and $M_{PP'}^2 \equiv (k_1 + k_2)^2$ is the invariant mass squared of the two pions. Relativistic corrections have been dropped in the derivation. The term λm_π^2 is called the σ term in [95] and vanishes in the chiral limit. Taking the soft pion limit and neglecting pion-pion rescattering effects, the form factors A , B , C and λ are constant. Here I consider the continuum contribution for $Y_b \rightarrow \Upsilon(1S)PP'$ in the case where Y_b may not be on-shell and the mass of P may be different from that of P' . The product E_1E_2 , appearing in the continuum amplitude in Eq. (C.4.1), is given by

$$\begin{aligned} E_1E_2 &= \left(\frac{q^0 k_1^0 - |\mathbf{q}||\mathbf{k}| \cos \theta}{\sqrt{s}} \right) \left(\frac{q^0 k_2^0 + |\mathbf{q}||\mathbf{k}| \cos \theta}{\sqrt{s}} \right), \\ &= \frac{(q^0)^2 k_1^0 k_2^0 + q^0(k_1^0 - k_2^0)|\mathbf{q}||\mathbf{k}| \cos \theta - |\mathbf{q}|^2 |\mathbf{k}|^2 \cos^2 \theta}{s}, \end{aligned} \quad (\text{C.4.2})$$

in which θ is the angle between q and k_1 in the PP' rest frame. Here the $\cos \theta$ term corresponds to a P -wave amplitude with $Y_1^0(\theta, \phi) = \sqrt{3/4\pi} \cos \theta$, which vanishes if P and P' have an identical mass. Since the PP' system must be either an S -wave or a D -wave, the $\cos \theta$ term is dropped for consistency. We then have

$$E_1E_2 \Rightarrow \frac{3(q^0)^2 k_1^0 k_2^0 - |\mathbf{q}|^2 |\mathbf{k}|^2}{3s} - \frac{|\mathbf{q}|^2 |\mathbf{k}|^2}{s} \left(\cos^2 \theta - \frac{1}{3} \right). \quad (\text{C.4.3})$$

Using this equation, the continuum contribution in Eq. (C.4.1) becomes

$$\begin{aligned} (\mathcal{M}^{\text{continuum}})_{\mu\nu} &= g_{\mu\nu} \frac{A}{f_P f_{P'}} (M_{PP'}^2 - m_P^2 - m_{P'}^2) + g_{\mu\nu} \frac{B}{f_P f_{P'}} E_1 E_2 \\ &\quad + (k_{1\mu} k_{2\nu} + k_{2\mu} k_{1\nu}) \frac{C}{f_P f_{P'}}, \\ &= g_{\mu\nu} \left[\frac{A}{f_P f_{P'}} (M_{PP'}^2 - m_P^2 - m_{P'}^2) + \frac{B}{f_P f_{P'}} \frac{3(q^0)^2 k_1^0 k_2^0 - |\mathbf{q}|^2 |\mathbf{k}|^2}{3s} \right] \\ &\quad + g_{\mu\nu} \left[-\frac{B}{f_P f_{P'}} \frac{|\mathbf{q}|^2 |\mathbf{k}|^2}{s} \right] \left(\cos^2 \theta - \frac{1}{3} \right) \\ &\quad + (k_{1\mu} k_{2\nu} + k_{2\mu} k_{1\nu}) \frac{C}{f_P f_{P'}}. \end{aligned} \quad (\text{C.4.4})$$

Note, that the coefficient of the A term is originated from $(k_1 \cdot k_2) = (M_{PP'}^2 - m_P^2 - m_{P'}^2)/2$. We adopted this expression as the continuum contribution.

In summary, we defined the continuum amplitudes as

$$\mathcal{M}_1^C(M_{PP'}^2) = \frac{A}{f_P f_{P'}} (M_{PP'}^2 - m_P^2 - m_{P'}^2) + \frac{B}{f_P f_{P'}} \frac{3(q^0)^2 k_1^0 k_2^0 - |\mathbf{q}|^2 |\mathbf{k}|^2}{3s},$$

$$\begin{aligned}\mathcal{M}_2^C(M_{PP'}^2) &= -\frac{B}{f_P f_{P'}} \frac{|\mathbf{q}|^2 |\mathbf{k}|^2}{s}, \\ \mathcal{M}_3^C(M_{PP'}^2) &= \frac{C}{f_P f_{P'}}.\end{aligned}\tag{C.4.5}$$

The energies of PP' in the rest frame of the initial state Y_b are expressed in terms of the variables in the PP' rest frame $|\vec{q}|$, $|\vec{k}|$ and θ as follows:

$$E_1 = \frac{m_{Y_b}^2 - m_\Upsilon^2 + M_{PP'}^2 - 4|\vec{q}||\vec{k}| \cos \theta}{4m_{Y_b}}, \quad E_2 = \frac{m_{Y_b}^2 - m_\Upsilon^2 + M_{PP'}^2 + 4|\vec{q}||\vec{k}| \cos \theta}{4m_{Y_b}}.\tag{C.4.6}$$

The product of them is then given by

$$\begin{aligned}E_1 E_2 &= \frac{(m_{Y_b}^2 - m_\Upsilon^2 + M_{PP'}^2)^2 - 16|\vec{q}|^2 |\vec{k}|^2 \cos^2 \theta}{16m_{Y_b}^2}, \\ &= \frac{(m_{Y_b}^2 - m_\Upsilon^2 + M_{PP'}^2)^2 - [(m_{Y_b}^2 - m_\Upsilon^2 + M_{PP'}^2)^2 - 4m_{Y_b}^2 M_{PP'}^2] \left(1 - \frac{4m_\pi^2}{M_{PP'}^2}\right) \cos^2 \theta}{16m_{Y_b}^2}, \\ &= \frac{1}{6} \left\{ \frac{M_{PP'}^2}{2} \left(1 - \frac{4m_\pi^2}{M_{PP'}^2}\right) + \frac{(m_{Y_b}^2 - m_\Upsilon^2 + M_{PP'}^2)^2}{4m_{Y_b}^2} \left(1 + \frac{2m_\pi^2}{M_{PP'}^2}\right) \right. \\ &\quad \left. - \frac{3}{2} \left[\frac{(m_{Y_b}^2 - m_\Upsilon^2 + M_{PP'}^2)^2}{4m_{Y_b}^2} - M_{PP'}^2 \right] \left(1 - \frac{4m_\pi^2}{M_{PP'}^2}\right) \left(\cos^2 \theta - \frac{1}{3}\right) \right\}.\end{aligned}\tag{C.4.7}$$

In the limit of heavy Y_b and Υ , one has $M_{PP'} \ll m_{Y_b} \approx m_\Upsilon$ and

$$\frac{(m_{Y_b}^2 - m_\Upsilon^2 + M_{PP'}^2)^2}{4m_{Y_b}^2} \approx \frac{(m_{Y_b}^2 - m_\Upsilon^2)^2}{4m_{Y_b}^2} \approx \frac{(m_{Y_b} - m_\Upsilon)^2 4m_{Y_b}^2}{4m_{Y_b}^2} \approx (m_{Y_b} - m_\Upsilon)^2 \equiv (\Delta M)^2,\tag{C.4.8}$$

in which the approximation $m_{Y_b} + m_\Upsilon \approx 2m_{Y_b}$ and $\Delta M \equiv m_{V'} - m_V$ is used.

If one keeps the C terms in Eq. (C.4.1), one finds the expression derived by Novikov and Shifman [97], using Eqs. (C.4.7) and (C.4.8), the above equation can be rewritten as

$$\begin{aligned}\mathcal{M}(V' \rightarrow V\pi\pi) &= \frac{F}{f_\pi^2} (\epsilon_{Y_b} \cdot \epsilon_\Upsilon^*) \left[M_{PP'}^2 - \beta(\Delta M)^2 \left(1 + \frac{2m_\pi^2}{M_{PP'}^2}\right) \right. \\ &\quad \left. + \frac{3}{2} \beta [(\Delta M)^2 - M_{PP'}^2] \left(1 - \frac{4m_\pi^2}{M_{PP'}^2}\right) \left(\cos^2 \theta - \frac{1}{3}\right) \right] \\ &\quad + \frac{C}{f_\pi^2} [(\epsilon_{Y_b} \cdot k_1)(\epsilon_\Upsilon^* \cdot k_2) + (\epsilon_{Y_b} \cdot k_2)(\epsilon_\Upsilon^* \cdot k_1)],\end{aligned}\tag{C.4.9}$$

in which $F \equiv A$ and $\beta \equiv -B/(6A)$. This continuum contribution describes the underlying process of the bottomonia transitions, which is explained in Sec. 3.3. The parameter β is usually of order $\mathcal{O}(1/10)$ for the bottomonia. Hence the D-wave contribution is small. The underlying process involves two gluon annihilation and is pictured in Fig. 3.13, where also the decay $\Upsilon(4S) \rightarrow \Upsilon(1S)\pi^+\pi^-$ as a representative $\Upsilon(nS)$ decay is shown.

We assumed, that all the form factors A , B and C in Eq. (C.4.1) have a common phase, originating from final-state interactions. Consequently, the parameter β is real, and F and C have the same phase.

The C term, originating from a spin-dependent interaction, is suppressed by the heavy-quark mass. Hence, neglecting the λ and C terms, one finds

$$\mathcal{M}(V' \rightarrow V\pi\pi) \approx f_\pi^{-2}(\epsilon_{Y_b} \cdot \epsilon_Y^*) F [(M_{PP'}^2 - 2m_\pi^2) - 6\beta E_1 E_2], \quad (\text{C.4.10})$$

and explicitly

$$\begin{aligned} \mathcal{M}(V' \rightarrow V\pi\pi) \approx \frac{F}{f_\pi}(\epsilon_{Y_b} \cdot \epsilon_Y^*) & \left[\left(1 - \frac{\beta}{2}\right) M_{PP'}^2 + (-2 + 2\beta) m_\pi^2 - \beta(\Delta M)^2 \left(1 + \frac{2m_\pi^2}{M_{PP'}^2}\right) \right. \\ & \left. + \beta \frac{3}{2} [(\Delta M)^2 - M_{PP'}^2] \left(1 - \frac{4m_\pi^2}{M_{PP'}^2}\right) \left(\cos^2 \theta - \frac{1}{3}\right) \right], \quad (\text{C.4.11}) \end{aligned}$$

The first line is the S -wave contribution of the dipion, whereas the second line is the D -wave contribution.

C.4.2 Scalar-resonance contribution $S \rightarrow \pi\pi$

Zweig allowed quark-rearrangement process for the 0^{++} light scalar tetraquark interchange, pictured in Fig. C.6. As described in the Eqs. (3.7.2) and (3.7.3), a two-body scattering process $ab \rightarrow R \rightarrow cd$, R being a resonance, can be described by the Breit-Wigner formula,

$$T_R(m_{ab}) \propto \frac{1}{m_{ab}^2 - m_R^2 + im_R \Gamma_R}, \quad (\text{C.4.12})$$

where m_{ab} is the invariant mass of the ab (and cd) system, M_R and Γ_R are the mass and the total decay width of R . The decay width depends in general on m_{ab} , since there is no first principle which forces the poles of the S matrix to be constant properties. In fact, the approximation of $\Gamma_R = \text{constant}$ is only valid in special cases, where the mass of the

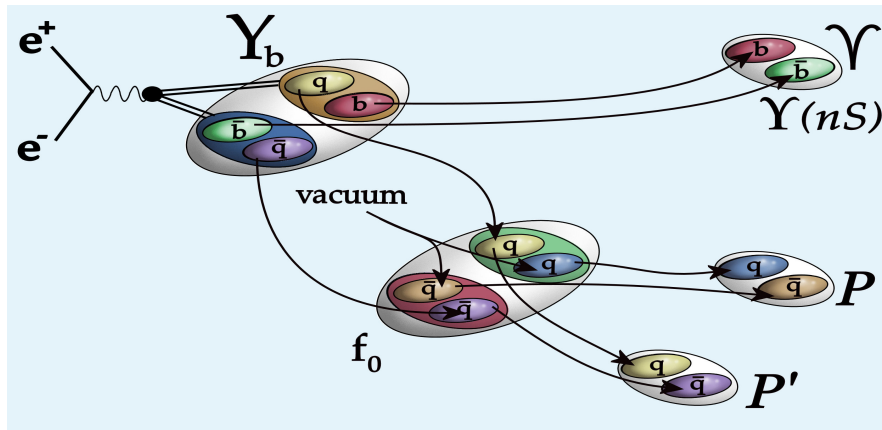


Figure C.6: Zweig allowed quark-rearrangement process for the interchange of a light scalar 0^{++} resonance.

resonance is large compared with the total decay width, and when the resonance mass is far away from thresholds. The approximation is then called *minimal width approximation*. The threshold problem also occurs in the present case for all scalar resonance contributions in the analysis of the Belle data on the exclusive channels. How to take that effect into account is described by the Flatté model [107], which is outlined below. Note, that the derivations are not only valid for scalar resonances, since the spin affects only the helicity distributions, whereas the invariant-mass distribution is for all kinds of resonances the same. However, since I only need the scalar resonances here, I will not discuss the spin part in the Flatté model.

The argument why the minimal width approximation can not (or only approximately) work at threshold is due to the fact, that a constant approximation for the width is only valid for an on-shell particle. Threshold effects are off-shell effects. First I will describe the on-shell decay, followed by the description of the Flatté model. The spin averaged partial decay width for the process $R \rightarrow PP'$ is given by

$$\Gamma_{R \rightarrow PP'}(m_R) = \frac{1}{8\pi} |\mathcal{M}|^2 \frac{|\mathbf{k}|}{m_R^2}, \quad (\text{C.4.13})$$

in which \mathbf{k} is the decay momentum defined in (3.6.2). If the decay is dominated by two-body decays one can approximate

$$\Gamma_{\text{tot}} \approx \frac{1}{8\pi} \sum_i |\mathcal{M}_i|^2 \frac{|\mathbf{k}_i|}{m_R^2}. \quad (\text{C.4.14})$$

By defining

$$\rho(s) \equiv \left[\left(1 - \frac{(m - m')^2}{s} \right) \left(1 - \frac{(m + m')^2}{s} \right) \right]^{1/2} \quad (\text{C.4.15})$$

with m and m' being the masses of P and P' respectively, one has $\mathbf{k}_i = m_R \rho_i(m_R^2)/2$. Further defining the constants f_i , called Flatté couplings, in units of energy via $f_i \equiv |\mathcal{M}_i|/\sqrt{16\pi m_R}$, the Eqs. (C.4.12) and (C.4.16) yield

$$T_r(m_{ab}) \propto \frac{1}{m_{ab}^2 - m_R^2 + i \sum_i f_i^2 \rho_i(m_R^2)} \quad \Gamma_{\text{tot}} \approx \sum_i \frac{f_i^2 \rho_i(m_R^2)}{m_R}. \quad (\text{C.4.16})$$

If the decaying particle is virtual, the particle is not decaying on-shell with mass m_R but with the energy m_{ab} , and one needs to replace $\rho_i(m_R^2) \rightarrow \rho_i(m_{ab})$. This is the Flatté model. In Fig. C.7 and C.8 a_0 is given as an example (the Flatté couplings for a_0 are listed in Tab. C.4.1). The former shows the width in dependence of the invariant mass, and the latter shows the contribution in the cross section for a single resonance exchange $|T_R(m_{ab})|^2$. The resonance a_0 has two dominant decay modes, $\eta\pi^0$ and $K\bar{K}$ also indicated in the figure. The Flatté model is compared with the constant width approximation (black line). One can see, that the decay width is enhanced smoothly at every threshold, where a new decay mode opens. The dynamic behavior at threshold is described by the phase space factor $\rho_i(m_{ab})$. Note, that beside the real (blue) part there is also an imaginary (orange) part in the decay width present when $\rho_i(s)$ becomes imaginary for $s \leq (m + m')^2$, which

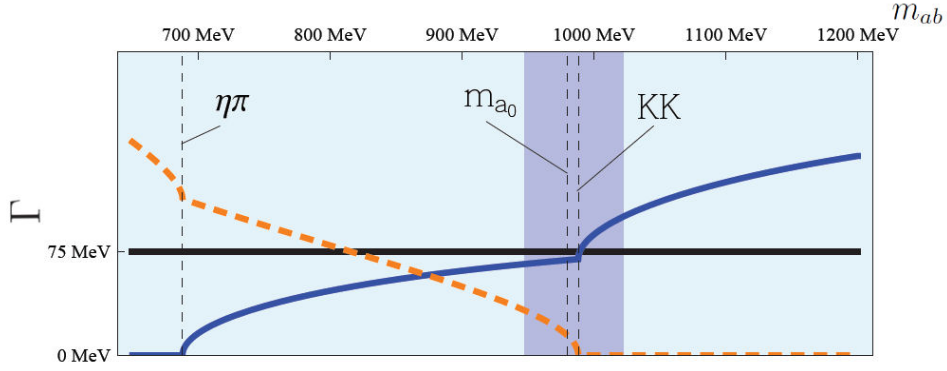


Figure C.7: Dynamic total decay width of a_0 as example for the Flatté model. The solid, blue line corresponds to the real part of the decay width and the dashed, orange line is the imaginary part. The solid black line corresponds to the minimal width approximation with the PDG value of $\Gamma \approx 75$ MeV. The shaded band of approximately 75 MeV corresponds to the energy range in which the resonance a_0 gives a sizable contribution to the amplitudes.

Table C.4.1: Masses and Flatté couplings in units of MeV.

	M_{f_0}	$f_{f_0\pi\pi}$	$f_{f_0K\bar{K}}$	M_{a_0}	$f_{a_0^0\eta\pi}$	$f_{a_0^0K\bar{K}}$
Crystal Barrel				982	324	329
BES	965	406	833			
KLOE	984	349	869	983	398	429

leads to a real contribution in the denominator of (C.4.12) and thus gives rise to a mass shift.

In our analysis we have to employ the Flatté formula for the scalar resonances $\sigma(600)$, $f_0(980)$ and $a_0^0(980)$, since their masses are located just around the $\pi\pi$ threshold for the former and the $K\bar{K}$ threshold for the latter two, as can be seen in Fig. C.7 for $a_0^0(980)$.

The couplings in (3.8.11) $g_{SPP'}$ for the scalar resonances define the amplitude by

$$\mathcal{A}(S \rightarrow PP') = g_{SPP'}(k_1 \cdot k_2) = g_{SPP'} \frac{m_S^2 - m_P^2 - m_{P'}^2}{2}. \quad (\text{C.4.17})$$

After specifying the amplitude, Eq. (C.4.13) yields a relation between the Flatté couplings $f_{SPP'}$ and the vertex couplings $g_{SPP'}$:

$$g_{SPP'} = f_{SPP'} \frac{8\sqrt{\pi}}{m_S^2 - m_P^2 - m_{P'}^2}, \quad (\text{C.4.18})$$

with the isospin relations

$$f_{f_0\pi^+\pi^-} = \sqrt{\frac{2}{3}} f_{f_0\pi\pi}, \quad f_{f_0K^+K^-} = \frac{1}{\sqrt{2}} f_{f_0K\bar{K}},$$

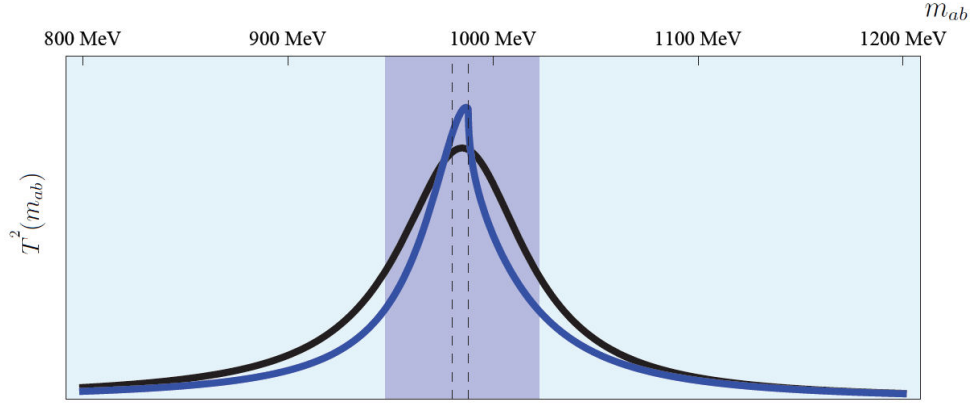


Figure C.8: Breit Wigner model for a_0 , comparison between the constant width approximation (black) and the Flatté model (blue). The shaded band indicates the constant width of $\Gamma \approx 75$ MeV, where the resonance has the dominant contribution to the amplitude.

$$f_{a_0^0 \eta \pi^0} = f_{a_0^0 \eta \pi}, \quad f_{a_0^0 K^+ K^-} = \frac{1}{\sqrt{2}} f_{a_0^0 K \bar{K}}, \quad (\text{C.4.19})$$

in which the sum over all members in one isospin multiplet is performed, *i.e.* $f_{f_0 \pi \pi}^2 = f_{f_0 \pi^+ \pi^-}^2 + f_{f_0 \pi^0 \pi^0}^2$, etc., explained in App. C.4.4. The value for the summed and exclusive couplings and amplitudes for $a_0(980) \rightarrow PP'$ and $f_0(980) \rightarrow PP'$, extracted from the data, are summarized in Tab. C.4.1 and Tab. C.4.2. The experiments, from where the data was obtained, are outlined at the end of this section.

For the σ meson, the coupling $g_{\sigma \pi^+ \pi^-}$ is extracted from the E791 data [89] with the relation

$$g_{\sigma \pi^+ \pi^-} = \frac{8m_\sigma}{m_\sigma^2 - 2m_\pi^2} \frac{\sqrt{\pi\Gamma_{\sigma \rightarrow \pi^+ \pi^-}}}{(m_\sigma^2 - 4m_\pi^2)^{1/4}} = \frac{8m_\sigma \sqrt{\pi\Gamma_\sigma \times (2/3)}}{(m_\sigma^2 - 2m_\pi^2)(m_\sigma^2 - 4m_\pi^2)^{1/4}} \approx 27 \text{ GeV}^{-1}, \quad (\text{C.4.20})$$

in which the Flatté coupling $f_{\sigma \pi \pi}$ is given by

$$f_{\sigma \pi \pi} = \frac{m_\sigma \sqrt{\Gamma_\sigma}}{(m_\sigma^2 - 4m_\pi^2)^{1/4}} \approx 437 \text{ MeV}. \quad (\text{C.4.21})$$

Table C.4.2: Flatté couplings and amplitudes in units of GeV.

	$f_{f_0 \pi^+ \pi^-}$	$f_{f_0 K^+ K^-}$	$f_{a_0^0 \eta \pi^0}$	$f_{a_0^0 K^+ K^-}$	$\mathcal{A}_{f_0 \pi^+ \pi^-}$	$\mathcal{A}_{f_0 K^+ K^-}$	$\mathcal{A}_{a_0^0 \eta \pi^0}$	$\mathcal{A}_{a_0^0 K^+ K^-}$
CB			0.320	0.230			2.3 ± 0.1	1.6 ± 0.3
BES	0.327	0.581			2.32 ± 0.25	4.12 ± 0.55		
KLOE	0.202	0.530	0.390	0.305	$1.43^{+0.03}_{-0.60}$	$3.76^{+1.16}_{-0.49}$	2.8 ± 0.1	2.16 ± 0.04

Below I summarize the different experiments, which contributed to the measurements of the Flatté couplings.

Crystal Barrel (CB): The Crystal Barrel experiment collected $p\bar{p}$ annihilation events at the Low Energy Antiproton Ring (LEAR) at CERN from 1989 to 1996. In [109], they extracted the Flatté couplings for the $a_0(980)$ resonance from the data for $p\bar{p} \rightarrow a_0^\pm(980)\pi^\mp \rightarrow K_L K^\pm \pi^\mp$:

$$f_{a_0\eta\pi} = 324 \pm 15 \text{ MeV} \quad \text{and} \quad f_{a_0K\bar{K}}^2/f_{a_0\eta\pi}^2 = 1.03 \pm 0.14, \quad (\text{C.4.22})$$

while the measured mass and the width are $M_{a_0} = 982 \pm 3 \text{ MeV}$ and $\Gamma_{a_0} = 92 \pm 8 \text{ MeV}$, respectively.

Beijing Spectrometer (BES): The Beijing Spectrometer (BES) is a detector for the Beijing Electron Positron Collider (BEPC) at the Institute of High Energy Physics (IHEP) in Beijing. The BES detector and the upgraded BES-II detector had operated from 1989 to 2004. The current detector BES-III is running with the higher-luminosity collider BEPCII, which has operated in the 2 GeV to 4.6 GeV energy range.

In [108], the BES collaboration measured the mass and the Flatté couplings for the $f_0(980)$ resonance via $J/\psi \rightarrow \phi\pi^+\pi^-$ and ϕK^+K^- , observed at BES-II:

$$\begin{aligned} M_{f_0} &= 965 \pm 8 \pm 6 \text{ MeV}, \\ f_{f_0\pi\pi}^2 &= 0.165 \pm 0.010 \pm 0.015 \text{ GeV}^2 \\ f_{f_0K\bar{K}}^2/f_{f_0\pi\pi}^2 &= 4.21 \pm 0.25 \pm 0.21, \end{aligned} \quad (\text{C.4.23})$$

K LOng Experiment (KLOE): The KLOE experiment had operated at the $e^+e^- \phi$ -factory DAΦNE at Frascati from 2000 to 2006, collecting about 2.5 fb^{-1} data. In [117], the mass and the Flatté couplings for the $f_0(980)$ resonance were measured through the process $\phi \rightarrow \pi^0\pi^0\gamma$, based on an integrated luminosity 450 pb^{-1} of data:

$$\begin{aligned} M_{f_0} &= 976.8 \pm 0.3_{-0.6}^{+0.9} \pm 10.1 \text{ MeV}, \\ A(f_0 \rightarrow \pi^+\pi^-) &= -1.43 \pm 0.01_{-0.06-0.60}^{+0.01+0.03} \text{ GeV}, \\ A(f_0 \rightarrow K^+K^-) &= 3.76 \pm 0.04_{-0.08-0.48}^{+0.15+1.16} \text{ GeV}. \end{aligned} \quad (\text{C.4.24})$$

where the parameters $g_{f_0\pi^+\pi^-}$ and $g_{f_0K^+K^-}$ in the paper correspond to the amplitudes defined in (C.4.17). In [118], the $\phi \rightarrow \pi^+\pi^-\gamma$ mode was also used to extract the $f_0(980)$ parameters, based on an integrated luminosity 350 pb^{-1} of data: $M_{f_0} = 983.0 \pm 0.6 \text{ MeV}$, $A(f_0 \rightarrow K^+K^-) = 5.89 \pm 0.14 \text{ GeV}$ and $A(f_0 \rightarrow K^+K^-)^2/A(f_0 \rightarrow \pi^+\pi^-)^2 = 2.66 \pm 0.10$. However, the charged channel suffers from a larger non-resonant background contribution, dominated by the ρ radiative tail [117]. The $a_0(980)$ parameters were measured from $\phi \rightarrow \eta\pi^0\gamma$, using a sample of 414 pb^{-1} [119]:

$$\begin{aligned} M_{a_0} &= 983 \pm 1 \text{ MeV}, \\ A(a_0^0 \rightarrow \eta\pi^0) &= 2.8 \pm 0.1 \text{ GeV}, \quad A(a_0^0 \rightarrow K^+K^-) = 2.16 \pm 0.04 \text{ GeV}. \end{aligned} \quad (\text{C.4.25})$$

In [110, 111], the KLOE collaboration reported their updated results for the above parameters, where the number of events were not increased from the above:

$$M_{f_0} = 984.7 \pm 1.9 \text{ MeV},$$

$$A(f_0 \rightarrow \pi^+\pi^-) = -1.82 \pm 0.19 \text{ GeV}, \quad A(f_0 \rightarrow K^+K^-) = 3.97 \pm 0.43 \text{ GeV}. \quad (\text{C.4.26})$$

determined from 450 pb^{-1} of data for $\phi \rightarrow \pi^0\pi^0\gamma$,

$$\begin{aligned} M_{f_0} &= 983.7 \text{ MeV}, \\ A(f_0 \rightarrow \pi^+\pi^-) &= -2.22 \text{ GeV}, \\ A(f_0 \rightarrow K^+K^-) &= 4.74 \text{ GeV}. \end{aligned} \quad (\text{C.4.27})$$

from 350 pb^{-1} of data for $\phi \rightarrow \pi^+\pi^-\gamma$, and

$$\begin{aligned} M_{a_0} &= 982.5 \pm 1.6 \pm 1.1 \text{ MeV}, \\ A(a_0^0 \rightarrow \eta\pi^0) &= 2.82 \pm 0.03 \pm 0.04 \text{ GeV}, \\ A(a_0^0 \rightarrow K^+K^-) &= 2.15 \pm 0.06 \pm 0.06 \text{ GeV}. \end{aligned} \quad (\text{C.4.28})$$

from about 430 pb^{-1} of data for $\phi \rightarrow \eta\pi^0\gamma$. Averaging over the $\pi^0\pi^0\gamma$ and $\pi^+\pi^-\gamma$ results naively, one obtains

$$\begin{aligned} f_{f_0\pi\pi} &= \sqrt{\frac{3}{2}} f_{f_0\pi^+\pi^-} = 0.349 \text{ GeV}, & f_{f_0K\bar{K}} &= \sqrt{2} f_{f_0K^+K^-} = 0.869 \text{ GeV}, \\ f_{a_0^0\eta\pi} &= f_{a_0^0\eta\pi^0} = 0.398 \text{ GeV}, & f_{a_0^0K\bar{K}} &= \sqrt{2} f_{a_0^0K^+K^-} = 0.429 \text{ GeV}, \end{aligned} \quad (\text{C.4.29})$$

where the averaged mass for $f_0(980)$ is $M_{f_0} = 984.2 \text{ MeV}$.

C.4.3 $f_2(1270)$ contribution $f_2(1270) \rightarrow \pi\pi$

Here I discuss the contribution of intermediate $f_2(1270)$ resonance interchange, pictured in Fig. C.9. The $f_2(1270)$ resonance, having the quantum numbers $I^G(J^{PC}) = 0^+(2^{++})$, decays dominantly ($\sim 85\%$) into two pions. Since this resonance is far from threshold and has a narrow width, the minimal width approximation is adopted. The difficulties arising from the inclusion of $f_2(1270)$ roots in its spin. Therefore this contribution leads to the most complex helicity amplitude, introducing a large D -wave contribution to the cross section. The helicity amplitudes are calculated in App. C.5.

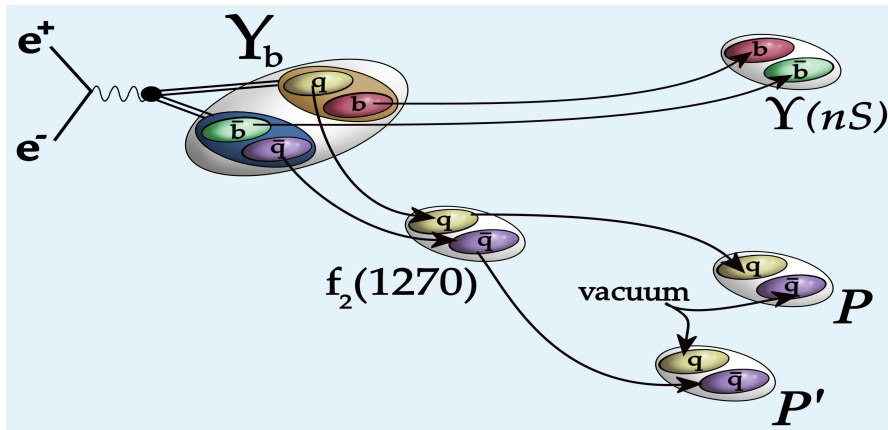


Figure C.9: Zweig allowed quark rearrangement diagrams for the intermediate $J^{PC} = 2^{++}$ $f_2(1270)$ meson interchange.

The interaction between the Y_b^I tetraquark and the $\Upsilon(nS)$, P and P' mesons is described by the Lagrangian (3.8.10) and the corresponding vertices in (3.8.11). The polarization tensor of a spin-2 particle is traceless $\epsilon_\mu{}^\mu = 0$. Using Eq. (3.8.11), the decay amplitude for $f_2(k_1 + k_2, \lambda_{f_2}) \rightarrow \pi^+(k_1) + \pi^-(k_2)$ is given by

$$\begin{aligned} \mathcal{M}(f_2 \rightarrow \pi^+ \pi^-) &= -2g_{f_2\pi^+\pi^-} k_{1\mu} k_{2\nu} \epsilon^{\mu\nu}(k_1 + k_2, \lambda_{f_2}), \\ &= \frac{g_{f_2\pi^+\pi^-}}{2} (k_1 - k_2)_\mu (k_1 - k_2)_\nu \epsilon^{\mu\nu}(k_1 + k_2, \lambda_{f_2}), \end{aligned} \quad (\text{C.4.30})$$

in which $\epsilon^{\mu\nu}$ is the polarization tensor, satisfying $\epsilon^{\mu\nu}(p, \lambda) = \epsilon^{\nu\mu}(p, \lambda)$, $p_\mu \epsilon^{\mu\nu}(p, \lambda) = p_\nu \epsilon^{\mu\nu}(p, \lambda) = 0$, $g_{\mu\nu} \epsilon^{\mu\nu}(p, \lambda) = 0$, $\epsilon^{\mu\nu}(p, \lambda) \epsilon_{\mu\nu}^*(p, \lambda') = \delta_{\lambda\lambda'}$, and the polarization sum is given by

$$\begin{aligned} B_{\mu\nu, \rho\sigma}(p) &\equiv \sum_\lambda \epsilon_{\mu\nu}(p, \lambda) \epsilon_{\rho\sigma}^*(p, \lambda) \\ &= \frac{1}{2} \left(g_{\mu\rho} - \frac{p^\mu p^\rho}{p^2} \right) \left(g_{\nu\sigma} - \frac{p^\nu p^\sigma}{p^2} \right) + \frac{1}{2} \left(g_{\mu\sigma} - \frac{p^\mu p^\sigma}{p^2} \right) \left(g_{\nu\rho} - \frac{p^\nu p^\rho}{p^2} \right) \\ &\quad - \frac{1}{3} \left(g_{\mu\nu} - \frac{p^\mu p^\nu}{p^2} \right) \left(g_{\rho\sigma} - \frac{p^\rho p^\sigma}{p^2} \right). \end{aligned} \quad (\text{C.4.31})$$

Note, that the polarization tensor can be decomposed into the products of polarization vectors for a spin-1 state:

$$\begin{aligned} \epsilon^{\mu\nu}(p, \pm 2) &= \epsilon^\mu(p, \pm 1) \epsilon^\nu(p, \pm 1), \\ \epsilon^{\mu\nu}(p, \pm 1) &= \frac{1}{\sqrt{2}} [\epsilon^\mu(p, \pm 1) \epsilon^\nu(p, 0) + \epsilon^\mu(p, 0) \epsilon^\nu(p, \pm 1)], \\ \epsilon^{\mu\nu}(p, 0) &= \frac{1}{\sqrt{6}} [\epsilon^\mu(p, 1) \epsilon^\nu(p, -1) + \epsilon^\mu(p, -1) \epsilon^\nu(p, 1) + 2\epsilon^\mu(p, 0) \epsilon^\nu(p, 0)]. \end{aligned} \quad (\text{C.4.32})$$

Using Eq. (C.4.30), the partial decay width for the process $f_2(1270) \rightarrow \pi^+ \pi^-$ reads:

$$\Gamma(f_2 \rightarrow \pi^+ \pi^-) = \frac{\rho_{\pi\pi}}{16\pi m_{f_2}} \frac{1}{5} \sum_{\lambda_{f_2}} |\mathcal{M}(f_2 \rightarrow \pi^+ \pi^-)|^2 = \frac{g_{f_2\pi^+\pi^-}^2 m_{f_2}^3}{480\pi} \left(1 - \frac{4m_\pi^2}{m_{f_2}^2} \right)^{5/2}, \quad (\text{C.4.33})$$

and after summing over the isospin multiplet, described in App. C.4.4, one finds:

$$\Gamma(f_2 \rightarrow \pi\pi) \equiv \Gamma(f_2 \rightarrow \pi^+ \pi^-) + \Gamma(f_2 \rightarrow \pi^0 \pi^0) = \frac{3}{2} \Gamma(f_2 \rightarrow \pi^+ \pi^-). \quad (\text{C.4.34})$$

C.4.4 Isospin decompositions

The u and d quarks and the \bar{u} and \bar{d} quarks belong to isospin doublets:

$$\begin{pmatrix} u \\ d \end{pmatrix}, \quad \begin{pmatrix} -\bar{d} \\ \bar{u} \end{pmatrix}. \quad (\text{C.4.35})$$

The three pions π^+ , π^- and π^0 belong to an isospin triplet:

$$|\pi^+\rangle = -|u\bar{d}\rangle = |1, 1\rangle, \quad |\pi^-\rangle = |d\bar{u}\rangle = |1, -1\rangle,$$

$$|\pi^0\rangle = \frac{1}{\sqrt{2}}|u\bar{u}\rangle - \frac{1}{\sqrt{2}}|d\bar{d}\rangle = |1, 0\rangle, \quad (\text{C.4.36})$$

in which the right-hand sides denote isospin states $|I, I_z\rangle$. The isospin states for two pions are given by

$$\begin{aligned} |2, \pm 2\rangle &= |\pi^\pm\pi^\pm\rangle, \\ |2, \pm 1\rangle &= \frac{1}{\sqrt{2}}|\pi^\pm\pi^0\rangle + \frac{1}{\sqrt{2}}|\pi^0\pi^\pm\rangle, && \text{isospin 2} \\ |2, 0\rangle &= \frac{1}{\sqrt{6}}|\pi^+\pi^-\rangle + \frac{1}{\sqrt{6}}|\pi^-\pi^+\rangle + \frac{2}{\sqrt{6}}|\pi^0\pi^0\rangle, \\ \hline |1, \pm 1\rangle &= \pm \frac{1}{\sqrt{2}}|\pi^\pm\pi^0\rangle \mp \frac{1}{\sqrt{2}}|\pi^0\pi^\pm\rangle, && \text{isospin 1} \\ |1, 0\rangle &= \frac{1}{\sqrt{2}}|\pi^+\pi^-\rangle - \frac{1}{\sqrt{2}}|\pi^-\pi^+\rangle, \\ \hline |0, 0\rangle &= \frac{1}{\sqrt{3}}|\pi^+\pi^-\rangle + \frac{1}{\sqrt{3}}|\pi^-\pi^+\rangle - \frac{1}{\sqrt{3}}|\pi^0\pi^0\rangle, && \text{isospin 0} \end{aligned} \quad (\text{C.4.37})$$

from which one finds the isospin decomposition,

$$\begin{aligned} |\pi^\pm\pi^\pm\rangle &= |2, \pm 2\rangle, \\ |\pi^\pm\pi^0\rangle &= \frac{1}{\sqrt{2}}|2, \pm 1\rangle \pm \frac{1}{\sqrt{2}}|1, \pm 1\rangle, \\ |\pi^\pm\pi^\mp\rangle &= \frac{1}{\sqrt{6}}|2, 0\rangle \pm \frac{1}{\sqrt{2}}|1, 0\rangle + \frac{1}{\sqrt{3}}|0, 0\rangle, \\ |\pi^0\pi^0\rangle &= \sqrt{\frac{2}{3}}|2, 0\rangle - \frac{1}{\sqrt{3}}|0, 0\rangle. \end{aligned} \quad (\text{C.4.38})$$

The kaons K^+ , K^- , K^0 and \bar{K}^0 belong to two isospin doublets:

$$\left(\begin{array}{c} K^+ = u\bar{s} \\ K^0 = d\bar{s} \end{array} \right), \quad \left(\begin{array}{c} \bar{K}^0 = -s\bar{d} \\ K^- = s\bar{u} \end{array} \right). \quad (\text{C.4.39})$$

The isospin states for the two-kaon systems involving $s\bar{s}$ are written as

$$\begin{aligned} |1, 1\rangle &= |K^+\bar{K}^0\rangle, \\ |1, 0\rangle &= \frac{1}{\sqrt{2}}|K^+K^-\rangle + \frac{1}{\sqrt{2}}|K^0\bar{K}^0\rangle, \\ |1, -1\rangle &= |K^0K^-\rangle, \\ |0, 0\rangle &= \frac{1}{\sqrt{2}}|K^+K^-\rangle - \frac{1}{\sqrt{2}}|K^0\bar{K}^0\rangle. \end{aligned} \quad (\text{C.4.40})$$

The η meson is an isospin singlet:

$$|\eta\rangle \approx \frac{1}{\sqrt{6}}|u\bar{u}\rangle + \frac{1}{\sqrt{6}}|d\bar{d}\rangle - \frac{2}{\sqrt{6}}|s\bar{s}\rangle = |0, 0\rangle. \quad (\text{C.4.41})$$

The isospin states for $\eta\pi$ systems are as follows:

$$|1, 1\rangle = |\eta\pi^+\rangle, \quad |1, 0\rangle = |\eta\pi^0\rangle, \quad |1, -1\rangle = |\eta\pi^-\rangle. \quad (\text{C.4.42})$$

Note, that the $f_0(980)$ and $a_0(980)$ are the isospin eigenstates:

$$|f_0\rangle = |0, 0\rangle, \quad |a_0^+\rangle = |1, 1\rangle, \quad |a_0^0\rangle = |1, 0\rangle, \quad |a_0^-\rangle = |1, -1\rangle. \quad (\text{C.4.43})$$

C.5 Helicity amplitudes

This section is concerned with the angular distribution stemming from the different continuum and resonant contributions. The discussion is outlined by taking the simplest scalar resonance S contribution as example, while neglecting the strong phase. The amplitude

$$\mathcal{M} \cong \begin{array}{c} \diagup \quad \diagdown \\ \quad \quad Y_b' \\ \diagdown \quad \diagup \\ \quad \quad R \end{array} \quad (\text{C.5.1})$$

for the corresponding decay reads:

$$\mathcal{M} = \sum_{\lambda_{Y_b}} \frac{\epsilon_{\Upsilon}^{*\mu}(\lambda_{\Upsilon}) k_1 \cdot k_2 g_{\sigma P P'} g_{Y_b^0 \Upsilon} (1S)_{\sigma} \epsilon_{Y_b \mu}(\lambda_{Y_b}) \epsilon_{Y_b}^{*\delta}(\lambda_{Y_b}) g_{e^+ e^- Y_b^I} [\bar{v}_e(p_1, \lambda_1) \gamma_{\delta} u_e(p_2, \lambda_2)]}{[s - m_{Y_b}^2 + im_{Y_b} \Gamma_{Y_b}] [M_{P P'}^2 - m_S^2 + im_S \Gamma_S]}, \quad (\text{C.5.2})$$

in which λ_1 and λ_2 are the polarizations of e^+ and e^- respectively. With the spin sum of Y_b is given by $\sum_{\lambda_{Y_b}} \epsilon_{Y_b}^{\nu}(\lambda_{Y_b}) \epsilon_{Y_b}^{*\delta}(\lambda_{Y_b}) = -g^{\nu\delta} + q^{\nu} q^{\delta} / q^2$, as known for spin 1 particles. The latter part, which is proportional to the momentum exchanged, vanishes due to the on-shell condition. Leaving implicit every term which is independent of the angles, Eq. (C.5.2) yields

$$\mathcal{M} \propto \epsilon_{\Upsilon}^{*\mu}(\lambda_{\Upsilon}) [\bar{v}_e(p_1, \lambda_1) \gamma_{\mu} u_e(p_2, \lambda_2)]. \quad (\text{C.5.3})$$

This is the helicity contribution of the scalar resonance part. In the same way all other contributions, which are given below, can be extracted. Before I come to that point, I discuss the polarization of the e^+e^- system, first in the e^+e^- rest frame where it is especially simple and then in the $\pi^+\pi^-$ rest frame, in which the Belle data is given.

Using the following spinors in the Weyl basis:

$$\begin{aligned} u_e(p, \lambda) &= \begin{pmatrix} \sqrt{p \cdot \sigma} \xi^{\lambda} \\ \sqrt{p \cdot \bar{\sigma}} \xi^{\lambda} \end{pmatrix} & \text{with } \xi^{1/2} &= \begin{pmatrix} 1 \\ 0 \end{pmatrix}, \quad \xi^{-1/2} = \begin{pmatrix} 0 \\ 1 \end{pmatrix}, \\ v_e(p, \lambda) &= \begin{pmatrix} \sqrt{p \cdot \sigma} \eta^{\lambda} \\ -\sqrt{p \cdot \bar{\sigma}} \eta^{\lambda} \end{pmatrix} & \text{with } \eta^{1/2} &= \begin{pmatrix} 0 \\ 1 \end{pmatrix}, \quad \eta^{-1/2} = \begin{pmatrix} -1 \\ 0 \end{pmatrix}, \end{aligned} \quad (\text{C.5.4})$$

the e^+e^- current which couples to the Y_b resonance can be calculated easily in the e^+e^- rest frame

$$\bar{v}_e(p_1', \lambda_1) \gamma^{\nu} u_e(p_2', \lambda_2) = \begin{cases} \sqrt{s} (0, \mp 1, -i, 0) & \text{for } \lambda_1 = \lambda_2 = \pm \frac{1}{2}, \\ 0 & \text{for } \lambda_1 = -\lambda_2 = \pm \frac{1}{2}, \end{cases} \quad (\text{C.5.5})$$

in which the first line in the right hand side has the same form as the polarization vectors for a vector-particle with helicity ± 1 (except for the normalization). Applying the Lorentz transformation from the e^+e^- rest frame to the dipion rest frame, given in Eq. (C.3.14),

one obtains the current in the dipion rest frame:

$$\bar{v}_e(p_1, \lambda_1) \gamma^\nu u_e(p_2, \lambda_2) = \begin{cases} \sqrt{s} e^{\pm i\varphi_{ee}} \left(\mp \frac{|\mathbf{q}|}{\sqrt{s}} \sin \vartheta_{ee}, \mp \cos \vartheta_{ee}, -i, \mp \frac{q^0}{\sqrt{s}} \sin \vartheta_{ee} \right) & \text{for } \lambda_1 = \lambda_2 = \pm \frac{1}{2}, \\ 0 & \text{for } \lambda_1 = -\lambda_2 = \pm \frac{1}{2}. \end{cases} \quad (\text{C.5.6})$$

Having calculated the polarization of the e^+e^- system and using the kinematics for the momenta and polarization vectors, which are defined in App. C.3, it is straightforward to derive the helicity amplitudes for all contributions. They are

$$\begin{aligned} \mathcal{M}_1^C : \quad \mathcal{H}_1^C &\equiv \epsilon_\Upsilon^{*\mu}(\lambda_\Upsilon) g_{\mu\nu} [\bar{v}_e(p_1, \lambda_1) \gamma^\nu u_e(p_2, \lambda_2)], \\ \mathcal{M}_2^C : \quad \mathcal{H}_2^C &\equiv \epsilon_\Upsilon^{*\mu}(\lambda_\Upsilon) g_{\mu\nu} \left(\cos^2 \theta - \frac{1}{3} \right) [\bar{v}_e(p_1, \lambda_1) \gamma^\nu u_e(p_2, \lambda_2)], \\ \mathcal{M}_3^C : \quad \mathcal{H}_3^C &\equiv \epsilon_\Upsilon^{*\mu}(\lambda_\Upsilon) (k_{1\mu} k_{2\nu} + k_{2\mu} k_{1\nu}) [\bar{v}_e(p_1, \lambda_1) \gamma^\nu u_e(p_2, \lambda_2)], \\ \mathcal{M}^{f_2} : \quad \mathcal{H}^{f_2} &\equiv -\frac{1}{2} \epsilon_\Upsilon^{*\mu}(\lambda_\Upsilon) \left(\bar{g}_{\mu\rho} \bar{g}_{\nu\sigma} - \frac{1}{3} \bar{g}_{\mu\nu} \bar{g}_{\rho\sigma} \right) \\ &\quad (k_1 - k_2)^\rho (k_1 - k_2)^\sigma [\bar{v}_e(p_1, \lambda_1) \gamma^\nu u_e(p_2, \lambda_2)], \end{aligned} \quad (\text{C.5.7})$$

in which $\bar{g}_{\mu\nu} = g_{\mu\nu} - p_\mu p_\nu / p^2$. The scalar resonances have the same structure as the the S-wave background \mathcal{M}_1^C , see Eq. (C.5.3). The results are listed in the following (with shortened $\sin \alpha \equiv s_\alpha$ and $\cos \alpha \equiv c_\alpha$ expressions). The spherical harmonics are given in App. A.3.

$$\mathcal{H}_1^C = \begin{cases} -\sqrt{2\pi s} (1 + c_{\vartheta_{ee}}) e^{\pm i\varphi_{ee}} Y_0^0(\theta, \phi) & \text{for } \{\lambda_1, \lambda_2, \lambda_\Upsilon\} = \left\{ \pm \frac{1}{2}, \pm \frac{1}{2}, \pm 1 \right\}, \\ \pm \sqrt{2\pi s} \frac{\sqrt{2}(q \cdot p)}{\sqrt{sm_\Upsilon}} s_{\vartheta_{ee}} e^{\pm i\varphi_{ee}} Y_0^0(\theta, \phi) & \text{for } \{\lambda_1, \lambda_2, \lambda_\Upsilon\} = \left\{ \pm \frac{1}{2}, \pm \frac{1}{2}, 0 \right\}, \\ -\sqrt{2\pi s} (1 - c_{\vartheta_{ee}}) e^{\pm i\varphi_{ee}} Y_0^0(\theta, \phi) & \text{for } \{\lambda_1, \lambda_2, \lambda_\Upsilon\} = \left\{ \pm \frac{1}{2}, \pm \frac{1}{2}, \mp 1 \right\}, \\ 0 & \text{otherwise,} \end{cases} \quad (\text{C.5.8})$$

$$\mathcal{H}_2^C = \begin{cases} -\sqrt{2\pi s} \frac{2}{3\sqrt{5}} (1 + c_{\vartheta_{ee}}) e^{\pm i\varphi_{ee}} Y_2^0(\theta, \phi) & \text{for } \{\lambda_1, \lambda_2, \lambda_\Upsilon\} = \left\{ \pm \frac{1}{2}, \pm \frac{1}{2}, \pm 1 \right\}, \\ \pm \sqrt{2\pi s} \frac{2\sqrt{2}(q \cdot p)}{3\sqrt{5}sm_\Upsilon} s_{\vartheta_{ee}} e^{\pm i\varphi_{ee}} Y_2^0(\theta, \phi) & \text{for } \{\lambda_1, \lambda_2, \lambda_\Upsilon\} = \left\{ \pm \frac{1}{2}, \pm \frac{1}{2}, 0 \right\}, \\ -\sqrt{2\pi s} \frac{2}{3\sqrt{5}} (1 - c_{\vartheta_{ee}}) e^{\pm i\varphi_{ee}} Y_2^0(\theta, \phi) & \text{for } \{\lambda_1, \lambda_2, \lambda_\Upsilon\} = \left\{ \pm \frac{1}{2}, \pm \frac{1}{2}, \mp 1 \right\}, \\ 0 & \text{otherwise.} \end{cases} \quad (\text{C.5.9})$$

$$\mathcal{H}_3^C = \begin{cases} -\sqrt{2\pi s}|\mathbf{k}|^2 \left[\frac{2}{3}(1+c_{\vartheta_{ee}})Y_0^0(\theta, \phi) - \frac{2}{3\sqrt{5}}(1+c_{\vartheta_{ee}})Y_2^0(\theta, \phi) \right. \\ \quad \left. \pm \frac{2\sqrt{2}q^0}{\sqrt{15s}}s_{\vartheta_{ee}}Y_2^{\mp 1}(\theta, \phi) - \frac{2\sqrt{2}}{\sqrt{15}}(1-c_{\vartheta_{ee}})Y_2^{\mp 2}(\theta, \phi) \right] e^{\pm i\varphi_{ee}} \\ \quad \text{for}\{\lambda_1, \lambda_2, \lambda_\Upsilon\} = \left\{ \pm\frac{1}{2}, \pm\frac{1}{2}, \pm 1 \right\}, \\ \pm\sqrt{2\pi s}|\mathbf{k}|^2 \left[\mp \frac{2p^0}{\sqrt{15}m_\Upsilon}(1+c_{\vartheta_{ee}})Y_2^{\pm 1}(\theta, \phi) \mp \frac{2p^0}{\sqrt{15}m_\Upsilon}(1-c_{\vartheta_{ee}})Y_2^{\mp 1}(\theta, \phi) \right. \\ \quad \left. + \frac{\sqrt{2}}{\sqrt{sm_\Upsilon}} \left(\frac{2q^0p^0}{3} - \frac{M_{P'P'}^2|\mathbf{q}|^2}{2|\mathbf{k}|^2} \right) s_{\vartheta_{ee}}Y_0^0(\theta, \phi) + \frac{4\sqrt{2}q^0p^0}{3\sqrt{5}sm_\Upsilon}s_{\vartheta_{ee}}Y_2^0(\theta, \phi) \right] e^{\pm i\varphi_{ee}} \\ \quad \text{for}\{\lambda_1, \lambda_2, \lambda_\Upsilon\} = \left\{ \pm\frac{1}{2}, \pm\frac{1}{2}, 0 \right\}, \\ -\sqrt{2\pi s}|\mathbf{k}|^2 \left[\frac{2}{3}(1-c_{\vartheta_{ee}})Y_0^0(\theta, \phi) - \frac{2}{3\sqrt{5}}(1-c_{\vartheta_{ee}})Y_2^0(\theta, \phi) \right. \\ \quad \left. \pm \frac{2\sqrt{2}q^0}{\sqrt{15s}}s_{\vartheta_{ee}}Y_2^{\pm 1}(\theta, \phi) - \frac{2\sqrt{2}}{\sqrt{15}}(1+c_{\vartheta_{ee}})Y_2^{\pm 2}(\theta, \phi) \right] e^{\pm i\varphi_{ee}} \\ \quad \text{for}\{\lambda_1, \lambda_2, \lambda_\Upsilon\} = \left\{ \pm\frac{1}{2}, \pm\frac{1}{2}, \mp 1 \right\}, \\ 0 \quad \text{otherwise,} \end{cases} \tag{C.5.10}$$

$$\mathcal{H}^{f_2} = \begin{cases} -\sqrt{2\pi s}|\mathbf{k}|^2 \left[-\frac{2}{3\sqrt{5}}(1+c_{\vartheta_{ee}})Y_2^0(\theta, \phi) \pm \frac{2\sqrt{2}q^0}{\sqrt{15s}}s_{\vartheta_{ee}}Y_2^{\mp 1}(\theta, \phi) \right. \\ \quad \left. - \frac{2\sqrt{2}}{\sqrt{15}}(1-c_{\vartheta_{ee}})Y_2^{\mp 2}(\theta, \phi) \right] e^{\pm i\varphi_{ee}} \quad \text{for}\{\lambda_1, \lambda_2, \lambda_\Upsilon\} = \left\{ \pm\frac{1}{2}, \pm\frac{1}{2}, \pm 1 \right\}, \\ \pm\sqrt{2\pi s}|\mathbf{k}|^2 \left[\mp \frac{2p^0}{\sqrt{15}m_\Upsilon}(1+c_{\vartheta_{ee}})Y_2^{\pm 1}(\theta, \phi) \mp \frac{2p^0}{\sqrt{15}m_\Upsilon}(1-c_{\vartheta_{ee}})Y_2^{\mp 1}(\theta, \phi) \right. \\ \quad \left. + \frac{4\sqrt{2}q^0p^0}{3\sqrt{5}sm_\Upsilon}s_{\vartheta_{ee}}Y_2^0(\theta, \phi) \right] e^{\pm i\varphi_{ee}} \quad \text{for}\{\lambda_1, \lambda_2, \lambda_\Upsilon\} = \left\{ \pm\frac{1}{2}, \pm\frac{1}{2}, 0 \right\}, \\ -\sqrt{2\pi s}|\mathbf{k}|^2 \left[-\frac{2}{3\sqrt{5}}(1-c_{\vartheta_{ee}})Y_2^0(\theta, \phi) \pm \frac{2\sqrt{2}q^0}{\sqrt{15s}}s_{\vartheta_{ee}}Y_2^{\pm 1}(\theta, \phi) \right. \\ \quad \left. - \frac{2\sqrt{2}}{\sqrt{15}}(1+c_{\vartheta_{ee}})Y_2^{\pm 2}(\theta, \phi) \right] e^{\pm i\varphi_{ee}} \quad \text{for}\{\lambda_1, \lambda_2, \lambda_\Upsilon\} = \left\{ \pm\frac{1}{2}, \pm\frac{1}{2}, \mp 1 \right\}, \\ 0 \quad \text{otherwise.} \end{cases} \tag{C.5.11}$$

C.6 Decay constant for the η meson

The PCAC results for the processes $\eta \rightarrow \gamma\gamma$ and $\eta' \rightarrow \gamma\gamma$ are given by [120]

$$\Gamma(\eta^{(\prime)} \rightarrow \gamma\gamma) = \frac{\alpha^2 m_{\eta^{(\prime)}}^3}{32\pi^3 (\tilde{f}_{\eta^{(\prime)}}^{\text{eff}})^2}. \tag{C.6.1}$$

In the above expression, the effective decay constants are defined by

$$\begin{pmatrix} (\tilde{f}_{\eta^{(\prime)}}^{\text{eff}})^{-1} \\ (\tilde{f}_{\eta^{(\prime)}}^{\text{eff}})^{-1} \end{pmatrix} = \frac{1}{3} \begin{pmatrix} \cos \phi & -\sin \phi \\ \sin \phi & \cos \phi \end{pmatrix} \begin{pmatrix} 5 f_q^{-1} \\ \sqrt{2} f_s^{-1} \end{pmatrix}, \quad (\text{C.6.2})$$

in which ϕ is the mixing angle between the flavor states $(u\bar{u} + d\bar{d})/\sqrt{2}$ and $s\bar{s}$ in the physical states η and η' , and $f_{q,s}$ obey the relations

$$\langle 0 | J_{\mu 5}^{q,s} | \eta^{(\prime)}(p) \rangle = i f_{\eta^{(\prime)}}^{q,s} p_\mu, \quad \begin{pmatrix} f_\eta^q & f_\eta^s \\ f_{\eta'}^q & f_{\eta'}^s \end{pmatrix} = \begin{pmatrix} \cos \phi & -\sin \phi \\ \sin \phi & \cos \phi \end{pmatrix} \begin{pmatrix} f_q & 0 \\ 0 & f_s \end{pmatrix}. \quad (\text{C.6.3})$$

In Ref. [121], the above parameters were determined phenomenologically by combining various observables, including the processes in Eq. (C.6.1):

$$\phi = (39.3 \pm 1.0)^\circ, \quad f_q = (1.07 \pm 0.02) f_\pi, \quad f_s = (1.34 \pm 0.06) f_\pi, \quad (\text{C.6.4})$$

which leads to [122]_{Sec. 2.1}

$$\tilde{f}_\eta^{\text{eff}} = 1.02 f_\pi, \quad \tilde{f}_{\eta'}^{\text{eff}} = 0.79 f_\pi. \quad (\text{C.6.5})$$

We approximated $f_\eta = f_\pi$ in our numerical analysis.

C.7 Fitting

In this section I describe how to perform a χ^2 fit. First I introduce the general formalism and explain afterwards how a fit to simultaneous spectra with different formulas, but depending fit parameters can be performed in Mathematica.

A fit function f depends on n unknown parameters \mathbf{p} (the fitting parameters) and on parameters \mathbf{x} of a certain space of arbitrary dimension, in which the data is taken (for example \sqrt{s} where \mathbf{x} is one-dimensional, space coordinates where \mathbf{x} is three-dimensional, ...). Thus every point in the data set, comprised of m points, has the information of its value y_j at point \mathbf{x}_j , $j = 1, \dots, m$ and corresponding errors σ_j . The χ^2 function is then defined by the sum over the weighted squares

$$\chi^2(\mathbf{p}) = \sum_{j=1}^m \left(\frac{y_j - f(\mathbf{x}_j, \mathbf{p})}{\sigma_j} \right)^2, \quad (\text{C.7.1})$$

in which the errors σ_j are assumed to be symmetric, since they are assumed to be Gaussian distributed. The implementation of antisymmetric errors needs further mathematical justification and the assumption of different error distributions (Poisson, etc.). In numerical computations (like for example in ROOT), the errors are usually implemented by taking the lower error if for $\Delta = y_j - f(\mathbf{x}_j, \mathbf{p})$ $\Delta \leq 0$ and the upper error if $\Delta > 0$. The so called p -value, the probability of obtaining data in a new run, which is at least as incompatible with the present data, is given by

$$p = \int_{\chi^2}^{\infty} dz \phi(z; n_d), \quad (\text{C.7.2})$$

where n_d is the number of degrees of freedom and

$$\phi(z; n) = \frac{z^{n/2-1} e^{-z/2}}{2^{n/2} \Gamma(n/2)}. \quad (\text{C.7.3})$$

The problem of performing the χ^2 fit is now reduced to the problem of finding the global minimum of the (positive definite) function in Eq. (C.7.1). Several minimization routines are available to fulfill this task, such as MINUIT. I sketch in this section the most important steps to perform a fit using Mathematica and its implemented routine **FindMinimum**. In Mathematica the contribution from one data point reads

$$\text{Chi2OnePoint} [\Delta_-, \sigma_+, \sigma_-] := \Delta^2 \left(\frac{\Theta[\Delta]}{\sigma_+^2} + \frac{\Theta[-\Delta]}{\sigma_-^2} \right), \quad (\text{C.7.4})$$

in which $\Theta[\Delta] \equiv \text{HeavisideTheta}[\Delta]$. The Mathematica predefined routines are printed thick, and our added routines are printed thick and blue. The $\chi^2(\mathbf{p})$ function is implemented via

$$\begin{aligned} \text{Chi2} [f_-, \text{Data}_-, \text{Error}_-, \text{ScanRange}_-, \mathbf{p}_-] := & \mathbf{N}[\text{Sum}[\text{Sum}[\\ & \text{If}[\text{Data}[[j, i, 1]] > \text{ScanRange}[[j, 1]] \&\& \text{Data}[[j, i, 1]] < \text{ScanRange}[[j, 2]], \\ & \text{Chi2OnePoint}[f[\mathbf{p}_-, \text{Data}[[j, i, 1]], j] - \text{Data}[[j, i, 2]], \\ & \text{Error}[[j, i, 1]], \text{Error}[[j, i, 2]], 0], \\ & \{i, 1, \text{Length}[\text{Data}[[j]]]\}, \{j, 1, \text{Length}[\text{Data}]\}]]; \end{aligned}$$

in which the additional sum over j implies, that more than one model function depending on the parameters \mathbf{p} can be fitted to different data sets. Thus the input function f is an array of length a . The input is organized as follows. The length of the arrays A is indicated in brackets $A[a, b, c, \dots]$ ($A[2]$ is a vector of length 2, $A[2, 2]$ is a 2 by 2 matrix, $A[2, k_i]$ is a matrix with 2 rows, where the first is of length k_1 and the second is of length k_2 , etc.): The functions f_j in the array of length a are the model functions, which need to be defined in Mathematica (in the upper example) via

$$f[\mathbf{p}_-, \mathbf{x}_-, j_-], \quad (\text{C.7.5})$$

The parameter dependence on \mathbf{x} can be different for every j (for $j = 1$ it can be a two dimensional space coordinate and for $j = 2$ a temperature, whatever the data sets provide as data sample). Correspondingly, the data sets are of length $\text{Data}[[a, k_j, 2]]$, where to every function f_j corresponds a data sample of length k_j with two entries, namely the coordinate $\mathbf{x}_{j,l}$ and the measured value at that point (so $\text{Data}[[1, 3, 2]]$ gives the third measured value of the data set 1 and $\text{Data}[[1, 3, 1]]$ gives the corresponding coordinate). The error array has the same structure $\text{Error}[[a, k_j, 2]]$, in which $\text{Error}[[a, k_j, 1]]$ gives the upper error to the measured value and $\text{Error}[[a, k_j, 2]]$ gives the lower value. The $\text{ScanRange}[[a, 2]]$ array allows to input the scan range for one dimensional parameter scan to fit parts of the data sets (with $\text{ScanRange}[[a, 1]]$ minimum and $\text{ScanRange}[[a, 2]]$ maximum value, for example $0.25 \text{ GeV} < \sqrt{s} < 1 \text{ GeV}$). The fits are performed with the use of the Mathematica routine **FindMinimum** $\{f, \text{cons}\}, \{\{x, x_0\}, \{y, y_0\}, \dots\}$, which searches for a local minimum for the parameters x, y, \dots subject to the constraints cons

with starting points x_0, y_0, \dots . To find the global minimum, it is necessary to find all or at least enough local minima. This is done by defining the fitting routine

```
Options[Fit] = { conditions → {}, monitor → 1};
```

```
Fit [ $\chi^2$  fkt _, ParRange _, ParameterNames _, CalcTime _, OptionsPattern[]] :=
Module[{ LocalTimeStart = AbsoluteTime[],
  LocalFitList = {},
  LocalTime = 0,
  LocalFitNumber = 0,
  LocalBestChi2 =  $\infty$ ,
  LocalNewMinimum },
(*-----Start Program-----*)
If[OptionValue[evalmonitor] > 0,
  Print["time passed: ", Dynamic[Round[LocalTime]],
    "number of fits:" , Dynamic[LocalFitNumber], "average time per fit:" ,
    Dynamic[Round[LocalTime / (LocalFitNumber + 0.1), 0.1]],
    " best  $\chi^2$ :" , Dynamic[LocalBestChi2]];
  Print["last values:"];
  Print[Dynamic[LocalNewMinimum]];];
(*-----*)
While[LocalTime < CalcTime ,
  LocalNewMinimum = FindMinimum[{ $\chi^2$  fkt ,
    OptionValue[conditions ]},
  Table[{ ParameterNames [[i]], NewRandSeed [ ParRange [[i]]},
    {i, 1, Length[ ParRange ]}]];
  LocalFitList =
    Prepend[ LocalFitList , LocalNewMinimum ];
  LocalFitNumber ++;
  LocalBestChi2 = Min[ LocalNewMinimum [[1]], LocalBestChi2 ];
  LocalTime = AbsoluteTime[] - TimeStart ;];
Return[Sort[ LocalFitList , #1[[1]] < #2[[1]]&]]];,
```

in which the function

```
NewRandSeed [ ParRange _] :=
Table[Random[Real, ParRange [[i, 1]], ParRange [[i, 2]],
  {i, 1, Length[ ParRange ]}];
```

is used to generate a new set of starting parameters. The input to the defined routine is the χ^2 function, depending on the fit parameters, which are listed in `ParameterNames`

of length b . The list `ParameterRange` $[[b, 2]]$ is of the same length and gives the intervals (minimum, maximum) for the `NewRandSeed` function to generate a new random tuple for the next attempt to find a local minimum. The number `CalcTime` gives the amount of time in seconds, which the routine is supposed to accumulate new fits. The Mathematica routine is usually quite fast and needs few seconds per fit for the fits performed in Sec. 3.8, which is a little slower than the ROOT fitting routine.

We also wrote a routine, which is based on the method of (intelligent) nested intervals and does neither need the Mathematica routine `FindMinimum` nor an analytic input function. It can handle any Mathematica predefined function, as long as the routine returns numeric values for a set of numeric input parameters, on the cost of being much slower. In this way the fitting routine can for example handle input with several numerical integrations. All three methods (ROOT, `FindMinimum` and the nested interval technique) are in agreement with each other. Our routine has also successful been used by [123]. I will only discuss the main part of the program. In case of interest, please write an e-mail to christian.hambrock@desy.de.

```
Options[ FitNested ] = { parstart -> Automatic, namelist -> Automatic,
                        evalmonitor -> 2};
```

```
FitNested [f, Data, Errors, ScanRange, ParRange, CalcTime, OptionsPattern[]] :=
Module[{
  LocalCurPar = If[OptionValue[ parstart ] == Automatic,
  NewRandSeed [ ParRange ], OptionValue[ parstart ],
  OptionValue[ parstart ] (* current parameters *) ,
  LocalTimeStart = AbsoluteTime[],
  LocalbestChi2 ,
  LocalBeforeChi2 = ∞,
  LocalNameList = If[OptionValue[ namelist ] == Automatic,
  Table[ "par[" <> ToString[i] <> "]" , {i, 1, Length[ ParRange ]}],
  OptionValue[ namelist ], OptionValue[ namelist ]],
  LocalAllFits = {},
  LocalShuffList ,
  LocalTotFits ,
  LocalSecToGo ,
  LocalCurBestChi2 ,
  LocalAL1Fits = True, (* ensures, that at least one fit is completed *)
  LocalP = Table[0, {i, 1, Length[ ParRange ]}], (* forces the program
  to make small steps for already well determined parameters *)
  LocalP2 = Min[Length[ ParRange ], MinimalizationP recision - 1]
  (* ensures, that the program starts with crude steps *) },
(*————— START Program —————*)
```

```

If[OptionValue[ evalmonitor ] > 0, LocalCurBestChi2 = ∞;
  LocalSecToGo = ∞;];
Print[ “ mom Chi2: ” ,Dynamic[ LocalCurBestChi2 ],
  “ data in current list: ” ,Dynamic[ LocalTotFits ],
  “ seconds to go: ” ,Dynamic[ LocalSecToGo ]];
(*-----*)
If[OptionValue[ evalmonitor ] > 1,
  Print[ “the precision is set to ” , MinimalizationP recision ];
  Print[ “parameters have good precision, if the numbers are close to” ,
    MinimalizationP recision ];
  Print[Dynamic[{ LocalNameList , LocalP , LocalCurPar }]];];
(*-----*)
LocalTotFits = 0;
ChiTest [ Par _ ] := Chi2 [f, Data , Errors , ScanRange , Par ];
LocalbestChi2 = Chi2 [f, Data , Errors , ScanRange , LocalCurPar ];
Print[ LocalbestChi2 ];
(*-----*)
While[AbsoluteTime[] – LocalTimeStart < CalcTime || LocalAL1Fits ,
  (*-----Start While -----*)
  LocalAL1Fits = True;
  LocalShuffList = ShuffledList [Length[ ParRange ]];
  Do[{ LocalCurPar , LocalbestChi2 , LocalP [[ LocalShuffList [[n]]]]} =
    MinimizePar [ LocalCurPar , LocalShuffList [[n]], ParRange ,
      LocalP [[n]], Max[ LocalP 2 , 0]] (* MINIMIZE CALLED HERE *)
    , {n, Length[ LocalCurPar ]}];
  LocalCurBestChi2 = LocalbestChi2 ;
  LocalSecToGo =
    Round[ CalcTime + LocalTimeStart – AbsoluteTime[]];
  (*- start if -*)
If[ LocalBeforeChi2 < Chi2Precision * LocalbestChi2 && LocalP 2 < 1,
  (* then: no Improvement; start new randseed *)
  LocalAllFits = Append[ LocalAllFits ,
    N[{ LocalCurPar , LocalbestChi2 }]];
  LocalCurPar = NewRandSeed [ ParRange ];
  LocalP = Table[0, {i, 1, Length[ ParRange ]}];
  LocalP 2 = Min[Length[ ParRange ], MinimalizationP recision – 1];
  LocalbestChi2 = Chi2 [f, Data , Errors , ScanRange , LocalCurPar ];
  LocalBeforeChi2 = ∞; LocalTotFits ++; LocalAL1Fits = False;

```

```

, (* else: continue *)
LocalBeforeChi2 = LocalbestChi2 ; LocalP 2 --];
(*- end if -*)];
(*-----End While-----*)
Return[Sort[ LocalAllFits , #1[[2]] < #2[[2]]&]];

```

The following minimization routine is called in the above procedure:

```

MinimizePar [ ParList _, nthPar _, ParRange _, Precision _, PrecisionTwo _] :=
Module[{
  LocalPrecision = Precision ,
  LocalParameters = ParList ,
  LocalParametersUp = ParList ,
  LocalParametersDown = ParList ,
  LocalUp = ParList [[ nthPar ]] + ( ParRange [[ nthPar , 2]]
    - ParList [[ nthPar ]])/2Precision ,
  LocalDown = ParList [[ nthPar ]] - ( ParList [[ nthPar ]]
    - ParRange [[ nthPar , 1]])/2Precision ,
  n = nthPar ,
  ChiS1 ,
  ChiS2 = ChiTest [ ParList ], ChiS3 },
For[l = 0, l < Max[ MinimalizationP precision
  - Precision - PrecisionTwo , 1], l + +,
  LocalParametersDown [[n]] = LocalParameters [[n]]
  - ( LocalParameters [[n]] - LocalDown )/2;
  LocalParametersUp [[n]] = LocalParameters [[n]]
  + ( LocalUp - LocalParameters [[n]] )/2;
  ChiS1 = ChiTest [ LocalParametersDown ]; ChiS2 = ChiS2 ;
  ChiS3 = ChiTest [ LocalParametersUp ];
Which[
  ChiS1 <= ChiS2 && ChiS1 <= ChiS3 ,
  ( LocalDown = LocalDown ; LocalUp = LocalParameters [[n]];
  LocalParameters = LocalParametersDown ; ChiS2 = ChiS1 ;
  LocalPrecision = LocalPrecision - 1/2; ),
  ChiS2 <= ChiS1 && ChiS2 <= ChiS3 ,
  ( LocalDown = LocalParametersDown [[n]];
  LocalUp = LocalParametersUp [[n]];
  LocalParameters = LocalParameters ; ChiS2 = ChiS2 ;
  LocalPrecision + +; ),
  ChiS3 <= ChiS1 && ChiS3 <= ChiS2 ,

```

```

      ( LocalDown = LocalParameters [[n]]; LocalUp = LocalUp ;
        LocalParameters = LocalParametersUp ; ChiS2 = ChiS3 ;
        LocalPrecision = LocalPrecision - 1/2;)
    ];];
  Return[{N[ LocalParameters ], ChiS2 ,
    Max[Min[Floor[ LocalPrecision ], MinimalizationPrecision - 1], 0]}];];

```

To avoid certain patterns in the minimization, the parameters are minimized in a random order, for which the following routine generates a shuffled list:

```

ShuffledList [ LengthShuffle _ ] :=
  Module[{
    InList = Table[i, {i, 1, LengthShuffle }],
    RandList = {},
    RandNumb },
    Do[ RandNumb = RandomInteger[{1, Length[ InList ]}];
      RandList = Append[ RandList , InList [[ RandNumb ]]];
      InList = Delete[ InList , RandNumb ];, {i, 1, LengthShuffle }];
    Return[ RandList ];];

```

(C.7.6)

In case of binned fits, the following functions are used.

```
Options[ BinFunction ] = { numericvalue → True};
```

```

BinFunction [ f _, x _, StepList _, Accuracy _, OptionsPattern[] ] :=
  Module[{
    LocalNumber = 1},
    (* returning the over bin averaged value: *)
    If[!Element[OptionValue[ numericvalue ], Reals],
      (*then:*)
      Return[Sum[HeavisideTheta[( x - StepList [[i, 1]])
        ( StepList [[i, 2]] - x )] * SepFunction [ f , x ,
          StepList [[i, 1]], StepList [[i, 2]], Accuracy ], {i, Length[ StepList ]}];,
      (*else:*)
      While[( StepList [[ LocalNumber , 1]] > OptionValue[ numericvalue ] ||
        StepList [[ LocalNumber , 2]] < OptionValue[ numericvalue ])&&
        LocalNumber <= Length[ StepList ], LocalNumber ++];
      (* returning the over bin averaged value: *)
      If[ LocalNumber > Length[ StepList ],
        Return[0],
        Return[ SepFunction [ f , x , StepList [[ LocalNumber , 1]],

```

```
StepList [[ LocalNumber , 2]], Accuracy ]];];];
```

with

```
SepFunction [ f _, x _, a _, b _, Accuracy _] :=
Module[{},
If[ Accuracy == ∞,
Return[Re[Normal[NIntegrate[ f , { x , a , b }, PrecisionGoal - > 1,
AccuracyGoal -> 1]/( b - a )]]],
Return[Re[Sum[ f /. { x -> a + i( b - a )/ Accuracy
-( b - a )/( Accuracy 2) }, { i, Accuracy }]]/ Accuracy ]];];
```

 (C.7.7)

The function f , depending on the parameter x , is split into bins, which are given by the array `StepList` `[[c, 2]]`, in which c is the number of bins and `StepList` `[[c, 1]]` and `StepList` `[[c, 2]]` define the interval (lower and upper value) of each bin. The accuracy gives the number of points over which the function f is averaged in each bin. For `Accuracy` = ∞ , the function is numerically integrated over the bin and the averaged value is returned. Note, that this possibility works only for the `FitNested` routine. The `numericvalue` option allows to give a numeric value for x , and the function will ignore all other bins, only returning the value in the corresponding bin to increase evaluation speed if necessary.

C.8 Tables for Chap. 3

Table C.8.1: Numerical yields of $\Upsilon(5S) \rightarrow \Upsilon(1S)\pi^+\pi^-$ and $\Upsilon(2S)\pi^+\pi^-$ transitions as functions of $M_{\pi^+\pi^-}$ and $\cos\theta$ taken from [91], which are shown in Figure 3.12. The uncertainties of the yields are statistical only.

Bin	$\Upsilon(1S)\pi^+\pi^-$		$\Upsilon(2S)\pi^+\pi^-$	
	$M_{\pi^+\pi^-}$ [GeV]	Yield	$M_{\pi^+\pi^-}$ [GeV]	Yield
1	[0.25, 0.35)	$1.83^{+1.84}_{-1.16}$	[0.25, 0.30)	0.0
2	[0.35, 0.45)	$25.03^{+5.70}_{-4.97}$	[0.30, 0.35)	$8.48^{+3.51}_{-2.82}$
3	[0.45, 0.55)	$13.67^{+4.66}_{-3.94}$	[0.35, 0.40)	$20.31^{+5.22}_{-4.52}$
4	[0.55, 0.65)	$11.21^{+3.99}_{-3.28}$	[0.40, 0.45)	$13.69^{+4.38}_{-3.70}$
5	[0.65, 0.75)	$18.16^{+5.12}_{-4.41}$	[0.45, 0.50)	$9.37^{+3.73}_{-3.02}$
6	[0.75, 0.85)	$28.70^{+6.18}_{-5.47}$	[0.50, 0.55)	$20.51^{+5.27}_{-4.58}$
7	[0.85, 0.95)	$34.84^{+6.70}_{-5.97}$	[0.55, 0.60)	$24.70^{+5.70}_{-4.97}$
8	[0.95, 1.05)	$34.35^{+6.57}_{-5.86}$	[0.60, 0.65)	$35.58^{+6.83}_{-6.10}$
9	[1.05, 1.15)	$28.49^{+6.03}_{-5.35}$	[0.65, 0.70)	$24.70^{+5.58}_{-4.88}$
10	[1.15, 1.25)	$60.91^{+8.57}_{-7.87}$	[0.70, 0.75)	$10.07^{+3.74}_{-3.03}$
11	[1.25, 1.35)	$50.99^{+7.48}_{-6.81}$	[0.75, 0.80)	$7.60^{+3.35}_{-2.64}$
12	[1.35, 1.45)	$14.00^{+4.09}_{-3.41}$	[0.80, 0.85)	$4.28^{+2.58}_{-1.88}$
Bin	$\cos\theta_{\text{Hel}}$	Yield	$\cos\theta_{\text{Hel}}$	Yield
1	[-1.0, -0.8)	$37.68^{+6.90}_{-6.24}$	[-1.0, -0.8)	$30.59^{+6.15}_{-5.46}$
2	[-0.8, -0.6)	$37.09^{+6.90}_{-6.20}$	[-0.8, -0.6)	$20.82^{+5.14}_{-4.49}$
3	[-0.6, -0.4)	$29.95^{+6.07}_{-5.41}$	[-0.6, -0.4)	$18.15^{+4.83}_{-4.14}$
4	[-0.4, -0.2)	$21.74^{+5.51}_{-4.84}$	[-0.4, -0.2)	$16.78^{+4.78}_{-4.07}$
5	[-0.2, +0.0)	$33.77^{+6.48}_{-5.85}$	[-0.2, +0.0)	$7.45^{+3.53}_{-2.78}$
6	[+0.0, +0.2)	$23.65^{+5.55}_{-4.84}$	[+0.0, +0.2)	$14.28^{+4.53}_{-3.76}$
7	[+0.2, +0.4)	$32.80^{+6.34}_{-5.67}$	[+0.2, +0.4)	$6.00^{+3.07}_{-2.36}$
8	[+0.4, +0.6)	$37.72^{+6.86}_{-6.17}$	[+0.4, +0.6)	$7.15^{+3.44}_{-2.75}$
9	[+0.6, +0.8)	$31.97^{+6.33}_{-5.65}$	[+0.6, +0.8)	$24.49^{+5.65}_{-4.95}$
10	[+0.8, +1.0)	$31.75^{+6.28}_{-5.58}$	[+0.8, +1.0)	$32.26^{+6.41}_{-5.65}$

Table C.8.2: Input parameters in GeV

$m_{Y_b} = 10.890$	$m_{\Upsilon(1S)} = 9.460$	$m_{\pi^0} = 0.135$
$m_{\pi^\pm} = 0.140$	$f_\pi = 0.130$	$m_{K^\pm} = 0.494$
$m_{K^0} = 0.498$	$f_K = 0.160$	$m_\eta = 0.548$
$m_\eta = 0.548$	$f_\eta = f_\pi = 0.130$	$m_\sigma = 0.478$ [89]
$\Gamma_\sigma = 0.324$ [89]	$m_{f_2} = 1.275$	$\Gamma_{f_2} = 0.185$
$\Gamma(f_2(1270) \rightarrow \pi\pi) = 0.157$	$\Gamma(f_2(1270) \rightarrow K\bar{K}) = 0.0085$	$\Gamma_{Y_b} = 0.03$
$\sqrt{s} = 10.87$		

Table C.8.3: Reduced partial decay widths for the tetraquarks $Y_{[bq]}^{(i)}$, the extracted value of the coupling constant F and the center of mass momentum $|\mathbf{k}|$ (top left). The reduced total decay widths for $Y_{[bq]}^{(i)}$ are also tabulated (top right) and for the tetraquarks $Y_{[bs]}^{(i)}$ (the lower two tables). The errors in the entries correspond to the errors in the decay widths in Tab. 3.6.2.

Decay Mode	Γ/κ^2 [MeV]	F	$ \mathbf{k} $ [GeV]
$Y_{[bq]}^{(1)} \rightarrow B \bar{B}$	< 8	2.15	1.3
$Y_{[bq]}^{(1)} \rightarrow B \bar{B}^*$	9_{-4}^{+4}	3.7	1.2
$Y_{[bq]}^{(1)} \rightarrow B^* \bar{B}^*$	28_{-7}^{+7}	1	1.1
$Y_{[bq]}^{(2)} \rightarrow B \bar{B}$	< 19	2.15	1.8
$Y_{[bq]}^{(2)} \rightarrow B \bar{B}^*$	22_{-9}^{+9}	3.7	1.7
$Y_{[bq]}^{(2)} \rightarrow B^* \bar{B}^*$	81_{-21}^{+21}	1	1.6
$Y_{[bq]}^{(3)} \rightarrow B \bar{B}$	< 22	2.15	2
$Y_{[bq]}^{(3)} \rightarrow B \bar{B}^*$	29_{-13}^{+13}	3.7	1.9
$Y_{[bq]}^{(3)} \rightarrow B^* \bar{B}^*$	115_{-30}^{+30}	1	1.8
$Y_{[bq]}^{(3)} \rightarrow \Lambda_b \bar{\Lambda}_b$	5_{-3}^{+3}	$1.1_{-0.35}^{+0.3}/3$	0.3
$Y_{[bq]}^{(4)} \rightarrow B \bar{B}$	< 20	2.15	1.9
$Y_{[bq]}^{(4)} \rightarrow B \bar{B}^*$	27_{-12}^{+12}	3.7	1.8
$Y_{[bq]}^{(4)} \rightarrow B^* \bar{B}^*$	106_{-27}^{+27}	1	1.8

1^{--} Tetraquark	Γ_{tot}/κ^2 [MeV]
$Y_{[bq]}^{(1)}$	44 ± 8
$Y_{[bq]}^{(2)}$	119 ± 24
$Y_{[bq]}^{(3)}$	171 ± 33
$Y_{[bq]}^{(4)}$	154 ± 30

Decay Mode	Γ/κ^2 [MeV]	F	$ \mathbf{k} $ [GeV]
$Y_{[bs]}^{(1)} \rightarrow B_s \bar{B}_s$	< 13	2.15	1.6
$Y_{[bs]}^{(1)} \rightarrow B_s \bar{B}_s^*$	17_{-7}^{+7}	3.7	1.6
$Y_{[bs]}^{(1)} \rightarrow B_s^* \bar{B}_s^*$	59_{-15}^{+15}	1	1.5
$Y_{[bs]}^{(2)} \rightarrow B_s \bar{B}_s$	< 24	2.15	2
$Y_{[bs]}^{(2)} \rightarrow B_s \bar{B}_s^*$	32_{-14}^{+14}	3.7	2
$Y_{[bs]}^{(2)} \rightarrow B_s^* \bar{B}_s^*$	129_{-33}^{+33}	1	1.9
$Y_{[bs]}^{(3)} \rightarrow B_s \bar{B}_s$	< 32	2.15	2.3
$Y_{[bs]}^{(3)} \rightarrow B_s \bar{B}_s^*$	43_{-19}^{+19}	3.7	2.2
$Y_{[bs]}^{(3)} \rightarrow B_s^* \bar{B}_s^*$	184_{-45}^{+45}	1	2.1
$Y_{[bs]}^{(3)} \rightarrow \Xi \bar{\Xi}$	10_{-5}^{+5}	$1.1_{-0.35}^{+0.3}/3$	0.6
$Y_{[bs]}^{(4)} \rightarrow B_s \bar{B}_s$	< 30	2.15	2.2
$Y_{[bs]}^{(4)} \rightarrow B_s \bar{B}_s^*$	42_{-18}^{+18}	3.7	2.2
$Y_{[bs]}^{(4)} \rightarrow B_s^* \bar{B}_s^*$	178_{-45}^{+45}	1	2.1
$Y_{[bs]}^{(4)} \rightarrow \Xi \bar{\Xi}$	8_{-5}^{+5}	$1.1_{-0.35}^{+0.3}/3$	0.5

1^{--} Tetraquark	Γ_{tot}/κ^2 [MeV]
$Y_{[bs]}^{(1)}$	88 ± 17
$Y_{[bs]}^{(2)}$	184 ± 35
$Y_{[bs]}^{(3)}$	267 ± 50
$Y_{[bs]}^{(4)}$	258 ± 48

Bibliography

- [1] A. Bevan, “Results from the B Factories,” pp. 145–164, 2008.
- [2] R. L. Jaffe, “Exotica,” *Phys. Rept.*, vol. 409, pp. 1–45, 2005.
- [3] S. Choi *et al.*, “Observation of a narrow charmonium - like state in exclusive $B^\pm \rightarrow K^\pm \pi^+ \pi^- J/\psi$ decays,” *Phys.Rev.Lett.*, vol. 91, p. 262001, 2003.
- [4] D. E. Acosta *et al.*, “Observation of the narrow state $X(3872) \rightarrow J/\psi \pi^+ \pi^-$ in $\bar{p}p$ collisions at $\sqrt{s} = 1.96$ TeV,” *Phys.Rev.Lett.*, vol. 93, p. 072001, 2004.
- [5] V. Abazov *et al.*, “Observation and properties of the $X(3872)$ decaying to $J/\psi \pi^+ \pi^-$ in $p \bar{p}$ collisions at $\sqrt{s} = 1.96$ TeV,” *Phys.Rev.Lett.*, vol. 93, p. 162002, 2004.
- [6] B. Aubert *et al.*, “Study of the $B \rightarrow J/\psi K^- \pi^+ \pi^-$ decay and measurement of the $B \rightarrow X(3872) K^-$ branching fraction,” *Phys. Rev.*, vol. D71, p. 071103, 2005.
- [7] A. Abulencia *et al.*, “Analysis of the quantum numbers J^{PC} of the $X(3872)$,” *Phys.Rev.Lett.*, vol. 98, p. 132002, 2007.
- [8] K. Abe *et al.*, “Observation of a new charmonium state in double charmonium production in e^+e^- annihilation at $\sqrt{s} \simeq 10.6$ GeV,” *Phys.Rev.Lett.*, vol. 98, p. 082001, 2007.
- [9] K. Abe *et al.*, “Observation of a near-threshold $\omega J/\psi$ mass enhancement in exclusive $B \rightarrow K \omega J/\psi$ decays,” *Phys.Rev.Lett.*, vol. 94, p. 182002, 2005.
- [10] B. Aubert *et al.*, “Observation of a broad structure in the $\pi^+ \pi^- J/\psi$ mass spectrum around 4.26 GeV/ c^2 ,” *Phys.Rev.Lett.*, vol. 95, p. 142001, 2005.
- [11] B. Aubert *et al.*, “Observation of $Y(3940) \rightarrow J/\psi \omega$ in $B \rightarrow J/\psi \omega K$ at BABAR,” *Phys.Rev.Lett.*, vol. 101, p. 082001, 2008.
- [12] Q. He *et al.*, “Confirmation of the $Y(4260)$ resonance production in ISR,” *Phys.Rev.*, vol. D74, p. 091104, 2006.
- [13] C. Yuan *et al.*, “Measurement of $e^+e^- \rightarrow \pi^+ \pi^- J/\psi$ cross-section via initial state radiation at Belle,” *Phys.Rev.Lett.*, vol. 99, p. 182004, 2007.
- [14] T. Aaltonen *et al.*, “Evidence for a Narrow Near-Threshold Structure in the $J/\psi \phi$ Mass Spectrum in $B^+ \rightarrow J/\psi \phi K^+$ Decays,” *Phys.Rev.Lett.*, vol. 102, p. 242002, 2009.

- [15] S. Uehara *et al.*, “Observation of a χ'_{c2} candidate in $\gamma\gamma \rightarrow D\bar{D}$ production at BELLE,” *Phys.Rev.Lett.*, vol. 96, p. 082003, 2006.
- [16] S.-K. Choi *et al.*, “Observation of a resonance-like structure in the $\pi^\pm\psi'$ mass distribution in exclusive $B \rightarrow K\pi^\pm\psi'$ decays,” *Phys.Rev.Lett.*, vol. 100, p. 142001, 2008.
- [17] R. Mizuk *et al.*, “Observation of two resonance-like structures in the $\pi^\pm\chi_{c1}$ mass distribution in exclusive $\bar{B}^0 \rightarrow K^-\pi^+\chi_{c1}$ decays,” *Phys.Rev.*, vol. D78, p. 072004, 2008.
- [18] B. Aubert *et al.*, “Search for the $Z(4430)$ at BABAR,” *Phys.Rev.*, vol. D79, p. 112001, 2009.
- [19] N. A. Tornqvist, “Isospin breaking of the narrow charmonium state of Belle at 3872 MeV as a deuson,” *Phys.Lett.*, vol. B590, pp. 209–215, 2004. This report supersedes the unpublished reminder hep-ph/0308277.
- [20] E. Braaten and M. Kusunoki, “Low-energy universality and the new charmonium resonance at 3870 MeV,” *Phys.Rev.*, vol. D69, p. 074005, 2004.
- [21] E. S. Swanson, “Short range structure in the $X(3872)$,” *Phys.Lett.*, vol. B588, pp. 189–195, 2004.
- [22] M. Voloshin, “Heavy quark spin selection rule and the properties of the $X(3872)$,” *Phys.Lett.*, vol. B604, pp. 69–73, 2004.
- [23] C. Thomas and F. Close, “Is $X(3872)$ a molecule?,” *Phys.Rev.*, vol. D78, p. 034007, 2008.
- [24] X. Liu, X.-Q. Zeng, and X.-Q. Li, “Possible molecular structure of the newly observed $Y(4260)$,” *Phys.Rev.*, vol. D72, p. 054023, 2005.
- [25] X. Liu, Y.-R. Liu, W.-Z. Deng, and S.-L. Zhu, “Is $Z^+(4430)$ a loosely bound molecular state?,” *Phys.Rev.*, vol. D77, p. 034003, 2008.
- [26] X. Liu, Z.-G. Luo, Y.-R. Liu, and S.-L. Zhu, “ $X(3872)$ and Other Possible Heavy Molecular States,” *Eur.Phys.J.*, vol. C61, pp. 411–428, 2009.
- [27] X. Liu and S.-L. Zhu, “ $Y(4143)$ is probably a molecular partner of $Y(3930)$,” *Phys.Rev.*, vol. D80, p. 017502, 2009.
- [28] J. L. Rosner, “Threshold effect and $\pi^\pm\psi(2S)$ peak,” *Phys.Rev.*, vol. D76, p. 114002, 2007.
- [29] C. Meng and K.-T. Chao, “ $Z^+(4430)$ as a resonance in the $D(1)(D(1)')D^*$ channel,” 2007.
- [30] N. Mahajan, “ $Y(4140)$: Possible options,” *Phys.Lett.*, vol. B679, pp. 228–230, 2009.
- [31] T. Branz, T. Gutsche, and V. E. Lyubovitskij, “Hadronic molecule structure of the $Y(3940)$ and $Y(4140)$,” *Phys.Rev.*, vol. D80, p. 054019, 2009.

- [32] G.-J. Ding, “Possible Molecular States of $D_s \bar{D}_s$ System and $Y(4140)$,” *Eur.Phys.J.*, vol. C64, pp. 297–308, 2009.
- [33] E. Kou and O. Pene, “Suppressed decay into open charm for the $Y(4260)$ being an hybrid,” *Phys.Lett.*, vol. B631, pp. 164–169, 2005.
- [34] F. E. Close and P. R. Page, “Gluonic charmonium resonances at BaBar and BELLE?,” *Phys.Lett.*, vol. B628, pp. 215–222, 2005.
- [35] L. Maiani, F. Piccinini, A. Polosa, and V. Riquer, “Diquark-antidiquarks with hidden or open charm and the nature of $X(3872)$,” *Phys.Rev.*, vol. D71, p. 014028, 2005.
- [36] L. Maiani, V. Riquer, F. Piccinini, and A. Polosa, “Four quark interpretation of $Y(4260)$,” *Phys.Rev.*, vol. D72, p. 031502, 2005.
- [37] L. Maiani, F. Piccinini, A. Polosa, and V. Riquer, “ X and Y ,” *AIP Conf.Proc.*, vol. 814, pp. 508–512, 2006.
- [38] L. Maiani, F. Piccinini, A. D. Polosa, and V. Riquer, “Diquark-antidiquark states with hidden or open charm,” *PoS*, vol. HEP2005, p. 105, 2006.
- [39] L. Maiani, A. Polosa, and V. Riquer, “The Charged $Z(4433)$: Towards a new spectroscopy,” 2007.
- [40] L. Maiani, A. D. Polosa, and V. Riquer, “The charged $Z(4430)$ in the diquark-antidiquark picture,” *New J. Phys.*, vol. 10, p. 073004, 2008.
- [41] N. Drenska, R. Faccini, and A. Polosa, “Higher Tetraquark Particles,” *Phys.Lett.*, vol. B669, pp. 160–166, 2008.
- [42] N. Drenska, R. Faccini, and A. Polosa, “Exotic Hadrons with Hidden Charm and Strangeness,” *Phys.Rev.*, vol. D79, p. 077502, 2009.
- [43] A. Ali, C. Hambroek, I. Ahmed, and M. J. Aslam, “A case for hidden $b\bar{b}$ tetraquarks based on $e^+e^- \rightarrow b\bar{b}$ cross section between $\sqrt{s} = 10.54$ and 11.20 GeV,” *Phys. Lett.*, vol. B684, pp. 28–39, 2010.
- [44] A. Ali, C. Hambroek, and M. J. Aslam, “Tetraquark interpretation of the BELLE data on the anomalous $\Upsilon(1S)\pi^+\pi^-$ and $\Upsilon(2S)\pi^+\pi^-$ production near the $\Upsilon(5S)$ resonance,” *Phys. Rev. Lett.*, vol. 104, p. 162001, 2010.
- [45] A. G. Grozin, “Heavy quark effective theory,” *Springer Tracts Mod. Phys.*, vol. 201, pp. 1–213, 2004.
- [46] P. Ball, V. M. Braun, and E. Gardi, “Distribution Amplitudes of the Λ_b Baryon in QCD,” *Phys.Lett.*, vol. B665, pp. 197–204, 2008.
- [47] P. Colangelo and A. Khodjamirian, “QCD sum rules, a modern perspective,” 2000.
- [48] A. B. Henriques, B. H. Kellett, and R. G. Moorhouse, “General Three Spinor Wave Functions and the Relativistic Quark Model,” *Ann. Phys.*, vol. 93, p. 125, 1975.

- [49] P. Ball, V. M. Braun, Y. Koike, and K. Tanaka, “Higher twist distribution amplitudes of vector mesons in QCD: Formalism and twist three distributions,” *Nucl. Phys.*, vol. B529, pp. 323–382, 1998.
- [50] A. F. Falk, “Hadrons of arbitrary spin in the heavy quark effective theory,” *Nucl. Phys.*, vol. B378, pp. 79–94, 1992.
- [51] A. G. Grozin and M. Neubert, “Asymptotics of heavy-meson form factors,” *Phys. Rev.*, vol. D55, pp. 272–290, 1997.
- [52] S. Groote, J. G. Korner, and O. I. Yakovlev, “An analysis of diagonal and non-diagonal QCD sum rules for heavy baryons at next-to-leading order in α_s ,” *Phys. Rev.*, vol. D56, pp. 3943–3954, 1997.
- [53] S. Groote, J. G. Korner, and A. A. Pivovarov, “On the evaluation of a certain class of Feynman diagrams in x-space: Sunrise-type topologies at any loop order,” *Annals Phys.*, vol. 322, pp. 2374–2445, 2007.
- [54] V. Braun, P. Gornicki, and L. Mankiewicz, “Ioffe - time distributions instead of parton momentum distributions in description of deep inelastic scattering,” *Phys. Rev.*, vol. D51, pp. 6036–6051, 1995.
- [55] V. M. Braun, D. Y. Ivanov, and G. P. Korchemsky, “The B -Meson Distribution Amplitude in QCD,” *Phys. Rev.*, vol. D69, p. 034014, 2004.
- [56] A. P. Bakulev and S. V. Mikhailov, “Lattice measurements of nonlocal quark condensates, vacuum correlation length, and pion distribution amplitude in QCD,” *Phys. Rev.*, vol. D65, p. 114511, 2002.
- [57] M. A. Shifman, A. I. Vainshtein, and V. I. Zakharov, “QCD and Resonance Physics: Applications,” *Nucl. Phys.*, vol. B147, pp. 448–518, 1979.
- [58] K. G. Chetyrkin, A. Khodjamirian, and A. A. Pivovarov, “Towards NNLO Accuracy in the QCD Sum Rule for the Kaon Distribution Amplitude,” *Phys. Lett.*, vol. B661, pp. 250–258, 2008.
- [59] V. L. Chernyak and A. R. Zhitnitsky, “Asymptotic Behavior of Exclusive Processes in QCD,” *Phys. Rept.*, vol. 112, p. 173, 1984.
- [60] B. O. Lange and M. Neubert, “Renormalization-group evolution of the B -meson light-cone distribution amplitude,” *Phys. Rev. Lett.*, vol. 91, p. 102001, 2003.
- [61] P. Ball and M. Boglione, “SU(3) breaking in K and K^* distribution amplitudes,” *Phys. Rev.*, vol. D68, p. 094006, 2003.
- [62] G. P. Lepage and S. J. Brodsky, “Exclusive Processes in Quantum Chromodynamics: Evolution Equations for Hadronic Wave Functions and the Form-Factors of Mesons,” *Phys. Lett.*, vol. B87, pp. 359–365, 1979.
- [63] F. X. Lee, “Predictive ability of QCD sum rules for decuplet baryons,” *Phys. Rev.*, vol. C57, pp. 322–328, 1998.

- [64] M. Beneke and H. G. Dosch, “Flavor dependence of the mixed quark gluon condensate,” *Phys. Lett.*, vol. B284, pp. 116–122, 1992.
- [65] H. G. Dosch, M. Eidemuller, M. Jamin, and E. Meggiolaro, “The gauge invariant quark correlator in QCD sum rules and lattice QCD,” *JHEP*, vol. 07, p. 023, 2000.
- [66] H. G. Dosch, M. Jamin, and S. Narison, “Baryon masses and flavour symmetry breaking of chiral condensates,” *Phys. Lett.*, vol. B220, p. 251, 1989.
- [67] M. J. A. Ahmed Ali, Christian Hambroek, “Growing evidence of Tetraquarks.” online at 2physics.com, [http://www.2physics.com/search/label/Elementary Particles](http://www.2physics.com/search/label/Elementary%20Particles) 2, May 2010.
- [68] Z. Matthews, “Evidence grows for tetraquarks.” online at physicsworld.com, <http://physicsworld.com/cws/article/news/42475>, Apr 2010.
- [69] M. Campbell, “Elusive tetraquark spotted in a data forest.” online at newscientist.com, <http://www.newscientist.com/article/dn18857-elusive-tetraquark-spotted-in-a-data-forest.html>, May 2010.
- [70] K. Rajagopal, “Color superconductivity,” Prepared for Cargese Summer School on QCD Perspectives on Hot and Dense Matter, Cargese, France, 6-18 Aug 2001.
- [71] P. Cvitanovic, “Group theory: Birdtracks, Lie’s and exceptional groups,” Princeton, USA: Univ. Pr. (2008) 273 p.
- [72] M. G. Alford and R. L. Jaffe, “Insight into the Scalar Mesons from a Lattice Calculation,” *Nucl. Phys.*, vol. B578, pp. 367–382, 2000.
- [73] C. Alexandrou, P. de Forcrand, and B. Lucini, “Evidence for diquarks in lattice QCD,” *Phys. Rev. Lett.*, vol. 97, p. 222002, 2006.
- [74] R. L. Jaffe, “Multi-Quark Hadrons. 2. Methods,” *Phys. Rev.*, vol. D15, p. 281, 1977.
- [75] R. L. Jaffe and F. E. Low, “The Connection Between Quark Model Eigenstates and Low-Energy Scattering,” *Phys. Rev.*, vol. D19, pp. 2105–2118, 1979.
- [76] R. L. Jaffe and F. Wilczek, “Diquarks and exotic spectroscopy,” *Phys. Rev. Lett.*, vol. 91, p. 232003, 2003.
- [77] C. Amsler *et al.*, “Review of particle physics,” *Phys. Lett.*, vol. B667, pp. 1–1340, 2008.
- [78] C. Quigg, “The lost tribes of charmonium,” *Nucl. Phys. Proc. Suppl.*, vol. 142, pp. 87–97, 2005.
- [79] B. Aubert *et al.*, “A Structure at 2175 MeV in $e^+e^- \rightarrow \phi f_0(980)$ Observed via Initial-State Radiation,” *Phys. Rev.*, vol. D74, p. 091103, 2006.
- [80] M. Ablikim *et al.*, “Observation of $Y(2175)$ in $J/\psi \rightarrow \eta\phi f_0(980)$,” *Phys. Rev. Lett.*, vol. 100, p. 102003, 2008.

- [81] C. P. Shen *et al.*, “Observation of the $\phi(1680)$ and the $Y(2175)$ in $e^+e^- \rightarrow \phi\pi^+\pi^-$,” *Phys. Rev.*, vol. D80, p. 031101, 2009.
- [82] C. Bignamini, B. Grinstein, F. Piccinini, A. D. Polosa, and C. Sabelli, “Is the $X(3872)$ Production Cross Section at Tevatron Compatible with a Hadron Molecule Interpretation?,” *Phys. Rev. Lett.*, vol. 103, p. 162001, 2009.
- [83] P. Artoisenet and E. Braaten, “Production of the $X(3872)$ at the Tevatron and the LHC,” *Phys.Rev.*, vol. D81, p. 114018, 2010.
- [84] A. Zupanc, “Hadron Spectroscopy Results from Belle,” 2009.
- [85] N. Drenska *et al.*, “New Hadronic Spectroscopy,” 2010.
- [86] G. 't Hooft, G. Isidori, L. Maiani, A. D. Polosa, and V. Riquer, “A Theory of Scalar Mesons,” *Phys. Lett.*, vol. B662, pp. 424–430, 2008.
- [87] I. Caprini, G. Colangelo, and H. Leutwyler, “Mass and width of the lowest resonance in QCD,” *Phys. Rev. Lett.*, vol. 96, p. 132001, 2006.
- [88] S. M. Roy, “Exact integral equation for pion pion scattering involving only physical region partial waves,” *Phys. Lett.*, vol. B36, p. 353, 1971.
- [89] E. M. Aitala *et al.*, “Experimental evidence for a light and broad scalar resonance in $D^+ \rightarrow \pi^-\pi^+\pi^+$ decay,” *Phys. Rev. Lett.*, vol. 86, pp. 770–774, 2001.
- [90] A. Ali, C. Hambrock, and S. Mishima, “Tetraquark-based analysis and predictions of the cross sections and distributions for the processes $e^+e^- \rightarrow \Upsilon(1S)(\pi^+\pi^-, K^+K^-, \eta\pi^0)$ near $\Upsilon(5S)$,” 2010.
- [91] K. F. Chen *et al.*, “Observation of anomalous $\Upsilon(1S)\pi^+\pi^-$ and $\Upsilon(2S)\pi^+\pi^-$ production near the $\Upsilon(5S)$ resonance,” *Phys. Rev. Lett.*, vol. 100, p. 112001, 2008.
- [92] W. Buchmuller and S. H. H. Tye, “Quarkonia and Quantum Chromodynamics,” *Phys. Rev.*, vol. D24, p. 132, 1981.
- [93] B. Aubert *et al.*, “Measurement of the $e^+e^- \rightarrow b\bar{b}$ cross section between $\sqrt{s} = 10.54$ GeV and 11.20 GeV,” *Phys. Rev. Lett.*, vol. 102, p. 012001, 2009.
- [94] I. Adachi *et al.*, “Observation of an enhancement in e^+e^- to $\Upsilon(1S)\pi^+\pi^-$, $\Upsilon(2S)\pi^+\pi^-$, and $\Upsilon(3S)\pi^+\pi^-$ production near $\sqrt{s} = 10.89$ GeV at Belle,” 2008.
- [95] L. S. Brown and R. N. Cahn, “Chiral Symmetry and $\psi' \rightarrow \psi + \pi + \pi$ Decay,” *Phys. Rev. Lett.*, vol. 35, p. 1, 1975.
- [96] M. B. Voloshin, “Adler’s Selfconsistency Condition in the Decay $\psi'(3700) \rightarrow \psi(3100)\pi\pi$,” *JETP Lett.*, vol. 21, pp. 347–348, 1975.
- [97] V. A. Novikov and M. A. Shifman, “Comment on the $\psi' \rightarrow J/\psi\pi\pi$ Decay,” *Zeit. Phys.*, vol. C8, p. 43, 1981.

- [98] Y.-P. Kuang and T.-M. Yan, “Predictions for Hadronic Transitions in the $B\bar{B}$ System,” *Phys. Rev.*, vol. D24, p. 2874, 1981.
- [99] A. Sokolov *et al.*, “Measurement of the branching fraction for the decay $\Upsilon(4S) \rightarrow \Upsilon(1S)\pi^+\pi^-$,” *Phys. Rev.*, vol. D79, p. 051103, 2009.
- [100] A. Ali, C. Hambrock, and S. Mishima, “work in progress,”
- [101] A. De Rujula, H. Georgi, and S. L. Glashow, “Hadron Masses in a Gauge Theory,” *Phys. Rev.*, vol. D12, pp. 147–162, 1975.
- [102] D. Ebert, R. N. Faustov, and V. O. Galkin, “Masses of tetraquarks with open charm and bottom,” 2010.
- [103] D. Ebert, R. N. Faustov, and V. O. Galkin, “Relativistic model of hidden bottom tetraquarks,” *Mod. Phys. Lett.*, vol. A24, pp. 567–573, 2009.
- [104] Z.-G. Wang, “Reanalysis of the mass spectrum of the scalar hidden charm and hidden bottom tetraquark states,” *Eur. Phys. J.*, vol. C67, pp. 411–423, 2010.
- [105] J.-R. Zhang and M.-Q. Huang, “Could $Y_b(10890)$ be the P -wave $[bq][\bar{b}\bar{q}]$ tetraquark state?,” *JHEP*, vol. 11, p. 057, 2010.
- [106] J.-L. Domenech-Garret and M.-A. Sanchis-Lozano, “QQ-onia package: a numerical solution to the Schrodinger radial equation for heavy quarkonium,” *Comput. Phys. Commun.*, vol. 180, pp. 768–778, 2009.
- [107] S. M. Flatte, “Coupled - Channel Analysis of the $\pi\eta$ and $K\bar{K}$ Systems Near $K\bar{K}$ Threshold,” *Phys. Lett.*, vol. B63, p. 224, 1976.
- [108] M. Ablikim *et al.*, “Resonances in $J/\psi \rightarrow \phi\pi^+\pi^-$ and ϕK^+K^- ,” *Phys. Lett.*, vol. B607, pp. 243–253, 2005.
- [109] A. Abele *et al.*, “ $p\bar{p}$ annihilation at rest into $K(L)K^+\pi^-$,” *Phys. Rev.*, vol. D57, pp. 3860–3872, 1998.
- [110] F. Ambrosino *et al.*, “Scalar mesons at KLOE,” *Nucl. Phys. Proc. Suppl.*, vol. 186, pp. 290–293, 2009.
- [111] F. Ambrosino *et al.*, “Study of the $a_0(980)$ meson via the radiative decay $\phi \rightarrow \eta\pi^0\gamma$ with the KLOE detector,” *Phys. Lett.*, vol. B681, pp. 5–13, 2009.
- [112] M. E. Peskin and D. V. Schroeder, “An Introduction to quantum field theory,” Reading, USA: Addison-Wesley (1995) 842 p.
- [113] G. P. Lepage and S. J. Brodsky, “Exclusive Processes in Perturbative Quantum Chromodynamics,” *Phys. Rev.*, vol. D22, p. 2157, 1980.
- [114] F. Mandl and G. Shaw, “Quantum Field Theory,” Chichester, Uk: Wiley (1984) 354 p. (A Wiley-interscience Publication).
- [115] E. Byckling and K. Kajantie, “Particle Kinematics,” *John Wiley and Sons*, 1973.

- [116] S. Dubynskiy and M. B. Voloshin, “Remarks on the amplitude of the decay $\Upsilon(3S) \rightarrow \Upsilon(1S)\pi\pi$,” *Phys. Rev.*, vol. D76, p. 094004, 2007.
- [117] F. Ambrosino *et al.*, “Dalitz plot analysis of $e^+e^- \rightarrow \pi^0\pi^0\gamma$ events at $\sqrt{s} \simeq M(\Phi)$ with the KLOE detector,” *Eur. Phys. J.*, vol. C49, pp. 473–488, 2007.
- [118] F. Ambrosino *et al.*, “Study of the decay $\Phi \rightarrow f_0(980)\gamma \rightarrow \pi^+\pi^-\gamma$ with the KLOE detector,” *Phys. Lett.*, vol. B634, pp. 148–154, 2006.
- [119] F. Ambrosino *et al.*, “Study of the radiative decay $\phi \rightarrow a_0(980)\gamma$ with the KLOE detector,” 2007.
- [120] T. Feldmann and P. Kroll, “Flavor symmetry breaking and mixing effects in the $\eta\gamma$ and $\eta'\gamma$ transition form factors,” *Eur. Phys. J.*, vol. C5, pp. 327–335, 1998.
- [121] T. Feldmann, P. Kroll, and B. Stech, “Mixing and decay constants of pseudoscalar mesons,” *Phys. Rev.*, vol. D58, p. 114006, 1998.
- [122] T. Feldmann and P. Kroll, “Mixing of pseudoscalar mesons,” *Phys. Scripta*, vol. T99, pp. 13–22, 2002.
- [123] C. Dappiaggi, T.-P. Hack, J. Moller, and N. Pinamonti, “Dark Energy from Quantum Matter,” 2010.

Index

- R_b -scan of BaBar data, 55
- BES (Beijing Spectrometer) experiment, 119
- Borel transform, 85
- Breit-Wigner model, 55
- CB (Crystal Barrel) experiment, 119
- Charge conjugation matrix, 79
- Coupling $Y_b e^+ e^-$, 50
- Data Belle $\Upsilon(1S) \pi^+ \pi^-$ and $\Upsilon(2S) \pi^+ \pi^-$, 37
- Decay $\Upsilon(nS) \rightarrow \Upsilon(mS) \pi^+ \pi^-$, 38
- Decay width $f_2(1270)$, 63
- Dimensional regularization, master integrals, 83
- Diquark, 27
- Diquark effective charge, 49
- Diquark *good, bad*, 30
- Dirac field, 80
- Dirac matrices, 79
- Discriminator, 29
- Exclusive, 40
- Feynman parameters, 84
- Flatté couplings, 63
- Gegenbauer polynomials, 22
- Gluon field, 81
- Hadronic molecules, 31
- HQET, 3
- Hybrid hadrons, 31
- Inclusive, 40
- Interpolating operators local b -baryon, 16
- Interpolating operators non-local b -baryon, 14
- Invariant mass, 37
- KLOE (K LOnG Experiment), 119
- Laplace transform inverse, *see* Borel transform
- Light-cone coordinates, 14
- Model b -baryon LCDAs, 21
- Model for $e^+ e^- \rightarrow Y_b \rightarrow \Upsilon(nS) PP'$, 60
- Model plots b -baryon LCDAs, 26
- Multiplet b -baryon ground states, 11
- One gluon exchange model, 28
- Parity transformation, 12
- Pauli matrices, 79
- Pentaquarks, 31
- Phase space n -body, 107
- Propagator b -quark, 4
- Propagator $f_2(1270)$, 63
- Propagator light-quark in QCD background, 19
- QCD sum rules, 86
- Rarita-Schwinger vector-spinor, 16
- Renormalization b -baryon LCDAs, 23
- Resonance interchange, 55
- Spherical harmonics, 82
- Spin decoupling heavy-quark, 5
- Spinors two component, 80
- Tetraquark, 27
- Tetraquark $e^+ e^-$ decay width, 51
- Tetraquark isospin breaking, 48
- Tetraquark masses, 48
- Tetraquark total decay width, 51
- Tetraquark two-body decay widths, 51
- Tetraquarks light $J^{PC} = 0^{++}$, 33
- Vacuum condensates non-local, 19
- Van Royen-Weisskopf formula, 49, 102
- Vertex $f_2 PP'$, 62
- Vertex $S PP'$, 62
- Vertex $Y_b^I \Upsilon(nS) f_2$, 62
- Vertex $Y_b^I \Upsilon(nS) S$, 62
- Vertex effective resonance, 62
- Vertices continuum contributions, 64
- Wilson line, 10